DEGRADATION TESTING OF MAGNESIUM AND ITS ALLOYS AIMING AT BIODEGRADABLE IMPLANT APPLICATIONS

Iñigo MARCO

Supervisor:
Prof. Dr. ir. Omer Van der Biest

Members of the Examination Committee:
Prof. Dr. ir. Patrick Wollants, Chairman
Prof. Dr. rer. nat. Regine Willumeit-Römer
Dr. rer. nat. Frank Feyerabend
Prof. Dr. ir. Jan Van Humbeeck
Prof. ir. Marc De Bonte
Prof. Dr. ir. Jennifer Patterson

Dissertation presented in partial fulfilment of the requirements for the degree of Doctor of Engineering Science (PhD): Materials Engineering

December 2016

Uitgegeven in eigen beheer, Iñigo MARCO, Kasteelpark Arenberg 44 bus 2450, B-3001 Heverlee (Belgium)

Acknowledgements

"It's supposed to be hard. If it wasn't hard, everyone would do it. It's the hard what makes it great."
(Tom Hanks)

Firstly, I would like to express my sincere gratitude to my promotor and mentor **Prof. Dr. ir. Omer Van der Biest** for the continuous support of my PhD study, for his patience, motivation, and expertise. His guidance helped me during my research. He highly contributed to the writing of this thesis and our publications. I really appreciate him for giving me the opportunity to work at the Department of Materials Engineering (MTM). I was still working on my master thesis at the University of Sheffield when I was told about this position as PhD student. Fortunately, the topic of this PhD was closely related to my previous research experience and, although it was hard to make the decision of coming to Leuven, I could not refuse such an offer. In the end, I am glad I took this step.

Besides my promotor, I would like to thank the rest of my thesis supervisory committee: **Prof. Dr. rer. nat. Regine Willumeit-Römer** (Helmholtz Zentrum Geeshacht (HZG)), and **Prof. Dr. ir. Jan Van Humbeeck**, for their constructive comments and encouragement, but also for pushing me in the correct direction throughout my research. I must thank them for their comments and suggestions. I wish to express my gratitude to all the examination committee, **Prof. ir. Marc de Bonte** and **Prof. Dr. ir. Jennifer Patterson** for reading this doctoral thesis carefully and for the detailed and constructive feedback. Special thanks to **Dr. rer. nat. Frank Feyerabend** for his advice and guidance on my experimental work and feedback on my writing. His visits to MTM were highly appreciated. Also thanks to him, I could perform some interesting experiments during my secondment at HZG. Also thanks to the chairman of my examination committee, **Prof. Dr. ir. Patrick Wollants**.

I would like to warmly thank my colleague and officemate **Andrea Gil** for the countless hours we spent in the office working-hard to achieve our respective PhD degrees. I appreciate all the coaching she did, the collaborations we had and also the great experiences during the many trips we did together. But especially thanks for all the fun we have had in the last 4 years, both in working and free time.

This thesis is also the result of many experiences I have encountered at MTM from dozens of remarkable people who I wish to acknowledge. For this reason thanks to **Kim Vanmeensel** and **Bram Neirinck** for all the help, support and kind advice during the time we shared in our more-than-half-Spanish office. I am glad we had the opportunity to sit next to each other for a bit more than 2 years. I learnt a lot from both, while they also guided me, especially in the beginning. Special thanks to Kim for all the fun we also had in our free time outside MTM, e.g. playing football. I must say that his football skills and enthusiasm never decreased.

This work would not have been possible without the help of technical staff from MTM. Thanks to **Joop van Deursen** for the quick works he did for me to build my experimental setups. Also thanks to **Pieter L'hoëst, Britt Vandenbroeck, Iris Cuppens, Paul Crabbe and Tom Van der Donck** for supplying me with everything I needed, and for the time they spent training me and working with me. And finally thanks to the administrative staff, especially **Huberte Cloosen, Mia Pierre, Mieke Van Audenhoven, Dirk Hoeybergh** for their assistance with financial and travel management, and other similar tasks.

This thesis is done within the MagnIM project supported by the PEOPLE Programme (Marie Skłodowska-Curie Actions) of the European Union's Seventh Framework Programme (FP7/2007-2013/) under REA grant agreement n°289163. The name of the project, "MagnIM", stands for "Magnesium Implant". MagnIM is a highly interdisciplinary European network where physicists, material scientists, biologists, medical doctors and surgeons from eight partners and six countries have intensively collaborated. Therefore, I also thank all the **colleagues and collaborators in the MagnIM project** in the following institutions: Helmholtz Zentrum Geeshacht (HZG), Medical University of Graz (MUG), Malmö University (MAH), Charles University in Prague, aap Biomaterials and Conmed. I will remember many great experiences from the workshops, visits and meetings we attended. I want to acknowledge **Kimmo Lähteenkorva** and **Ophir Ortiz** for letting us visit Conmed in Tampere (Finland) and also in Largo (Florida, US).

I want to thank the rest of the powder metallurgy group: **Jef Vleugels, Karel, Thomas, Fei, Chen, Bolu, Despoina, Vera, Akhilesh, Nachiketa** and **Annabel**. It was a great experience to be part of this group, and I will warmly remember the great PM weekend trips we had. I would also like to thank the rest of my friends and colleagues from MTM: **Bey, Gokul, Nicolo, Oksana, Gregory, Gijs, Nick, Stijn, Joris, Franziska, Agha, Anastasiya, Joao, Minxian, Maria, Lucas, Ehsan, Maxime, Louis, Ali, Xiebin, Bin** and anyone else who shared nice moments with me at MTM. I am truly lucky to have met them and to be able to spend some fun time together with them. I also want to mention **Sergio Portoles**. Without his help I would not have had such an easy start in Leuven. He also helped me taking the decision to come to Leuven when I was still struggling with my master thesis in Sheffield. I also want to thank **Javier Trinidad, Gurutze Arruebarrena and Eneko Saez de Argandoña** for introducing me to the biodegradable Mg implant field at Mondragon University.

A special thanks to my partner, **Lies**, who was always my support. Specially thanks for listening to my problems and helping me 24/7. With her help and advice I have managed to finish this PhD degree. We had the luck to meet at MTM, and thereby, my decision to come to Leuven is proved right. I also want to thank **Lies' family** for the support I received from them.

I also want to mention **my family,** for supporting me accross the distance to achieve my goals throughout this thesis, and my life in general. I really enjoyed the time we spend when you visited me.

Iñigo Marco

Leuven, December 2016

Abstract

Magnesium and its alloys are increasingly interesting materials for biodegradable implant applications. The advantage of these implants is that they gradually degrade in the human body after fulfilling the purpose of their implantation. For instance, biodegradable implants can be used in orthopaedic applications such as fracture stabilisation, eliminating the need of a second operation for non-degradable implant, e.g. titanium removal. One challenge of biodegradable Mg implants is that the properties required by the implants are application-specific. This means that the implant must be selected depending on both implantation site and patient characteristics in order to obtain the correct implant performance during the healing process.

Therefore, in this thesis, swift and slow degrading Mg alloys are studied, by adding silver (Ag) and gadolinium (Gd) as alloying elements, respectively. On the one hand, corrosion can be accelerated by adding Ag increasing the antibacterial properties of the Mg alloy. On the other hand, Mg-Gd binary alloys show a slow degradation due to the reduction of the influence of impurities such as Fe, Ni or Cu. Pure Mg and Mg-4Y-3RE are also included as references to other studies. The reason to choose Mg-4Y-3RE is because it is similar to the alloys currently applied as biodegradable implants. Thus, the degradation behaviour of these Mg based materials are studied by applying electrochemical and immersion testing techniques. In order to understand the Mg degradation, many factors have to be considered regarding testing conditions and material.

Firstly, the testing conditions have a large influence on the Mg alloy degradation behaviour. These conditions are mainly defined by electrolyte, buffering, atmosphere, electrolyte volume to sample surface (V/S) ratio and sample positioning. With the aim to investigate some of these factors different testing conditions have been applied in immersion tests in vitro of the Mg based materials introduced above. The media applied in vitro are: phosphate buffered saline (PBS), Hank’s balanced salt solution (HBSS) and Dulbecco’s modified eagle medium (DMEM). When DMEM is applied also 5 vol.% of CO_2 is added to the atmosphere to increase the buffering capacity. Large differences in degradation rate are found between Mg-Gd and Mg-Ag in PBS and HBSS while in DMEM the difference in degradation rate is reduced. Basically the chlorine content in the medium and the degradation layer formation process have a crucial influence on the degradation behaviour.

Secondly, the degradation behaviour of the material also depends on the different alloying additions and processing routes which induce considerable alterations of the microstructure and impurity content. Therefore, the degradation behaviour of pure Mg, Mg-10Gd and Mg-2Ag, produced in disc and pin shape, are compared by in vitro and in vivo experiments, respectively. This analysis reveals the large influence of the impurity content of Fe and Ni as well as the grain size on the degradation performance in vivo, whereas the role of alloying additions such as Gd and Ag are found less important. In this study, the degradation rate and the surface layers determined in DMEM are found more comparable to those determined in vivo. This indicates that DMEM mimics more closely in vivo conditions. However, to achieve this mimicking when DMEM is applied, the need of sterilization measures has been identified. Otherwise, medium contamination will accelerate the Mg degradation behaviour by acidifying the electrolyte and dissolving Ca and P rich corrosion products present at the degradation layer.

Electrochemical methods, such as potentiodynamic polarization (PDP) experiments, give a quick comparison between the degradation profiles of different Mg alloys. This technique is commonly used as the first test for degradation characterization. Surface layer formation during polarization under non-dynamic conditions is considered to play a major role in the results. The use of the rotating disc electrode (RDE) can induce a dynamic flow around the Mg working electrode, increasing the transport of the dissolved Mg^{2+} ions away from the surface and thus reducing the surface layer formation. Parameters such as rotation speed and scan rate have been analysed finding that values higher than 1500 rpm for the rotation and 5 mV/s for the scan rate allow for more reproducible measurements without degradation layer deposition. Hence, PDP measurements with the RDE can show repeatedly characteristic curves of the material-electrolyte system and give what is considered a better estimation of the initial degradation rate.

Surface treatments are widely studied in order to tailor the surface properties and the degradation behaviour of Mg implants. Some coatings could allow the addition of a drug to the implant which could help during the first inflammatory reaction or during the healing process. In this thesis, the first steps towards a new biodegradable drug delivery system are shown. This system consists of metal organic frameworks (MOFs). MOFs are promising materials as drug nano-carriers for their nanoporous structure and, in literature, they are also considered “bio-friendly”. Mg can be used as the metal in the MOF structure, which is called Mg-MOF. Currently, Mg-MOF is produced hydrothermally, and in this thesis, the principles of electro-synthesis of Mg-MOF layers on a Mg substrate, are demonstrated.

Degradatietesten van magnesium en magnesium legeringen voor biologisch afbreekbare implantaten

Samenvatting

Magnesiumlegeringen zijn interessante materialen voor bio-afbreekbare implantaten. Het voordeel van zulke implantaten ligt in het feit dat ze langzaam door het menselijk lichaam worden afgebroken nadat ze hun taak hebben vervuld. Zo kunnen dus bio-afbreekbare implantaten bijvoorbeeld gebruikt worden in de orthopedie als breukstabilisatoren. Een daarop volgende operatie om een niet-afbreekbaar implantaat weg te nemen, bv. uit titaan, is dus niet langer nodig. De uitdaging bij bio-afbreekbare implantaten uit magnesium is dat de vereiste eigenschappen specifiek zijn voor elke toepassing. Dit betekent dat het implantaat geselecteerd dient te worden op basis van zowel de implantatielocatie als de karakteristieken van de patiënt zodat het implantaat correct functioneert gedurende het genezingsproces.

Voor dit doel worden in deze thesis snel- en traagafbrekende magnesiumlegeringen onderzocht. Daarvoor werden respectievelijk zilver (Ag) en gadolinium (Gd) als legeringselementen toegevoegd. Enerzijds kan de toevoeging van zilver de corrosiesnelheid van magnesium verhogen wat de antibacteriële eigenschappen verbetert. De toevoeging van gadolinium leidt anderzijds tot een langzame degradatie omdat de invloed van onzuiverheden zoals ijzer, nikkel of koper wordt verlaagd. Ter vergelijking met andere studies zijn ook zuiver magnesium en magnesiumlegering Mg-4Y-3RE onderzocht. Mg-4Y-3RE is gekozen omdat het gelijkaardig is aan de legeringen die momenteel worden gebruikt voor bio-afbreekbare implantaten. Het degradatiegedrag van deze magnesium-gebaseerde legeringen is bestudeerd aan de hand van elektrochemische en immersietechnieken. Om het degradatiegedrag van magnesium te kunnen begrijpen dienen meerdere factoren met betrekking tot de gebruikte omstandigheden en materialen in rekening gebracht te worden.

Ten eerste hebben de testomstandigheden een grote invloed op het degradatiegedrag van magnesiumlegeringen. Deze parameters bestaan hoofdzakelijk uit het elektroliet, buffers, atmosfeer, de verhouding tussen het elektrolietvolume en de oppervlakte van het monster (V/S-ratio) en de positionering van het monster. Om enkele van deze verschillende testomstandigheden te onderzoeken zijn in vitro-immersietesten uitgevoerd op de eerder vermelde magnesiumlegeringen. De oplossingen die in de “in vitro” testen werden gebruikt zijn fosfaat-gebufferde zoutoplossingen (PBS), Hanks gebalanceerde zoutoplossing (HBSS) en Dulbecco’s gemodificeerde eagle medium (DMEM). Bij het gebruik van DMEM werd ook 5 vol.% CO_2 toegevoegd aan de atmosfeer om de buffercapacitieit te verhogen. In PBS werden grote verschillen in de

degradatiesnelheid opgemerkt tussen Mg-Gd en Mg-Ag terwijl de verschillen in DMEM verkleinden. Het chloorgehalte van de oplossing en de vorming van een laag degradatieproducten hebben een cruciale invloed op het degradatiegedrag.

Ten tweede hangt het degradatiegedrag van het materiaal af van de verschillende legeringselementen en bewerkingsstappen die significante wijzingen kunnen aanbrengen in de microstructuur en de hoeveelheid onzuiverheden. Daarom werd het degradatiegedrag van zuiver magnesium, Mg-10Gd en Mg-2Ag, geproduceerd in schijf- of pinvorm, vergeleken met respectievelijk “in vitro” testen en “in vivo” testen. Deze analyse toonde de grote invloed aan van ijzer- en nikkelonzuiverheden, alsook die van de korrelgrootte op het “in vivo” degradatiegedrag. Daarbij was de rol van Gd- en Ag-toevoegingen van minder belang. Uit deze studie bleek dat de degradatiesnelheid en de oppervlaktelagen bepaald in DMEM beter overeenkwamen met “in vivo” testen. DMEM is dus een betere imitatie voor “in vivo” testen. Echter, om het imitatiegedrag van DMEM te bereiken is sterilisatie ook noodzakelijk. Zo niet zal contaminatie van het medium de degradatie van magnesium versnellen door het verzuren van het elektroliet waardoor corrosieproducten, rijk aan calcium en fosfor, die aanwezig zijn in de degradatielaag oplossen.

Elektrochemische methodes, zoals potentiodynamische polarisatie (PDP) laten toe om snel een vergelijking te maken van het degradatieprofiel van verschillende magnesiumlegeringen. Deze test wordt dan ook vaak als eerste gebruikt om de degradatie te karakteriseren. De vorming van een oppervlaktelaag onder polarisatie bij niet-dynamische condities, heeft een grote invloed op het resultaat. Het gebruik van een roterende schijfelektrode (RDE) kan een dynamische stroming op gang brengen rond de magnesium werkelektrode. Hierdoor verhoogt het transport van opgeloste Mg^{2+}ionen weg van het oppervlak en vermindert de drijfkracht voor de vorming van een oppervlaktelaag. Parameters, zoals de rotatiesnelheid en de scansnelheid, zijn geanalyseerd en het bleek dat rotatiesnelheden hoger dan 1500 rpm en scansnelheden boven 5 mV/s toelaten om meer reproduceerbare data te verkrijgen zonder de vorming van een degradatielaag. Zodoende kunnen PDP-experimenten met een RDE karakteristieke curves opleveren van het materiaal-elektrolietsysteem en een betere schatting van de initiële degradatiesnelheid.

Oppervlaktebehandelingen zijn goed bestudeerd om de oppervlakte-eigenschappen en het degradatiegedrag van magnesiumimplantaten te beïnvloeden. Bepaalde implantaatcoatings kunnen een geneesmiddel bevatten dat helpt bij het bestrijden van ontstekingsreacties of in latere stappen van het genezingsproces. In deze thesis is de eerste stap getoond naar een nieuwe manier om een bio-afbreekbaar systeem op te bouwen voor de toediening van geneesmiddelen. Dit systeem bestaat uit zogenaamde Metaal-Organische structuren (MOFs). MOFs zijn veelbelovende materialen om medicijnen in nanovorm te vervoeren omwille van hun nanoporeuze structuur. In de literatuur worden ze aanzien als biocompatibel. Magnesium kan de rol van metaal aannemen in MOFs, wat leidt tot een Mg-MOF. Momenteel worden Mg-MOFs hydrothermaal geproduceerd. In deze thesis is het principe aangetoond om Mg-MOFs aan te maken bij middel van elektrosynthese op een magnesium substraat. Dit zorgt voor de capaciteit om geneesmiddelen te transporteren.

Symbols and abbreviations

Symbols:

ΔW	mass difference	[g]
A	sample area	[cm^2]
t	immersion time	[h]
ρ	density	[$g\ cm^{-3}$]
V_{H2}	H_2 volume corresponds	[ml]
T	temperature	[K]
ω	Rotation speed	[rpm or rad s^{-1}]
δ	Diffusion layer thickness	[cm]
D_o	Diffusion coefficient of the species	[$cm^2\ s^{-1}$]
ν	Kinematic viscosity	[$cm^2\ s^{-1}$]
i_{corr}	Corrosion current density	[A cm^{-2} or A m^{-2}]
E_{corr}	Corrosion potential	[V vs reference]
E_o	Standard potential	[V vs reference]
β_a	Anodic slope	[V $decade^{-1}$]
β_c	Cathodic slope	[V $decade^{-1}$]
R_p	Polarization resistance	[$\Omega\ cm^2$]
n or z	number of electrons	[no units]
m	Mg mass	[mol]
Q	Charge	[C]

Constants:

F	Faraday constant, 96.485	[C/mol]
R	The universal gas constant, 8.314	[J/(mol·K)]
	or in other units 0.082	[atm L $mol^{-1}\ K^{-1}$]
Re_c	Reynolds number- turbulent limit, $2x10^5$	[no units]
P_{atm}	atmospheric pressure, 1.013	[atm]
M	Mg molar mass, 24.31	[$g\ mol^{-1}$]

Abbreviations:

ASTM	American Society for Testing and Materials
BET	Brunauer-Emmett-Teller surface coefficient
BSA	Bovine serum albumin
Ca-P	Calcium phosphate
CPE	Constant phase element
CPO	Coordination Polymer from Oslo
DHTA	2,5-dihydroxyterephthalic acid
DLM	Degradation layer mass
DMEM	Dulbecco’s modified eagle medium
DR	Degradation rate
DR H2	degradation rate by H_2 evolution
EBSS	Earl’s balanced salt solution
ECAP	equal channel angular pressing
ECS	Enhanced catalytic surface
EIS	Electrochemical impedance spectroscopy
EIS	Electrochemical impedance spectroscopy
FBS	Fetal bovine serum
HA	Hydroxyapatite
HBSS	Hank’s balanced salt solution
HCP	Hexagonal close-packet
HER	H_2 evolution reaction
ICP-OES	Inductively coupled plasma - optical emission spectroscopy
MEM	Minimum essential medium
ML	Mass loss
MOF	Metal organic framework
MR	Mass reduction
NDE	Negative difference effect
OCP	Open circuit potential
P-B	Pilling-Bedworth ratio
PBS	Phosphate buffered saline
PDP	Potentiodynamic polarization
PGA	polyglycolide
PLA	poly-L-lactide
PTFE	Polytetrafluoroethylene or Teflon
RDE	Rotating disc electrode
RE	Rare earth
REE	Rare earth elements
SBF	Simulated body fluid
SEM	Scanning electron microscopy
SVET	Scanning vibrating electrode technique
TCP	Tricalcium phosphate
UV	Ultra-violet
V/S	Electrolyte volume to sample surface ratio
XRD	X-ray diffraction
WP	Work-package

Table of contents

Chapter 1:
Introduction and literature review

1.1. Background on magnesium as a biodegradable implant

Magnesium (Mg) and its alloys are promising materials for many applications. Its low density makes Mg an interesting material for reducing the mass of structures, for example in airplanes, where the low weight is an added value. Throughout history, Mg has also been used as igniting bands or wires for flash lights of the photographic industry or for pyrotechnical use due to its chemical reactivity in contact with oxygen [1]. In addition, Mg offers great potential in biomedicine, and it is one of the most promising materials for biodegradable implant applications [2, 3].

Magnesium ion is the fourth most abundant metal ion in cells and participates in the normal formation and remodelling of bone. Therefore, Mg is one of the most important factors in bone health. Traditionally calcium has received an enormous amount of attention, but Mg plays an even more important role in bone healing and healthy bone formation. Among other activities, magnesium regulates the active calcium transport [4-6]. Higher Mg intakes have shown to lead to a greater bone mineral density in elderly men and women [7]. Magnesium hydroxide therapy appears to have prevented fractures and resulted in a significant increase in bone density [6]. As a result, there has been a growing interest in the role of Mg ion especially in relation to bone metabolism.

Non-degradable implants such as steel-based, cobalt-chromium and titanium-based implants are commonly used in orthopaedic surgery. Although they are inert implants and promote osseointegration, they are also associated with interference on imaging techniques, and may induce stress shielding, osteopenia, inflammation of adjacent tissues or sarcoma which leads to the implant explantation [8]. Castellani et al. investigated whether bone-implant interface strength and osseointegration of a novel biodegradable magnesium alloy, based on WE43 (a Mg alloy with 4 wt.% Y, 3 wt.% rare earths (i.e. Ce, Nd, Gd) and less tha 1 wt.% of Zr), is comparable to that of a titanium control (Ti-6Al-7Nb) currently in clinical use [9]. Biomechanical push-out testing, micro CT and SEM were performed in 72 Sprague-Dawley rats 4, 12 and 24 weeks after implantation to address this question. Castellani et al. concluded that the tested biodegradable Mg implant is superior to the titanium control with respect to bone-implant interface strength and osseointegration [9]. These results suggest that the investigated biodegradable magnesium alloy not only stimulates bone formation but also achieves excellent interfacial strength fulfilling two critical requirements for bone implant applications.

Degradable polymeric implants, such as poly-L-lactide (PLA) and polyglycolide (PGA) homopolymers, are also currently being investigated. However, their degradation rate can be too low and can induce foreign body reactions [10, 11]. Moreover, as shown in Table 1, biodegradable polymers are mechanically weaker as compared to Mg [12, 13].

Hence, as stated above, magnesium can be used as biodegradable temporal implant due to its similar density and mechanical properties compared to cortical bone [2, 12, 13] (Table 1), and non-toxicity [14, 15]. In addition, Mg shows a good biocompatibility in many biomedical applications considering both the material and the biological host. To avoid misunderstandings, the term biocompatibility must be defined, which is the ability of a material to perform with an appropriate host response in a specific application [16]. Due to complete Mg biodegradation [17], no second surgery for the removal of the implant is needed, which lowers health costs and improves the quality-life of the patient. Hereby, it is especially interesting for younger patients.

Table 1. Density and mechanical properties of different biomaterials. Data from Ref. [2, 12, 13, 18].

	Density (g/ cm^3)	Elastic modulus (GPa)	Compressive yield strength (MPa)	Fracture toughness (MPa/m^2)
Cortical bone	1.8-2.1	3.0-20	130-180	3.0-6.0
Synthetic HA	3.1	73-117	600	0.7
Mg alloy	1.74-2	41-45	65-100	14-40
Ti Alloy	4.4-4.5	110-117	758-1117	55-115
Stainless steel	7.9-8.1	189-205	170-310	50-200
Co-Cr alloy	8.3-9.2	230	450-1000	-
PGA	1.61	6.5	-	-
PLA	1.24	2.5	-	-

Surgeons have explored Mg and its alloys for numerous clinical applications, including the cardiovascular, musculoskeletal and general surgery, for more than 100 years [1]. Some application examples are: plates, screws or intramedullary fixator in orthopaedic applications, stents for revascularization, scaffolds for tissue engineering, suture staples and wire [19], or even new applications can be aimed, e.g. in dental applications as metallic mesh implant for jaw bone generation. Fig. 1 depicts examples of

Mg implants. However, its degradation performance is often uncontrolled and unpredictable, which limits its applicability.

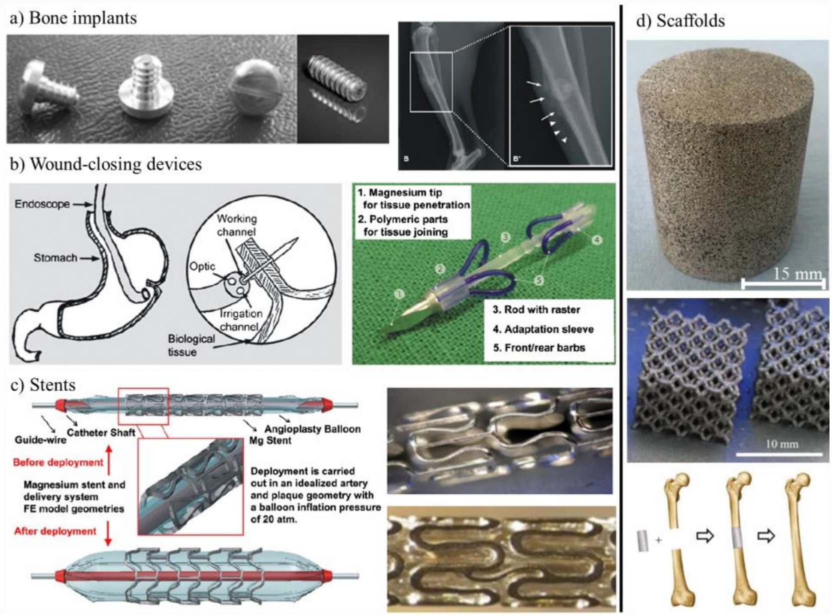

Figure 1. Examples of biodegradable Mg implant applications in biomedicine. (a) Screws for orthopaedic applications [19, 20]. (b) Wound-closing devices [20]. (c) stents for artery revascularization [19, 20]. (d) scaffolds for tissue engineering produced by replication casting [21] or by selective laser melting [22]. Figures are edited and reprinted with permission.

1.1.1. History of biodegradable magnesium

The history of biodegradable magnesium implants started shortly after the discovery of elemental magnesium by Sir Humphrey Davy in 1808. But it was his assistant, Michael Faraday, who enabled the production of Mg metal by electrolysis of fused anhydrous $MgCl_2$ in 1833 [1]. Only at the end of the 19th and mainly at the beginning of the 20th century was Mg widely investigated as biomedical device breaking the paradigm in biomaterial science to develop only highly corrosion resistant metals.

In 1878 Edward C. Huse used Mg wires as ligatures to stop bleeding vessels [23]. In 1900 Payr applied Mg connectors for anastomosis of arterial and venous blood vessels in pigs and dogs (Fig. 2a) [24]. In 1906 Lambotte and Verbrugge used Mg plate and steel screws for fixating humerus fractures in children (Fig 2b) [25]. From this study Lambotte learned that Mg could only be implanted without combining it with other metallic implants to prevent macrogalvanic corrosion. In all his studies, the patient healed without complications except for the H_2 gas cavities observed which did not cause pain (Fig. 2b).

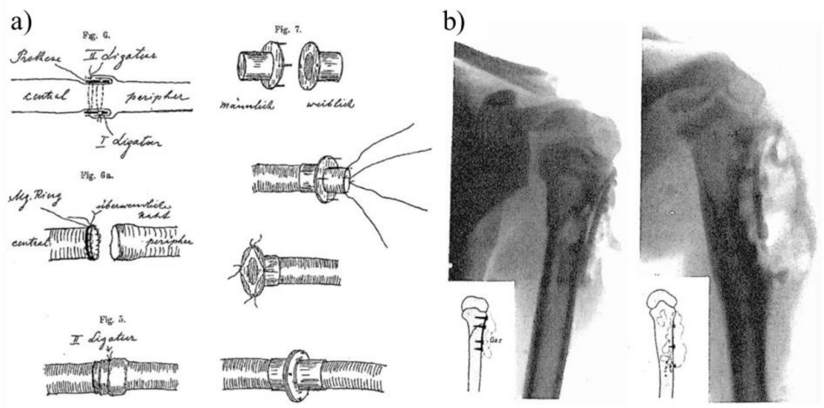

Figure 2. Magnesium research in biomedicine during the 19th and 20th century. (a) Tubal magnesium connectors designed by Payr for vessel anastomosis [24]. (b) magnesium plate and screws used by Verbrugge [25] to stabilize a diaphyseal humerus fracture in an 8 year old child, where gas cavities are visible and the plate was corroded at 3 weeks after the operation [1]. Figures are edited and reprinted with permission.

Although these investigations revealed obvious advantages of Mg alloys, they were abandoned due to their, at that time considered undesirable degradation in addition to the boom of inert stainless steel. As Mg alloy technology advanced, both the mechanical and corrosion properties have been improved and the idea of temporary implant materials is, thus, rediscovered. Therefore, several key issues for biodegradable magnesium alloys have been widely investigated over the last decade, including the selection of alloying elements, adjustment of microstructural and mechanical properties, biodegradation mechanisms and their influencing factors, control of degradation rates and ion release; and in vitro and in vivo biocompatibility.

1.2. Biodegradable Mg implants

Even though Mg and its alloys have been investigated as implants for more than one century, many commercial implants made of Mg and its alloys are still not available. Luthringer et al. reviewed in 2014 the state of the art of the latest biodegradable Mg products [26].

MAGNEZIX® compression screw (CS) is one example of the few orthopaedic Mg implants available [26]. The first one was developed by Syntellix AG (Hannover, Germany) (Fig. 3a). This screw is based on the Mg alloy system Mg-Y-RE-Zr which is the commercial WE43 alloy. This alloy contains 4 wt.% of yttrium, 3 wt.% of rare earths (Nd, Gd or Ce); and less than 1 wt.% of zirconium. Comparing this Mg implant to titanium as a standard, it has shown good biocompatibility and osteoconductive properties as a fixator during chevron osteotomy in patients with a mild hallux valgus [27]. MAGNEZIX ® CS is clinically used in metacarpals, metatarsals, phalanges and humerus fractures, and to date, there have been approx. 3,000 operations world-wide performed with the MAGNEZIX® CS 3.2 screw [28]. Magnesium Elektron (Swinton, England) is also developing a Mg based biodegradable implant material through its SynerMag Technology Centre [29]. This material is already certified for human applications by ISO 13485:2012 [30].

Mg based stents are being developed by BIOTRONIK (Berlin, Germany) (Fig. 3b). The first generation of stents made of 92.5% magnesium and 7.5% rare-earths were developed for clinical studies within the PROGRESS-AMS (Clinical Performance and Angiographic Results of Coronary Stenting with Absorbable Metal Stents or PROGRESS-AMS). After 4 months, AMS stents were nearly completely degraded although restenosis was also observed [31, 32] [32, 33]. Follow-up tests with coronary angiography and intravascular ultrasound (IVUS) at four, 12, and 28 months, and clinical assessment at 6 and 12 months revealed a device and procedural success rates of 100% [33, 34] [34, 35]. The second generation of BIOTRONIK AMS (Drug-Eluting Absorbable Metal Scaffold or DREAMS) was developed to elute Paclitaxel, originally used in cancer therapy as an antiproliferative drug, with a poly(lactic-co-glycolic acid) carrier. The stent scaffold was changed as well as the magnesium-alloy composition [35, 36] [36, 37]. Development of the BIOTRONIK AMS was furthered by adding tantalum radiopaque end markers and replacing Paclitaxel with Sirolimus (DREAMS 2G AMS). Between Oct 8, 2013, and May 22, 2015, 123 patients with 123 coronary target lesions were enrolled in this study showing implantation of the DREAMS 2G device in de-novo coronary lesions for treatment of obstructive coronary disease is feasible, with favourable safety and performance outcomes at 12 months [37]. Based on this study, Magmaris achieved CE marking in June 2016 [38].

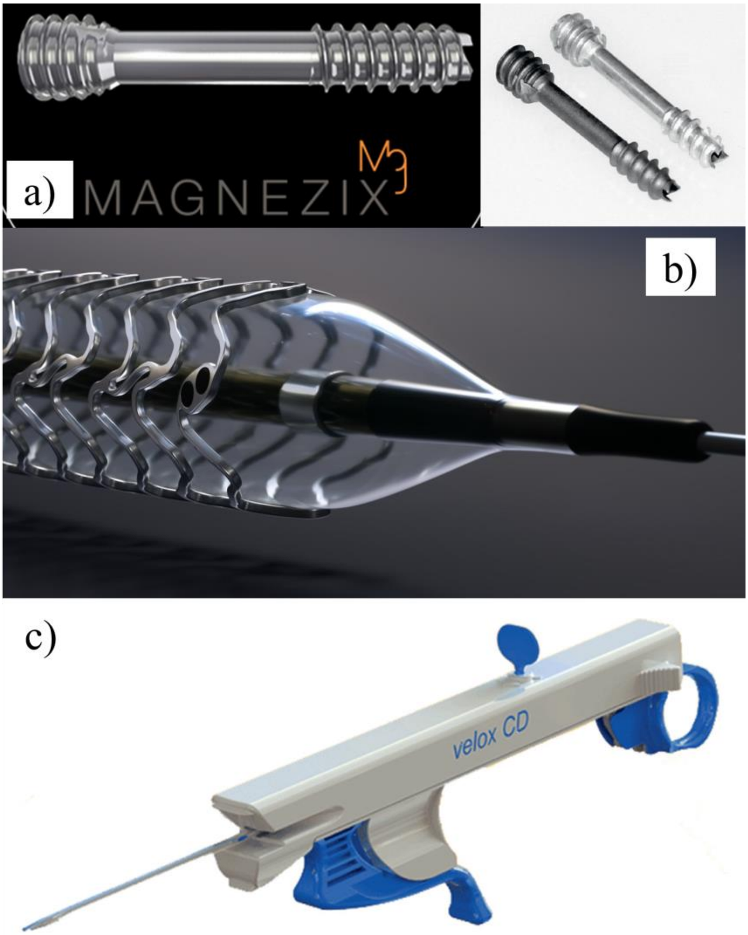

Figure 3. Biodegradable Mg implants: (a) MAGNEZIX ® CS from Syntellix AG (Hannover, Germany) [26, 28]; (b) Magnesium absorbable-drug eluting stent from BIOTRONIK (Berlin, Germany) [26]; and (c) Velox CD (Transluminal Technologies LLC, Syracuse, USA) Mg wound-closure device [26]. Permission to edit and reprint these figures is requested to Biotronik, Syntellix AG and Transluminal Technologies LLC.

Velox CD (Transluminal Technologies LLC, Syracuse, USA) is a complete device for wound closure of arteriotomies (Fig. 3c). The implant is made from a biocompatible and fully bioabsorbable magnesium alloy (containing magnesium, aluminium and iron). After placement, the intravascular part dissolves after 24h, whereas the extracellular part dissolves after two weeks. The device has been tested in 42 patients [39].

1.3. Magnesium biodegradation mechanism

Pure magnesium forms crystals with an hexagonal close-packed structure (HCP). The starting materials and the processing routes determine the grain size and the impurity content. When alloying elements are added, these can form secondary phases or intermetallics in combination with Mg which mainly form at the grain boundaries. Some alloying elements have a large solubility limit in Mg, and these can remain distributed inside the Mg grains after the casting process. The alloying elements can also interact with the impurities forming precipitates. The casting parameters and the applied heat treatments, if any, also determine the distribution of these secondary phases, alloying elements in solid solution or the precipitates in the bulk material.

Mg is one of the most reactive metals and it is known for its low corrosion resistance in many conditions. Therefore, its applicability is sometimes restricted due to the low corrosion resistance.

When Mg is immersed in a simulated body fluid (SBF) the degradation process starts in order to achieve an equilibrium status. For this reason, the anodic and cathodic reactions start by exchanging electrons between them, (Eqs. 1 and 2 respectively). In this process, metallic Mg oxidizes to Mg^{2+} giving two electrons to the cathodic reaction. The dissolution of Mg in water has a standard electrode potential (E_o) of -2.363 V [40]. H_2O molecule present in the SBF takes these two electrons, generating H_2 and increasing the OH^- ion concentration, and thus, the pH. $Mg(OH)_2$ is formed when the concentration of Mg^{2+} and OH^- reach the solubility limit ($1.1 \cdot 10^{-4}$ M in water at 25°C), or in other words at a high pH (Eq. 3). In the overall reaction in water 1 mol of Mg dissolved is directly related to 1 mol of H_2 gas generated (Eq. 4) [41]. E_o data from Ref. [40].

$\mathrm{Mg} \rightarrow \mathrm{Mg}^{2+} + 2\mathrm{e}^-$ Anodic reaction (E_o = -2.363 V) (1)

$2\mathrm{H_2O} + 2\mathrm{e}^- \rightarrow 2\mathrm{OH}^- + \mathrm{H_2}$ Cathodic reaction (E_o = +0.826 V) (2)

$\mathrm{Mg}^{2+} + 2\mathrm{OH}^- \rightarrow \mathrm{Mg(OH)_2}$ Product formation (3)

$\mathrm{Mg} + 2\,\mathrm{H_2O} \rightarrow \mathrm{Mg(OH)_2} + \mathrm{H_2}$ Overall reaction (E_o = -1.065 V) (4)

Fig. 4 shows the degradation process progression from the start of the immersion until an advanced corrosion stage [19]. At the beginning of this process the as-prepared surface is exposed to the electrolyte and anodic and cathodic reactions start. The Mg grain acts as the anode and the cathodic reaction takes place at the most noble sites of the sample. These noble sites are: grain boundaries, secondary phases and precipitates (Fig. 4a). Thus, there is an electron exchange between these two types of regions, and Mg dissolves at the same rate as H_2 is generated. Once the Mg^{2+} concentration and the pH increase reaching the solubility limit, $Mg(OH)_2$ is formed and it precipitates at the Mg surface (Fig. 4b).

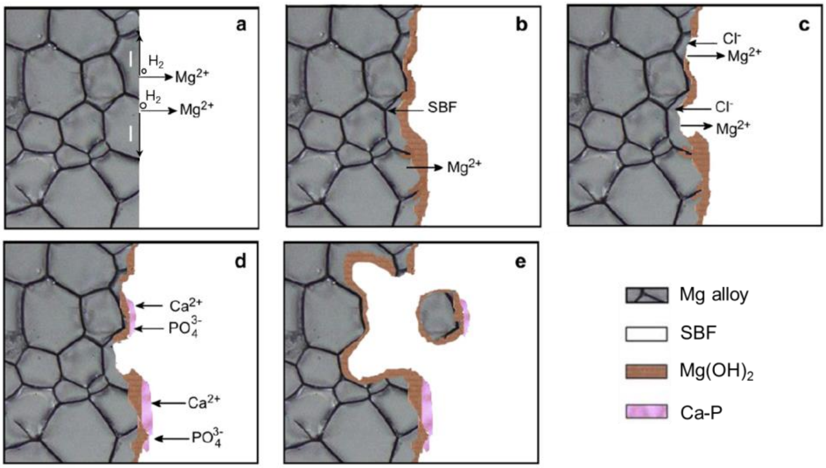

Figure 4. Schematic representation of the biodegradation process of magnesium and its alloys from Ref. [19]. (a) depicts Mg^{2+} ion release into the electrolyte, hydrogen generation and electron exchange between the anodic and cathodic sites. (b) represents the $Mg(OH)_2$ layer formation. (c) shows pitting due to Cl^- ions. (d) indicates Ca-P structure formation. (d) illustrates the particle undermining mechanism which can release single grains or even larger Mg particles. Figures are edited and reprinted with permission.

In long term immersion experiments, chlorine ions (Cl^-) can induce pitting corrosion. Pitting of magnesium is observed for Cl^- concentrations exceeding 30 mM [43]. The $Mg(OH)_2$ layer can be dissolved in local sites by Cl^- ions and form $MgCl_2$ (Eq. 5) [44-46]. $MgCl_2$ has a rather high solubility limit in water, e.g. at room temperature the solubility limit is 5.6 M, while for $Mg(OH)_2$ it is $1.1 \cdot 10^{-4}$ M. This exposes the uncovered area to the electrolyte, accelerating the degradation process at these sites. According to reaction 5, this mechanism is also able to increase the pH.

$$\mathrm{Mg(OH)_2(s) + 2Cl^- \rightarrow MgCl_2(s) + 2OH^-} \qquad \text{Pitting mechanism (5)}$$

Once the pitting corrosion starts at one site, the corrosion reactions can remain taking place at the same site promoting a localized corrosion mode. This mode can take place around secondary phases and precipitates which are more noble than magnesium [47, 48].

In the body the presence of PO_4^{3-} and Ca^{2+} ions can promote the precipitation of calcium orthophosphate structures (Fig. 4d). The undissolved $Mg(OH)_2$ film on the surface of Mg alloy is considered to provide favourable sites for Ca-P formation. There are many different Ca-P structures [49] and these layers can be similar to hydroxyapatite (HA) which is typically written as $Ca_{10}(PO_4)_6(OH)_2$, and is the mineral part of bone. Within this calcium phosphate structures several elements are replaceable: Na^+, K^+, Mg^{2+}, Sr^{2+} for Ca^{2+}; CO_3^{2-} for PO_4^{3-} or HPO_4^{2-} ; F^-, Cl^-, CO_3^{2-} for OH^- [49]. Many authors have reported Mg and Ca phosphate on the degradation layer formed on Mg based materials tested in different SBFs [50-55] and in animal experiments [42, 56]. In summary, these calcium orthophosphate structures are related to bone mineralization and it is proposed that Mg promotes new bone formation creating hydroxyapatite-like structures as described in reaction 6:

$$\mathrm{xMg^{2+} + yCa^{2+} + zPO_4^{3-} + OH^- \rightarrow Mg_x\,Ca_y(PO_4)_z - (OH)} \qquad (6)$$

Another mechanism observed during long term degradation tests is the particle undermining mode [47, 48]. This mode consists of the release of Mg particles or even full grains into the electrolyte due to the corrosion of surrounding material and grain boundaries (Fig. 4e). Hence, these particles do not react electrochemically generating H_2 gas. When gravimetry and hydrogen evolution are applied, this particle release causes a difference between these two methods. This mechanism is similar to intergranular corrosion. In the case of Mg corrosion, the grain boundaries are cathodic to the grain interior. The corrosion process tends to be concentrated in the area adjoining the grain boundary until eventually the grain may be undercut and fall out [48].

Under physiological testing conditions a CO_2 buffering system is usually applied in order to mimic the natural buffering system in the human body (reaction 7) [50, 57-62]. Moreover, some SBF and cell culture media include sodium bicarbonate ($NaHCO_3$) to buffer the electrolyte (reaction 8). Thus, as shown in Fig. 5, under physiological conditions also magnesium carbonate ($MgCO_3$) can be formed due to the CO_2 and the $NaHCO_3$ present in the electrolyte according to reaction 9 [50]. This $MgCO_3$ deposition process can also decrease the pH. When the electrolyte contains Ca ions, Mg can be replaced by Ca^{2+} in the carbonate structure in reaction 9, thus the layer can be a $(Mg)CO_3$ and $CaCO_3$ compound [45].

$$\mathrm{H_2O + CO_2(g) \rightarrow H_2CO_3 \rightarrow HCO_3^- + H^+} \qquad (7)$$

$$\mathrm{NaHCO_3 \rightarrow Na^+ + HCO_3^-} \qquad (8)$$

$$\mathrm{Mg^{2+} + HCO_3^- \rightarrow MgCO_3 + H^+} \qquad (9)$$

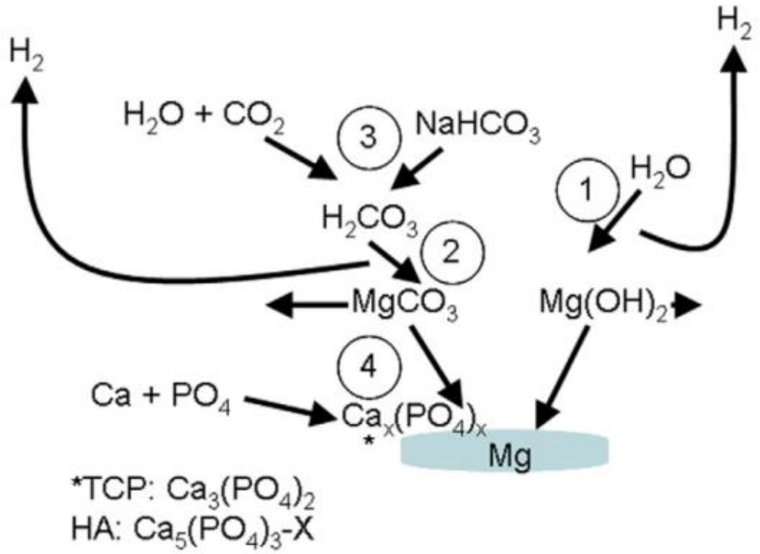

Figure 5. Corrosion product formation during the initial steps of Mg corrosion under cell culture conditions. (1) $Mg(OH)_2$ formation due to contact with water; (2) $MgCO_3$ formation due to the presence of carbon dioxide; (3) increase in the content of HCO_3^- due to the buffering system; and (4) calcium phosphate formation: TCP = tricalcium phosphate, HA = hydroxyapatite, X = OH, Cl, … from Ref [50]. This figures is reprinted with permission.

The surface film or degradation layer formation is a co-precipitation process. When the concentrations of certain components reach the solubility limit, different compounds precipitate forming the degradation layer with the above described corrosion products. In a real application, solid material products will remain in immediate proximity to the implant without any known unfavourable effects, whereas ions and gases can, depending on their release rate, negatively influence the tissue's energetic viability [63].

Magnesium alloys are highly susceptible to galvanic corrosion [64] because Mg is one of the most anodic metals. More noble metals, such as Ni, Fe, and Cu, constitute efficient cathodes for magnesium and cause severe galvanic corrosion [47, 48]. But other metals that combine an active corrosion potential with a high hydrogen overpotential, such as Al, Zn, Cd, and Sn, are much less damaging. Cathodes can be external as other metals in contact with magnesium promoting macrogalvanic corrosion, or may be internal as second or impurity phases generating microgalvanic corrosion. Applying Mg as biomaterial, macrogalvanic corrosion was observed by Lambotte in 1900. Lambotte combined Mg screws with a steel plate to stabilize a diaphyseal humerus fracture in an 8 year old child, registering a large gas cavity and a fast degradation process [25].

1.4. Parameters influencing degradation

Many parameters concerning the Mg based material fabrication and parameters related to the testing environment have an influence on the degradation results. These parameters are summarized in Fig. 6. The starting materials, the alloying elements, if any, and the alloy processing parameters have a strong influence on the material's degradation properties through the materials microstructure described by the grain size, the impurity content, the type and amount of secondary phases, their distribution and the surface structure. In addition, the testing conditions have also a large impact. Different methods and testing conditions may alter the degradation rate and the formation and composition of the degradation layer and thus define the corrosion mode. Below, a literature based review from all these parameters and their influence is described.

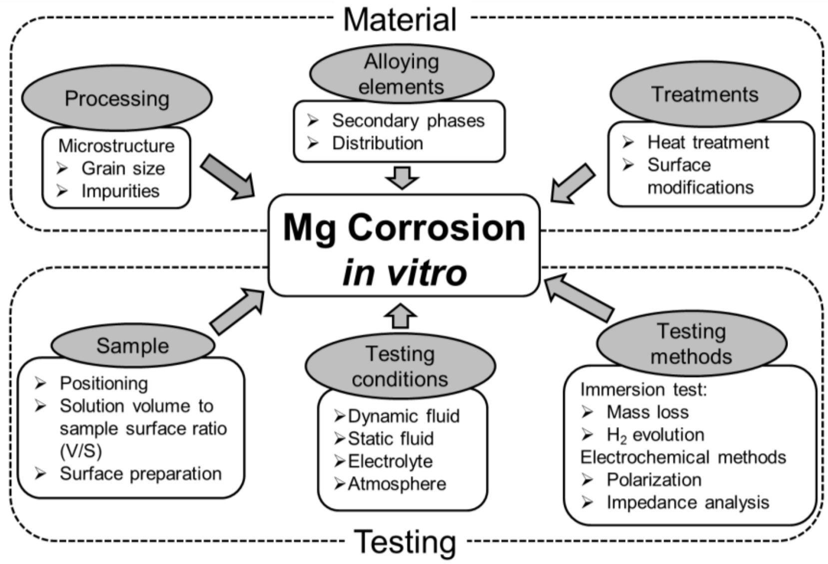

Figure 6. Diagram with the parameters influencing Mg corrosion in vitro divided into two general subgroups: material characteristics and testing conditions.

1.5. Influence from the material processing

Mg alloys are currently prepared firstly by casting. Pure magnesium melts at 651°C at atmospheric pressure, and to completely melt Mg alloys, higher temperatures, around 700-750°C, are commonly applied. In order to protect the melt from ignition with oxygen the casting is done under a protective atmosphere of argon (Ar) and 2 to 5 vol.% of sulphur hexafluoride (SF_6), which produces a Mg fluoride layer for further protection [65]. In the casting process, the cooling rate [66] and the contact with the moulds and tools made of steel, for instance, will start to determine the grain size and impurity content.

It is generally accepted that a fine grain size and homogeneous microstructure is desirable for a better corrosion performance [66]. According to literature, Mg is more susceptible to corrosion attack at defects such as grain boundaries or inhomogeneities. The grain boundary is the area where atoms are arranged more loosely and disordered, making a separation between two grains, where atoms are highly oriented. Hence, grain boundaries represent cathodic sites and Mg grains anodic ones. These sites couple to each other electrochemically and promote the corrosion process (Eqs. 1 and 2). As the grain size decreases, the grain boundary area obviously increases. Thus, grain refinement will increase the density of cathodic sites which couple to the anodic ones and, subsequently, the area susceptible to corrode so that the material will degrade homogeneously avoiding local corrosion attacks. At the same time, the decrease of the grain size is detrimental to the influence of Cl^- ions, which accelerates the occurrence of Mg corrosion.

The presence of secondary phases or impurities plays a similar role as the increase of grain boundary area. If secondary phases are concentrated in just a few sites, this will promote local corrosion attacks. Therefore, a uniform distribution of these phases over the Mg alloy volume is beneficial to promote homogeneous corrosion behaviour. This desired distribution in the matrix can be achieved by a proper heat treatment specific for each Mg alloy [67, 68].

Many authors aim to improve the mechanical properties of the Mg alloys, but by doing so they are also influencing the degradation properties. Since the dominant mechanism of plastic deformation in metals is dislocation movement, impeding their movement leads to a significant improvement of the strength. The following mechanisms can be used to achieve this objective:

- By severe plastic deformation: to increase the dislocation density (work hardening) with processes at high or low temperatures such as rolling, extrusion or equal channel angular pressing (ECAP) [42, 69-71]

- By grain size refinement: increasing the number of grains per unit length by rapid solidification [72] or by adding alloying elements such as Ca or Sr [69, 73].

- By addition of alloying elements: increasing the concentration of dissolved alloying elements in the Mg matrix (solid solution strengthening) or introducing fine intermetallic particles (precipitation strengthening) [74-76].

1.5.1. Impurities

Impurities have been proven to play a major role in Mg degradation. Although it is generally thought that Mg corrodes quickly [77], it has recently been proven that ultrahigh-purity Mg degrades very slowly in vivo and in vitro with a rate of only 10 µm/year [58]. Hanawalt and co-workers elucidated the effects of different impurities in Mg, such as Fe, Co, Cu and Ni, on the resultant corrosion (Fig. 7). They defined tolerance limits, which are impurity contents above which the corrosion rate of Mg increases dramatically. The values were 170 ppm for Fe, 1000 ppm for Cu and 5 ppm for Ni [78], although the experimental data from different Mg alloys show large differences in the tolerance limits. Other impurities have a moderate tolerance limit, such as Ag, Ca and Zn.

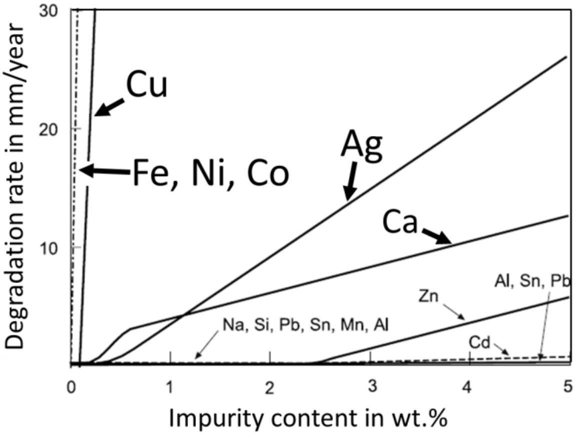

Figure 7. Influence of impurities on the corrosion rate of Mg in NaCl based solutions.

Manganese (Mn) has also attracted the attention of many researchers as both impurity and alloying element. Mn is added to many commercial alloys, particularly those of the AZ series to improve corrosion resistance [48]. Interestingly, Mn is able to pick up impurities and form intermetallic phases during casting which are less favourable to promote electrochemical dissolution than the impurity elements themselves. Therefore, Mn increases the tolerance limit of the Mg alloy to impurities [48, 80-84]. Song et al. write that the tolerance limit of Fe is 0.032 times the Mn content; and this actually means that if there is manganese in a magnesium alloy, then the alloy would be able to tolerate an amount of the iron impurity equal to 0.032 of the manganese concentration (by weight). This means that Mn itself does not improve the corrosion resistance, but it reduces the harmful effect of Fe, Ni and Cu. However, Mn can have a negative influence when the purity of the Mg based material is high [58, 59, 85].

As shown in Fig. 8, Liu et al. compared the corrosion rate of 5 different Mg alloys with the Fe minus the tolerance limit defined by the Mn content; finding different trends for each alloy [81]. Thus once the tolerance limit is exceeded the corrosion rate under their specific spray test increases linearly with the Fe content.

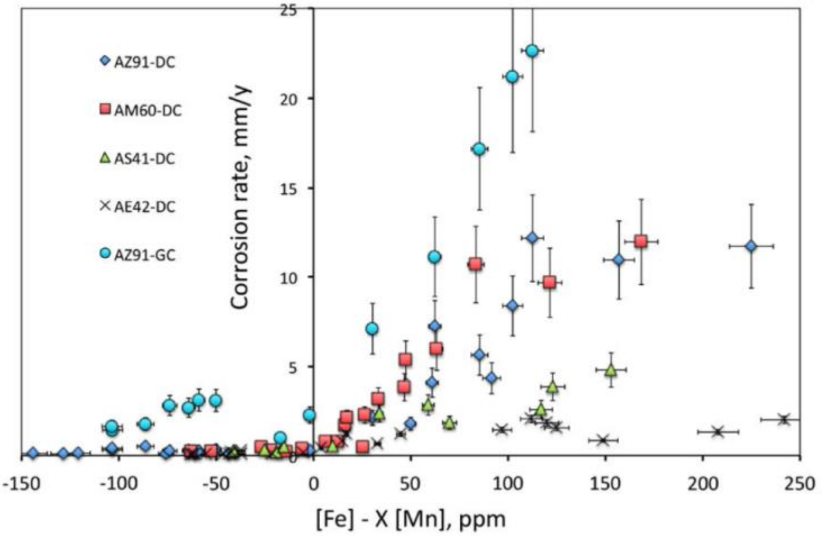

Figure 8. Influence of Fe and Mn as impurities on Mg corrosion [81]. Corrosion rate in salt spray of Mg alloys: AZ91, AM60, AS41 and AE42 (mm/y), as a function of the alloy iron content [Fe] above the tolerance limit (X) defined by the Mn content [Mn]. Original data from Hillis and co-workers [83, 86-88]. This figure is reprinted with permission.

Silicon (Si) has recently also been evaluated as an impurity with an important role in Mg corrosion [89]. The presence of traces of Si promotes precipitation of Fe-rich impurity particles in Mg alloys; thereby it promotes localized corrosion around these larger particles [90].

Thus, the Fe/Mn and Fe/Si ratios become as important as the Fe, Ni and Cu impurity content itself. It is noteworthy that most of the impurity investigations are generally performed in NaCl based solutions which do not include the main mechanisms occurring under physiological conditions [48, 78, 81-83]. In any case, this indicates the importance of impurity control during all the processing steps, and thereby, the impurities must be included in the degradation discussion.

1.5.2. Alloying elements

There are many reasons to alloy Mg. Improving mechanical and corrosion properties is the main one. Although the formation of secondary phases with a more noble character than Mg does, in principle, not improve the corrosion behaviour, they can improve the mechanical strength and the ductility. This is desirable for load bearing implant applications. Up to now, currently investigated alloying elements for biomedical applications are: aluminium, zinc, manganese, silicon, calcium, strontium, lithium, silver, bismuth, zirconium; and rare earth elements (REE) such as gadolinium, yttrium, neodymium, cerium, or dysprosium. Below, the state of the art of gadolinium and silver is shown as they are the selected alloying elements for this doctoral thesis, although some of the currently investigated elements are also mentioned (Al, Ca, Zn, Sr, Si, Mn).

a) Gadolinium

Rare earth elements (REE), such as Gd, Dy, Y, Nd and Ce are strong candidates to alloy Mg because they can improve mechanical properties and facilitate control of the degradation properties [91-93]. For example, the ‘‘scavenger effect” of REE on Mg-alloys improves the corrosion resistance by the formation of intermetallic compounds with impurities, which deteriorate Mg degradation properties [86, 94]. Gadolinium (Gd) is a promising alloying element due to its large solubility limit in Mg (23.49 wt.%) (Fig. 9a) [95]. This large solubility allows the adjustment of mechanical properties by precipitation and solid solution strengthening. The formation of intermetallic phases, such as Mg_5Gd, is proven to improve the mechanical properties [91]. In literature it is stated that the corrosion behaviour of Mg-Gd binary alloys improves with an increasing amount of Gd of up to 10 wt.% (Fig. 9b) [91, 93]. Furthermore, Guo et al. found $Gd(OH)_3$

in the degradation layer, which can also contribute to the corrosion protection [96].

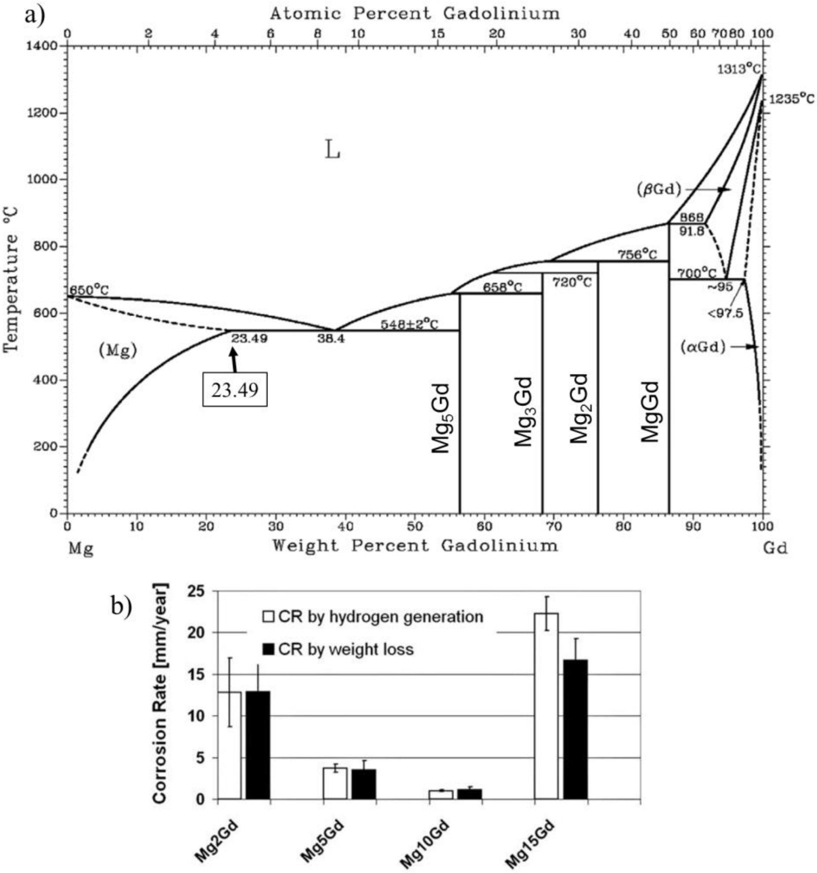

Figure 9. (a) Mg-Gd phase diagram from Ref. [97] and (b) degradation rates of Mg-Gd binary alloys with 2, 5, 10 and 15 wt.% of Gd [91]. Figures are edited and reprinted with permission.

Cuboid shaped particles have been reported in Mg-Gd [91, 92] and in Y containing alloys [98-100] (Fig. 10). These cubes could be GdH_2 and YH_2 particles formed during the casting or even during storage due to the contact of the material with hydrogen sources. The main source of hydrogen is the H_2O molecules present in the air. Qiuming et al. observed by TEM GdH_2 cubic particles in Mg-Gd alloys proving that hydrides can form [101]. Moreover, the presence of DyH_2 has also been proven in Mg20Dy alloys [102] which indicates that these cubic shaped hydride particles can precipitate with many REEs.

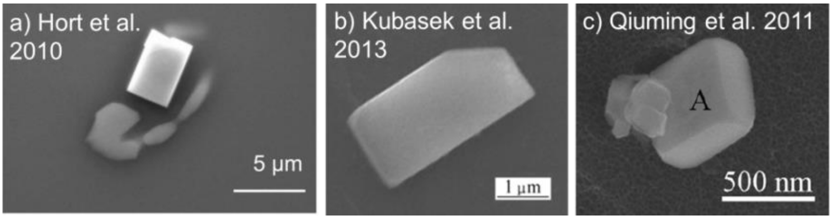

Figure 10. Cuboid shaped particles found in Mg-Gd alloys in: (a) Mg-15Gd alloy from Ref. [91]; (b) Mg-5Gd alloy from Ref. [92]; and (c) Mg-15Gd alloy. Qiuming et al. showed experimental proof of the existence of GdH_2 in cuboid shape [101]. Figures are edited and reprinted with permission.

Cytotoxicity tests of Gd with osteoblast cells indicated that Mg-Gd based implant material could be acceptable for medical applications [103]. Although many authors state that gadolinium is highly toxic, the acute toxicity is only moderate [91]. Grillo et al. reported cytotoxic effects of a mixture of La and Gd at concentrations lower than 200 µM while DNA damage was detected for 1600 µM of Gd [104]. In toxicology, the median lethal dose (LD50) is a measure of the lethal dose of a toxin, radiation, or pathogen. The value of LD50 for a substance is the dose required to kill half the members of a tested population after a specified test duration. The intraperitoneal LD50 dose of $GdCl_3$ was 550 mg kg^{-1} in mice, while $GdNO_3$ induced acute toxicity at a concentration of 300 mg kg^{-1} in mice and 230 mg kg^{-1} in rats, respectively [105, 106]. However, there is an increasing evidence that many REE exhibit anticarcinogenic properties [107] and Gd-based elements are used as magnetic resonance contrasts [108-110]. However, there are indications that Gd ions released by transmetallation can induce nephrogenic systemic fibrosis in patients with renal failure, although not in healthy patients [111]. Finally, Gd has also been observed to have a certain retention rate in bone prior to redistribution to spleen and liver [112].

b) Silver

An option to achieve faster degradation rates is to add elements which can decrease the corrosion properties. Silver (Ag), for instance, is considered as an impurity with a low tolerance limit and accelerates resorption (see Ref. [78] and page 471 in Ref. [79]). On the one hand, Ag is one of the most noble metals with a standard potential (E_o) in water at 25°C of +0.80 V vs SHE. On the other hand, the E_o of Mg in water at 25°C is -2.37 V vs SHE, which makes it one of the less noble metals. Thus, the combination of Ag and Mg in contact with an electrolyte is expected to accelerate the Mg-Ag corrosion process by creating many microgalvanic couples.

Although magnesium metal by itself has shown in vitro antibacterial properties against Escherichia coli, Pseudomonas aeruginosa and Staphylococcus aureus [113], Ag can also be added to Mg to enhance the antibacterial properties of implant material [114]. Tie et al. [61] demonstrated that the killing rate of Mg-Ag alloys against Staphylococcus aureus and Staphylococcus epidermidis, famous ‘superbugs’ that cannot be killed by most antibiotics, exceeded 90%. Moreover, metallic silver was proven to pose minimal risk to health [115]. Metallic and alloyed silver did not show any cytotoxicity in silver-containing medical devices [116]. A small amount of silver content in alloys or coatings was also reported to improve cytocompatibility and cell viability [116, 117] although elementary silver exhibits a dose-dependent cytotoxity. When 2 wt.% of Ag is added in Mg-Ag binary alloys the degradation rate of the material is already increased, although additions of 4 and 6 wt.% of Ag were also analysed finding similar results [61]. These additions of Ag are expected to be safe for the human body.

Tie et al. also reported silver rich secondary phases which are Mg_4Ag or perhaps partially it could be $Mg_{54}Ag_{17}$ [61]. However, the Mg-Ag binary diagram, calculated by Pandat software (from Computherm) using the database PanMg_2016, includes Mg_3Ag and Mg_4Ag as intermetallic phases. Zheng reported the solid solubility of Ag in Mg as 3.83 at.% (15.14 wt.%) [118], while the calculated diagram indicates a solubility of 3.5 at.% (13.78 wt.%).

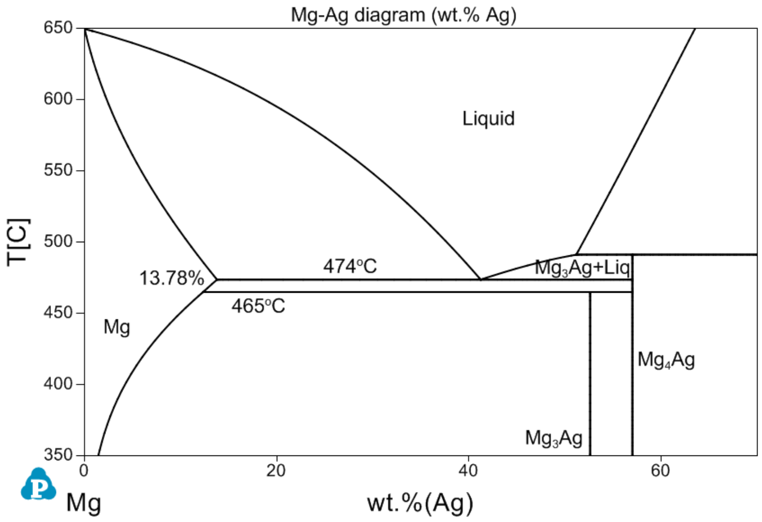

Figure 11. Mg-Ag binary phase diagram from Pandat software (by Computherm) using the database PanMg_2016 (image provided by Andrea Gil-Santos).

c) Aluminium

As mentioned above, the selection of the alloying elements can be critical for the biodegradation behaviour. Although aluminium (Al) is one of the common alloying elements of Mg alloy due to the appearance of the β $Mg_{17}Al_{12}$ phase, it is considered unfavourable to the human body since it could cause Alzheimer’s disease. It has been demonstrated that aluminium ions can easily combine with inorganic phosphates, leading to a lack of phosphate in the human body, which induces dementia [119-121]. Whilst being environmentally abundant, aluminium is not essential for life. On the contrary, aluminium is a widely recognized neurotoxin that inhibits more than 200 biologically important functions and causes various adverse effects in plants, animals, and humans [121]. Thus, well-known Al containing commercial alloys, such as AZ31 or AZ91, are no longer considered as implant candidates. AZ31 and AZ91 are Mg alloys with 1wt.% of Zn and 3wt.% and 9 wt.% of Al respectively.

d) Calcium

Calcium is the main component of human bone in the hydroxyapatite structure and improves bone healing because Ca ions are essential in cellular signalling [122]. In addition, Ca seems to better incorporate into bones in the presence of Mg ions [123].

In magnesium metallurgy, calcium can act as a deoxidant in the Mg melt during casting or in subsequent heat treatment, preventing the material from igniting [79]. In Mg alloys it promotes grain refinement improving corrosion and mechanical properties. The Mg_2Ca secondary phase in the Mg-Ca binary alloys can decrease corrosion resistance and increase the yield strength with increase in Ca content [124].

e) Zinc

Zinc is considered a crucial trace element for the human body and it is necessary for many biological functions [125, 126]. As an alloying element in Mg, it positively influences bone healing and cell reactions [127, 128].

Metallurgically, Mg-Zn alloys are known to increase the age hardening response as Zn produces intermetallic compounds and these refine the grain size [100, 129]. Mg_7Zn_3 can form as a secondary phase in the Mg-Zn binary alloy.

f) Strontium

Strontium (Sr) has been determined as a potential element for use in medical applications [73] of magnesium alloys. Sr is a component of human bone and it has been known to promote the growth of osteoblasts and prevent bone resorption [130]. Moreover, its role in bone, heart and muscle function was shown in the 1950's and 1960's [131].

As a grain refiner for Mg alloys, Sr can improve the mechanical properties of some Mg alloys, as well as improve the corrosion resistance of Mg [132-134]. $Mg_{17}Sr_2$ can form in the Mg-Sr binary system [69, 73]. Tie et al. recently showed promising corrosion and biocompatible properties of Mg-1Sr alloy, which stimulated new bone formation and showed no adverse effects after 16 weeks of implantation in New Zealand White Rabbits [135]. The biocompatibility and suitable biodegradability of Mg-1.0Ca-0.5Sr also have recently been reported in rat tibiae [136].

g) Silicon

Silicon can be tolerated in the human body and a small content of Si has been reported to be essential in mammals [137]. Moreover, it may be important for the growth and development of bone and connective tissue [138]; and it also helps to build the immune system [139].

However, as-cast Mg-Si alloys showed low ductility and strength because of the large Mg_2Si particle size and the brittle eutectic phase [140]. Srinivasan et al. found that fine and evenly distributed Mg_2Si intermetallic with polygon shape effectively inhibited the corrosion compared to the Chinese-script shaped Mg_2Si [141].

h) Manganese

Manganese also plays an important role in the metabolic cycle of, e.g., amino acids and carbohydrates [142].

Mn has the function of refining the grain size [143], and improving the tensile strength and corrosion properties of magnesium alloys [3, 144]. Mn also decreases the corrosion rate of Mg via transforming iron and other metal elements to harmless intermetallic compounds [80].

1.6. Influence of immersion testing conditions

1.6.1. Electrolyte

In order to obtain in vitro corrosion data comparable to in vivo testing, the most important factors are the selection of the electrolyte [145] and the testing conditions [146, 147]. Many authors report results in NaCl based solution in order to get fundamental knowledge of corrosion behaviour of Mg and its alloys [148-154]. However, this approach is considered inappropriate for biodegradable implant research because it neglects many influential factors on the in vivo degradation and the degradation layer formation, for example pH and ionic concentration. Zhen et al. [145] suggested to select electrolytes containing the components similar to blood plasma [155] or human whole blood [54]. In order to simulate physiological pH and ionic composition $H_2PO_4^-$ and HCO_3^- based buffering systems are generally applied. Most of the electrolytes used in literature are summarized in Table 2. These electrolytes are: phosphate buffered saline (PBS) [156, 157], Hank’s balanced salt solution (HBSS) [51, 52, 158-161], Ringer’s solution [45, 144], Earl’s balanced salt solution (EBSS) [162], minimum essential medium (MEM) [162], F-12K medium [73], Dulbecco’s modified eagle medium (DMEM) [61, 62, 163, 164] and a wide range of SBF [44, 165, 166]. All these electrolytes can include or exclude proteins, such as, fetal bovine serum (FBS) or bovine serum albumin (BSA). Other components such as dextrose/glucose, phenol red or HEPES as an additional buffering system can be incorporated in the medium [167, 168], which makes the electrolyte selection even broader. Hence there is clearly a lack of consensus on the most suitable medium for in vitro testing.

The most important aspect to consider when selecting the medium is the electrolyte composition. The chlorine level in plasma is 103 mM and electrolytes with a higher Cl^- content will promote the degradation process and induce pitting corrosion [45]. The presence of Ca^{2+} and PO_4^{3-} ions allows the formation of calcium phosphate corrosion products. The content of HCO^{3-} is also critical not only to buffer the pH within the physiological range (7.4-8) but also for the precipitation of magnesium carbonate on the surface film [50]. Finally the presence of biological entities and organic compounds, such as proteins, cells, vitamins or amino acids, can influence the degradation results by adsorption on the degradation layer and protecting the material from further corrosion [163, 168]. According to ISO10993, sterility during evaluation of medical devices should be maintained. Thus, sterility during testing under cell culture conditions must be assured due to the risk of contamination by microorganisms [169-171].

Table 2. Ionic composition of different media used for Mg biodegradation testing compared to body plasma and whole blood. Units are in mmol/L, unless otherwise indicated.

	PBS [a]	HBSS [a]	Ringer's	EBSS	MEM	F-12K	DMEM	SBF	Plasma [b]	Whole blood
References	[156, 172]	[51, 52, 158-161]	[45, 144]	[162]	[162]	[73]	[61, 62, 163, 164]	[166]	[146, 155, 173, 174]	[54, 155, 173]
Na^+	154.1	142.8	156.4	144	143	161.7	155.3	142.0	142	136-145
K^+	4.1	5.8	5.8	5.4	5.4	3.8	5.3	5.0	5	3.6-5.2
Ca^{2+}	-	-	2.2	1.8	1.8	0.9	1.80	2.5	2.5	2.1-2.6
Mg^{2+}	-	-	-	0.4	0.4	2.1	0.81	1.0	1.5	0.75-0.95
Cl^-	140.6	143.3	163.2	125	125	136.5	115.7	109.0	103	98-107
HCO_3^-	-	4.2	2.4	26	26	29.8	44.05	27.0	27	23-29 (44.7)[c]
$H_2PO_4^-$	1.5	0.4	-	1	0.9	0.49	-	-	-	-
HPO_4^{2-}	8.1	0.3	-	-	-	0.8	0.91	1.0	1	0.8-1.4
SO_4^{2-}	-	-	-	-	0.4	1.6	0.81	1.0	0.5	0.8-1.3
Cu^{2+} (μM)	-	-	-	-	-	0.01	-	-	3-32	12-32
Fe^{2+} (μM)	-	-	-	-	-	2.9	-	-	11-86	7,520-10,027
Zn^{2+} (μM)	-	-	-	-	-	0.5	-	-	10-18	92-107
Amino acids	-	-	-	-	0.0055	-	10.60	-	Variable	no data
D-Glucose	-	5.6	-	5.6	5.6	-	25	-	3.6-5.2	no data
Vitamins	-	-	-	-	0.03	-	0.15	-	Variable	no data
Proteins (g L^{-1})	-	-	-	-	-	-	-	-	63 - 80	no data
Phenol red	-	-	-	0.03	0.03	-	0.04	-	-	-

[a] PBS and HBSS can include Ca^{2+} and Mg^{2+} by adding 140 mg/L $CaCl_2$ and 200 mg/L $MgSO_4$-7H_2O.

[b] 55% of whole blood; amount of proteins 7-9% (consisting of 80% albumin, 16% globulin and 4% fibrinogen).

[c] Theoretically calculated available bicarbonate when fully released (enzymatically by carbonic anhydrase) from erythrocytes.

1.6.2. V/S ratio

The electrolyte volume to sample surface ratio (V/S) is an important parameter to take into account during degradation testing. Kirkland et al. showed the influence of the V/S ratio on pure Mg corrosion in HBSS after 1 week [175]. As depicted in Fig. 12, when the V/S ratio is higher than approximately 35 ml/cm^2 the corrosion rates no longer increase with increasing V/S. When the V/S is small, the initial degradation occurs faster, raising the pH quickly. Therefore, the degradation layer is also formed quickly which slows down the dissolution reaction. The standards outlined by the American Society for Testing and Materials (ASTM) for determining mass loss of structural metals could be suitable for Mg, since the recommended V/S ratios are from 20 to 40 ml/cm^2 [176]. Thus, the best practice recommended is to maintain the volume of medium as large as practicably possible and over 35 ml/cm^2, so that the V/S does not play a major role [175]. However, in H_2 evolution testing, the larger the volume, the larger is the H_2 amount in liquid solution, which, if not corrected, is a source of data error.

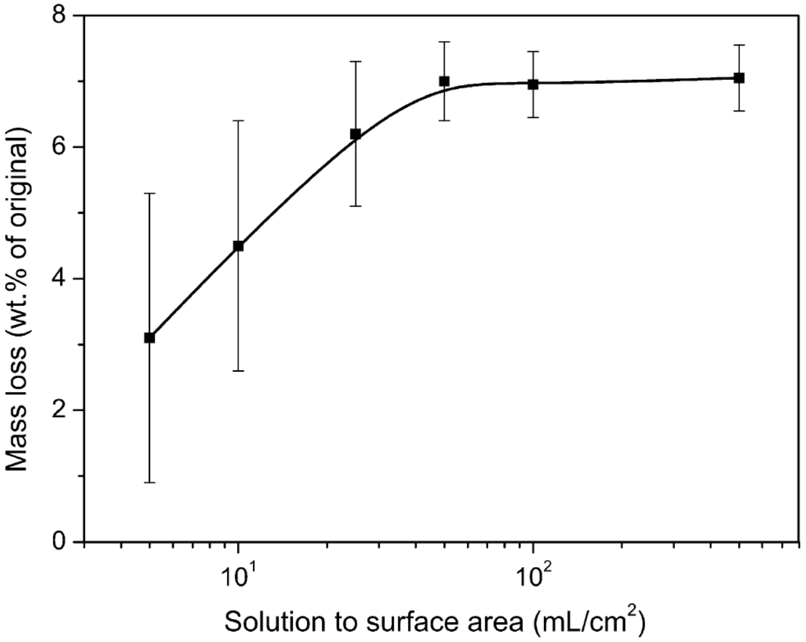

Figure 12. Mass loss as a function of solution volume to surface area for pure Mg after 1 week immersion (HBSS, pH 7.4, T_{phy}). The data demonstrate the recommendation to maintain the volume of medium as large as possible and higher than 35 ml/cm^2 [175]. This figure is reprinted with permission.

Yang et al. concluded that the V/S ratio should be considered in terms of clinical relevance when aiming at biomedical applications: low V/S ratio (0.67 ml/cm^2) to simulate Mg in cortical bone or muscle tissue; and high V/S ratio (6.7 ml/cm^2) to simulate the effects in a bone marrow cavity [53, 145]. Unfortunately, in some studies, this ratio is not taken into account for discussion, or not even reported [89], which complicates the comparability.

In cell culture studies, the dimensions of the well plates constrain the volume of electrolyte. In these cases, the use of a bioreactor with flow can avoid this problem and increase the V/S ratio [177]. In H_2 evolution studies, this ratio is mainly restricted by the geometry of the beakers and funnels that can be installed in the eudiometer filled with electrolyte for gas evolution [178].

1.6.3. Setup

The setup plays an important role on Mg degradation testing. Hofstetter et al. [58] applied a setup which provided similar corrosion behaviour of Mg based materials in vitro and in vivo, as depicted in Fig. 13. This setup allows hydrogen evolution and mass loss testing and at the same time solves different disadvantages that other setups have.

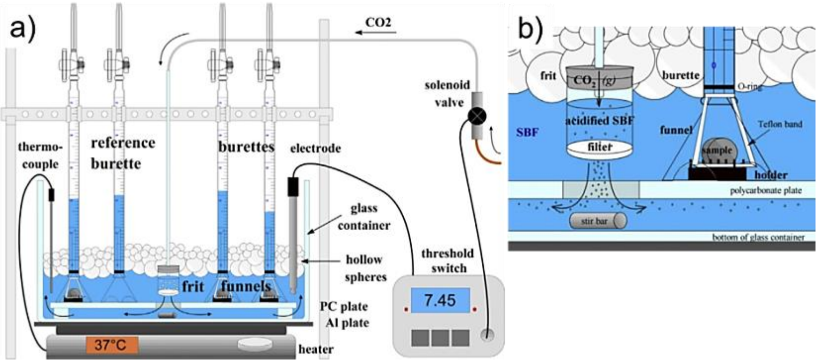

Figure 13. Degradation testing setup applied by Hofstetter et al. [58]. Figures are edited and reprinted with permission.

One difference between living bodies and the above described electrolytes is the ability to naturally maintain the pH within the physiological range (7.4-8). In order to reproduce this buffering capacity, CO_2 can be added into the atmosphere applying 5 vol. % of CO_2 to the air in the chamber [50, 62, 163, 179] or directly bubbling into the solution [57-59, 159]. In Fig. 13a, the pH is buffered over the entire immersion time at a fixed pH (7.45) by infusing CO_2 in the electrolyte and thus correcting pH fluctuations in situ. The increase of the local pH inside the funnel is solved by stirring one single large SBF bath.

This induces a dynamic electrolyte flow, avoiding a local pH increase around the sample and inside the funnel. In this case, the V/S ratio is large enough not to show the influence described above, and the use of a control sample allows to determine variations due to atmospheric pressure changes and errors caused by artifacts. However, when a large bath is used and the hydrogen is measured, some H_2 stays in liquid solution giving reduced corrosion rates by the H_2 evolution method. As Kirkland et al. suggest, this data should be corrected in large baths by adding the H_2 gas in liquid solution approximately calculated by the solubility of H_2 in water at 37°C [180]. Finally, the evaporation can be reduced by using inert polymer balls on top of the SBF.

Only a few studies have taken into account the sample positioning during in vitro tests. The positioning defines the contact of the sample with the electrolyte. Samples that are lying on top of a beaker or a dwell-plate expose only a portion of their surfaces to the medium, which reduces the effective surface area and complicates data analysis. As shown in Fig. 13b, this problem can be solved using a sample holder which allows the samples to stand exposing most of the area to the electrolytes. Another solution is to hang the sample with an inert fishing line or similar wires [181]. However, in both cases, small defects are introduced, such as the hole drilled to hang the sample or the area in contact with the holder.

1.6.4. Electrolyte replacement

During long-term immersion testing at 37°C and when high humidity is not applied, the electrolyte can evaporate reducing the volume. This can cause an increase of pH and concentration of species, changing the alloy degradation performance [182]. Therefore, long immersion testing (> 7 days) should be abandoned because the pH and species concentration are far from a true situation. In some studies the medium is replaced periodically in order to correct the evaporation and to maintain the pH in the physiological range [157, 183]. In general, replacing the testing solution regularly is time consuming and reduces the accuracy of the gas volume measurement and pH after every change.

1.6.5. Surface preparation

Bracht et al. recently showed that storage can have an influence on the degradation behaviour of Mg based materials; thus, while storing the material, a natural ageing process has been observed as well as an increase in oxygen-enriched regions on the implant surface [184]. Hence, untreated surfaces may form a MgO layer during storage time from the exposure to air or even $Mg(OH)_2$ in the presence of moisture. Therefore, in order to have an oxide-free substrate surface a surface preparation process is needed. Mueller et al. reviewed surface preparations for different electrochemical corrosion testing. Grinding and polishing are the most commonly applied methods [185]. However, these are only applicable for simple geometries and screw shaped implants require another type of preparation, e.g. chemical polishing.

In a real application implants are sterilized, delivered and stored. This might induce a surface film which will be present on the implant during the real application. Seitz et al. showed that different sterilization processes such as steam, ethylene oxide steam, gamma and dry heat sterilization methods will apply harsh conditions to the implant inducing damage to it. These methods have demonstrated significant although not large impacts on the mechanical characteristics of the material's strength in tensile, bending and compression tests [186]. Moreover, sterilization processes could alter surface characteristics and their interaction with biological entities, such as cells. Liu et al., analysed the influence of steam autoclave, ethylene oxide steam, glutaraldehyde, dry heat and Co60 gamma (γ) ray radiation sterilization methods on the biocompatibility of the material, by analysing the hemolysis percentage of the material in contact with human osteosarcoma cells (MG63) [187]. Liu concluded that gamma sterilization induced the best biocompatibility properties of the implant surface. Hence, sterilization methods that do not expose the sample to high temperatures or aggressive environments seem recommendable, such as UV or gamma radiation. In summary, the sterilization and the storage parameters have to be taken into consideration.

1.6.6. Data analysis

For the analysis of the degradation rate (DR), the use of a common unit is advocated to increase comparability among studies. A suitable one, already widely used in literature, is millimetre per year, denoted as mm/y or mmpy [146]. Alternatively, $mg/cm^2/day$ can be found, and it can be related to mm/y through the calculation of the material density. The mm/y gives information of the thickness of material lost over time, but it presumes a homogenous corrosion. It does not account for pitting or localised corrosion.

The DR can be calculated from mass loss or hydrogen evolution data, but in some cases these two methods lead to differences between results. In the mass loss method the corrosion products are removed from the specimens by chromic acid solution (200 g/L CrO_3, 10-20 g/L $AgNO_3$ [163, 188-190]) before weighing them. The total weight difference over the immersion time defines the DR. DR by the mass loss method is calculated in this way [191]:

$$\mathrm{DR} = 87600\ \frac{\Delta \mathrm{W}}{\mathrm{A\,t\,\rho}} \qquad \text{Mass loss (10)}$$

where the mass difference between before testing and after chromic acid cleaning is ΔW (g), A is the sample area (cm^2), t is the immersion time (h), alloy density is ρ (g cm^{-3}). When chromic acid treatment is not applied even mass gain of specimens can be reported [192].

When the hydrogen evolution method is employed for degradation rate calculation, hydrogen is collected to monitor the DR over the immersion time. The H_2 collected allows the calculation of the DR by the ideal gas law as follows:

$$\mathrm{DR} = 87.6\ \frac{\mathrm{P_{atm}V_{H2}\,M}}{\mathrm{R\,T\,A\,t\,\rho}} \qquad H_2\ \text{evolution method (11)}$$

where P_{atm} (1.013 atm) is the atmospheric pressure, H_2 volume corresponds to V_{H2} (ml), M is Mg molar mass (24.31 g mol^{-1}), R is the ideal gas constant (0.082 atm L mol^{-1} K^{-1}) and T is the temperature (K). In case of rapidly degrading materials, the difference between DR determined from H_2 and from mass loss is explained by three mechanisms: particle undermining [47], the amount of H_2 dissolved in the electrolyte and not collected at the eudiometers; and H_2 diffusion into the Mg sample [60, 193, 194]. It is known that Mg metal can store a significant amount of hydrogen [195]. Moreover, as shown in Section 1.5.2.a, in Mg-RE alloys hydrides can form in cuboid shape [102], which could also absorb hydrogen from the environment, also explaining the difference between DRs from mass loss and H_2 evolution.

1.6.7. pH and osmolality

Complementarily to the H_2 gas evolution evaluation, periodic measurements of pH and osmolality are also recommended to monitor the degradation process [163, 196, 197]. As indicated by Eq. 2, during Mg degradation OH^- ions are released increasing the pH. Thus, a higher pH can be translated into a faster degradation profile of the material. In parallel, the osmolality gives information about the ionic strength of the electrolytes. This can be monitored and compared to the initial values, in order to determine the increase of Mg^{2+} and other ions in the electrolyte and in this case, a higher osmolality also indicates a faster DR.

1.6.8. Biological entities

The presence of biological entities and organic compounds, such as proteins, cells, vitamins or amino acids, can influence unpredictably the degradation results. During the healing process Mg can have contact with several different biological entities, such as macrophages during the inflammatory reaction [198, 199]. Mg can promote bone generation, bone growth and bone remodelling stimulating the osteoblast, chondrocyte, osteoclast differentiation and proliferation, respectively [200-202]. However, the degradation testing should not include too many factors in order to enable the data interpretation.

Yamamoto et al. compared the degradation rate of pure Mg in NaCl, Earle (+) solution, Eagle's minimum essential medium (E-MEM) and E-MEM with fetal bovine serum (FBS) [168]. It was concluded that the lowest DR was detected in E-MEM+FBS which is attributed to the contribution of the adsorbed proteins to make the insoluble salt layer denser or more effective as a barrier against corrosion [168]. Liu et al. observed the influence of bovine serum albumin (BSA) on Mg polarization and immersion corrosion results. It was concluded that a higher BSA concentration is beneficial to the mitigation of the corrosion process of the AZ91 in SBF [203] and Mg-Ca alloys in 0.9 wt. % NaCl solution [204]. Wang et al. observed a similar influence of albumin on Mg1Mn alloy, especially during the initial degradation stage [205]. The adsorption of proteins on surfaces is a complex process that involves van der Waals, hydrophobic and electrostatic interactions and hydrogen bonding. Thus, it is generally believed that proteins interact and alter the corrosion behaviour of metals via adsorption, chelation and formation of a protective layer.

Interestingly, Yang et al. did not observe adsorption of proteins at low concentrations of fetal bovine serum (FBS) to Mg-Dy alloys at physiologically relevant conditions, so that the proteins stay in solution. On the other hand, when the concentration was >80% of FBS a depletion of proteins from solution was observable, indicating the protein adsorption [163].

1.7. Electrochemical testing

Electrochemical methods can be applied in order to get a fast comparison of corrosion reactions between different Mg alloys. However, many results applying electrochemical and immersion experiments aiming at biomedical applications can be found in literature, showing that these two methods do not lead to the same corrosion rate for the same nominal material [146]. Here, electrochemical methods and their applicability are reviewed.

1.7.1. Potentiodynamic polarization

Potentiodynamic polarization (PDP) or linear sweep voltammetry experiments give a quick comparison between the degradation profile of different Mg alloys [134, 196]. In this method, a linear potential scan is performed around the open circuit potential (OCP) of the sample measuring the current with an external circuit. With the Tafel extrapolation the corrosion current density (i_{corr}) at the corrosion potential (E_{corr}) is a measure of the exchange of electrons between the anodic and the cathodic reaction (Fig 14). This Tafel fit assumes that the process is controlled by the charge transfer. The electrochemical kinetics follow the Butler-Volmer equation, with a uniform corrosion mode and no additional electrochemical reactions involved [206]. In order to calculate the corrosion current density the Tafel fit should be done over the voltage range: ±500 mV and ±150 mV around the corrosion potential to determine the anodic and the cathodic slopes, as recommended by Kirkland et al. [175]. Fig. 14 shows how different fitting ranges can determine different i_{corr}.

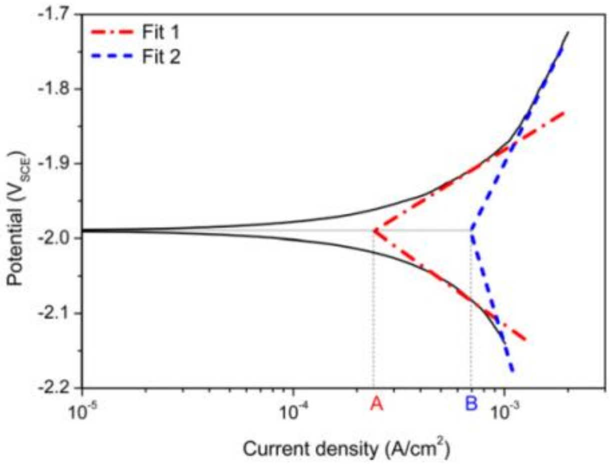

Figure 14. Example of Tafel-type analysis of a set of data where slopes determined by different investigators result in different current densities (A and B) [175]. This figure is reprinted with permission.

Thus, i_{corr} is transformed into DR by Faraday's law (Eq. 12) as follows:

$$DR = 3{,}1536 \cdot 10^{8} \frac{i_{corr}\, M}{n\, F\, \rho} \qquad \text{DR with } i_{corr} \quad (12)$$

where i_{corr} is the current density in (A cm^{-2}), M is Mg molar mass (24.31 g mol^{-1}), n is the valence number of electrons transferred per Mg ion (considered as 2), F is the Faraday constant (96,485 A s mol^{-1}) and the alloy density is ρ (g cm^{-3}).

This technique can also characterize quantitatively the protectiveness of the surface film and corrosion resistance of the material. According to the following equation, the polarization resistance of the sample (R_p) in Ω cm^2 can be assessed [188, 207, 208] applying the Stern-Geary equation [209]:

$$R_p = \frac{\beta_a\, \beta_c}{2.3\, (\beta_a + \beta_c)\, i_{corr}} \qquad R_p \text{ from } i_{corr} \quad (13)$$

where β_a and β_c are the anodic and cathodic slopes (V $decade^{-1}$), respectively.

1.7.2. Open circuit potential

Open circuit potential (OCP) is a fast measurement that can allow quick ranking of Mg alloys regarding their corrosion resistance. This test measures the potential of the pristine Mg surface against a reference. When the same reference is used, results with different alloys can be directly compared. At the start of the test more cathodic values are measured, i.e. lower than -2V (see example in Fig. 15a [210]). Then OCP values get more positive with time until a plateau is reached. The speed of reaching this plateau is related to the degradation layer precipitation phenomena on the pristine surface [52, 211].

Hence, the faster the OCP changes during the first immersion seconds, the faster the degradation reaction and its concomitant degradation layer formation. As shown in Fig. 15b, OCP phenomena strongly depend on the electrolyte in which the testing takes place [212]. The OCP should normally equal to the E_{corr} if these two measurements are performed consecutively.

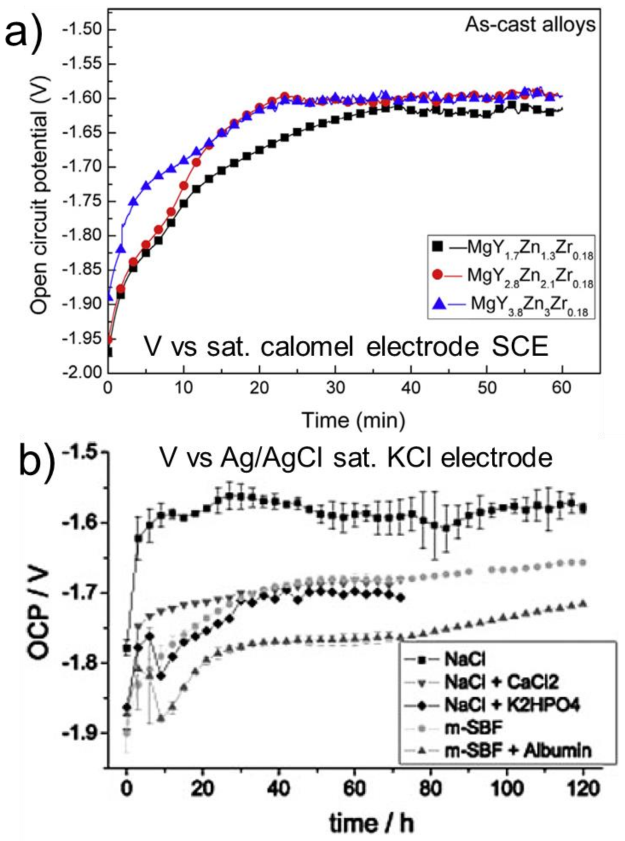

Figure 15. (a) OCP measurement allows quick ranking of Mg-alloy, such as Mg-Y-Zn-Zr, according to their corrosion profile [210]. (b) Electrolyte influence on the OCP measurement of over long time immersion tests in: 0.9 w.% NaCl, NaCl+$CaCl_2$, NaCl+ K_2HPO_4, modified SBF (m-SBF), and m-SBF+albumin [212]. Figures are edited and reprinted with permission.

1.7.3. Electrochemical impedance spectroscopy

Electrochemical impedance spectroscopy (EIS) can be applied to characterize the degradation layer performance during a prolonged immersion test [197, 208, 212] or under different testing conditions [182, 203]. One of the positive aspects of EIS analysis is that it introduces a minimal disturbance to the corrosion process, as it applies a typically lower than 10mV amplitude signal around the OCP varying the frequency, e.g. from 100 kHz to 0.05Hz. With this technique it is also possible to assess the polarization resistance (R_p) of the degradation layer, applying an appropriate equivalent circuit model. This measurement can be compared quantitatively with i_{corr} calculated by polarization experiments (Eq. 13) and some authors found a good correlation between these two methods [188, 189, 213-215]. Thus, R_p can be translated into a DR with the above described Eqs. 12 and 13.

Moreover, a good understanding of the degradation layer formation must be had, and an appropriate equivalent circuit must be applied, in order to get relevant results. These models, basically, use electrical elements such as resistances (R), capacitances (C), or constant phase elements (CPE) when the material is porous or cracked, and inductances (L) when there is negative complex impedance at low frequencies. Each electrical element is related to each component of the real system, such as, electrolyte, interface, degradation layer, cracks, porosity or adsorption of proteins. Liu et al. [216] presented the equivalent circuit which is usually used in many studies to fit the EIS results (Fig. 16) [149, 217, 218]. In this model presented by Liu et al., R_{sol} is the solution resistance, R_{pore} is the sum of the resistances of all pores and cracks in the surface film, R_{ct} is the charge transfer resistance, CPE_{film} represents constant phase elements of the corrosion products film, CPE_{dl} is the sum of constant phase elements of the double layer located at the interface between the bottom of the pores and the Mg substrate.

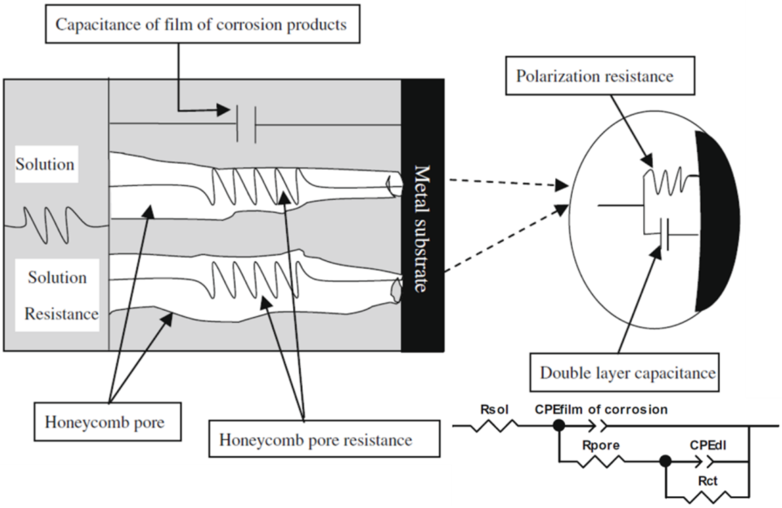

Figure 16. Commonly applied equivalent circuit to fit EIS data and its equivalency to the degradation layer and metal substrate [216]. This figure is reprinted with permission.

However, there are many authors fitting their EIS results to different equivalent circuits [197, 204, 213, 216, 219, 220]. King et al. found a good correlation between EIS data and immersion test results with mass loss and hydrogen collection, as shown in Fig. 17a [220]. The degradation rate is calculated with Faraday's law and the polarization resistance is determined by the Stern-Geary equation applying the low frequency data and the inductive loop. As depicted in Fig. 17b, the end of the inductive loop at the cross with the zero of the imaginary axis represents the solution resistance plus the polarization resistance.

R_p is the equivalent resistance of the entire circuit (Fig. 17c) when frequency trends to 0, so that capacitances trend to ∞ and the inductance to 0. This calculation is done as follows:

$$\frac{1}{R_p} = \frac{1}{R_1+R_2} + \frac{1}{R_3} \qquad \text{Polarization resistance calculation (14)}$$

However, Shi et al. also applied the equivalent circuit proposed by King et al., shown in Fig. 17c, not finding a good correlation between EIS and immersion tests with different high purity Mg, Mg-5Zn, Mg-0.1Zr and Mg-0.1Sr alloys [213]. Thus, there is some criticism regarding the data analysis of EIS technique.

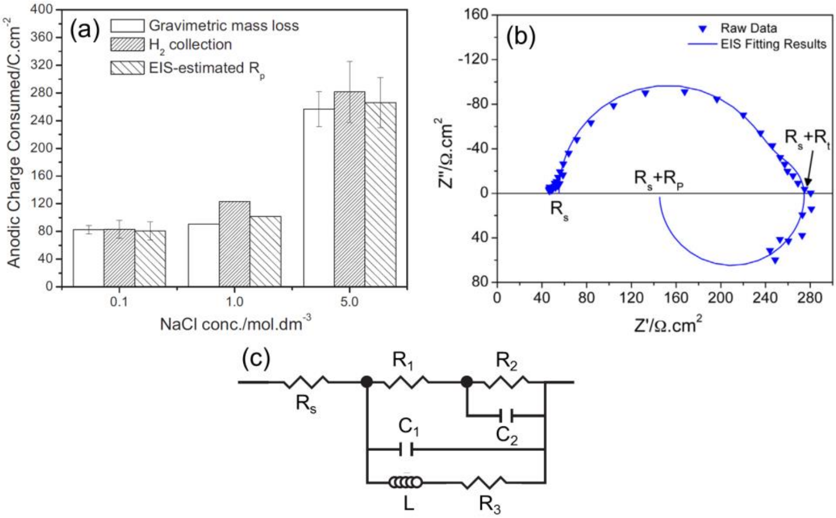

Figure 17. (a) EIS and immersion tests data showed good agreement when the R_p applied is calculated as recommended by King et al [220]. (b) Fitting of experimental data including the low frequency range shown at the Nyquist plot. Figs. a and b from Ref. [220]. (c) Equivalent circuit proposed when inductive loop is measured. Figures are edited and reprinted with permission.

1.7.4. Negative difference effect

Magnesium dissolution is different from other metals, as Mg can support cathodic hydrogen evolution on its surface during anodic polarization [48, 221, 222]. The phenomenon of cathodic hydrogen evolution upon anodically polarised Mg is characterised by the rate of the hydrogen evolution reaction increasing with anodic polarisation, a phenomenon called the negative difference effect (NDE) [223-225]. As shown in Fig. 18a, Song and Atrens reported this gas evolution during anodic polarization [47, 48]; which recently has been expanded to larger cathodic and anodic applied current densities by Frankel et al. (Fig. 18b) [221].

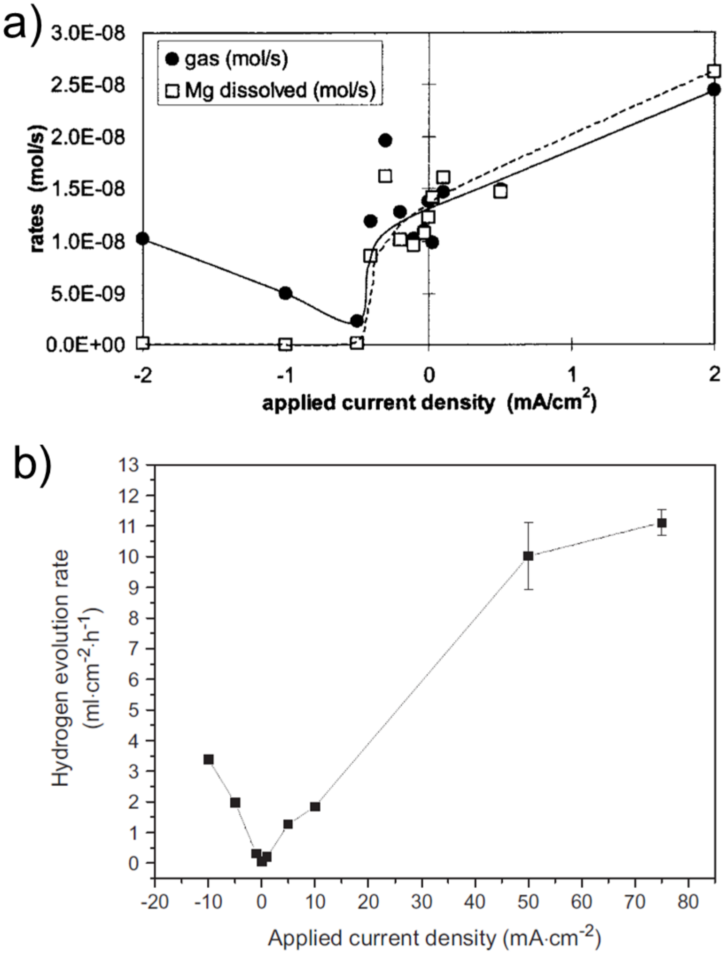

Figure 18. At the cathodic site there is only gas release and no mass loss but when the applied potential becomes more anodic the hydrogen evolution rate actually increases. (a) Data by Song and Atrens up to a 2 mA/cm^2 [47, 48]. (b) More recent extended data up to 75 mA/cm^2 by Frankel et al. [221]. Figures are edited and reprinted with permission.

When potentiodynamic polarization (PDP) tests are performed the scanning is done from the cathodic to the anodic region passing by the open circuit potential or corrosion potential (E_{corr}). When no electrolyte flow is induced accelerated anodic curves are measured, as shown in Fig. 19a. Ideally the cathodic and the anodic curves shown should be symmetric around the E_{corr}. However, the asymmetric anodic curve is the result of the enhanced cathodic and anodic reactions. Fig. 19b shows how the cathodic reaction is accelerated during anodic polarization and in parallel the anodic current is higher than the expected. It is also possible to observe how the electron exchange between the anodic and the cathodic reactions or the corrosion current density (i_{corr}) at the E_{corr} is determined by the Tafel extrapolation. Thus, the enhanced reactions result in a distorted measured anodic curve, as shown in Fig 19a.

Recently, Curioni developed a test set-up which allows the measurement of the H_2 gas generation during polarization experiments (Fig. 19c). This setup allows the determination of the gas evolution in situ, and thus, the cathodic current density can be quantified. And, as shown in Fig. 19d, Curioni could determine the expected anodic and cathodic curves (Fig. 19b) and compare them to the experimental anodic curve typically measured.

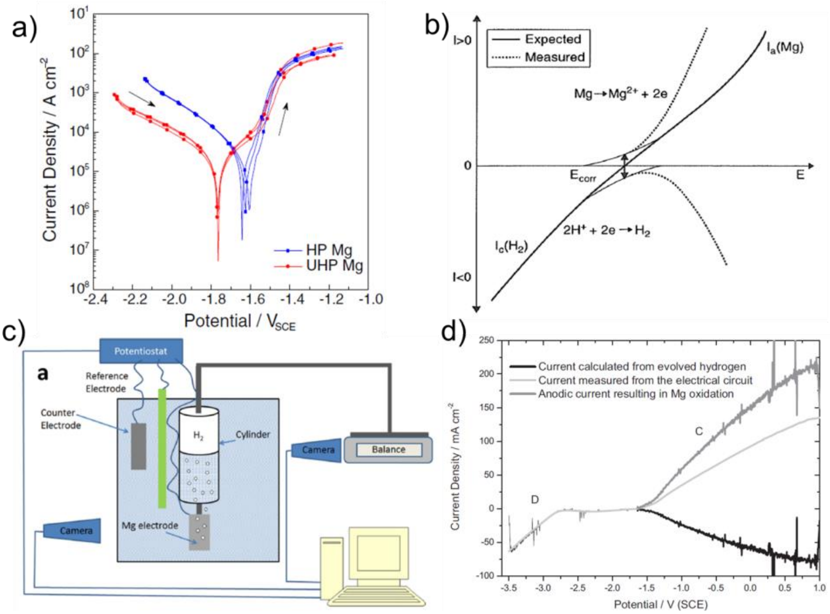

Figure 19. Negative difference effect and its influence on the polarization measurements. (a) Abnormal anodic curves commonly determined, example from Fajardo et al. [226]. (b) Explanation of the enhanced anodic and cathodic reactions from Bender et al. [227]. (c) Innovative in situ hydrogen measurement setup during polarization experiments. (d) Empirical results demonstrating the enhanced anodic and cathodic reactions at applied anodic potentials [222]. Figures are edited and reprinted with permission.

1.7.5. Theories related to NDE

Thomas et al. summarized the theories explaining Mg degradation mechanisms and some can also help to explain the NDE [41], such as:

- Unipositive Mg
- Enhanced catalytic surface theory
- Mg dissolution into particles
- Impurities based models
- Magnesium hydride intermediate models

a) Unipositive Mg

The unipositive Mg theory became popular in the past two decades, by the reports of Atrens, Song and co-workers [47, 48, 213, 224, 228-231]. Initially in 1929, Gomberg et al. [232] postulated the existence of halides of unipositive Mg (Mg^{+}) in ether-benzene solutions. Afterwards in 1954, Petty et al. borrowed this postulate and related the NDE to the existence of a Mg^{+} intermediate during Mg corrosion [233]. Song and Atrens extended this notion, and proposed a mixed electrochemical/chemical model for the NDE. In this model, Mg is first electrochemically dissolved to form Mg^{+} ions according to the following reaction (15):

$$\mathrm{Mg} \rightarrow \mathrm{Mg}^{+} + \mathrm{e}^{-} \qquad \text{1st anodic reaction (15)}$$

Subsequently, a chemical reaction of Mg^{+} with water takes place which is explained with a rapid electron release transforming Mg^{+} into Mg^{2+}, releasing hydrogen gas as shown in reaction (16). Reaction is considered to be controlled partially by reaction (17), with a proportionality designated as k, and a second electrochemical oxidation step shown as reaction (17):

$$(1-\mathrm{k})\mathrm{Mg}^{+} + (1-\mathrm{k})\mathrm{H_2O} \rightarrow (1-\mathrm{k})\mathrm{Mg}^{2+} + (1-\mathrm{k})\mathrm{OH}^{-} + (1-\mathrm{k})\frac{1}{2}\mathrm{H_2} \qquad (16)$$

$$\mathrm{kMg}^{+} \rightarrow \mathrm{kMg}^{2+} + \mathrm{ke}^{-} \qquad \text{2nd anodic reaction (17)}$$

Thus the cathodic hydrogen evolution reaction also follows this proportionality, and in any case, in the overall reaction 1 mol of Mg dissolved is directly related to 1 mol of H_2 generated:

$$(1+k)H^{+} + (1+k)e^{-} \rightarrow (1+k)\frac{1}{2}H_2 \qquad \text{Cathodic reaction (18)}$$

$$\mathrm{Mg} + 2\,\mathrm{H_2O} \rightarrow \mathrm{Mg(OH)_2} + \mathrm{H_2} \qquad \text{Overall reaction (19)}$$

Many authors use the monovalent Mg ion theory to explain the low corrosion rates determined by electrochemical techniques in comparison with immersion techniques [189, 208, 213, 214]. However, it is important to note that the Mg^+ species has never been experimentally detected. Recently, Samaniego et al. [234] repeated the same experiments performed by Petty et al. [233] concluding that there is no need to hypothesise the formation of Mg^+ at the Mg electrode. Therefore, the only evidence for the existence of Mg^+, albeit circumstantial, has thus been proved wrong (in 2014) and therefore should not be further cited in the context of the NDE. Another interesting finding of Samaniego et al. [234] was that SO_2 reduction from sulphate increased as the applied potential became more noble, which is an NDE effect for sulphate on Mg. The sulphate kinetics on Pt, in contrast, followed the expected behaviour of being lower at higher potentials. The dissolving Mg surface is apparently active for cathodic reactions other than the hydrogen evolution reaction.

b) Enhanced catalytic surface theory

There has been significant recent works showing reproducible and independent evidence that the NDE can be explained by the enhanced catalytic surface (ECS) theory, so that the Mg dissolution does not occur via the Mg^+ mechanism [220, 222, 235-240]. These recent works have employed a combination of methodologies including electrochemical experiments coupled with hydrogen collection [221, 222, 241], real-time video imaging [240], as well as the scanning vibrating electrode technique (SVET) [236, 238].

The ECS theory considers the creation of dark corrosion products during anodic polarization which act as cathodes enhancing the H_2 evolution reaction (HER) by coupling these sites to the surrounding uncovered Mg surface, which is the anode. As shown in Fig 20a, dark corrosion products can act as cathodes promoting the H_2 evolution reaction (HER) and dissolving the surrounding Mg which acts as anode [241]. In this reaction there is an electron exchange between these two areas which is not measured by an external circuit and this explains the negative difference effect (NDE). Also Curioni showed that the kinetics of the HER on Mg increased with an increased coverage of the dark corroded regions on pure Mg (Fig. 20b) [222]. The spreading of dark regions on pure Mg surface under impressed anodic currents is physically depicted in Fig. 20c [222].

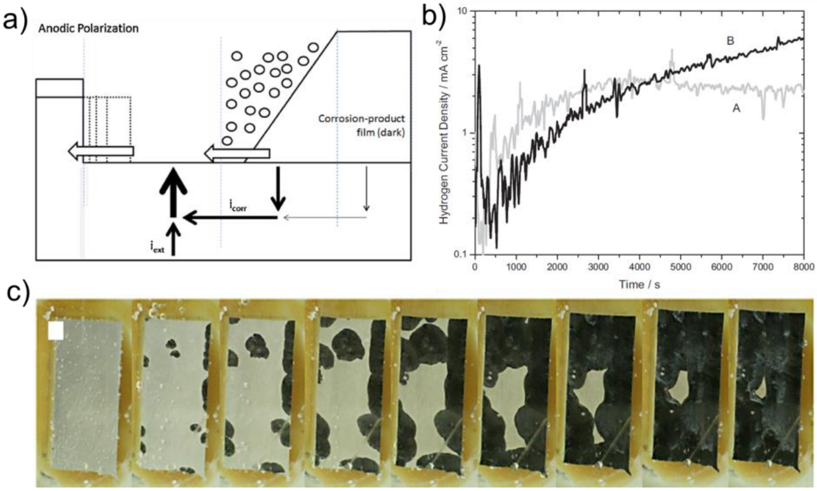

Figure 20. (a) Dark corrosion layer and the surrounding Mg act as cathode and anode respectively, exchanging electrons between these two areas. Therefore, current (i_{corr}) is exchanged between these two areas, resulting in a reduced current measured externally (i_{ext}) and a slower corrosion process than the actual process. This phenomenon explains the negative difference effect (NDE). Figure (a) is from Curioni et al. [241]. (b-c) Propagation of the dark film corroding at OCP enhances the HER from Curioni [222]. (b) Shows the i_{corr} estimated from the hydrogen generation from of 2 samples (A and B) tested at the same nominal conditions and (c) the dark corrosion product formed on sample A during this experiment. The time spacing between images in (c) is 1000 s. Figures are edited and reprinted with permission.

Taheri et al. analysed such dark corroded regions finding that the dark region is composed of an inner compact oxide (MgO) and an outer layer of $Mg(OH)_2$ [239], as previously reported by Nordlien et al. [242]. Moreover, Taheri et al. showed that noble impurity elements, like Fe, released from the Mg surface may be entrapped in the $Mg(OH)_2$ layer, which may further activate the cathodic reaction [239]. Williams et al. [238] and afterwards Fajardo et al. [226] also indicated that iron particle impurities influence the anodic polarization behaviour, which can be attributed also to other impurity elements [78].

Williams et al. carried out in-situ scanning vibrating electrode (SVET) measurements on pure Mg during galvanostatic anodic polarization at 1 mA/cm^2 in 2 M NaCl solution (Fig. 21) [236]. Via this experiment, the temporal evolution and distribution of the anodes and cathodes on pure Mg during anodic polarisation was revealed. Fig. 21a shows that some areas on Mg become anodes (depicted as red areas) after about 7 min of immersion. And with time, these anodic areas transform into cathodes (depicted in blue in Fig. 21b) and the surrounding areas become anodes, so that these transformed areas sustain the HER. With further progress of time, almost all prior anodic sites transform into cathodic sites (Fig. 21c-d). SVET-derived integrated anodic and cathodic current evolutions over time are depicted in Fig. 21d. Initially, the cathodic current is zero, meaning that when the sample surface is freshly prepared no cathodic sites can be detected, but with time the anodic and cathodic current increase. The anodic activity shows a higher current “noise” level. Note also that in Figs. 21a-d the cathodic current density detected by the SVET does not exceed 20 mA/cm^2 at any locality while the anodic current exceeds this value.

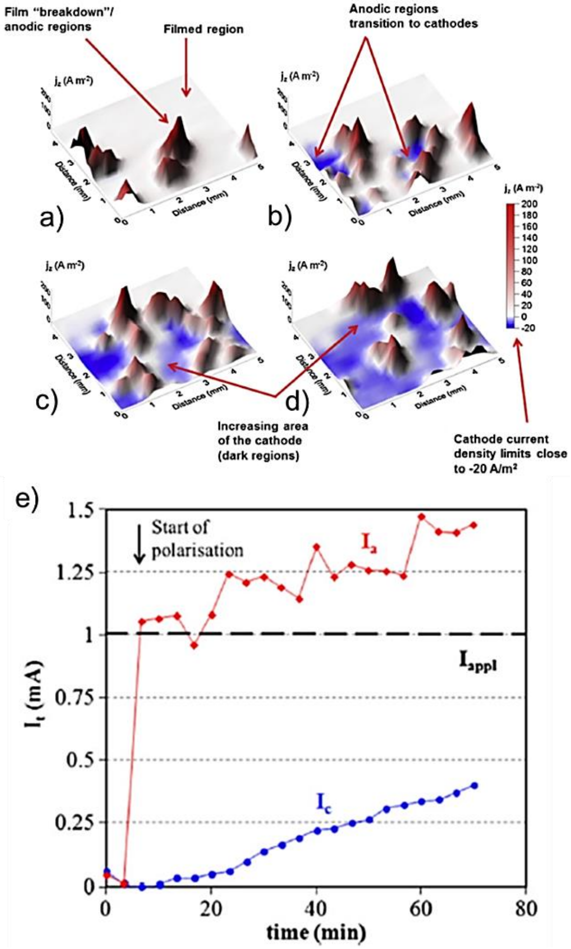

Figure 21. Surface maps showing current density distributions above a Mg surface immersed in a 2 M NaCl (aq) electrolyte at (a) 7, (b) 28, (c) 48 and (d) 68 min after starting galvanostatic polarization. (e) shows a plot of time dependent SVET-derived integrated current, normalised for a 1 cm^2 area. Figure from Ref. [236]. Figures are edited and reprinted with permission.

In conclusion, the Mg dissolution reaction involves 2 electrons which are exchanged electrochemically and the reactions remain as explained in Section 1.3 (noted as reaction 1-4).

c) Mg dissolution into particles

Straumanis and co-workers [243] proposed that Mg dissolved as minute particles or flakes (i.e. clusters of many Mg atoms), which could also be entrapped in the $Mg(OH)_2$ film. The purported disintegration of a metal into particles and flakes was also reported by Hoey et al. [244]. If such metallic Mg particles are released by the metal electrode either into the surface film or into solution, the subsequent corrosion of these particles by reaction would result in the generation of H_2 with no flow of current through the measuring system. The resulting NDE associated with the separate dissolution of metallic Mg entrapped in the film during anodic polarisation has been termed the ‘‘chunk effect’’ [243]. This mechanism is related to the particle undermining model presented in Section 1.3 (Fig. 4e).

d) Impurities based model

As mentioned in Section 1.5.1, Hanawalt and co-workers demonstrated the effects of different impurities in Mg, such as Fe, Cu and Ni, on the resultant corrosion, defining their tolerance limits [78]. McNulty and Hanawalt later studied the corrosion of high purity Mg in 3 wt.% NaCl solution using hydrogen collection and anodic polarisation. They observed that the corrosion rate of Mg was initially high and decreased within 24 h [245]. This was attributed to the corrosion film formation on top of not only Mg but also on the cathodic particles, decreasing the cathodic activity. It was also considered that some cathodic impurities, dislodged during Mg dissolution, could re-precipitate onto the Mg surface itself increasing the HER and the film formation would also cover these particles [245]. Later, Glicksmann showed that such metals deposited on the Mg surface, or on the oxide film, were proven to be the preferential sites for the HER [246].

e) Magnesium hydride intermediate models

Perrault presented a modified (but not experimentally validated) Pourbaix diagram (Fig. 22) for Mg by including MgH_2 [247]. He hypothesised a two-way mechanism for Mg dissolution that included a general mechanism involving reactions (1-4) and another new mechanism involving a MgH_2 intermediate [247]. Gulbrandsen subsequently performed ex-situ XRD studies on Mg electrodes exposed to HCO_3^-/CO_3^{2-} buffer and showed MgH_2 formation on Mg [248]. Thus, it was hypothesised that some hydrogen evolution may take place due to involvement of the MgH_2 intermediate during Mg dissolution (Eq. 20):

$$MgH_2 + 2H_2O \rightarrow Mg^{2+} + 2OH^- + 2H_2 \qquad \text{Magnesium hydride (20)}$$

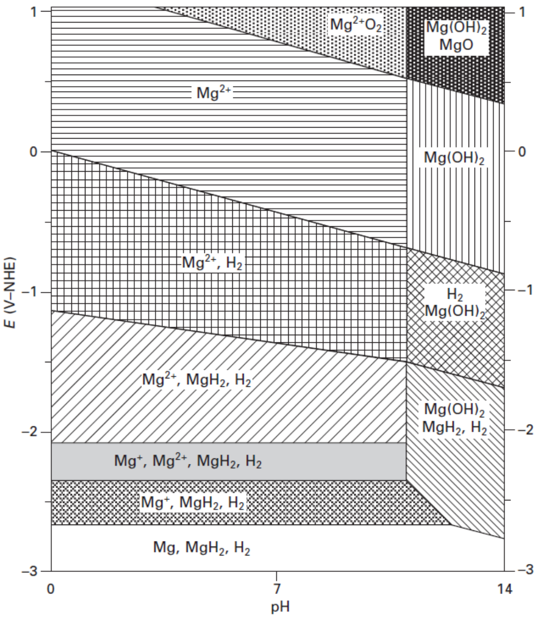

Figure 22. Pourbaix diagram (E-pH) with possible stable substances in a Mg-H_2O electrochemical system [249]; data source: Ref. [247]. This figure is reprinted with permission.

Despite the fact that Atrens, Song and co-workers agreed with this model [48, 228-230], this mechanism has not been experimentally validated in the context of NDE.

1.7.6. Rotating disc electrode

The rotating disc electrode (RDE), where the Mg working electrode is a disc in rotation, can reduce the corrosion product deposition on the sample surface. The fluid flow can remove the dissolved Mg^{2+} ions from the surroundings of the Mg surface and this, in principle, reduces the formation of a degradation layer which influences the polarization measurement. The RDE is a well-known hydrodynamic method which attains the steady state rather quickly [250]. Bender et al. developed a polarization method which applies a RDE and after preliminary investigations, 2000 rpm was considered the most effective rotation speed [227, 251, 252]. However, there is no experimental proof of why 2000 rpm is an optimal value. In any case, this could help to determine the polarization behaviour of film free Mg samples.

1.8. In vitro and in vivo testing

Martinez-Sanchez et al. reviewed the degradation rates (DR) of different Mg alloys determined in different studies in vitro and in vivo [146]. In some cases, a lack of information to calculate the DR was detected, and the highly variable methodological procedures in previous studies are some of the limiting factors of the comparability. In addition, some in vivo studies are only qualitative and lack quantification of corrosion observations; and in general, degradation studies of the same Mg-based material do not include enough material data to allow complete interpretation of the results. They suggest that, perhaps a round-robin laboratory approach would be very helpful for this aim.

Nevertheless, from the data collected in the above mentioned review [146], it was highlighted that the variability in experimental set-ups is not as large as would be expected; and when comparing in vitro-in vivo DR, the correlation factor indicated that DRs in vivo are between 1 and 5 order of magnitude lower than the DR in vitro. However, this difference in values is reduced when selecting the media which better mimics physiological conditions (such as SBF, EBSS or cell culture media). As shown in Fig. 23, Galli et al. have recently reported difficulties to distinguish newly formed bone from the degradation layer after in vivo experiments by synchrotron radiation imaging [253]. The blue arrows indicate the contours of residual metallic alloy and red arrows the degradation layer, still shaped as threads, in contact with bone.

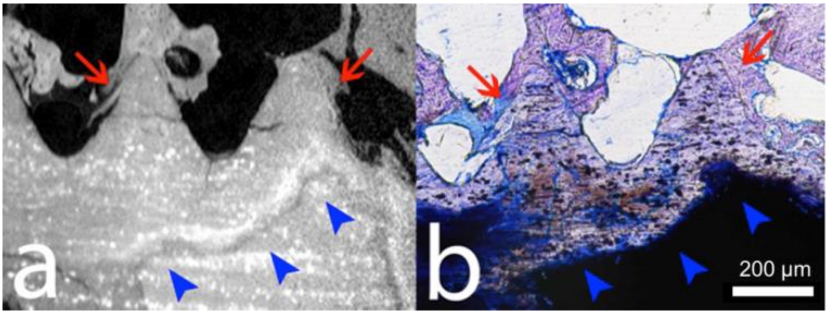

Figure 23. (a) µCT slice image of Mg-4Y-3RE alloy in rat bone after 3 months; and (b) its corresponding histology image [253]. Blue arrows indicate the contours of the residual metallic alloy; red arrows: degradation layer, still shaped as threads, in contact with bone (toluidine blue). Note that in (a) the greyish area above and under the blue arrows correspond to the degradation layer and implant respectively. These two parts could not easily be distinguished by synchrotron radiation imaging technique. Reprinted with permission.

1.9. In vitro cytotoxicity testing applied to immersion testing

Recently, Wang et al, reported the up-to-date recommendations for modifying current cytotoxicity testing standards for biodegradable magnesium-based materials [254]. Table 3 shows these recommendations which can be also partially applied to get in vitro degradation data more comparable to in vivo.

Table 3. Newly reported recommendations for improved cytotoxicity testing of biodegradable Mg materials [254].

Parameter	Recommendation
Temperature	37 ± 1°C
Duration	72 ± 2 h.
Medium	Cell culture medium with serum
Sterilization during testing	UV radiation (no contamination until 72h)
Atmosphere (incubator)	5 vol. % CO_2 and high humidity
V/S ratio (dependant on the sample)	• Flat samples with different thickness: 0.16, 0.33, 0.8 ml/cm^2 • Solid and porous devices with irregular shape: 5 and 10 ml/g respectively.
Dilution of extracts	More than 6 and less than 10 times

For instance, the duration of 3 days seems also appropriate for biodegradation tests since too long tests will not accurately mimic the pH and ion concentration during a real application. Moreover, the sterilization of the test equipment when cell culture medium is applied is found necessary. The influence of the contamination might be of interest. The V/S ratio for cytotoxicity tests are in general low, due to the high concentration of cells and the small capacity of well-plates used. Thus, the degradation behaviour is slowed down as explained in Section 1.6.2. The addition of 5 vol.% of CO_2 and high humidity are also commonly applied in biodegradation tests to buffer the medium and reduce water evaporation respectively [50, 62, 163, 179]. Finally, the dilution is not considered necessary as it is only applied for extracts of Mg to interact with cell cultures. The cell culture medium contains a similar ion concentration as compared to body plasma and whole blood (shown in Table 3).

1.10. Surface modifications

Currently, many researchers study surface modifications on Mg alloys aiming at biodegradable implant applications. The modifications can help to tailor degradation behaviour, mechanical properties and biological response of the material. Some examples of different surface modification techniques are: chemical conversion treatment, arc deposition, ion implantation, sputtering, thermal spraying, laser technology, electrodeposition or electrosynthesis, polymer-based coating, heat treatment, mechanical treatment, and physical or chemical vapour deposition [20, 255].

New biomaterials can offer the possibility to deliver a drug during the first inflammatory reaction caused by the Mg implants. Metal organic frameworks (MOFs) are newly developed materials which can be used as drug delivery system [256, 257]. The MOF structure consists of organic molecules as segments or ligands and metal ions as nodes which can construct a nanoporous 3D structure [258]. This MOF can be applied on a Mg substrate using Mg as the metal in the MOF structure (Mg-MOF) [259]. This Mg-MOF can possibly tune the degradation behavior of a Mg implant with the additional drug delivery function.

1.10.1. Mg-MOF as drug carrier

Metal organic frameworks (MOFs) are novel materials designed for different applications with a growing interest since their discovery in 1989 by Robson [258], especially in the last 15 years (Fig. 24) [260]. This increasing interest is due to the nanoporosity with tuneable pore size and topology. This leads to Brunauer-Emmett-Teller (BET) specific surface areas up to 7.000 m^2/g [261]. MOFs are designed with versatile architectures aiming at different applications, e.g. ion exchange or gas separation processes [260, 262-264].

But MOFs are also interesting materials for biomedical applications [256]. Horcajada et al. showed a drug delivery system based on MOF as drug nanocarrier [265-267]. Fe and 5 different organic ligands were used to synthesize Fe-MOFs. These were loaded with drugs, e.g. ibuprofen.

Mg can be used as the metal in the MOF structure (Mg-MOF) which could be applied as a coating on Mg implants and thus add drug storage and drug delivery capacity to the implant surface [268]. In addition, it could help to tune the degradation behaviour of the Mg-based implant. Dietzel et al. successfully synthesised hydrothermally Mg-MOF with DHTA (2,5-dihydroxyterephthalic acid) as ligand and $MgNO_3$ as the metal source, in two different structures CPO-26-Mg and CPO-27-Mg (Fig. 25) [259]. Ameloot et al. investigated for the first time the electrochemical synthesis of Cu based MOFs as a coating by deposition during anodic polarization [269]. Thus, Mg-MOFs could be applied to Mg implants as a newly developed coating material as drug carrier.

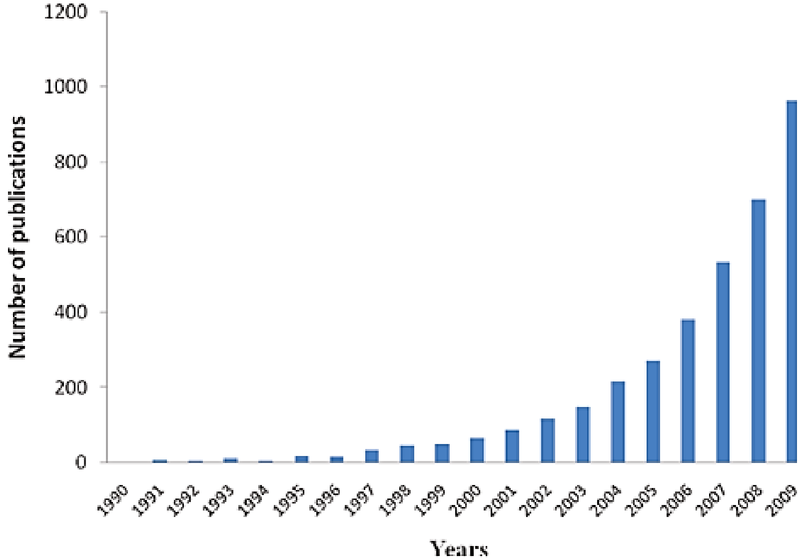

Figure 24. The trend of the number of MOF related publications shows an exponentially growing interest in the last 15 years [256]. This figure is reprinted with permission.

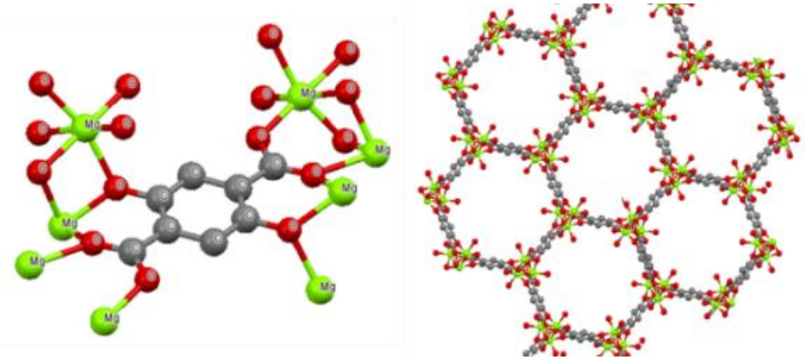

Figure 25. Mg-MOF structure synthesized hydrothermally CPO-27-Mg. Figures are generated by Mercury 3.5.1. software with the data from Dietzel et al. [259].

References

[1] F. Witte, Acta Biomater. 23, Supplement (2015) S28-S40.

[2] M.P. Staiger, A.M. Pietak, J. Huadmai, G. Dias, Biomaterials 27 (2006) 1728-1734.

[3] F. Witte, N. Hort, C. Vogt, S. Cohen, K.U. Kainer, R. Willumeit, F. Feyerabend, Curr. Opinion in Solid State and Mater. Sci. 12 (2008) 63-72.

[4] M.A. Kenney, H. McCoy, L. Williams, Calcified Tissue International 54 (1994) 44-49.

[5] M.S. Seelig, J. Am. Coll. Nutr. 12 (1993) 442-458.

[6] J.E. Sojka, C.M. Weaver, Nutr. Rev. 53 (1995) 71-74.

[7] K.L. Tucker, M.T. Hannan, H. Chen, L.A. Cupples, P.W.F. Wilson, D.P. Kiel, Am. J. Clin. Nutr. 69 (1999) 727-736.

[8] J.M. Banovetz, R. Sharp, R.A. Probe, J.O. Anglen, J. Orthop. Trauma 10(6) (1996) 389-394.

[9] C. Castellani, R.A. Lindtner, P. Hausbrandt, E. Tschegg, S.E. Stanzl-Tschegg, G. Zanoni, S. Beck, A.-M. Weinberg, Acta Biomater. 7 (2011) 432-440.

[10] A. Weiler, H.J. Helling, U. Kirch, T.K. Zirbes, K.E. Rehm, J. Bone and Joint Surgery, British Volume 78-B (1996) 369-376.

[11] O.M. Bostman, J. Bone and Joint Surgery, British Volume 73-B (1991) 679-682.

[12] I. Johnson, D. Perchy, H. Liu, J. Biomed. Mater. Res. Part A 100A (2012) 477-485.

[13] X.-N. Gu, Y.-F. Zheng, Front. Mater. Sci. China 4 (2010) 111-115.

[14] J. Fischer, D. Proefrock, N. Hort, R. Willumeit, F. Feyerabend, Mater. Sci. Eng. B 176 (2011).

[15] J. Fischer, M.H. Prosenc, M. Wolff, N. Hort, R. Willumeit, F. Feyerabend, Acta Biomater. 6 (2010).

[16] D.F. Williams, Biomaterials 35 (2014) 10009-10014.

[17] T. Kraus, S.F. Fischerauer, A.C. Hänzi, P.J. Uggowitzer, J.F. Löffler, A.M. Weinberg, Acta Biomater. 8 (2012) 1230-1238.

[18] K. Van de Velde, P. Kiekens, Polymer Testing 21 (2002) 433-442.

[19] Y.F. Zheng, X.N. Gu, F. Witte, Mater. Sci. Eng.: R. 77 (2014) 1-34.

[20] G. Wu, J.M. Ibrahim, P.K. Chu, Surf. Coat. Technol. 233 (2013) 2-12.

[21] J. Trinidad, I. Marco, G. Arruebarrena, J. Wendt, D. Letzig, E. Sáenz de Argandoña, R. Goodall, Adv. Eng. Mater. 16 (2014) 241-247.

[22] L. Jauer, B. Jülich, M. Voshage, W. Meiners, Eur. Cell Mater. 30 2015, p. 1.

[23] E.C. Huse, Chicago Med. J. Exam. (1878) 172-182.

[24] E. Payr, Arch. Klin. Chir. 62 (1900) 67-93.

[25] V. J., Bull. Mém. Soc. Nat. Cir. 59 (1937) 813-823.

[26] B.J.C. Luthringer, F. Feyerabend, R. Willumeit-Römer, Magnes. Res. 27 (2014) 142-154.

[27] H. Windhagen, K. Radtke, A. Weizbauer, J. Diekmann, Y. Noll, U. Kreimeyer, R. Schavan, C. Stukenborg-Colsman, H. Waizy, BioMedical Engineering OnLine 12 (2013) 62-62.

[28] Syntellix_AG, http://www.syntellix.us/en/syntellix/ (accessed 08/11/2016).

[29] Magnesium elektron, http://www.magnesium-elektron.com/products-services/synermag-bioabsorbable-technology (accessed 08/11/2016).

[30] Magnesium elektron, http://www.magnesium-elektron.com/magnesium-elektron-achieves-iso-134852012-certification-its-synermag-technology-centre (accessed 08/11/2016).

[31] P. Peeters, M. Bosiers, J. Verbist, K. Deloose, B. Heublein, J Endovasc Ther 12 (2005) 1-5.

[32] H. Eggebrecht, J. Rodermann, P. Hunold, A. Schmermund, D. Bose, M. Haude, R. Erbel, Circulation 112 (2005) e303-304.

[33] R. Waksman, R. Erbel, C. Di Mario, J. Bartunek, B. de Bruyne, F.R. Eberli, P. Erne, M. Haude, M. Horrigan, C. Ilsley, D. Bose, H. Bonnier, J. Koolen, T.F. Luscher, N.J. Weissman, JACC Cardiovasc Interv 2 (2009) 312-320.

[34] R. Erbel, C. Di Mario, J. Bartunek, J. Bonnier, B. de Bruyne, F.R. Eberli, P. Erne, M. Haude, B. Heublein, M. Horrigan, C. Ilsley, D. Böse, J. Koolen, T.F. Lüscher, N. Weissman, R. Waksman, The Lancet 369 (2007) 1869-1875.

[35] M. Haude, R. Erbel, P. Erne, S. Verheye, H. Degen, D. Böse, P. Vermeersch, I. Wijnbergen, N. Weissman, F. Prati, R. Waksman, J. Koolen, The Lancet 381 (2013) 836-844.

[36] R. Waksman, F. Prati, N. Bruining, M. Haude, D. Bose, H. Kitabata, P. Erne, S. Verheye, H. Degen, P. Vermeersch, L. Di Vito, J. Koolen, R. Erbel, Circ Cardiovasc Interv 6 (2013) 644-653.

[37] M. Haude, H. Ince, A. Abizaid, R. Toelg, P.A. Lemos, C. von Birgelen, E.H. Christiansen, W. Wijns, F.-J. Neumann, C. Kaiser, E. Eeckhout, S.T. Lim, J. Escaned, H.M. Garcia-Garcia, R. Waksman, The Lancet 387 (2016) 31-39.

[38] Biotronik, http://www.magmaris.com/en (accessed 08/11/2016).

[39] R.G. Buchheit, S. Green, Meeting Abstracts MA2011-02 (2011) 1802-1802.

[40] G.L. Song, Corrosion of Magnesium Alloys, Woodhead, Cambridge, 2011.

[41] Lide, CRC Handbook of Chemistry and Physics (87th ed.). Boca Raton, FL: CRC Press, 2006.

[42] S. Thomas, N.V. Medhekar, G.S. Frankel, N. Birbilis, Curr. Opin. Solid State Mater. Sci. 19 (2015) 85-94.

[43] Z. Li, X. Gu, S. Lou, Y. Zheng, Biomaterials 29 (2008) 1329-1344.
[44] B.A. Shaw, Corrosion resistance of magnesium alloys, ASM int., UK, 2003.
[45] H.R.B. Rad, M.H. Idris, M.R.A. Kadir, S. Farahany, A. Fereidouni, M.Y. Yahya, Front. Manu. Design Sci. 121-126 (2012) 568-572.
[46] M. Jamesh, S. Kumar, T.S.N.S. Narayanan, Corros. Sci. 53 (2011) 645-654.
[47] W.-D. Mueller, M. Fernandez Lorenzo de Mele, M.L. Nascimento, M. Zeddies, J. Biomed. Mater. Res. Part A 90A (2009) 487-495.
[48] G.L. Song, A. Atrens, Adv. Eng. Mater. 5 (2003) 837-858.
[49] G.L. Song, A. Atrens, Adv. Eng. Mater. 1 (1999) 11-33.
[50] S.V. Dorozhkin, Biomatter 1 (2011) 121-164.
[51] R. Willumeit, J. Fischer, F. Feyerabend, N. Hort, U. Bismayer, S. Heidrich, B. Mihailova, Acta Biomater. 7 (2011) 2704-2715.
[52] H. Kuwahara, Y. Al-Abdullat, N. Mazaki, S. Tsutsumi, T. Aizawa, Mater. Trans.(Japan) 42 (2001) 1317-1321.
[53] Y. Zong, G. Yuan, X. Zhang, L. Mao, J. Niu, W. Ding, Mater. Sci. Eng.: B 177 (2012) 395-401.
[54] L. Yang, E. Zhang, Mater. Sci. Eng.: C 29 (2009) 1691-1696.
[55] F. Feyerabend, H.-P. Wendel, B. Mihailova, S. Heidrich, N.A. Agha, U. Bismayer, R. Willumeit-Römer, Acta Biomater. 25 (2015) 384-394.
[56] S. Zhang, J. Li, Y. Song, C. Zhao, X. Zhang, C. Xie, Y. Zhang, H. Tao, Y. He, Y. Jiang, Y. Bian, Mater. Sci. Eng.: C 29 (2009) 1907-1912.
[57] L. Xu, G. Yu, E. Zhang, F. Pan, K. Yang, J. Biomed. Mater. Res. Part A 83A (2007) 703-711.
[58] M. Schinhammer, J. Hofstetter, C. Wegmann, F. Moszner, J.F. Loeffler, P.J. Uggowitzer, Adv. Eng. Mater. 15 (2013) 434-441.
[59] J. Hofstetter, E. Martinelli, A.M. Weinberg, M. Becker, B. Mingler, P.J. Uggowitzer, J.F. Löffler, Corros. Sci. 91 (2015) 29-36.
[60] J. Hofstetter, E. Martinelli, S. Pogatscher, P. Schmutz, E. Povoden-Karadeniz, A.M. Weinberg, P.J. Uggowitzer, J.F. Löffler, Acta Biomater. (2015) 347-353.
[61] N.I. Zainal Abidin, B. Rolfe, H. Owen, J. Malisano, D. Martin, J. Hofstetter, P.J. Uggowitzer, A. Atrens, Corros. Sci. 75 (2013) 354-366.
[62] D. Tie, F. Feyerabend, W.-D. Mueller, R. Schade, K. Liefeith, K.U. Kainer, R. Willumeit, European Cells and Materials 25 (2013) 284-298.
[63] F. Feyerabend, H. Druecker, D. Laipple, C. Vogt, M. Stekker, N. Hort, R. Willumeit, J. Mater. Sci. - Mater. Med. 23 (2012) 9-24.
[64] J.M. Seitz, R. Eifler, F.W. Bach, H.J. Maier, J. Biomed. Mater. Res. Part A 102 (2014) 3744-3753.
[65] G.L. Song, Corrosion electrochemistry of magnesium (Mg) and its alloys, in: G.L. Song (Ed.) Corrosion of Magnesium Alloys, Woodhead Publishing, 2011, pp. 3-65.

[66] S.P. Cashion, The use of sulphur hexafluoride (SF6) for protecting molten magnesium, Department of mining, minerals and materials engineering, vol PhD thesis, The University of Queensland, 1998.
[67] Y. Liu, D. Liu, C. You, M. Chen, Front. Mater. Sci. 9 (2015) 247-253.
[68] A.F. Lotfabadi, H.R. Bakhsheshi-Rad, M.H. Idris, E. Hamzah, M. Kasiri-Asgarani, Canadian Metallurgical Quarterly (2015), pp. 53-64.
[69] W. Zhou, T. Shen, N.N. Aung, Corros. Sci. 52 (2010), 1035-1041.
[70] X.N. Gu, X.H. Xie, N. Li, Y.F. Zheng, L. Qin, Acta Biomater. 8 (2012) 2360-2374.
[71] X.N. Gu, N. Li, Y.F. Zheng, F. Kang, J.T. Wang, L. Ruan, Mater. Sci. Eng.: B 176 (2011) 1802-1806.
[72] T. Hama, Y. Kariyazaki, N. Hosokawa, H. Fujimoto, H. Takuda, Mater. Sci. Eng.: A 551 (2012) 209-217.
[73] F. Hehmann, F. Sommer, H. Jones, R.G.J. Edyvean, JOM Science 24 (1989) 2369-2379.
[74] M. Bornapour, N. Muja, P. Shum-Tim, M. Cerruti, M. Pekguleryuz, Acta Biomater. 9 (2013) 5319-5330.
[75] C.H. Cáceres, D.M. Rovera, J. Light Metals 1 (2001) 151-156.
[76] L. Gao, R.S. Chen, E.H. Han, J. Alloys Compd. 472 (2009) 234-240.
[77] J. Van der Planken, JOM Science 4 (1969) 927-929.
[78] J.M. Seitz, M. Durisin, J. Goldman, J.W. Drelich, Adv. Healthc. Mater. 4 (2015) 1915-1936.
[79] J. Hanawalt, C. Nelson, J. Peloubet, American Institute of Mining and Metallurgical Engineers (AIME) 147 (1942) 273.
[80] J.-Y. Lee, G. Han, Y.-C. Kim, J.-Y. Byun, J.-i. Jang, H.-K. Seok, S.-J. Yang, Metals Mater. Int. 15 (2009) 955-961.
[81] M. Liu, P.J. Uggowitzer, A.V. Nagasekhar, P. Schmutz, M. Easton, G.-L. Song, A. Atrens, Corros. Sci. 51 (2009) 602-619.
[82] M. Liu, P. Uggowitzer, P. Schmutz, A. Atrens, JOM 60 (2008) 39-44.
[83] K.N. Reichek, K.J. Clark, J.E. Hillis, SAE transactions 94 (1985) 318-329.
[84] G.L. Makar, J. Kruger, International Materials Reviews 38 (1993) 138-153.
[85] J. Hofstetter, M. Becker, E. Martinelli, A.M. Weinberg, B. Mingler, H. Kilian, S. Pogatscher, P.J. Uggowitzer, J.F. Löffler, JOM 66 (2014) 566-572.
[86] W.E. Mercer, J.E. Hillis, Society of Automotive Engineers, Detroit, MI (1992).
[87] J.E. Hillis, S.O. Shook, Composition and performance of an improved magnesium AS41 alloy, SAE Technical Paper 890205, 1989.
[88] J.E. Hillis, K.N. Reichek, High purity magnesium AM60 alloy: the critical contaminant limits and the salt water corrosion performance, SAE Technical Paper 860288, 1986.

[89] L. Yang, X. Zhou, S.-M. Liang, R. Schmid-Fetzer, Z. Fan, G. Scamans, J. Robson, G. Thompson, J. Alloys Compd. 619 (2015) 396-400.

[90] V. Mitrovic-Scepanovic, R.H. Packwood, G.J.C. Carpenter, R.J. Brigham, Canadian Metallurgical Quarterly 33 (1994) 61-65.

[91] N. Hort, Y. Huang, D. Fechner, M. Stoermer, C. Blawert, F. Witte, C. Vogt, H. Druecker, R. Willumeit, K.U. Kainer, F. Feyerabend, Acta Biomater. 6 (2010) 1714-1725.

[92] J. Kubasek, D. Vojtech, Trans. Nonferrous Met. Soc. China 23 (2013) 1215-1225.

[93] R. LL, Magnesium alloys containing rare earth elements-structure and properties, London: Taylor and Francis, 2003.

[94] W.-j. Liu, F.-h. Cao, Z. Zhang, J.-q. Zhang, Corros. Sci. and Protection Technology 21 (2009) 82-84.

[95] L.L. Rokhlin, Metal Science and Heat Treatment 48 (2006) 487-490.

[96] X.-W. Guo, J.-W. Chang, S.-M. He, W.-J. Ding, X. Wang, Electrochim. Acta 52 (2007) 2570-2579.

[97] N.-H. AA., Phase diagrams of binary magnesium alloys, Metals Park, OH: ASM International, 1998.

[98] Y.H. Kang, D. Wu, R.S. Chen, E.H. Han, Journal of Magnesium and AlloysJournal of Magnesium and Alloys 2 (2014) 109-115.

[99] T. Rzychoń, A. Kiełbus, Journal of Achievements in Materials and Manufacturing Engineering 21 (2007) 31-34.

[100] Z. Su, C. Liu, Y. Wan, Materials and Design 45 (2013) 466-472.

[101] Q. Peng, Y. Huang, J. Meng, Y. Li, K.U. Kainer, Intermetallics 19 (2011) 382-389.

[102] W. Gan, Y. Huang, L. Yang, K.U. Kainer, M. Jiang, H.-G. Brokmeier, N. Hort, Journal of Applied Crystallography 45 (2012) 17-21.

[103] F. Feyerabend, J. Fischer, J. Holtz, F. Witte, R. Willumeit, H. Druecker, C. Vogt, N. Hort, Acta Biomater. 6 (2010) 1834-1842.

[104] C.A. Grillo, F. Alvarez, M. de Mele, Colloids and Surfaces B-Biointerfaces 117 (2014) 312-321.

[105] T.J. Haley, K. Raymond, N. Komesu, H.C. Upham, Br J Pharmacol Chemother 17 (1961) 526-532.

[106] D.W. Bruce, B.E. Hietbrink, K.P. Dubois, Toxicol Appl Pharmacol 5 (1963) 750-759.

[107] D. Magda, R.A. Miller, Semin Cancer Biol 16 (2006) 466-476.

[108] U. Nyman, B. Elmstahl, P. Leander, M. Nilsson, K. Golman, T. Almen, Radiology 223 (2002) 311-318; discussion 328-319.

[109] H. Ersoy, F.J. Rybicki, Journal of magnetic resonance imaging: JMRI 26 (2007) 1190-1197.

[110] M.C. Heinrich, M.K. Kuhlmann, S. Kohlbacher, M. Scheer, A. Grgic, M.B. Heckmann, M. Uder, Radiology 242 (2007) 425-434.

[111] M.A. ten Dam, J.F. Wetzels, Neth J Med 66 (2008) 416-422.

[112] P. Wedeking, K. Kumar, M.F. Tweedle, Nucl Med Biol 20 (1993) 679-691.

[113] H.E. Friedrich, B.L. Mordike, Magnesium technology, Springer-Verlag Berlin Heidelberg, 2006.

[114] D.A. Robinson, R.W. Griffith, D. Shechtman, R.B. Evans, M.G. Conzemius, Acta Biomater. 6 (2010) 1869-1877.

[115] C. Marambio-Jones, E.M.V. Hoek, Journal of Nanoparticle Research 12 (2010) 1531-1551.

[116] P.L. Drake, K.J. Hazelwood, Ann Occup Hyg 49 (2005) 575-585.

[117] M. Bosetti, A. Masse, E. Tobin, M. Cannas, Biomaterials 23 (2002) 887-892.

[118] J. Hardes, A. Streitburger, H. Ahrens, T. Nusselt, C. Gebert, W. Winkelmann, A. Battmann, G. Gosheger, Sarcoma 2007 (2007) 26539.

[119] Y. Zheng, Mg-Ag-Based Alloy Systems for Biomedical Applications, Magnesium Alloys as Degradable Biomaterials, CRC Press, 2015, pp. 269-284.

[120] J.L. Domingo, J Alzheimers Dis 10 (2006) 331-341.

[121] L. Tomljenovic, J Alzheimers Dis 23 (2011) 567-598.

[122] M. Kawahara, M. Kato-Negishi, International Journal of Alzheimer's Disease 2011 (2011) 276393.

[123] J.Z. Ilich, J.E. Kerstetter, J Am Coll Nutr 19 (2000) 715-737.

[124] C.M. Serre, M. Papillard, P. Chavassieux, J.C. Voegel, G. Boivin, J. Biomed. Mater. Res. 42 (1998) 626-633.

[125] Y.S. Jeong, W.J. Kim, Corros. Sci. 82 (2014) 392-403.

[126] Y. Sun, B. Zhang, Y. Wang, L. Geng, X. Jiao, Materials and Design 34 (2012) 58-64.

[127] K.M. Hambidge, C.E. Casey, N.F. Krebs, 1 - Zinc, in: W. Mertz (Ed.) Trace Elements in Human and Animal Nutrition (Fifth Edition), Academic Press, San Diego, 1986, pp. 1-137.

[128] H. Tapiero, K.D. Tew, Biomed Pharmacother 57 (2003) 399-411.

[129] M. Stefanidou, C. Maravelias, A. Dona, C. Spiliopoulou, Arch Toxicol 80 (2006) 1-9.

[130] N. Li, Y. Zheng, JOM Science and Technology 29 (2013) 489-502.

[131] S.G. Dahl, P. Allain, P.J. Marie, Y. Mauras, G. Boivin, P. Ammann, Y. Tsouderos, P.D. Delmas, C. Christiansen, Bone 28 (2001) 446-453.

[132] S.P. Nielsen, Bone 35 (2004) 583-588.

[133] R.V. Suganthi, K. Elayaraja, M.I.A. Joshy, V.S. Chandra, E.K. Girija, S.N. Kalkura, Mater. Sci. Eng.: C 31 (2011) 593-599.

[134] X. Zeng, Y. Wang, W. Ding, A. Luo, A. Sachdev, Metallurgical and Mater. Trans. A 37 (2006) 1333-1341.

[135] X.N. Gu, X.H. Xie, N. Li, Y.F. Zheng, L. Qin, Acta Biomater. 8 (2012).

[136] D. Tie, R. Guan, H. Liu, A. Cipriano, Y. Liu, Q. Wang, Y. Huang, N. Hort, Acta Biomater. 29 (2016) 455-467.

[137] I.S. Berglund, B.Y. Jacobs, K.D. Allen, S.E. Kim, A. Pozzi, J.B. Allen, M.V. Manuel, Mater. Sci. Eng.: C. 62 (2016) 79-85.

[138] E.M. Carlisle, 7 - Silicon, in: W. Mertz (Ed.) Trace Elements in Human and Animal Nutrition (Fifth Edition), Academic Press, San Diego, 1986, pp. 373-390.

[139] S. Sripanyakorn, R. Jugdaohsingh, H. Elliott, C. Walker, P. Mehta, S. Shoukru, R.P. Thompson, J.J. Powell, Br J Nutr 91 (2004) 403-409.

[140] M.F. McCarty, Medical Hypotheses 49 (1997) 175-176.

[141] M. Mabuchi, K. Kubota, K. Higashi, JOM Science 31 (1996) 1529-1535.

[142] A. Srinivasan, S. Ningshen, U. Kamachi Mudali, U.T.S. Pillai, B.C. Pai, Intermetallics 15 (2007) 1511-1517.

[143] E. Zhang, D. Yin, L. Xu, L. Yang, K. Yang, Mater. Sci. Eng.: C 29 (2009) 987-993.

[144] S.A. Khan, Y. Miyashita, Y. Mutoh, Z.B. Sajuri, Mater. Sci. Eng.: A 420 (2006) 315-321.

[145] F. Rosalbino, S. De Negri, A. Saccone, E. Angelini, S. Delfino, J. Mater. Sci. - Mater. Med. 21 (2010).

[146] Z. Zhen, T.-f. Xi, Y.-f. Zheng, Trans. Nonferrous Met. Soc. China 23 (2013) 2283-2293.

[147] A.H. Martinez-Sanchez, B.J.C. Luthringer, F. Feyerabend, R. Willumeit, Acta Biomater. 13 (2015) 16-31.

[148] L.-N. Zhang, Z.-T. Hou, X. Ye, Z.-B. Xu, X.-L. Bai, P. Shang, Frontiers of Materials Science 7 (2013) 227-236.

[149] K. Zhang, X. Zhang, X. Deng, X. Li, M. Ma, Journal of Magnesium and Alloys 1 (2013) 134-138.

[150] Y. Zhang, C. Yan, F. Wang, W. Li, Corros. Sci. 47 (2005) 2816-2831.

[151] N. Birbilis, M.A. Easton, A.D. Sudholz, S.M. Zhu, M.A. Gibson, Corros. Sci. 51 (2009) 683-689.

[152] T. Abu Leil, N. Hort, W. Dietzel, C. Blawert, Y. Huang, K.U. Kainer, K.P. Rao, Trans. Nonferrous Met. Soc. China 19 (2009) 40-44.

[153] M.-C. Zhao, M. Liu, G.-L. Song, A. Atrens, Corros. Sci. 50 (2008) 3168-3178.

[154] Y. Song, D. Shan, R. Chen, E.-H. Han, Corros. Sci. 52 (2010) 1830-1837.

[155] G. Ben-Hamu, D. Eliezer, W. Dietzel, K.S. Shin, Corros. Sci. 50 (2008) 1505-1517.

[156] J.E. Gamble, Chemical anatomy, physiology and pathology of extracellular fluid, Cambridge, MA: Harvard University Press, 1967.

[157] M. Alvarez-Lopez, M.D. Pereda, J.A. del Valle, M. Fernandez-Lorenzo, M.C. Garcia-Alonso, O.A. Ruano, M.L. Escudero, Acta Biomater. 6 (2010) 1763-1771.

[158] J. Trinidad, G. Arruebarrena, I. Marco, I. Hurtado, E. Saenz de Argandona, Proc Inst Mech Eng H 227 (2013) 1301-1311.

[159] H. Wang, Y. Estrin, Z. Zúberová, Mater. Lett. 62 (2008) 2476-2479.

[160] N.I. Zainal Abidin, D. Martin, A. Atrens, Corros. Sci. 53 (2011) 862-872.

[161] J. Hanks, R. Wallace, Proceedings of the Society for Experimental Biology and Medicine 71(2) (1949) 196-200.

[162] X. Yunchang, H. Tao, P.K. Chu, J. Electrochem. Soc. 157 (2010) C238-243.

[163] J. Walker, S. Shadanbaz, N.T. Kirkland, E. Stace, T. Woodfield, M.P. Staiger, G.J. Dias, J. Biomed. Mater. Res. Part B-Applied Biomaterials 100B (2012) 1134-1141.

[164] L. Yang, N. Hort, R. Willumeit, F. Feyerabend, Corros. Eng. Sci. Techn. 47 (2012) 335-339.

[165] D. Tie, F. Feyerabend, N. Hort, R. Willumeit, D. Hoeche, Adv. Eng. Mater. 12 (2010) 699-704.

[166] T. Kokubo, H. Takadama, Biomaterials 27 (2006) 2907-2915.

[167] L. Müller, F.A. Müller, Acta Biomater. 2 (2006) 181-189.

[168] S.N. Dezfuli, Z. Huan, J.M.C. Mol, M.A. Leeflang, J. Chang, J. Zhou, Progress in Natural Science: Materials International 24 (2014) 531-538.

[169] A. Yamamoto, S. Hiromoto, Mater. Sci. Eng.: C 29 (2009) 1559-1568.

[170] J.A. Ryan, General guide for identifying and correcting common cell culture growth and attachment problems, Corning, Inc. Technical Bulletin, 2008.

[171] K. Deva, e. al., International Journal of Animal Biotechnology 1 (2011) 8-12.

[172] M.T. Madigan, Brock biology of microorganisms, Benjamin Cummings, San Francisco, 2012.

[173] J. Trinidad, G. Arruebarrena, I. Marco, I. Hurtado, E.S. de Argandoña, Proc. Inst. Mech. Eng. H 227 (2013) 1301-1311.

[174] C. Prohaska, K. Pomazal, I. Steffan, Fresenius J Anal Chem 367 (2000) 479-484.

[175] J.L. Gamble, Chemical anatomy, physiology and pathology of extracellular fluid : a lecture syllabus, Dept. of Pediatrics, Harvard Medical School, Cambridge, 1941.

[176] N.T. Kirkland, N. Birbilis, M.P. Staiger, Acta Biomater. 8 (2012) 925-936.

[177] A. International, Standard Practice for Laboratory Immersion Corrosion Testing of Metals, ASTMG31-72, West Conshohocken, PA, 2004.

[178] D. Porchetta, J. Gonzales, F. Feyerabend, R. Willumeit-Römer, M. Behbahani, C. Ptock, Comparative study on degradation behaviour of magnesium alloys Mg-Y-RE and Mg-Ca-Zn in a dynamic bioreactor testing setup, 7th biometals, vol 3, Eur. Cell Mater., 2015, p. 52.
[179] I. Marco, F. Feyerabend, R. Willumeit-Römer, O. van der Biest, Influence of Testing Environment on the Degradation Behavior of Magnesium Alloys for Bioabsorbable Implants, TMS2015 Supplemental Proceedings, John Wiley and Sons, Inc., 2015, pp. 497-506.
[180] D. Tie, F. Feyerabend, W.-D. Mueller, R. Schade, K. Liefeith, K.U. Kainer, R. Willumeit, European Cells & Materials 25 (2013) 284-298.
[181] Grischuk, 11 (1957) 136.
[182] H. Du, Z. Wei, X. Liu, E. Zhang, Materials Chemistry and Physics 125 (2011).
[183] W.F. Ng, K.Y. Chiu, F.T. Cheng, Mater. Sci. Eng. C-Materials for Biological Applications 30 (2010).
[184] A.C. Hänzi, I. Gerber, M. Schinhammer, J.F. Löffler, P.J. Uggowitzer, Acta Biomater. 6 (2010) 1824-1833.
[185] K. Bracht, N. Angrisani, J.M. Seitz, R. Eifler, A. Weizbauer, J. Reifenrath, Biomed Eng Online 14 (2015) 92.
[186] W.-D. Mueller, M.L. Nascimento, M. Fernandez Lorenzo de Mele, Acta Biomater. 6 (2010) 1749-1755.
[187] J.-M. Seitz, K. Collier, E. Wulf, D. Bormann, N. Angrisani, A. Meyer-Lindenberg, F.-W. Bach, Adv. Eng. Mater. 13 (2011) 1146-1151.
[188] X.L. Liu, W.R. Zhou, Y.H. Wu, Y. Cheng, Y.F. Zheng, Mater Sci Eng C Mater Biol Appl 33 (2013) 4144-4154.
[189] F. Cao, Z. Shi, J. Hofstetter, P.J. Uggowitzer, G. Song, M. Liu, A. Atrens, Corros. Sci. 75 (2013) 78-99.
[190] Z. Shi, F. Cao, G.-L. Song, M. Liu, A. Atrens, Corros. Sci. 76 (2013) 98-118.
[191] N.I. Zainal Abidin, A.D. Atrens, D. Martin, A. Atrens, Corros. Sci. 53 (2011) 3542-3556.
[192] ASTM-G31-72, Standard Practice for Laboratory Immersion Corrosion Testing of Metals, ASTMG31-72, vol Annual Book of ASTM Standards., American Society for Testing and Materials, Philadelphia, Pennsylvania, USA, 2004.
[193] L. Xu, E. Zhang, D. Yin, S. Zeng, K. Yang, J. Mater. Sci. - Mater. Med. 19 (2008) 1017-1025.
[194] S. Remennik, I. Bartsch, E. Willbold, F. Witte, D. Shechtman, Mater. Sci. Eng. B-Advanced Functional Solid-State Materials 176 (2011) 1653-1659.
[195] A. Atrens, G.-L. Song, M. Liu, Z. Shi, F. Cao, M.S. Dargusch, Adv. Eng. Mater. 17 (2015) 400-453.

[196] K. Nogita, S. Ockert, J. Pierce, M.C. Greaves, C.M. Gourlay, A.K. Dahle, International Journal of Hydrogen Energy 34 (2009) 7686-7691.
[197] Z. Li, X. Gu, S. Lou, Y. Zheng, Biomaterials 29 (2008).
[198] M. Jamesh, S. Kumar, T.S.N.S. Narayanan, Corros. Sci. 53 (2011).
[199] T. Huehnerschulte, J. Reifenrath, B. von Rechenberg, D. Dziuba, J. Seitz, D. Bormann, H. Windhagen, A. Meyer-Lindenberg, BioMedical Engineering OnLine 11 (2012) 14.
[200] I. Roth, S. Schumacher, T. Basler, K. Baumert, J.-M. Seitz, F. Evertz, P. Müller, W. Bäumer, M. Kietzmann, Progress in Biomaterials 4 (2015) 21-30.
[201] L. Wu, F. Feyerabend, A.F. Schilling, R. Willumeit-Römer, B.J.C. Luthringer, Acta Biomater. 27 (2015) 294-304.
[202] L. Wu, B.J.C. Luthringer, F. Feyerabend, A.F. Schilling, R. Willumeit, Acta Biomater. 10 (2014) 2843-2854.
[203] F. Feyerabend, F. Witte, M. Kammal, R. Willumeit, Tissue Eng 12 (2006) 3545-3556.
[204] C. Liu, Y. Xin, X. Tian, P.K. Chu, JOM Research 22 (2007) 1806-1814.
[205] C.L. Liu, Y.J. Wang, R.C. Zeng, X.M. Zhang, W.J. Huang, P.K. Chu, Corros. Sci. 52 (2010) 3341-3347.
[206] Y. Wang, C.S. Lim, C.V. Lim, M.S. Yong, E.K. Teo, L.N. Moh, Mater. Sci. Eng.: C 31 (2011) 579-587.
[207] E. McCafferty, Corros. Sci. 47 (2005) 3202-3215.
[208] G.R. Argade, K. Kandasamy, S.K. Panigrahi, R.S. Mishra, Corros. Sci. 58 (2012) 321-326.
[209] M. Liu, P. Schmutz, P.J. Uggowitzer, G. Song, A. Atrens, Corros. Sci. 52 (2010) 3687-3701.
[210] M. Stern, A.L. Geary, J. Electrochem. Soc. 104 (1957) 56-63.
[211] Z. Zhang, X. Liu, W. Hu, J. Li, Q. Le, L. Bao, Z. Zhu, J. Cui, J. Alloys Compd. 624 (2015) 116-125.
[212] M.-C. Zhao, M. Liu, G.-L. Song, A. Atrens, Adv. Eng. Mater. 10 (2008) 104-111.
[213] R. Rettig, S. Virtanen, J. Biomed. Mater. Res. Part A 85A (2008) 359-369.
[214] Z. Shi, F. Cao, G.-L. Song, A. Atrens, Corros. Sci. 88 (2014) 434-443.
[215] Z. Qiao, Z. Shi, N. Hort, N.I. Zainal Abidin, A. Atrens, Corros. Sci. 61 (2012) 185-207.
[216] F. Cao, Z. Shi, G.-L. Song, M. Liu, A. Atrens, Corros. Sci. 76 (2013) 60-97.
[217] W. Liu, F. Cao, L. Chang, Z. Zhang, J. Zhang, Corros. Sci. 51 (2009) 1334-1343.
[218] Q. Qu, J. Ma, L. Wang, L. Li, W. Bai, Z. Ding, Corros. Sci. 53 (2011) 1186-1193.

[219] W. Liu, F. Cao, A. Chen, L. Chang, J. Zhang, C. Cao, Corros. Sci. 52 (2010) 627-638.
[220] W. He, E. Zhang, K. Yang, Mater. Sci. Eng.: C 30 (2010) 167-174.
[221] A.D. King, N. Birbilis, J.R. Scully, Electrochim. Acta 121 (2014) 394-406.
[222] G.S. Frankel, A. Samaniego, N. Birbilis, Corros. Sci. 70 (2013) 104-111.
[223] M. Curioni, Electrochim. Acta 120 (2014) 284-292.
[224] G. Song, S. Song, Adv. Eng. Mater. 9 (2007) 298-302.
[225] A. Atrens, W. Dietzel, Adv. Eng. Mater. 9 (2007) 292-297.
[226] T.R. Thomaz, C.R. Weber, T. Pelegrini Jr, L.F.P. Dick, G. Knörnschild, Corros. Sci. 52 (2010) 2235-2243.
[227] S. Fajardo, G.S. Frankel, Electrochim. Acta 165 (2015) 255-267.
[228] S. Bender, J. Göllner, A. Heyn, C. Blawert, P. Bala Srinivasan, Corrosion and surface finishing of magnesium and its alloys, in: M.O. Pekguleryuz, K.U. Kainer, A.A. Kaya (Eds.), Fundamentals of Magnesium Alloy Metallurgy, Woodhead Publishing, 2013, pp. 232-265.
[229] A. Atrens, G.-L. Song, F. Cao, Z. Shi, P.K. Bowen, J. Magnesium and Alloys 1 (2013) 177-200.
[230] G. Song, A. Atrens, D. St John, X. Wu, J. Nairn, Corros. Sci. 39 (1997) 1981-2004.
[231] A.D. Atrens, I. Gentle, A. Atrens, Corros. Sci. 92 (2015) 173-181.
[232] Z. Shi, A. Atrens, Corros. Sci. 77 (2013) 403-406.
[233] M. Gomberg, Rec. Trav. Chim. 48 (1929) 847.
[234] R.L. Petty, A.W. Davidson, J. Kleinberg, JACS 76 (1954) 363-366.
[235] A. Samaniego, B.L. Hurley, G.S. Frankel, J. Electroanal. Chem. 737 (2015) 123-128.
[236] N. Birbilis, A.D. King, S. Thomas, G.S. Frankel, J.R. Scully, Electrochim. Acta 132 (2014) 277-283.
[237] G. Williams, N. Birbilis, H.N. McMurray, Electrochem. Commun. 36 (2013) 1-5.
[238] G.S. Frankel, A. Samaniego, N. Birbilis, Corros. Sci. 70 (2013) 104-111.
[239] G. Williams, H. Neil McMurray, J. Electrochem. Soc. 155 (2008) C340-C349.
[240] M. Taheri, J.R. Kish, N. Birbilis, M. Danaie, E.A. McNally, J.R. McDermid, Electrochim. Acta 116 (2014) 396-403.
[241] N.T. Kirkland, G. Williams, N. Birbilis, Corros. Sci. 65 (2012) 5-9.
[242] M. Curioni, F. Scenini, T. Monetta, F. Bellucci, Electrochim. Acta 166 (2015) 372-384.
[243] J.H. Nordlien, S. Ono, N. Masuko, K. Nisancioglu, Corros. Sci. 39 (1997) 1397-1414.

[244] M.E. Straumanis, B.K. Bhatia, J. Electrochem. Soc. 110 (1963) 357-360.

[245] G.R. Hoey, M. Cohen, J. Electrochem. Soc. 105 (1958) 245-250.

[246] R.E. McNulty, J.D. Hanawalt, Transactions of The Electrochemical Society 81 (1942) 423-433.

[247] R. Glicksmann, J. Electrochem. Soc. 106 (1959) 83.

[248] G.G. Perrault, Journal of Electroanal. Chem. and Interfacial Electrochemistry 27 (1970) 47-58.

[249] E. Gulbrandsen, Electrochim. Acta 37 (1992) 1403-1412.

[250] A.J. Bard, L.R. Faulkner, Electrochemical Methods: Fundamentals and Applications, Wiley, 2000.

[251] S. Bender, J. Goellner, A. Heyn, E. Boese, Mater. Corros.-Werkstoffe Und Korrosion 58 (2007) 977-982.

[252] B.E. Bender S., Heyn A. and Goellner J., Corrosion behaviour of magnesium alloys: material specific corrosion testing, in: Wiley-VCH (Ed.) 7th International Conference on Magnesium Alloys and Their Applications, Wiley-VCH, Weinheim, Germany, 2007, pp. 721 -726.

[253] S. Galli, J.U. Hammel, J. Herzen, G. Szakács, F. Lukáč, M. Vlček, I. Marco, A. Wennerberg, R. Willumeit-Römer, R. Jimbo, Eur. Cell Mater. 30 (2015) 93.

[254] J. Wang, F. Witte, T. Xi, Y. Zheng, K. Yang, Y. Yang, D. Zhao, J. Meng, Y. Li, W. Li, K. Chan, L. Qin, Acta Biomater. 21 (2015) 237-249.

[255] J. Yang, F. Cui, I.S. Lee, Annals of Biomedical Engineering 39 (2011) 1857-1871.

[256] S. Keskin, S. Kızılel, Industrial and Engineering Chemistry Research 50 (2011) 1799-1812.

[257] P. Horcajada, T. Chalati, C. Serre, B. Gillet, C. Sebrie, T. Baati, J.F. Eubank, D. Heurtaux, P. Clayette, C. Kreuz, J.-S. Chang, Y.K. Hwang, V. Marsaud, P.-N. Bories, L. Cynober, S. Gil, G. Ferey, P. Couvreur, R. Gref, Nature Materials 9 (2010) 172-178.

[258] B.F. Hoskins, R. Robson, JACS 111 (1989) 5962-5964.

[259] P.D.C. Dietzel, V. Besikiotis, R. Blom, JOM Chemistry 19 (2009) 7362-7370.

[260] C. Janiak, J.K. Vieth, New Journal of Chemistry 34 (2010) 2366-2388.

[261] O.K. Farha, I. Eryazici, N.C. Jeong, B.G. Hauser, C.E. Wilmer, A.A. Sarjeant, R.Q. Snurr, S.T. Nguyen, A.Ö. Yazaydın, J.T. Hupp, JACS 134 (2012) 15016-15021.

[262] Y.-S. Bae, C.Y. Lee, K.C. Kim, O.K. Farha, P. Nickias, J.T. Hupp, S.T. Nguyen, R.Q. Snurr, Angewandte Chemie International Edition 51 (2012) 1857-1860.

[263] Z. Bao, S. Alnemrat, L. Yu, I. Vasiliev, Q. Ren, X. Lu, S. Deng, Langmuir 27 (2011) 13554-13562.

[264] C. Janiak, Dalton Transactions (2003) 2781-2804.

[265] P. Horcajada, T. Chalati, C. Serre, B. Gillet, C. Sebrie, T. Baati, J.F. Eubank, D. Heurtaux, P. Clayette, C. Kreuz, J.-S. Chang, Y.K. Hwang, V. Marsaud, P.-N. Bories, L. Cynober, S. Gil, G. Ferey, P. Couvreur, R. Gref, Nat. Mater. 9 (2010) 172-178.
[266] P. Horcajada, C. Serre, G. Maurin, N.A. Ramsahye, F. Balas, M. Vallet-Regi, M. Sebban, F. Taulelle, G. Ferey, JACS 130 (2008) 6774-6780.
[267] P. Horcajada, C. Serre, M. Vallet-Regí, M. Sebban, F. Taulelle, G. Férey, Angewandte Chemie International Edition 45 (2006) 5974-5978.
[268] R.C. Huxford, J. Della Rocca, W. Lin, Curr. Opinion in Chemical Biology 14 (2010) 262-268.
[269] R. Ameloot, L. Stappers, J. Fransaer, L. Alaerts, B.F. Sels, D.E. De Vos, Chem. Mater. 21 (2009) 2580-2582.

Chapter 2:
Context, objectives and outline of this thesis

2.1. Context

This thesis is done within the MagnIM project which is supported by the PEOPLE Programme (Marie Skłodowska-Curie Actions) of the European Union's Seventh Framework Programme (FP7/2007-2013/) under REA grant agreement n°289163. MagnIM stands for "Magnesium Implant".

MagnIM is a highly interdisciplinary European network where physicists, material scientists, biologists, medical doctors and surgeons from eight different organizations and six countries have intensively collaborated. The aim of the project is the development of biodegradable magnesium based implant materials. More specifically Mg is alloyed in order to tailor both degradation and mechanical properties aiming at biodegradable implant applications. Therefore, silver (Ag) and gadolinium (Gd) are selected as alloying elements in order to increase and decrease the degradation rate of the respective Mg binary alloys. As explained in sections 1.5.2.a and b, 2-6 wt.% of Ag and 5-10 wt.% of Gd have been added to Mg in previous studies. Specifically, Mg-2Ag and Mg-10Gd are chosen for the MagnIM project due to their corrosion performance as potential implant material candidates. To facilitate data comparability with other studies pure Mg (99.956%) and Mg-4Y-3RE alloy are included in the project. In the MagnIM project the same alloys have been used for the different studies. These studies are organized in 4 work-packages (WPs): material production, in vitro degradation analyses, in vitro biocompatibility testing, and in vivo experiments:

1. The material production WP, as its name indicates, takes care of the Mg alloy production. The processing should be repeatable and defect-less. Moreover, this work group also does fundamental research concerning the development of different Mg alloys.
2. The in vitro degradation WP is where this thesis is mainly included. This WP is in charge of the degradation characterization via immersion and electrochemical testing with pure Mg (99.956%), Mg-4Y-3RE, Mg-Gd and Mg-Ag alloys. Many testing conditions

are applied in order to analyse their influence on the degradation performance of the studied Mg alloys.

3. The in vitro biocompatibility WP studies the interaction between Mg-based materials and biological entities, e.g. cells or proteins. In this WP the inflammatory reaction is modelled, a novel 3D bone tissue culture model is developed and the antibacterial influence of the selected Mg alloys is also analysed, among other studies.
4. In the in vivo WP many animal studies in rats and mice are performed with pure Mg, Mg-2Ag, Mg-10Gd and Mg-4Y-3RE in screw and pin shape. These studies were compared to in vitro studies with the same materials in disc shape.

2.2. Objectives

As stated in Chapter 1, magnesium and its alloys show an unpredictable degradation behaviour because of the sound influence of the impurity content, microstructure and testing conditions. Its abnormal anodic polarization behaviour and the influence of many parameters make hard the interpretation of degradation results. Immersion testing under near physiological conditions is of great interest due to the similarities with in vivo conditions. Thus, these degradation studies are compared to less physiological experiments as well as to in vivo tests. However, in order to facilitate data interpretation biological entities, such as proteins and cells, are excluded from immersion tests.

Hence, this PhD aims to contribute to the development of the degradation testing of Mg and its alloys by the following actions:

- The rotating disc electrode (RDE) during polarization measurements is applied and these results are compared to static conditions. This would reveal the influence of the degradation layer formation during the Mg anodic polarization. The influence of testing parameters such as the rotation speed and the scan rate are also studied.
- In vitro immersion tests of Mg-Gd and Mg-Ag binary alloy systems together with commercially pure Mg (99.956%) and Mg-4Y-3RE as references are studied under a range of conditions. The so called physiological conditions or cell culture conditions are applied for immersion testing by applying an electrolyte with similar composition and pH to body plasma.
- Further research under is done under physiological conditions due to the risk of contamination, which can influence the degradation process of Mg alloys.

- Degradation layers and the degradation rates obtained in vitro and in vivo are compared with pure Mg, Mg-10Gd and Mg-2Ag alloys produced in pin and disc shape. In this analysis, the impurity content and grain size are assessed.

Moreover, this thesis develops a new Mg-MOF coating synthesis which has potentially an added functionality as drug delivery system and can change the degradation behaviour of the Mg substrate.

2.3. Outline of this thesis

Chapter 1 includes an introduction about biodegradable Mg implant and a literature review of the current state-of-the-art of Mg degradation and its characterization. Here, the theories and the current opinion on Mg degradation phenomena are described. This review also includes a detailed analysis of the different parameters with an influence on the Mg degradation behaviour, i.e. material microstructure, alloying additions, impurity content and testing conditions. The different electrochemical techniques applied for Mg degradation characterization are also reviewed, together with the current Mg degradation theories. The use of the RDE as a recommendation found in literature is also addressed. The relation between in vitro degradation testing and in vitro cytotoxicity and in vivo testing are also briefly reviewed. Finally, Mg-MOF coatings as a drug delivery system are found of interest in literature, and thus, included in this review.

The context, objectives and the outline of this thesis are explained in the current **Chapter 2**. The MagnIM project context is explained in order to let the reader understand why certain decisions are made regarding the Mg alloy selection.

In **Chapter 3**, polarization measurements with the RDE are analysed and compared to static measurements with pure Mg (99.956%). These experiments are performed in phosphate buffered saline (PBS) solution. The degradation layer deposition is analysed and the relation between results and the negative difference effect is assessed.

In order to investigate the degradation of Mg alloys different testing conditions are applied in **Chapter 4** and results are compared to in vivo degradation. These conditions apply three different electrolytes: PBS, Hank’s balanced salt solution (HBSS) and Dulbecco’s modified eagle medium (DMEM). The hydrogen and pH evolution are registered and degradation rates compared both, in vitro and in vivo. The degradation layers formed in all conditions are studied to find physiological conditions that are the most comparable to in vivo. The importance of the impurities and surface finishing are highlighted in this study.

Chapter 5 analyses the influence of sterilization, or in other words, contamination medium during immersion testing of Mg-based materials. Cell culture media contain a source of energy, and therefore, microorganisms can easily proliferate in these media. This proliferation induces an acidic pH and accelerates Mg degradation. Thereby, the use of sterilization measures, such as antibiotics or UV-C radiation, is found recommendable.

The in vitro study shown in Chapter 4 is expanded in **Chapter 6**. Other compositions of Mg-Gd and Mg-Ag alloys are included in the in vitro tests in the three degradation media applied in Chapter 4: PBS, HBSS and DMEM. The influence of alloying additions of RE and Ag, impurity content, grain size and the applied electrolyte in the immersion testing results is identified. Observations on the degradation mechanism of the studied alloys are analysed. In this Chapter, the microhardness of these alloys is also assessed. Finally, the RDE is applied during polarization measurements with these alloys to compare DRs with results from the initial hydrogen evolution.

Chapter 7 investigates the electrosynthesis of Mg-MOF structures on a pure Mg substrate and compares the degradation performance of coated samples to uncoated samples. A first biocompatibility test is performed via cell viability experiments with murine pre-osteoblastic cells.

At the end of this thesis, the main conclusions of this study are included in **Chapter 8**. Complementarily, the future perspective of biodegradable Mg implant is described and future studies are briefly proposed.

Note that for better understanding of the material characteristics the author recommends reading Chapter 6 before Chapters 4 and 5, since a deeper analysis of the material is included in Chapter 6.

Chapter 3:

Polarization measurements from a rotating disc electrode for characterization of magnesium corrosion

Adapted from:

I. Marco, O. Van der Biest. Polarization measurements from a rotating disc electrode for characterization of magnesium corrosion, Corros. Sci. 102 (2015) 384-393.

3.1. Introduction

Mg has rather unpredictable corrosion properties. Many results applying electrochemistry and immersion experiments aiming at biomedical applications can be found in literature, showing that these two methods do not lead to the same corrosion rate for the same material [6]. Thus, a better understanding of these measurements is needed.

As explained in Section 2.5.4., Mg exhibits an abnormal anodic polarization behaviour because of the so called negative difference effect (NDE) [7-9]. For most metals, a potential polarity reversal from cathodic to anodic causes an acceleration of the anodic reaction and simultaneously a decrease of the cathodic hydrogen generation rate. However, for Mg, the hydrogen evolution rate actually increases when the applied potential becomes more anodic [10-12]. Many authors use the monovalent Mg ion theory to explain the low corrosion rates determined by electrochemical techniques in comparison with immersion techniques [14-17]. However Samaniego et al. [18] recently demonstrated that the evidence for the Mg^+ existence claimed by Petty et al. 60 years ago is not entirely valid [19]. This has led to many rejecting the Mg^+ theory to explain the NDE in favour of the enhanced catalytic surface (ECS) theory [11, 20-24]. ECS describes the creation of dark corrosion products on the surface of the corroding metal during anodic polarization which act as cathodes coupled with the surrounding anode, i.e., the uncovered Mg surface.

As mentioned in Section 2.7, the use of the rotating disc electrode (RDE) can reduce corrosion product formation on the Mg surface by accelerating the diffusion kinetics of Mg ions away from the surface. This Chapter compares this method to static measurements in order to show that the very recently advanced concepts of the ECS theory can be usefully applied. Moreover, this Chapter also determines the influence of testing parameters such as the rotation speed and the scan rate on the polarization measurements with RDE for magnesium degradation characterization in a medium which is used in biodegradable implant research. By minimizing the chances for the formation of a degradation layer the intrinsic corrosion response of a particular magnesium alloy can be assessed. This information is of interest in the modelling of the degradation of a biometal in a particular medium in vitro but also under more realistic conditions in vivo.

3.2. Experimental methods

3.2.1. Materials and methods

Pure Mg samples were cast by permanent mould gravity casting at 680˚C in neutral atmosphere (Ar + SF_6), extruded at 300˚C from 110 mm diameter to 12 mm at a speed of 0.7 mm/s. Finally, samples were machined into discs (10x1.5 mm). This processing route was chosen to obtain a fine and homogeneous grain size (22.6 ± 5.2 µm). The measured density of the pure Mg was 1.74 g/cm^3 and the Vicker's hardness was 43.8 ± 3.2 kg/mm^2 HV 0.3 kg. Table 4 shows the chemical composition of the pure Mg used in this work, determined by inductively coupled plasma - optical emission spectroscopy (ICP-OES, Varian 720 ES).

Table 4. Chemical composition (wt.-ppm) of pure Mg.

Material	Fe	Mn	Si	Ni	Co	Cu	Al	Mg
pure Mg	46	334	130	<10	<1	14	45	balance

3.2.2. Electrochemical experiments

PDP experiments were carried out with the rotating disc electrode as shown in Fig. 26 (EG&G model 616). The sample preparation and surface finishing was done firstly by grinding with 1000 and then 4000 grit SiC paper, and finally by polishing with a 3 µm diamond suspension. The samples were placed in a sealed PTFE clamp and connected electrically to the potentiostat (EG&G model 273). This clamp left the surface of the sample in a recess (see detail in Fig. 26) which will enable an air bubble to remain on the surface when the RDE is immersed, interrupting the electrical contact and disturbing the signal during the first 10- 20 s. The electrochemical cell consisted of a classical three-electrode cell with a rotating working electrode, Pt mesh as counter electrode and Ag/AgCl saturated with KCl as reference electrode, with a potential of +197 mV against a standard hydrogen electrode. The working electrode had an exposed surface of 50 mm^2. When static conditions and a broad scan range of ±1.5 V vs OCP were applied the PTFE clamp was not used. In this case, samples were embedded in resin connected with a wire in order to position the sample upwards and let the H_2 bubbles get to the atmosphere. Otherwise the large H_2 accumulation in the clamped samples recess would disturb the measurement by reducing the sample-electrolyte contact area.

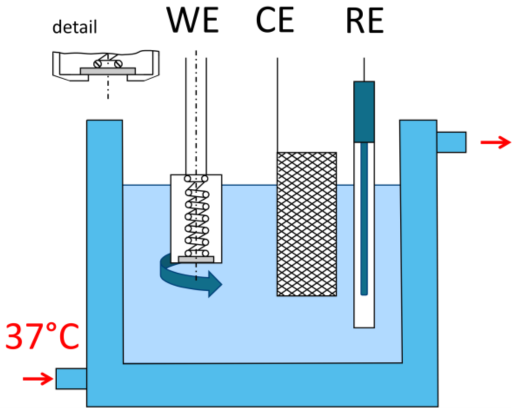

Figure 26: Experimental setup with the rotating disc electrode as working electrode (WE), platinum mesh as counter electrode (CE) and Ag/AgCl saturated KCl as reference electrode (RE). The clamp detail shows the recess which is initially filled with air and disturbs the first seconds of an open circuit potential (OCP) measurement.

The solution mainly used in this research was phosphate buffered saline (PBS 4417, Sigma-Aldrich), but also Hank's balanced salt solution (HBSS 14175, Life technologies) was used for comparison. PBS and HBSS are commonly used solutions in research on bioabsorbable Mg implant degradation [19-27]. The composition of these two electrolytes is summarized in Table 5. The main component of PBS is NaCl but it also includes sodium phosphate, dibasic anhydrous sodium phosphate, and potassium chloride. HBSS, in contrast to PBS, also includes sodium bicarbonate and $_D$-glucose. The volume of electrolyte applied was 400 mL. The temperature for all experiments was controlled with a double walled beaker connected to a water bath (VWR model 1136-1D) at 37 ± 0.5°C. The measured conductivity and pH of PBS at this temperature was 20.5 mS/cm and 7.47, respectively. During polarizations with different parameters the pH was stable within the range from 7.4 to 7.5. The measured conductivity of HBSS at 37°C was 13.7 mS/cm, in the same range as PBS.

Table 5. Ionic composition of PBS and HBSS used for Mg biodegradation testing in mmol/L.

	Na^+	K^+	Cl^-	HCO_3^-	$H_2PO_4^-$	HPO_4^{2-}	D-Glucose
PBS	154.1	4.1	140.6	-	1.5	8.1	-
HBSS	142.8	5.8	143.3	4.2	0.44	0.34	5.6

In order to calculate the corrosion current density the Tafel extrapolation was applied, as recommended by Kirkland et al. [28]. This Tafel fit was performed over the voltage range: ±500 mV and ±300 mV around the corrosion potential to determine the anodic and the cathodic slopes. This analysis is carried out using the software of CorrView-3.3c (by Scribner Associates, Inc., USA).

Consecutive PDP experiments have been performed to get an overview of the rotation speed effect on the experiment. In this way the rotation speed at which the sample remains nominally unchanged can be determined.

Firstly, a sample with a freshly polished surface was clamped and immersed while it already was in rotation. The OCP measurement was started immediately after immersion. The OCP was measured for 120 s before all polarization tests in order to check the stability of the potential and to make sure that air bubbles do not perturb the measurement. The PDP started immediately after OCP and consecutive PDP had a time interval of 5 s approximately. The scanned potential range at 2000 rpm was ±500 mV around the OCP with a scan rate of 1 mV/s; and ±250 mV around the OCP with 2, 5, 10, 15 and 20 mV/s. The experiment termination was done by raising the sample while still rotating, and drying it as quickly as possible.

3.2.3. Degradation layer characterization

Cu Kα (40 kV, 40 mA) X-ray diffraction (XRD, 3003-TT Seifert) analysis was done at a scanning rate of 0.02°/s and with a grazing incident beam angle of 0.5° to identify the degradation layer composition formed at the surface after the polarization experiments. The scanned 2θ range was defined from 20° to 80° in order to detect relevant intensity peaks.

Furthermore, imaging with the scanning electron microscope (SEM-XL/30 FEG, Philips) was done to characterize the degradation layer morphology. This equipment also gives the ability to characterize qualitatively the composition of different degradation layers with the energy dispersive spectroscopy (EDS, EDAX) technique. For quantification of the surface covered by corrosion products the software ImageJ (version 1.47v, Wayne Rasband) was utilized.

3.3. Results and discussion

3.3.1. Influence of the rotation speed

To analyse the optimal rotation speed it is necessary to mention that RDE will not have a positive influence on the measurement at very low or high rotation speeds (ω). On the one hand, when ω is small, the influence of the degradation layer deposition and the uncontrolled mass transport is still noticeable during the polarization measurement. On the other hand, the upper limit for ω is governed by the onset of turbulent flow. This occurs at a critical Reynolds number ($Re_c = 2 \times 10^5 = \omega_c \cdot r^2/\nu$; where r is the radius, ν is the kinematic viscosity and ω_c is the upper angular speed) [29]. Hence, ω for this system electrochemical cell (2.5 cm radius and approximately the kinematic viscosity of PBS at 37°C of $\nu \approx 7 \times 10^{-7}$ m^2/s) should be lower than 2.140 rpm. Also, at high ω, there can be excessive splashing or the formation of a vortex around the electrode. When this vortex is formed in the centre of the beaker, when in excess of the turbulent limit, the sample is immersed as far as possible from the vortex without touching the beaker. In this way, the disturbance caused by the vortex stopping the electrical contact between the sample and the electrolyte is avoided. In practice, as Bard and Faulkner concluded, this parameter is limited in most RDE studies to $100 \text{ rpm} < \omega < 10{,}000 \text{ rpm}$ [30].

3.3.2. Open circuit potential

The influence of the rotation speed on the open circuit potential of pure Mg in PBS at 37°C is shown in Fig. 27. At 3000 rpm the OCP becomes stable around -1.97 V, increasing slightly between 1000 and 2500 rpm to values around -1.95 V. At 500 and 250 rpm a considerable potential increase to -1.91 V and -1.87 V respectively can be determined. At 100 rpm the potential becomes stable at -1.84 V. Finally without rotation the sample shows the effect of the forming degradation layer, increasing the OCP linearly during the first 120 s of immersion. Fig. 27 shows the OCP after 50 s because during the first 10-40 s after immersion there were air bubbles caused by the clamp design preventing sample-electrolyte electrical contact. Removal of these bubbles takes up to 40 s until a potential is registered. For this reason the OCP data during the first 50 s are not shown.

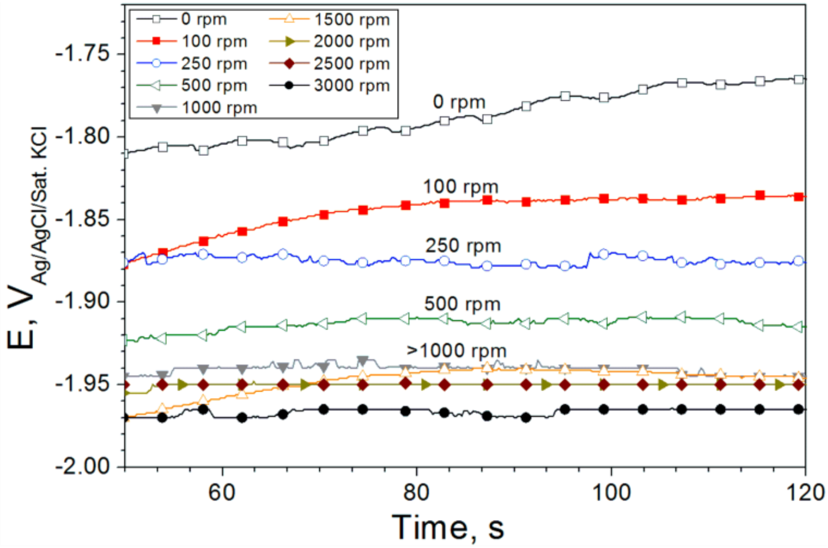

Figure 27: Open circuit potential of pure Mg at different ω in PBS at 37°C demonstrates the influence of rotation on avoiding degradation layer formation and on reducing the thickness of the hydrodynamic boundary layer, which stabilizes the open circuit potentials.

These OCP potential shifts at low rpm are caused by a layer of $Mg(OH)_2$ (see the evidence below in Fig. 32) which is related to the diffusion layer thickness described in RDE theory [30]. According to Bard and Faulkner, it is assumed that the convection maintains the concentrations of all species uniform and equal to the bulk values beyond a certain distance from the electrode (δ). Within this layer the mass transfer takes place by diffusion. Eq. 21 describes the steady-state diffusion layer model for the RDE, where δ is the diffusion layer thickness in cm for species at an electrode fed by convective transfer; D_O is the diffusion coefficient of the species in cm^2/s; ω is the angular frequency of rotation (rad/s); and ν is the kinematic viscosity (cm^2/s).

$$\delta = 1.61\, D_O^{1/3} \omega^{-1/2} \nu^{1/6} \tag{21}$$

This indicates that an increase in ω induces a thinner diffusion layer. Table 6 shows estimated values of the diffusion layer thickness at different ω. For this approximation, the diffusion coefficient of Mg^{2+} ions in aqueous solutions is considered approximately from 10^{-9} m^2/s to 10^{-10} m^2/s [31-33], and the kinematic viscosity of PBS at 37°C is $7 \cdot 10^{-3}$ cm^2/s [34]. At 100 rpm δ is approximately between 22 μm and 47 μm, and when ω > 2000 rpm then δ < 10 μm. Thus, at slow rotation the diffusion layer is considered thick enough to facilitate the formation a degradation layer. Note that a thinner δ would also increase the concentration gradient between the surface where ions are generated at a rate determined by the applied potential and the concentration in the bulk of the electrolyte. Thus at higher rpm, the diffusion flux of Mg^{2+} away from the sample would also increase.

Table 6. Estimation of the diffusion layer (δ) in μm at different rotation speeds (ω) in rpm. The kinematic viscosity of PBS at 37°C is 7 x 10^{-3} cm^2/s [34]; and δ_{max} and δ_{min} are calculated for an approximated diffusion coefficient between $D_o=10^{-9}$ m^2/s and $D_o=10^{-10}$ m^2/s, respectively [31-33].

ω	100	500	1000	1500	2000	3000
δ_{max}	47	21	15	12	10	8.6
δ_{min}	22	9.7	6.9	5.6	4.9	4.0

3.3.3. First potentiodynamic polarization

Here the first polarizations are compared at different rotation speeds. The corrosion potential (E_{corr}) between 3000 and 1500 rpm was measured around values close to -1.95 V. At 1000 rpm the sample already slightly shows the effect of a depositing degradation layer and a wider diffusion layer δ. This effect is increased at lower spinning rates showing a E_{corr} shift to more noble values (Fig. 28a). At 1000 rpm the measured E_{corr} increased to -1.936 V and in static conditions to -1.751 V against the same potential reference. The corrosion current density (i_{corr}) was calculated with the Tafel extrapolation. i_{corr}, ideally, determines the electron exchange between the anodic and the cathodic reactions assuming that no other electron consuming reactions are taking place. The determined i_{corr} decreases with slower spinning speeds (Fig. 28b). For fast rotation rates, between 3000 rpm and 1500 rpm, the i_{corr} was determined within the range from 6.8 A/m^2 to 5.3 A/m^2. Then from 1000 rpm to static conditions the measured electron flow density is gradually reduced almost linearly from 4.6 A/m^2 to 0.9 A/m^2.

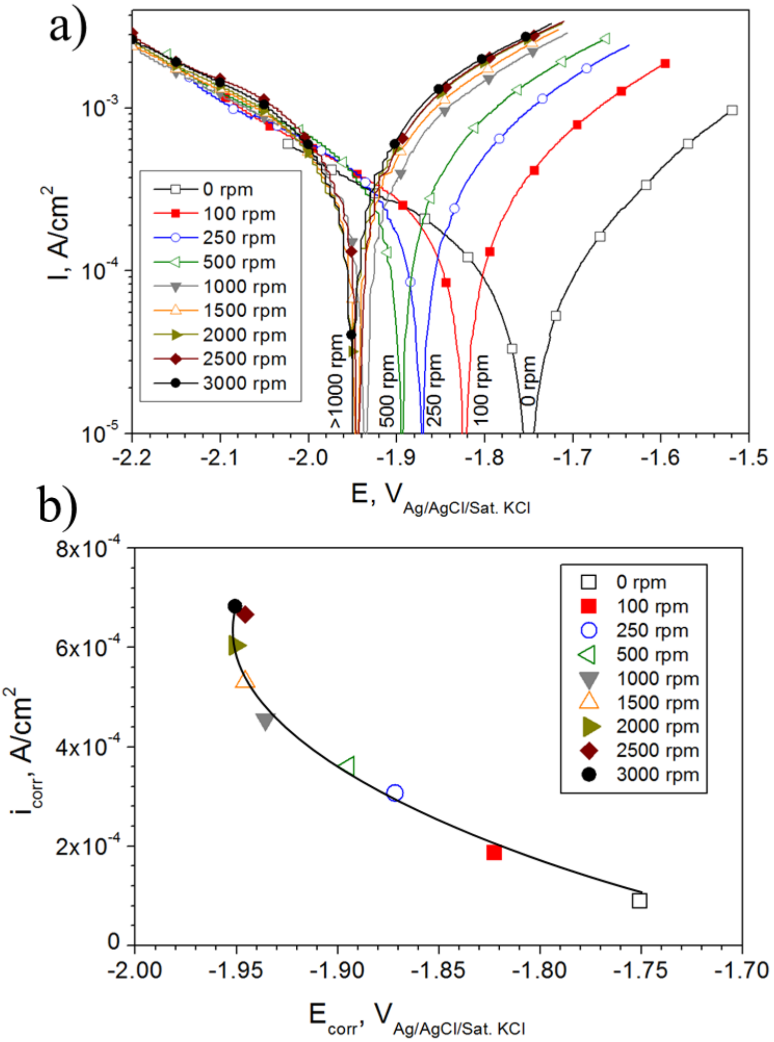

Figure. 28: First potentiodynamic polarization (PDP) curves of pure Mg (a) and i_{corr} vs E_{corr} calculated from these first PDP at different ω (b). These data show a trend to stable E_{corr} with small differences in i_{corr} at ω higher than 1000 rpm.

3.3.4. Consecutive polarizations

The corrosion potential increases after every consecutive polarization (Fig. 29). This E_{corr} increase is strongly reduced with rotation. This can be seen by the slowly increasing E_{corr} over 20 polarizations for all the rotation speeds (Fig. 29a). The potential increases with a slightly asymptotic tendency for all the rotation speeds, however for 0 rpm the potential increase is very pronounced over 10 polarizations. The slower the rotation is the higher E_{corr} becomes.

Similarly i_{corr} stabilizes after 10 polarizations for high ω (Fig. 29b). The current densities are stable at 5.3 A/m^2 for 3000 rpm and at 4.8 A/m^2 for 2000 rpm. For 500 rpm, 100 rpm and static conditions the i_{corr} does not vary significantly from the first polarization, and i_{corr} is stabilized at 3.2 A/m^2, 1.7 A/m^2 and 0.5 A/m^2, respectively.

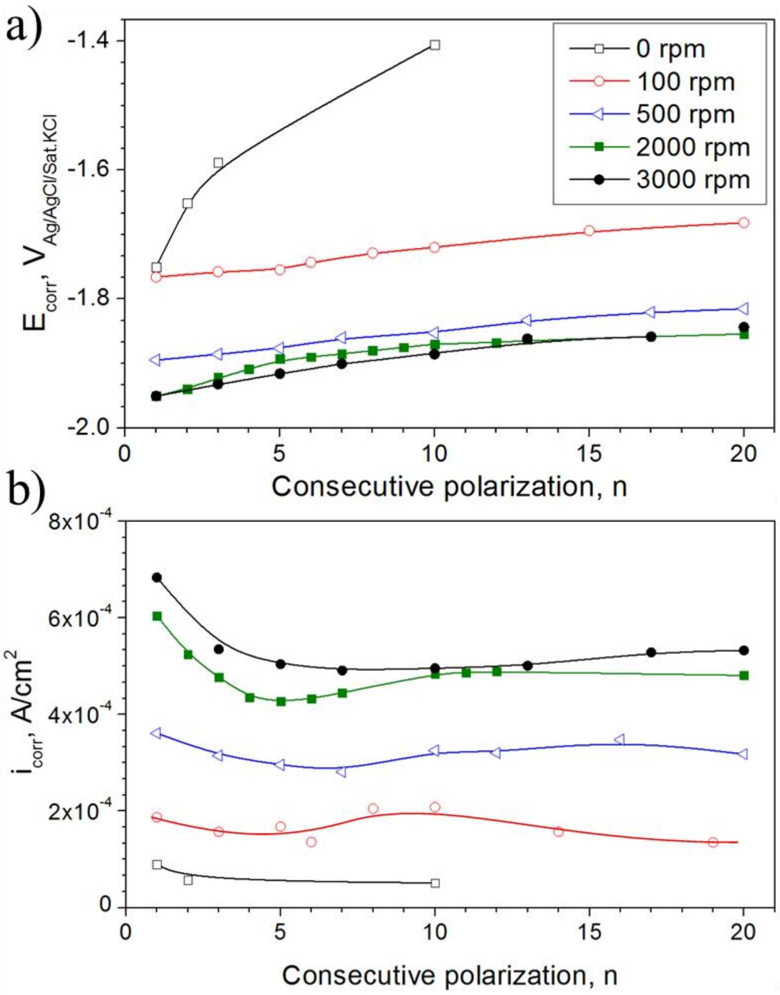

Figure 29: Corrosion potential (E_{corr}) (a) and current density (i_{corr}) (b) tendency over consecutive polarization experiments at different rotation speeds. Consecutive polarizations can indicate changes on the sample surface after each polarization, and in this case, when a rotation faster than 2000 rpm is applied no large E_{corr} and i_{corr} shifts are observed.

The concentration of Mg^{2+} in the electrolyte bath increases during every anodic polarization, which can cause changes in PDP results. 400 mL of PBS have been used in these experiments without changing the electrolyte during many experiments. According to Faraday's law, the increase of Mg^{2+} ions, can be approximated by the charge transferred (Eq. 22):

$$m = Q/(F \cdot z) \tag{22}$$

where m is Mg mass dissolved in mol, Q is the charge in coulomb, F is the Faraday constant (96,485 C/mol) and z is the valency number of electrons transferred per Mg ion, which is considered as 2. The charge varies after every polarization also depending on ω. For the majority of the polarizations, e.g. at 2000 rpm, the charge increases up to 0.128 C/cm^2 at the 1st polarization and 0.062 C/cm^2 at the 20th. This would suppose an increase of Mg^{2+} concentration in 400 mL PBS of 0.83 μM and 0.40 μM for the 1st and the 20th polarization respectively, and since the pH stays between 7.4 and 7.5 this means that the electrolyte can be used around 1800 times before 1.5 mM of Mg^{2+} is reached, which is approximately the concentration of Mg^{2+} in blood plasma and simulating body fluids [27, 35, 36]. However, for static conditions after the 10th polarization the charge from the anodic scan is 2.3 C/cm^2, which approaches the most extreme situation. This means that every polarization increases 15 μM and that 1.5 mM would be reached after 100 static polarizations. Thus, an electrolyte, such as PBS, with a volume of 400 mL does not require changing when ω equals 2000 rpm. However, it should be considered when consecutive static polarizations are performed with more than one sample.

3.3.5. Degradation layer formation

The imaging of the degradation layer clarifies the influence that the spinning has on the polarization behaviour. SEM images in static and dynamic conditions show different ratios of covered and uncovered areas depending on the rotation speed (Fig. 30). The faster the rotation, the less corrosion products can be found.

The crystalline structure of the degradation layer can be determined by X-ray diffraction. This technique has been applied to degraded samples after consecutive polarization experiments in static and dynamic conditions at 0 and 2000 rpm, respectively (Fig. 31). The peaks detected from the measurement of the degradation layer are typical of α -Mg. This can be explained by a larger interaction volume of the x-ray source in comparison to the surface film thickness. During PDP under static conditionsmagnesium phosphate ($Mg_2P_2O_7$) and magnesium hydroxide ($Mg(OH)_2$) crystalline structures can be identified, but at 2000 rpm only one characteristic peak from $Mg(OH)_2$ is detected. However, at 0 rpm, more characteristic peaks from $Mg(OH)_2$ are identified, showing that a thicker degradation layer is formed under static conditions.

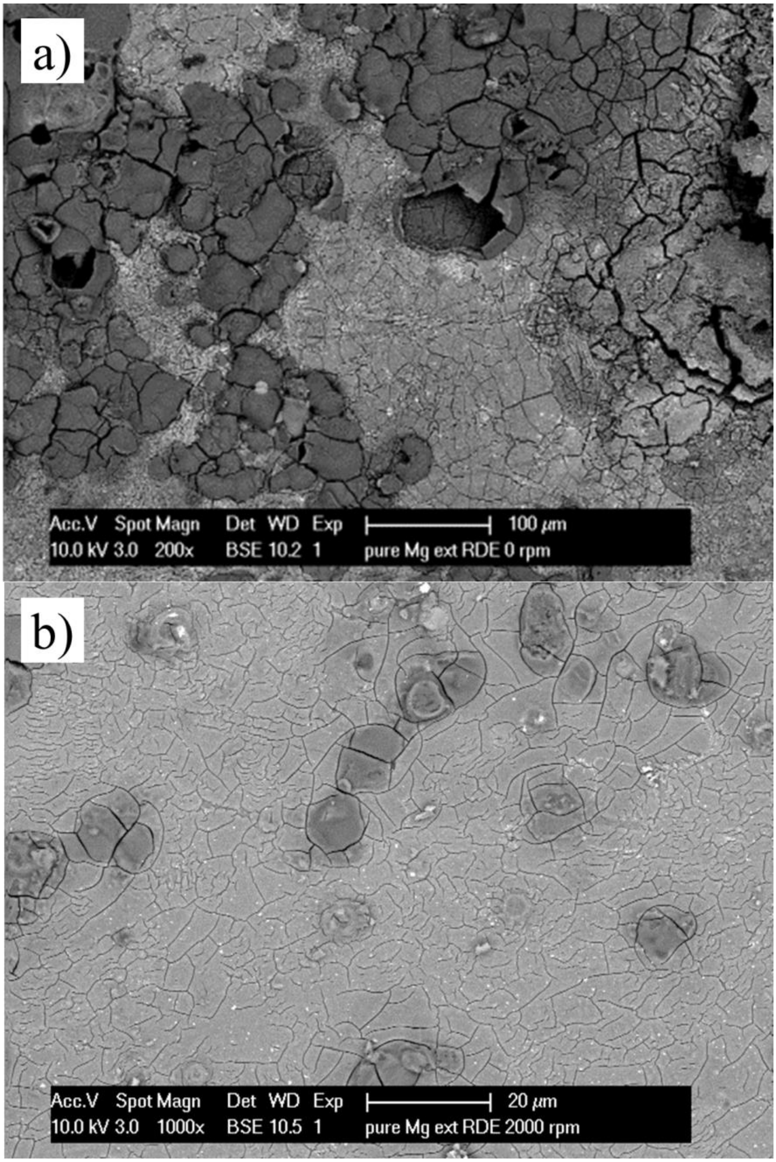

Figure 30: SEM images from the degradation layer in static (0 rpm) (a) and dynamic conditions (2000 rpm) (b) after OCP and 10 and 20 PDP experiments, respectively, in PBS at 37°C. The surface coverage of dark corrosion products is higher under static conditions than at 2000 rpm.

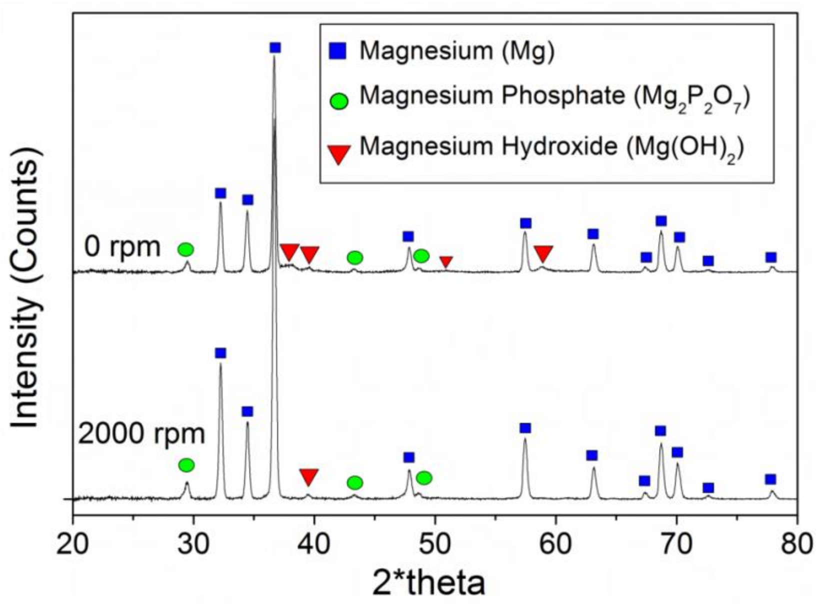

Figure 31: XRD spectra of pure Mg tested at 2000 rpm and static conditions showing a more detectable $Mg(OH)_2$ layer for static testing. Mg phosphate is also deposited due to the high concentration of phosphates in PBS.

In Fig. 32, three different regions can be distinguished after 10 PDPs under static conditions with the backscattered electron mode, which gives elemental contrast. The darker regions (Fig. 32a) are composed of $Mg(OH)_2$ shown by the EDX measurement ratio of 1 part of Mg for 2 parts of O. Some NaCl is present because PBS solution is mainly composed of NaCl. Samples were removed from the electrolyte without rinsing which can explain the small amount of NaCl deposited as particles. The dark region is a thick $Mg(OH)_2$ layer which is considered to be made of the corrosion products causing the ECS reaction as explained in Section 2.6.2. These sites act as cathodes promoting the dissolution of the surrounding Mg. The cracking can be caused by the dehydration of the surface when the sample is removed from the solution and dried. After 10 PDP under static conditions the sample surface covered by the above described dark corrosion products is approximately 87 ± 1%.

The less dark regions (Fig. 32b) are composed of $Mg(OH)_2$ and Mg phosphate, where Na can also be present. These sites are considered to be cathodes which couple to the dark corrosion products (Fig. 32a), promoting the hydrogen evolution and the Mg dissolution.

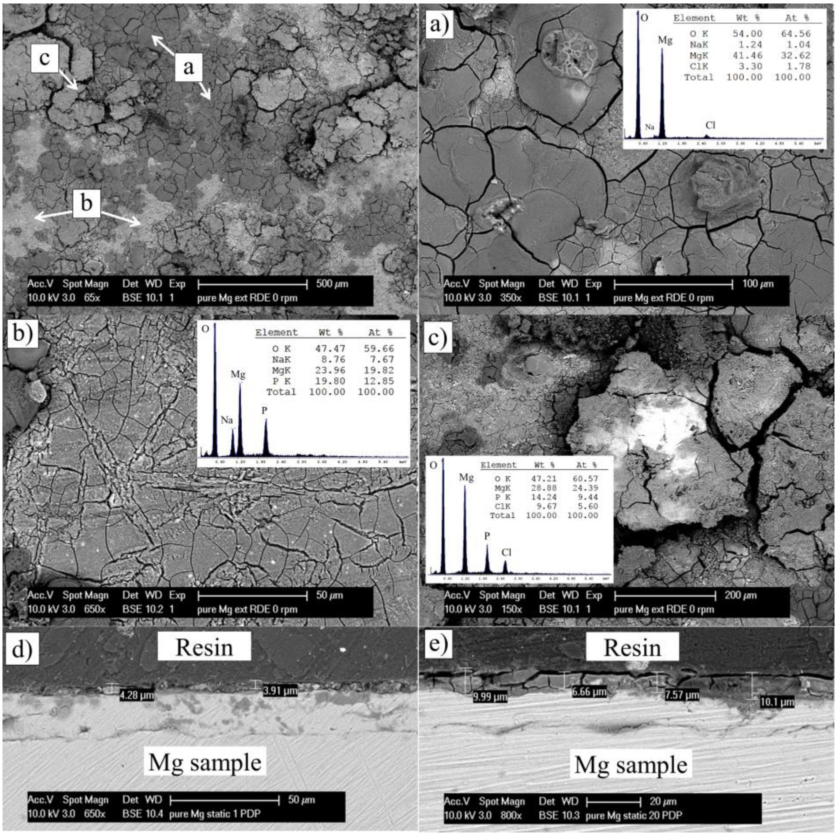

Element	Wt %	At %
O K	54.00	64.56
NaK	1.24	1.04
MgK	41.46	32.62
ClK	3.30	1.78
Total	100.00	100.00

Element	Wt %	At %
O K	47.47	59.66
NaK	8.76	7.67
MgK	23.96	19.82
P K	19.80	12.85
Total	100.00	100.00

Element	Wt %	At %
O K	47.21	60.57
MgK	28.88	24.39
P K	14.24	9.44
ClK	9.67	5.60
Total	100.00	100.00

Figure 32: SEM images from the degradation layer after 10 static polarization experiments. Three different regions are identified as (a), (b) and (c) with their respective SEM image at higher magnification. (a) shows a darker degradation layer which act as cathode promoting the enhance surface reaction. (b) is the less covered area which act as the anode. (c) shows cracked corrosion products. (d) and (e) show the degradation layer thickness after 1 and 20 polarizations under static conditions, respectively.

Finally, largely cracked regions (Fig. 32c) are composed of $Mg_2P_2O_7$ and $Mg(OH)_2$, which are the only crystalline structures detectable from the surface by the XRD technique as shown in Fig. 31. These cracked regions appear as a result of many consecutive polarization experiments accelerating Mg dissolution by the ECS reaction. The presence of Cl^- in these cracked regions can dissolve $Mg(OH)_2$ and, thereby, break down the degradation layer and leaving the Mg sample exposed to the medium [37-39]. The presence of Cl typically indicates pitting corrosion but in this case it might be the reason for the larger crack size.

Fig. 32d and e shows the degradation layer thickness after 1 and 20 PDPs under static conditions, respectively. After the first polarization the degradation layer thickness is approximately 4 µm and after the 20th it increased to 10 µm. These layers are not negligible and as stated above, they influence the polarization results greatly. Note that the thickness is not completely homogeneous over the entire surface.

The degradation layer after 20 PDPs at 2000 rpm is composed of similar compounds but, in this case, the surface covered by dark corrosion products is only 17 ± 0.7% (Fig. 33). Brighter areas (Fig. 33a) are protected with a thin $Mg(OH)_2$, and also, there are traces of $Mg_2P_2O_7$ with a bit of Na (white dots). The strong Mg peak indicates that the Mg under this layer is measured. Some impurity points can be present on the surface, accelerating the dissolution process and creating corrosion products around them.

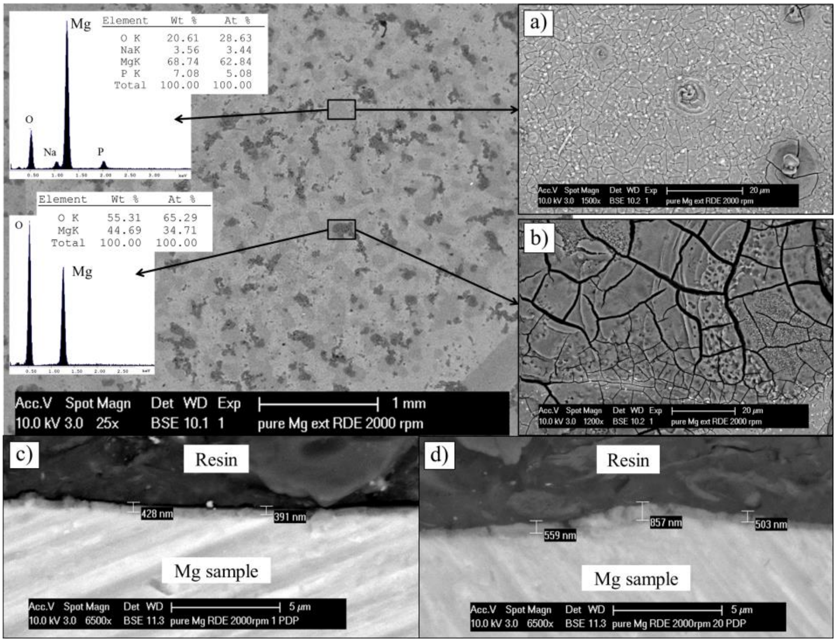

Element	Wt %	At %
O K	20.61	28.63
NaK	3.56	3.44
MgK	68.74	62.84
P K	7.08	5.08
Total	100.00	100.00

Element	Wt %	At %
O K	55.31	65.29
MgK	44.69	34.71
Total	100.00	100.00

Figure 33: SEM images from the degradation layer after 20 dynamic polarization experiments at 2000 rpm. Two different regions are identified as uncovered (a) and covered areas (b). (a) is the dark corrosion product free area which act as anode and (b) is the covered area which act as cathode. (c) shows the degradation layer thickness after 1 polarization at 2000 rpm and (d) after 20 polarizations. The thickness is less than 1 µm when RDE is applied with a small increase from the first to the 20th polarization.

Also, in this case, there are darker areas (Fig. 33b), which are composed of a thicker $Mg(OH)_2$ layer. In this case the area covered by dark corrosion products is much less (~17%) in comparison with static conditions (~87%). Hence, when 2000 rpm is applied the ECS reaction is not driving the corrosion performance during anodic polarization. Fig. 33c shows that the degradation layer thickness after 1 PDP at 2000 rpm is approximately 400 nm while, as shown in Fig. 33d, after 20 PDP at 2000 rpm it only increased to 500-800 nm. Thus, the degradation layer is thinner under rotation at 2000 rpm comparing to static conditions which correlates with consecutive polarization results shown in Fig. 29.

3.3.6. Enhanced catalytic surface theory (ECS)

The electrochemical reactions measured by PDP are described in Section 1.3 (page 21) (Eqs. 1 and 2); and in the overall reaction of Mg with water, $Mg(OH)_2$ can form and 1 mol of Mg dissolved is directly related to 1 mol of H_2 generated (Eq. 4). The ECS theory has been recently formulated to explain the abnormal anodic polarization behaviour shown by Mg [6, 14-18]. This theory (see Ref. [40] for a review) consists of the creation of cathodic sites during anodic polarization, where MgO and $Mg(OH)_2$ deposit, which enhances the H_2 evolution by coupling these sites with the surrounding uncovered Mg surface [6, 16]. In some cases, these cathodic sites can include iron or other impurities [17, 18], hence, the purity of the material influences the anodic polarization behaviour [41]. Perhaps, even more important for these results is the recent finding that the hydrogen evolution reaction (HER) is enhanced by the presence of a $Mg(OH)_2$ coating when compared to a pristine Mg surface [42].

Fig. 34a compares static and dynamic conditions for identical polarization parameters in two different electrolytes, PBS and HBSS. On the one hand, when rotation is applied, PDP measurements of the working electrode show symmetric anodic and cathodic curves and similar i_{corr} and E_{corr} in both media. On the other hand, under static conditions, the results show non-symmetric anodic and cathodic curves, and in some cases, an anodic slope change at a certain potential (Fig. 34b). In literature, these two characteristics are commonly shown in PDP curves [7, 43-48]. The ECS theory allows the explanation of this behaviour [6, 14-18]. Firstly, when the anodic polarization is initiated under static conditions, dark regions are generated on the surface where, according to Taheri et al., MgO and $Mg(OH)_2$ precipitate [18]. During anodic polarization, as shown by Curioni, the propagation rate of these dark regions is increased and therefore so is the HER [6]. Thus, these $Mg(OH)_2$ dark sites exchange electrons with the surrounding uncovered Mg surface resulting in a reduced measured current by the external circuit which is lower than the real anodic current [49].

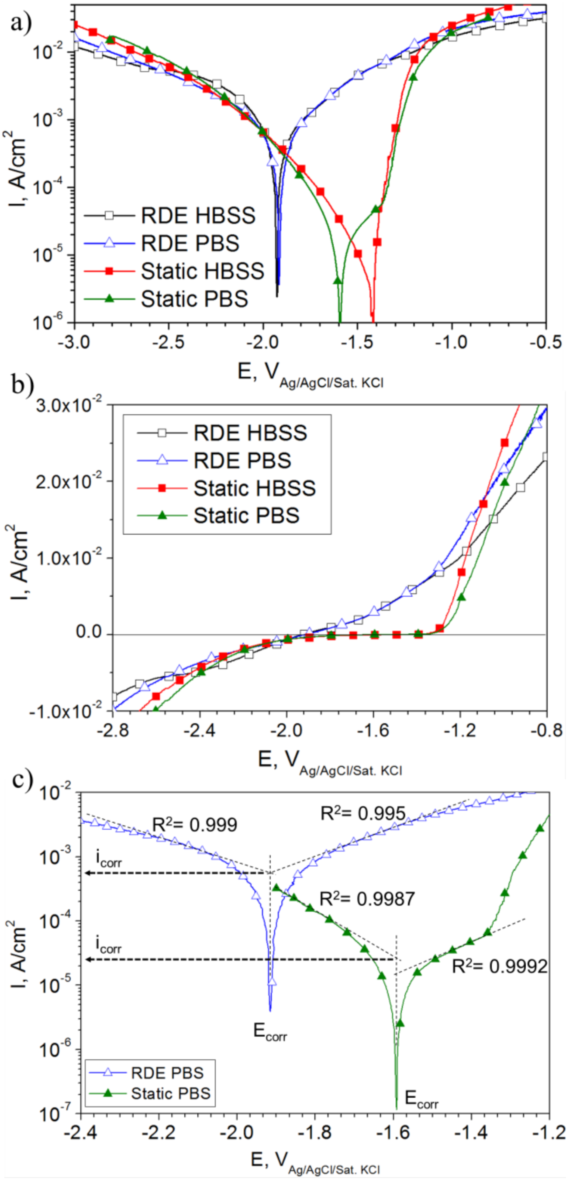

Figure 34: PDP of pure Mg in HBSS and PBS at 37°C at 2000 rpm and in static conditions (±1.0 V and ±1.5V vs OCP). (a) Polarization curves with RDE are characteristic of the material independently whether PBS or HBSS is used as electrolyte. (b) The pronounced anodic polarization related to the negative difference effect (NDE) is not measured when rotation is applied

due to the reduced corrosion product deposition on the surface of the sample. (c) Simple Tafel extrapolation applying both the anodic and the cathodic curves is possible when RDE is applied. R^2 indicates the goodness of fit.

Williams et al., found with the help of the scanning vibrating electrode technique (SVET) anodic and cathodic currents emanating from different sites of the sample which is related to the location of the dark corrosion products [15]. Therefore, the anodic polarization promotes Mg dissolution and hydrogen generation around the dark corrosion products. This also explains the sudden increase of the anodic curves (indicated with red arrows in Fig. 34b) registered under static conditions. However, during anodic polarization of rotating Mg samples the area covered with dark spots (Figs. 30 and 32) and the concomitant catalytic cathodic reaction (Fig. 34) are strongly reduced.

The Tafel fit assumes that the process is controlled by the charge transfer and that electrochemical kinetics follow the Butler-Volmer equation. With the RDE the mass transport is controlled by diffusion only influencing the degradation layer deposition and not the electrochemical reactions. This method provides comparable results to other techniques, such as immersion tests [50]. This polarization technique and the Tafel fit is commonly used by many authors to characterize the corrosion properties of Mg alloys and compare them [8-10, 51, 52]. Due to the pronounced anodic curves obtained, some authors only measure the cathodic curve and then calculate the current density with the cathodic slope and the corrosion potential [41, 42]. As shown in Fig. 34c, with the RDE this is no longer necessary since the anodic behavior is not influenced by the negative difference effect. Thus, simple extrapolation is possible and both curves can be used for the determination of i_{corr}. Note that the correct Tafel extrapolation require some other assumptions, such as uniform corrosion mode and no additional reactions [50], thus polarization data must be carefully taken into consideration.

3.3.7. Influence of the scan rate

The scan rate and range also had an influence on the results during consecutive polarization experiments at 2000 rpm, mainly due to prolonged anodic Mg dissolution. However, the most interesting data for corrosion characterization is obtained around the E_{corr} where i_{corr} of the cathodic and anodic reactions are measured. Hence, it is not necessary to polarize the sample far into the anodic potential axis from the E_{corr} values [28]. However, this range has to be large enough to determine the Tafel slopes to estimate i_{corr} [50].

Fig. 35 shows minor effects of the scan rate on the first polarization. At 1 and 2 mV/s i_{corr} was found to be 8.6 and 7.9 A/m^2, respectively. Applying scan rates between 5 and 20 mV/s, i_{corr} was measured between 6.8 and 5.8 A/m^2.

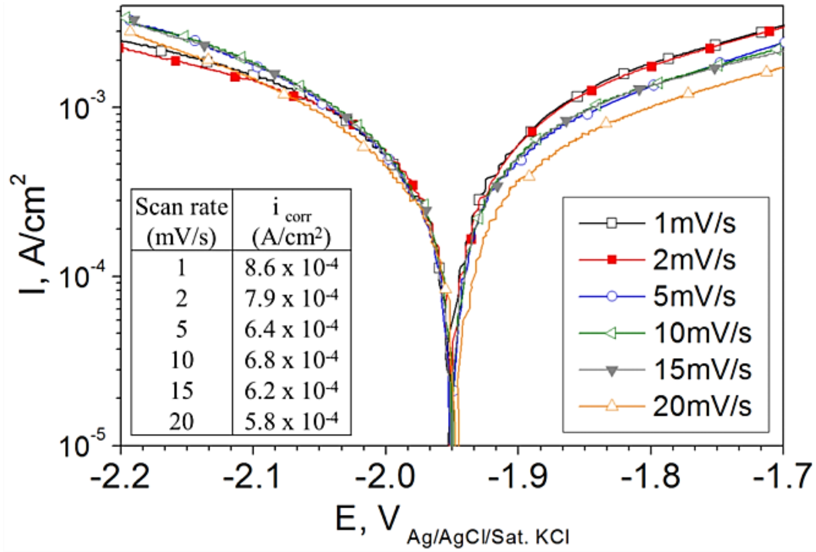

Scan rate (mV/s)	i_{corr} (A/cm^2)
1	8.6×10^{-4}
2	7.9×10^{-4}
5	6.4×10^{-4}
10	6.8×10^{-4}
15	6.2×10^{-4}
20	5.8×10^{-4}

Figure 35: There is a minimal influence of the scan rate on the E_{corr} at the first polarization applying 2000 rpm with different Mg samples prepared in the same way. The variation in i_{corr} is significantly reduced when the scan rate > 5 mV/s.

Fig. 36 shows the effect of the scanning rates on consecutive PDP on pure Mg. At slow scan rates, 1 mV/s and 2 mV/s (Fig. 36a and b), the shift in E_{corr} between the first and the sixth PDP measurement is approximately 250 and 150 mV, respectively. In contrast, higher scan rates (5, 10, 15 and 20 mV/s) show small shifts between the first and the sixth PDP (6, 22, 14 and 12 mV, respectively) (Fig. 36c-f). Thus, at slow scanning rates the E_{corr} shift is larger than with faster rates. This is because faster scans induce an external potential to the Mg working electrode during less amount of time. Thus, the surface experiences minor changes over consecutive polarization experiments.

According to Kirkland et al. an increased amount of noise can be observed at low scan rates (1 mV/s and 2 mV/s) due to the longer polarization time [28]. However, in the present case the registered noise at all these scan rates is similar, showing no particular dependency on scan rates. It appears that the noise level is defined by the rotation speed and the accuracy of the cell and its devices, or even external influences. A higher level of noise is also noticeable during the first polarization compared to the consecutive ones, especially at 1 and 2 mV/s (Fig. 36a and b).

The scanning range also has an influence because the larger this range is, the more time the sample is polarized and degraded in the anodic region. Thus, polarization away from OCP results in perturbations of the sample surface before the scan is complete. Similarly, large cathodic polarizations will alter the local pH, thereby changing testing conditions. This alteration is suppressed by the agitation of the solution. In literature, it is stated that a range of 150 mV below the OCP to 500 mV above provides ample data for analysis without affecting the corrosion process noticeably [28, 53].

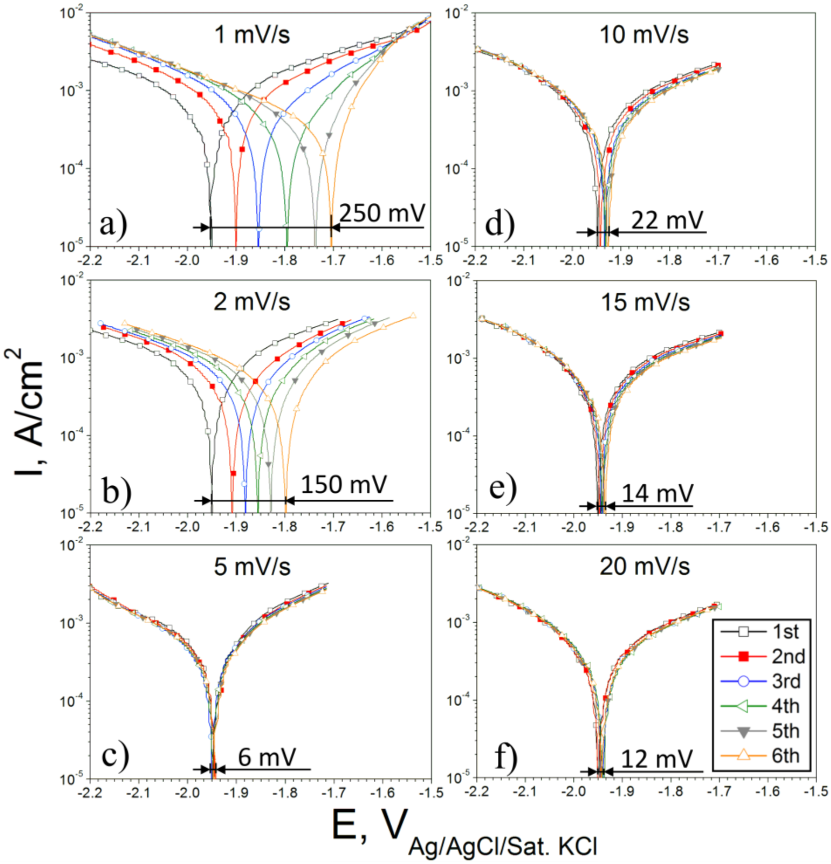

Figure 36: Influence of the scan rate on six consecutive polarizations at 2000 rpm. 5 mV/s seems to have the less influence although 10, 15 and 20 mV/s show also slight potential shifts. 1 and 2 mV/s polarizes the samples for longer time, shifting the E_{corr} because of the degradation layer formation.

Thus, here, the applied scanning range of 500 mV around OCP with 1 mV/s also causes a larger E_{corr} shift (Fig. 36a). This shows that a slow scan rate in combination with a broad scan range has a great influence on consecutive polarizations. In contrast, applying a scan range of 250 mV neither the first polarization curve nor the sample surface are highly influenced by the applied scan rate.

3.4. Conclusions

This work shows the influence of the rotation speed on the first and also on consecutive polarization measurements of pure Mg in PBS at 37°C. In order to perform reproducible measurements the appropriate ω range is defined as 1500-2000 rpm for the setup used.

The first PDP is not significantly influenced by the scan rate. Furthermore, higher scan rates than 5 mV/s provide quick and reproducible measurements with minimal degradation layer deposition and low signal to noise level.

The use of RDE reduces the pronounced anodic current increase related to the negative difference effect. This is due to the reduction of the formation of corrosion products on the Mg surface which can act as cathodes. There is an electron exchange with the Mg around them, which act as the anode. These electrons are not measured by the external circuit, and thus, the corrosion process and the H_2 generation are accelerated. When the working electrode is under rotation, the enhanced cathodic activity at anodic overpotentials is not measured and more symmetric anodic and cathodic curves are determined. This symmetry allows simple Tafel extrapolation and provides similar results even in different media, such as PBS or HBSS, showing repeatedly characteristic curves of the material. All these observations are consistent with the enhanced catalytic surface theory as an explanation for the negative difference effect.

The presence of dissolved magnesium (Mg^{2+}) during polarization experiments induces a degradation layer which covers the sample even when rotation is applied. This layer and the diffusion layer caused by the rotation shift the corrosion potential towards more anodic values and reduces the current flow. When the sample rotates during the polarization with the RDE only a thin $Mg(OH)_2$ layer is formed because most of the Mg^{2+} diffuses away from the surface of the sample so that the Mg^{2+} concentration does not reach a high value. However, the use of the rotating disc electrode does not completely avoid the formation of a degradation layer after several polarizations but it reduces greatly its influence on polarization measurements. Approximately 83% of the surface remains uncovered after 20 polarizations with the RDE.

References

[1] A.H. Martinez-Sanchez, B.J.C. Luthringer, F. Feyerabend, R. Willumeit, Acta Biomater. 13 (2015) 16-31.
[2] G. Song, S. Song, Adv. Eng. Mater. 9 (2007) 298-302.
[3] A. Atrens, W. Dietzel, Adv. Eng. Mater. 9 (2007) 292-297.
[4] T.R. Thomaz, C.R. Weber, T. Pelegrini Jr, L.F.P. Dick, G. Knörnschild, Corros. Sci. 52 (2010) 2235-2243.
[5] G.S. Frankel, A. Samaniego, N. Birbilis, Corros. Sci. 70 (2013) 104-111.
[6] M. Curioni, Electrochim. Acta 120 (2014) 284-292.
[7] G.L. Song, A. Atrens, Adv. Eng. Mater. 1 (1999) 11-33.
[8] Z. Shi, F. Cao, G.-L. Song, M. Liu, A. Atrens, Corros. Sci. 76 (2013) 98-118.
[9] Z. Shi, F. Cao, G.-L. Song, A. Atrens, Corros. Sci. 88 (2014) 434-443.
[10] Z. Qiao, Z. Shi, N. Hort, N.I. Zainal Abidin, A. Atrens, Corros. Sci. 61 (2012) 185-207.
[11] M. Liu, P. Schmutz, P.J. Uggowitzer, G. Song, A. Atrens, Corros. Sci. 52 (2010) 3687-3701.
[12] A. Samaniego, B.L. Hurley, G.S. Frankel, Journal of Electroanal. Chem. 737 (2015) 123-128.
[13] R.L. Petty, A.W. Davidson, J. Kleinberg, JACS 76 (1954) 363-366.
[14] N. Birbilis, A.D. King, S. Thomas, G.S. Frankel, J.R. Scully, Electrochim. Acta 132 (2014) 277-283.
[15] G. Williams, N. Birbilis, H.N. McMurray, Electrochem. Commun. 36 (2013) 1-5.
[16] G.S. Frankel, A. Samaniego, N. Birbilis, Corros. Sci. 70 (2013) 104-111.
[17] G. Williams, H. Neil McMurray, J. Electrochem. Soc. 155 (2008) C340-C349.
[18] M. Taheri, J.R. Kish, N. Birbilis, M. Danaie, E.A. McNally, J.R. McDermid, Electrochim. Acta 116 (2014) 396-403.
[19] C. Schille, M. Braun, H.P. Wendel, L. Scheideler, N. Hort, H.P. Reichel, E. Schweizer, J. Geis-Gerstorfer, Mater. Sci. Eng.: B 176 (2011) 1797-1801.
[20] J. Trinidad, G. Arruebarrena, I. Marco, I. Hurtado, E. Saenz de Argandona, Proc. Inst. Mech. Eng. Part H 227 (2013) 1301-1311.
[21] X. Yunchang, H. Tao, P.K. Chu, J. Electrochem. Soc. 157 (2010) C238-243.
[22] A. Yamamoto, S. Hiromoto, Mater. Sci. Eng.: C 29 (2009) 1559-1568.
[23] T. Kokubo, H. Takadama, Biomaterials 27 (2006) 2907-2915.
[24] Y. Zong, G. Yuan, X. Zhang, L. Mao, J. Niu, W. Ding, Mater. Sci. Eng.: B 177 (2012) 395-401.
[25] N.I. Zainal Abidin, D. Martin, A. Atrens, Corros. Sci. 53 (2011) 862-872.
[26] W. He, E. Zhang, K. Yang, Mater. Sci. Eng.: C 30 (2010) 167-174.

[27] D. Tie, F. Feyerabend, N. Hort, R. Willumeit, D. Hoeche, Adv. Eng. Mater. 12 (2010) 699-704.

[28] N.T. Kirkland, N. Birbilis, M.P. Staiger, Acta Biomater. 8 (2012) 925-936.

[29] A.C. Riddiford, Advances in electrochemistry and electrochemical engineering 4 (1966) 47-116.

[30] A.J. Bard, L.R. Faulkner, Electrochemical Methods: Fundamentals and Applications, Wiley, 2000.

[31] V.M.M. Lobo, A.C.F. Ribeiro, L.M.P. Verissimo, Berichte der Bunsengesellschaft für physikalische Chemie 98 (1994) 205-208.

[32] P.S. Salmon, W.S. Howells, R. Mills, J. Phys. C: Solid State Phys. 20 (1987) 5727.

[33] L. Yuan-Hui, S. Gregory, Geochim. Cosmochim. Acta 38 (1974) 703-714.

[34] I. Fluxion Biosciences, Viscosity: understanding effects of viscosity in the BioFlux system, in: T. note (Ed.) 2008.

[35] F. Feyerabend, H. Druecker, D. Laipple, C. Vogt, M. Stekker, N. Hort, R. Willumeit, J. Mater. Sci. - Mater. Med. 23 (2012) 9-24.

[36] L. Choudhary, R.K. Singh Raman, J. Hofstetter, P.J. Uggowitzer, Mater. Sci. Eng.: C 42 (2014) 629-636.

[37] M. Jamesh, S. Kumar, T.S.N.S. Narayanan, Corros. Sci. 53 (2011) 645-654.

[38] W.-D. Mueller, M. Fernandez Lorenzo de Mele, M.L. Nascimento, M. Zeddies, J. Biomed. Mater. Res. Part A 90A (2009) 487-495.

[39] H.R. Bakhsheshi-Rad, M.H. Idris, M.R. Abdul-Kadir, A. Ourdjini, M. Medraj, M. Daroonparvar, E. Hamzah, Materials and Design 53 (2014) 283-292.

[40] S. Thomas, N.V. Medhekar, G.S. Frankel, N. Birbilis, Curr. Opin. Solid State Mater. Sci. 19 (2015) 85-94.

[41] S. Fajardo, G.S. Frankel, Electrochim. Acta 165 (2015) 255-267.

[42] S.H. Salleh, S. Thomas, J.A. Yuwono, K. Venkatesan, N. Birbilis, Electrochim. Acta 161 (2015) 144-152.

[43] J.W. Seong, W.J. Kim, Acta Biomater. 11 (2015) 531-542.

[44] M.-C. Zhao, M. Liu, G.-L. Song, A. Atrens, Adv. Eng. Mater. 10 (2008) 104-111.

[45] W. Liu, F. Cao, L. Chang, Z. Zhang, J. Zhang, Corros. Sci. 51 (2009) 1334-1343.

[46] E. Zhang, L. Yang, J. Xu, H. Chen, Acta Biomater. 6 (2010) 1756-1762.

[47] X. Xia, Q. Chen, Z. Zhao, M. Ma, X. Li, K. Zhang, J. Alloys Compd. 623 (2015) 62-68.

[48] G.L. Song, A. Atrens, Adv. Eng. Mater. 5 (2003) 837-858.

[49] M. Curioni, F. Scenini, T. Monetta, F. Bellucci, Electrochim. Acta 166 (2015) 372-384.

[50] E. McCafferty, Corros. Sci. 47 (2005) 3202-3215.

[51] A.D. King, N. Birbilis, J.R. Scully, Electrochim. Acta 121 (2014) 394-406.

[52] F. Cao, Z. Shi, G.-L. Song, M. Liu, A. Atrens, Corros. Sci. 76 (2013) 60-97.

[53] N.T. Kirkland, M.P. Staiger, D. Nisbet, C.H.J. Davies, N. Birbilis, JOM 63 (2011) 28-34.

Chapter 4:
In vivo and in vitro degradation comparison of pure Mg, Mg-10Gd and Mg-2Ag: a short term study

Adapted from:

I. Marco, A. Myrissa, F. Feyerabend, R. Willumeit-Römer, A. Weinberg, O. van der Biest. In vivo and in vitro biodegradation comparison of pure Mg, Mg-10Gd and Mg-2Ag: a short term study. Eur. Cell Mater. Revision under review.

4.1. Introduction

As mentioned in Section 2.7, although some attempts to correlate in vitro and in vivo results have been done [1-3], in general the comparison between different methods is lacking [4]. In some cases the immersion testing conditions apply different electrolytes, buffering and solution volume to sample surface ratio (V/S), and as a result, the comparison with in vivo experiments is hardly possible [3]. Hence, the need for a standardized in vitro testing method which can be compared to in vivo has been identified [4, 5]. For this reason, three electrolytes commonly used in literature have been selected for the in vitro study in this work: phosphate buffered saline (PBS) [6-8], Hank's balanced salt solution or Hank's solution (HBSS) [9, 10] and a cell culture basal medium: Dulbecco's modified eagle medium (DMEM) [11-15], which is similar to plasma and whole blood but without any protein content [16]. Hofstetter et al. applied a setup with comparable in vitro and in vivo results, which consists of simulated body fluid (SBF) continuously buffered with CO_2 at a pH of 7.4 in one single stirred bath [17]. In the present work, cell culture conditions are applied with DMEM in a similar setup where the 5 vol.% of CO_2 is added to the atmosphere instead of to the electrolyte.

Since the required resorption rate for Mg-alloys depends on the application, different alloying elements, which can tune these rates, are selected. Here, the selected elements are silver (Ag) and gadolinium (Gd). On the one hand, Ag is considered as an impurity with a low tolerance limit which accelerates the degradation process [18]. Moreover, Ag is known by its antibacterial properties [12], also shown by Mg [19, 20]. On the other hand, Mg-Gd is reported as a slowly degrading alloy. Gd can form intermetallic compounds with impurities less harmful to the corrosion resistance [21], and it also improves the mechanical properties [22, 23].

This chapter compares the degradation performance of different Mg alloys produced in disc and pin shape in in vitro and in vivo conditions, respectively. The DRs and the degradation layers formed are compared after 7 days. In the analysis, the impurity level and the grain size are of high importance. Difficulties to distinguish bone from the degradation layer after in vivo experiments by micro computed tomography (μCT) have been recently reported [24]. These difficulties are related to the resolution of the tomographic method and equipment used and to differences in X-ray absorption between bone and the degradation layer. Therefore, this chapter also analyses the degradation layer trying to clarify the differences between bone and these layers, and comparing the layers formed during in vivo and in vitro experiments.

4.2. Experimental methods

4.2.1. Material preparation

The raw materials used for the Mg alloy production were: magnesium (99.99%, Xinxiang Jiuli Magnesium co. Ltd, China), gadolinium (99.95%, Grirem Adv. Mater. Co. Ltd., China) and silver (99.99%, ESG Edelmetall-Handel GmbH & Co. KG, Germany). All the alloys underwent thermomechanical processing steps at elevated temperatures appropriate for each alloy in order to homogenize their composition and microstructure. Ingots were cast in a permanent mould casting at 680-720˚C in protective atmosphere (Ar + 2 vol.% SF_6) and heat treated for 6h at 420-430°C for Mg-2Ag and 500-550°C for Mg-10Gd. Then Mg-10Gd and Mg-2Ag samples were extruded at 370-450˚C from 30 mm diameter to 12 mm with a speed of 2.5-4.5 mm/sec, and pure Mg was reduced in diameter from 110 mm to 12 mm at 300°C at 0.7 mm/s without any heat treatment. Finally the wires were cut into discs with 10 mm diameter and 1.5 mm thickness, with a mass of approximately 180 mg for each disc.

For the in vivo experiments, same materials were used in pin shape and in order to achieve this, the extrusion was done to a final rod diameter of 6 mm. The extruded pure Mg (99.956%) and Mg-10Gd rods (d=6 mm) were further reduced to 1.6 mm diameter by turning (Ernst Wittner GmbH, Vienna, Austria). The Mg-2Ag extruded rods were drawn to wires using hardened steel drawplates. The wires were annealed at 300 °C for 45 min in the furnace applying 1 to 3 wire drawing steps and then they were drawn to a diameter of 1.6 mm. After production, the samples were sterilized by gamma radiation dose at 29.2 kGy (BBF GmbH, Stuttgart, Germany) and afterwards, no surface preparation was applied.

The chemical composition and impurity content were determined by inductively coupled plasma optical emission spectroscopy (ICP-OES, Varian 720 ES). For the grain size analysis samples were embedded in epoxy resin and the surfaces prepared by grinding with SiC sandpaper of 1000 grit to 4000 grit (Matador 991A, Remscheid, Germany), and finally by polishing with diamond suspension of 3 µm (Kemet, Maidstone, England). Then, pure Mg and Mg-10Gd containing alloys were etched in picric acid solution (6 g of picric acid, 5mL of acetic acid, 10 mL of H_2O and 100 mL of ethanol) for 2 s, while the etching of Mg-2Ag was done as quickly as manually possible (less than 1 s). The grain size is determined by optical microscopy and the linear intercept method applying the software ImageJ (version 1.47v, Wayne Rasband). The density was measured with Archimedes's method comparing the mass of the samples in air and in ethanol at 25°C.

4.2.2. In vitro degradation testing

In this in vitro degradation study, two different testing setup configurations were applied during 4 to 7 days (Fig. 37). On the one hand, phosphate buffered saline (PBS 4417, Sigma Aldrich, St. Louis, USA) and Hank's balanced salt solution (HBSS, Life Technologies 14175, Grand Island, USA) in air at 37˚C were used as non-physiological testing conditions (Fig. 37a). PBS and HBSS are commonly applied electrolytes in Mg degradation experiments as they have a high amount of buffering capacity and they contain phosphates and, in HBSS, also carbonates. On the other hand, testing under near physiological conditions or cell culture conditions was applied. This consisted of immersion in Dulbecco's modified eagle medium Glutamax-I (DMEM 61965, Invitrogen, Paisley, UK) in air with 5 vol. % CO_2 at 37±0.5˚C with the same stirred bath of 600 ml where the CO_2 level in the atmosphere was stabilized by a CO_2 controller (ProCO2, BioSpherix, Lacona, USA) (Fig. 37b). A 5 vol. % CO_2 is commonly used to assure a saturation of CO_2, and thereby, correct the pH increase caused by the Mg degradation process, similarly as the human body does. In literature it is recommended to apply one single bath for more physiological electrolyte concentrations [17, 25, 26]. However, for testing in PBS and HBSS each sample is immersed in one single bath to allow single pH measurements. In both configurations, experiments were performed with six samples of each alloy. Table 2, in page 36, shows the composition of the media used for the in vitro study.

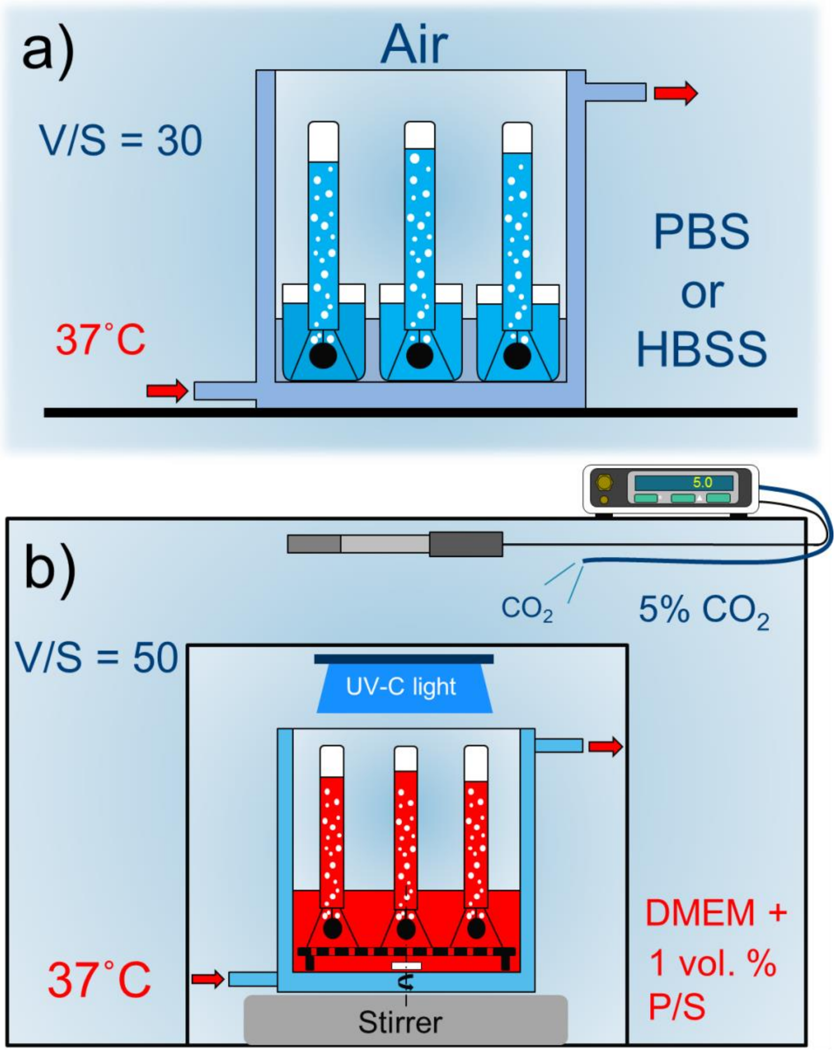

Figure 37: Immersion test setups in a) PBS and HBSS; and b) DMEM and 5 vol.% CO_2 under sterile conditions. One single bath is stirred in DMEM in order to assure the same pH and sterile conditions in the entire bath, while in PBS and HBSS the analysis is done individually since medium contamination does not occur.

Under physiological conditions an empty control position test was performed without a sample in order to see the gas accumulation due to artifacts created by the stirring and the CO_2 in solution. UV-C radiation was applied and antibiotics, 1 vol. % of penicillin streptomycin (Penicillin-Streptomycin (10,000 U/mL) 15140, Gibco, Grand Island, NY) were added to DMEM in order to avoid or, at least, delay the medium contamination by proliferation of microorganisms [27-29]. The UV-C radiation was applied with UV lamps (JKL components type BF8100 UVC, Thief River Falls, USA) with a wavelength of 254 nm. The pH was measured after calibration, at different time points with a standard electrode system and a pH meter (WTW pH340i, sensor WTW SenTix 41-3, Weilheim, Germany). The duration of the test depended on the limit of H_2 collection and the risk of DMEM contamination.

As mentioned by Zhen et al. and Yang et al., the ratio of solution volume to sample surface (V/S) should be considered in the testing [30, 31]. The V/S ratio applied in this study was 30 ml/cm^2 for PBS and HBSS testing and 50 mL/cm^2 for immersion in DMEM. As Kirkland et al. stated, at V/S ratios higher than 30 the V/S ratio has no longer a statistically significant influence on the DR [32]. Hence, the difference in V/S in these two setups is not expected to be relevant.

The surface finishing of the discs was done firstly by grinding all the surfaces with SiC sandpaper of 1000 grit to 4000 grit (Matador 991A, Remscheid, Germany), and finally by polishing with diamond suspension of 3 µm (Kemet, Maidstone, England). The DRs were determined by mass loss (ML) measurements using chromic acid (20 g chromium (VI) oxide (1257, Vel, Belgium), 1 g $AgNO_3$ (85228, Sigma Aldrich, Steinheim, Germany) and 100 ml distilled H_2O) for removal of the corrosion products.

DR is calculated from both the H_2 evolution and the mass loss at the last time point of each immersion test and after chromic acid cleaning as explained in Section 1.6.6 in equations 11 and 10 respectively [33]. Basically H_2 is converted to the dissolved Mg mass applying the ideal gas law and considering that 1 mol of Mg^{2+} corresponds to 1 mol of H_2. The unit mm/year requires the assumption of a uniform corrosion, which is not the case in long term experiments, and it might not represent the long term corrosion behaviour.

The gas volume that was detected at the control position test in DMEM can be deducted from the collected hydrogen from each sample in order to calculate the DR by H_2. As Kirkland et al. suggested, the gas solubility must be taken into consideration [32] because H_2 will only be collected when the electrolyte is saturated. If this H_2 gas in liquid solution is not corrected, it would be a large source of error when the collected H_2 is small. This gas in solution is approximated by the H_2 solubility in water at 37°C, which is 18.8 ml per litre of electrolyte [34]. Thus, in the present work the H_2 dissolved in the liquid has been added to the gas data.

4.2.3. In vivo experiments

All animal experiments were performed under ethical respect for animals and were authorized by the Austrian Ministry of Science and Research (accreditation number BMWF-66.010/0078-II/3b/2011). 3 male Sprague-Dawley rats (n=1 rat/per group) of 150-170 grams weight and 5 weeks of age were used within this study. Cylindrical pins of 1.6 mm diameter and 8 mm length of pure Mg, Mg-10Gd and Mg-2Ag were used for the implantation. 2 pins of each alloy were implanted transcortically in the femoral bones of each rat. The entire implantation surgery took place under general anesthesia and the postoperative treatment is described in detail by [35]. µCT scans were performed at 1 and 7 days after the operation with Siemens Inveon µCT. During the µCT scans, the animals were anesthetized with volatile isoflurane (Forane#, Abbot AG, Baar, Switzerland). Siemens Inveon Acquisition Workplace 1.2.2.2 was the µCT scan software and scans of the rats were performed with a tungsten source at 70 kV voltage, 500 µA current, and 1000 ms exposure time. The effective pixel size was 35.04 µm. An aluminium filter with a thickness of 0.5 mm was used. 3-D morphometric analysis was done and the pin volume and surface and gas volume were evaluated by using the software Mimics (Version 18.0, Materialise, Leuven, Belgium) as described by Kraus et al. [35].

The DR (n=2 bones per group) was calculated in mm/year for 7 days after the operation by the Eq. 23:

$$\mathrm{DR_i} = \frac{\Delta \mathrm{x_i}}{\Delta \mathrm{t}} \text{ with } \Delta \mathrm{x_i} = \frac{\Delta \mathrm{V_i}}{\mathrm{S_i}} \tag{23}$$

where i is the observation time point, ΔV_i is the change of the volume between the observation time point i-1 and i (Δt) in mm^3, S_i is the surface area at the observation time point i in mm^2 and Δx_i is the degradation width [36]. As mentioned above, the time points i are 1 and 7 days. Pin volume reduction was also calculated in % for 7 days after the operation.

The animals were euthanized 7 days after the operation as described in [35]. The bones were explanted and directly frozen at -80°C without applying any fixation. Then they were sent with dry ice to KU Leuven for the degradation layer analysis.

4.2.4. Degradation layer analysis

Both in vitro and in vivo tested samples were embedded in a high infiltration epoxy resin, and after cutting and polishing, they were coated with Pt by sputtering to make the surface electrically conductive. Elemental mapping was performed with cross sections of tested samples using the Electron Probe Micro Analysis device (EPMA, JEOL Ltd. JXA-8530F). All maps were acquired at 10 kV, 20 nA and 30 ms per dwell time, which is the acquisition time per pixel. Additionally, imaging was done by scanning electron microscopy (SEM, XL30 FEG, Philips) and elemental point analysis by energy dispersive X-ray spectroscopy (EDX, EDAX). Elemental mapping analysis was also performed in other studies to characterize the degradation layer formed on Mg samples [37, 38].

4.3. Results

4.3.1. Material characterization

Table 7 shows the composition of the studied Mg alloys in disc and pin shape together with the impurity content of Fe, Mn, Si, Ni, Co Cu and Al. The grain size and the alloy density are also included in Table 2 (page 36). These data are used in the discussion allowing better analysis of degradation results.

Table 7. Composition, impurity content in weight percent (wt.%), parts per million (ppm), grain size and density comparison of pure Mg, Mg-10Gd and Mg-2Ag in disc and pin shape. Note that the Fe, Ni and Cu impurity content is higher for pins than for discs due to the processing route and the lack of surface preparation.

		Gd	Ag	Fe	Mn	Si	Ni	Co	Cu	Al	Mg	Grain size	Density
		wt.%	wt.%	ppm	ppm	ppm	ppm	ppm	ppm	ppm	wt.%	µm	g/cm^3
pure Mg	disc	-	-	46	334	130	4	1	14	45	balance	22.6±5.2	1.740
	pin	-	-	161	217	147	14	3	20	20	balance	18.3±9.1	1.742
Mg-10Gd	disc	8.63	-	47	101	55	9	1	2	97	balance	17.8±5.7	1.854
	pin	10.89	-	158	108	66	20	3	31	99	balance	19.9±7.4	1.901
Mg-2Ag	disc	-	1.88	50	82	90	4	1	8	38	balance	43.7±8.5	1.762
	pin	-	1.80	357	86	105	14	2	17	38	balance	25.6±9.0	1.757

4.3.2. Degradation tests

a) In vitro immersion tests

Fig. 38 shows the gas and pH evolution of pure Mg, Mg-10Gd and Mg-2Ag as function of time in PBS, HBSS and DMEM. Pure Mg and Mg-10Gd show similar H_2 evolution curves in PBS and HBSS (Fig. 38a and b), although HBSS is slightly more aggressive than PBS to these two alloys. The pH also shows higher values in HBSS (9-9.5) than in PBS (<8.5) for these two alloys during the entire immersion time, demonstrating that HBSS has a weak buffering power (Fig. 38d-f). However, Mg-2Ag alloys have a higher H_2 evolution slope in PBS than in HBSS (Fig. 38c). The pH in this case is lower in PBS (9-9.5) than in HBSS (10-10.5) (Fig. 38f). Thus, a lower H_2 evolution slope equals to a lower DR and, consequently, a lower pH value is measured.

In DMEM the biodegradation process is slower for these three Mg based materials. There is a first gas increase for the three materials during the first 10h in DMEM reaching a maximum collected gas of 0.3-0.6 ml/cm^2 (Fig. 38a-c). Then, the gas volume decreases during the rest of the immersion time with an approximate rate of 0.1 ml/cm^2/day. With a position control test (without samples) a similar gas evolution is registered, but lower in volume, proving that some gas is CO_2 from the buffering system (Fig. 38a and b). Due to the nature of the biodegradation process of Mg the rest must be H_2. The initial pH of DMEM is 7.4 but during testing the pH increases getting stabilized at values between 7.7 and 7.9. The control position also reveals a pH of 7.6-7.7 which corresponds to the pH range of DMEM in 5 vol.% of CO_2. This indicates an increase of pH smaller than 0.3 between tests with and without Mg samples in DMEM. The fluctuation of the atmospheric pressure can also be a source of errors in the H_2 data recording, but it is considered the smallest error, as shown by Hofstetter et al. [17]. Data in Fig. 37 is shown, in some cases, until the 4th day because the test was finished prematurely in different tests for different reasons: (1) in PBS and HBSS Mg-2Ag exceeded the limit of the gas storage capacity or (2) for pure Mg in PBS a linear behaviour is expected, as it is measured with Mg-10Gd; and (3) in DMEM, the test with pure Mg and Mg-2Ag was stopped due to risk of contamination by microorganisms after the 4th day, even though sterilization measures are equally applied in all the tests. This contamination is detected when the DMEM becomes turbid and the pH starts to decrease.

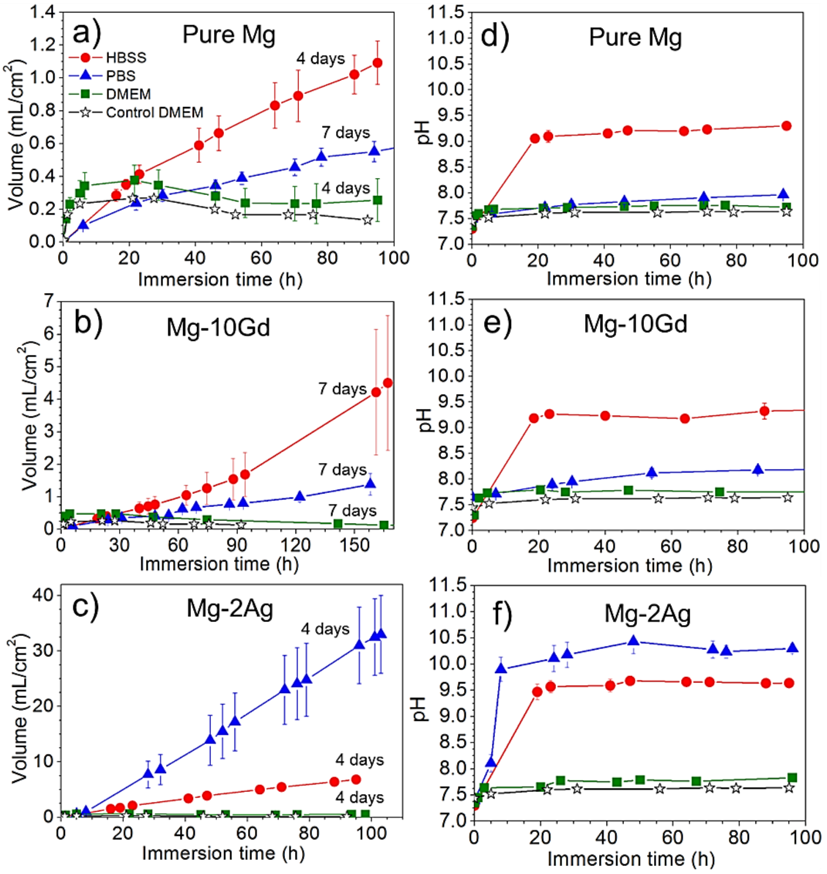

Figure 38: Hydrogen evolution of (a) pure Mg, (b) Mg-10Gd and (c) Mg-2Ag, in PBS, HBSS and DMEM; and pH evolution of (d) pure Mg; (e) Mg-10Gd; (f) Mg-2Ag in the same media for the first 100 h. Six samples were tested in each medium for 4-7 days, and the data shown are the means with indication of the standard deviation. The total duration of each test is indicated next to each H_2 evolution curve.

In PBS and HBSS, severe localized and pitting corrosion can be observed on Mg-2Ag, while pure Mg and Mg-10Gd show generally a homogeneous corrosion mode. A less aggressive degradation process has been observed in DMEM. In this case, the degradation is homogeneous for every Mg-based material.

b) In vitro degradation rate

The DRs are calculated from the ML and the hydrogen generation. The DR results at the end of the immersion in each test are shown in Table 8. ML and

H_2 methods correlate closely. The DRs given by these two methods show systematically higher values for ML than for H_2 evolution. According to ML method pure Mg degrades slower than 1.1 mm/year in every testing condition. Mg-10Gd degrades also at low DR under the three conditions. Finally, the DR of Mg-2Ag decreases from 16.7 mm/year in PBS to 5.4 mm/year in HBSS and 2.2 mm/year in DMEM. Thus, Mg-2Ag shows the highest DR in the three testing conditions compared to pure Mg and Mg-10Gd.

Table 8. DR of pure Mg, Mg-10Gd and Mg-2Ag, in mm/year, calculated from the hydrogen collection and mass loss in PBS, HBSS, DMEM and by pin volume and surface in vivo at the end of each test.

		DR pure Mg [mm/year]	DR Mg-10Gd [mm/year]	DR Mg-2Ag [mm/year]
PBS	Mass loss	0.28±0.07	0.61±0.10	16.7±3.0
PBS	Hydrogen	0.19±0.02	0.40±0.10	15.1±3.0
HBSS	Mass loss	0.72±0.31	1.57±0.62	5.4±0.7
HBSS	Hydrogen	0.57±0.07	1.23±0.56	3.5±0.4
DMEM	Mass loss	1.07±0.10	0.42±0.12	2.2±0.3
DMEM	Hydrogen	0.57±0.07	0.20±0.01	0.68±0.04
In vivo	Pin volume and surface	0.15±0.03	1.11±0.05	0.13±0.04

4.3.3. In vivo degradation rate

The µCT scans in Fig. 39 show the degradation performance after 7 days of implantation of pure Mg, Mg-8 µCT scan images with pure Mg show gas formation in the intramedullary cavity around the implant as well as in the surrounding tissue. 7 days after the operation, the gas is localized only within the intramedullary cavity around the implant. The gas volume, 7 days after the implantation, was calculated to be 3.4 ± 1.93 mm^3 (Fig. 39b). Bone contact is observed since the first day due to the press fit implantation procedure of the pin.

In Mg-10Gd µCT scan images, very small pockets of gas bubbles are observed in the surrounding tissue around the implant 1 day after the implantation. 7 days after the operation, the gas formation is not obvious. The gas volume 7 days after the implantation was calculated to be 0.23 ± 0.32 mm^3 (Fig. 39b). In Mg-10Gd, the bone contact seems to be tight since the first post-operative day, likely due to the press fit implantation of the pin.

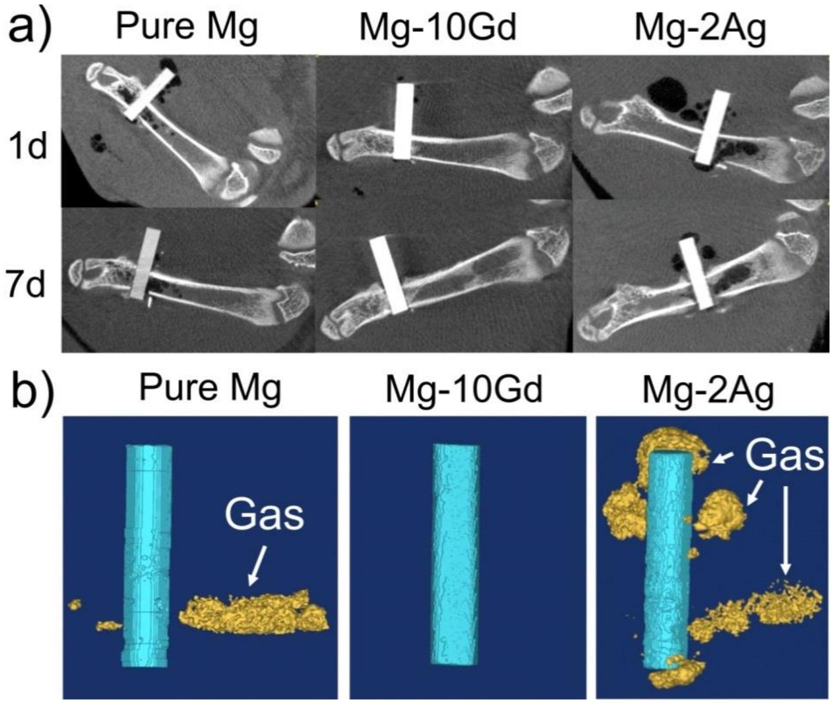

Figure 39: (a) µCT scans of Sprague Dawley rats implanted with pure Mg, Mg-10Gd and Mg-2Ag alloys 1 and 7 days after the operation. The effective pixel size was 35.04 µm. (b) 3D reconstructed images of the different alloys with the surrounding gas release 7 days post-operative.

Mg-2Ag µCT scan images show, 1 day after implantation, a high amount of gas formation within the intramedullary cavity around the implant as well as in the surrounding tissue. 7 days after the operation, the gas bubbles are decreased in the surrounding tissue but they are still present in the intramedullary cavity around the implant. The gas volume 7 days after the implantation was calculated to be 6.52 ± 8.41 mm^3 (Fig. 39b). Tight bone contact is also here observed since the first day.

In vivo DR in mm/year calculated from the pin volume loss and pin surface measured 7 days after implantation are shown in Table 8. Regarding the pure Mg and Mg-2Ag pins, a lower loss of pin volume is calculated which is comparable to the low DR of these materials in DMEM. A high DR of Mg-10Gd pin in vivo as compared to the low DR Mg-10Gd discs in any in vitro immersion test is highlighted.

In all µCT images, no biodegradation is obvious only by visible examination, because the study period is rather short. But with the analysis with Mimics software slight pin volume reductions can be calculated.

However, in vivo micro CT results were used to examine bone growth and degradation behaviour to provide proper information on volume and surface in the ongoing degradation process in the same living animal. Unfortunately, a higher resolution and better contrast between degradation layer and bone is only possible after the explantation of the bone and the use of higher resolution ex vivo scanning protocols.

4.3.4. Degradation layers

a) In vitro

The degradation layers formed on pure Mg in PBS, HBSS and DMEM analysed by elemental mapping are shown in Fig. 40a-c. Mg-10Gd and Mg-2Ag are not shown because pure Mg closely represents the surface layers formed in these three electrolytes for the three materials.

Firstly, in PBS, a layer containing Mg, O, P and C with traces of Na and K can be found (Fig. 40a). Thus, C is also present although PBS does not contain any C source. Secondly, in HBSS, also Mg, O, P, C and traces of Na, K and Ca can be found (Fig. 40b). There is a lower O and a higher C level at the outside of the degradation layer. The P level is also higher at the inner side of the layer formed in HBSS. Finally, in DMEM, the degradation layer contains different elements in two different regions, one rich in Mg, O and C and another one in P and Ca (Fig. 40c). Note that in some cases there is a rim next to the Mg sample or the C containing resin which is an artifact caused by a large interaction volume of the beam.

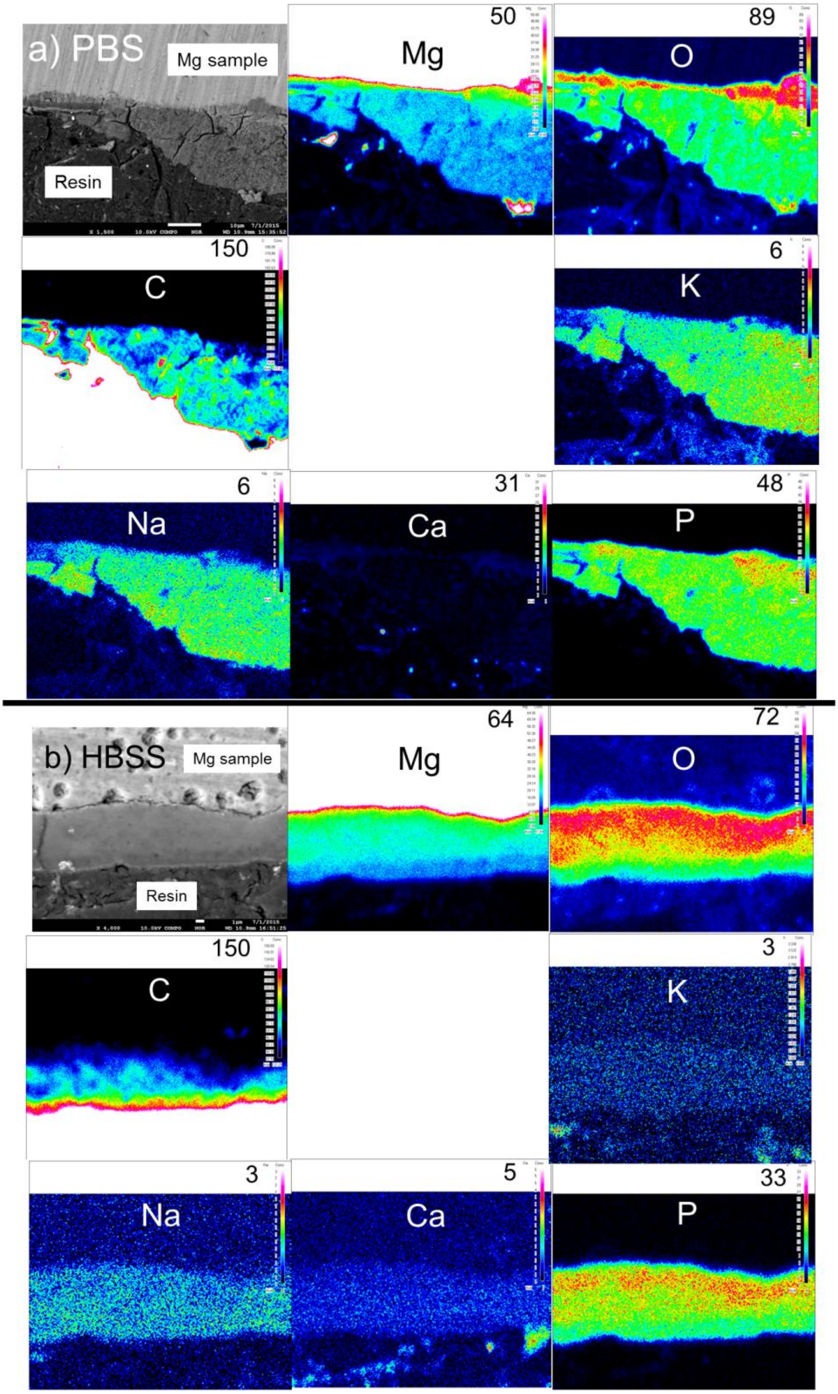

*Figure 40 continues in the next page.

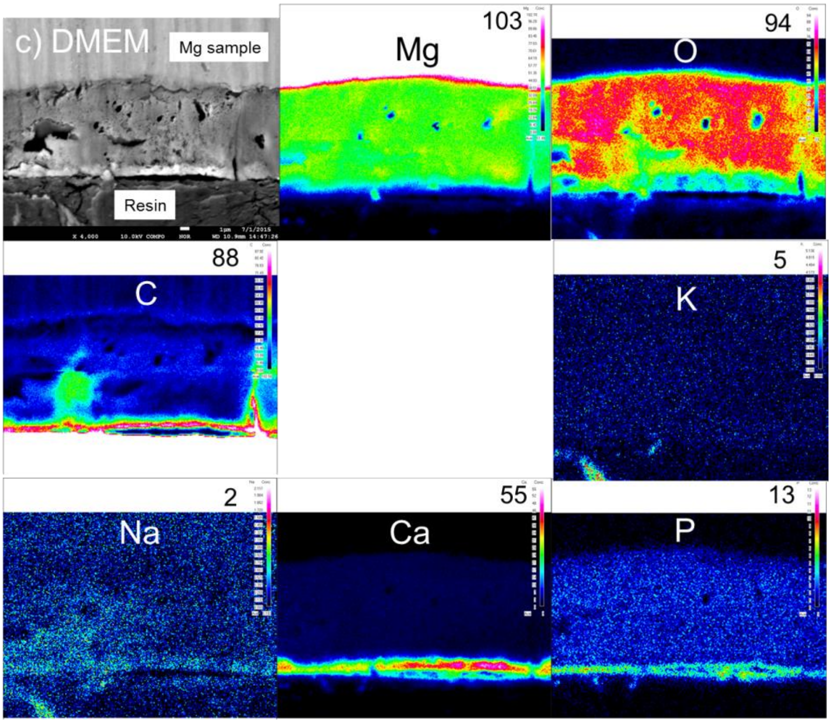

Figure 40: Elemental mapping of the degradation layer formed on pure Mg samples immersed in (a) PBS, (b) HBSS and (c) DMEM for 7 days. The number on top of each picture indicates the maximum intensity on the scale bar. PBS maps were acquired with a resolution of 0.5 x 0.5 µm in approximately 1 h and 15 min, while HBSS and DMEM maps were acquired in 1 hour with a resolution of 0.1 x 0.1 µm.

b) In vivo

The degradation layers formed on pure Mg, Mg-10Gd and Mg-2Ag in vivo are characterised by elemental mapping (Fig. 41). Different layers can be found in vivo with respect to the thickness and the composition depending on location (Fig. 42), and thus, two areas have been characterized for pure Mg and Mg-10Gd. Fig. 41a shows pure Mg in close contact with cortical bone. The elemental mapping indicates a higher Ca and P level in bone than in the degradation layer. Bone also contains traces of Cl. There are sites rich in Mg and O area next to the Mg sample. Na and K are also incorporated in this layer. The C rich area highlights the presence of biological entities.

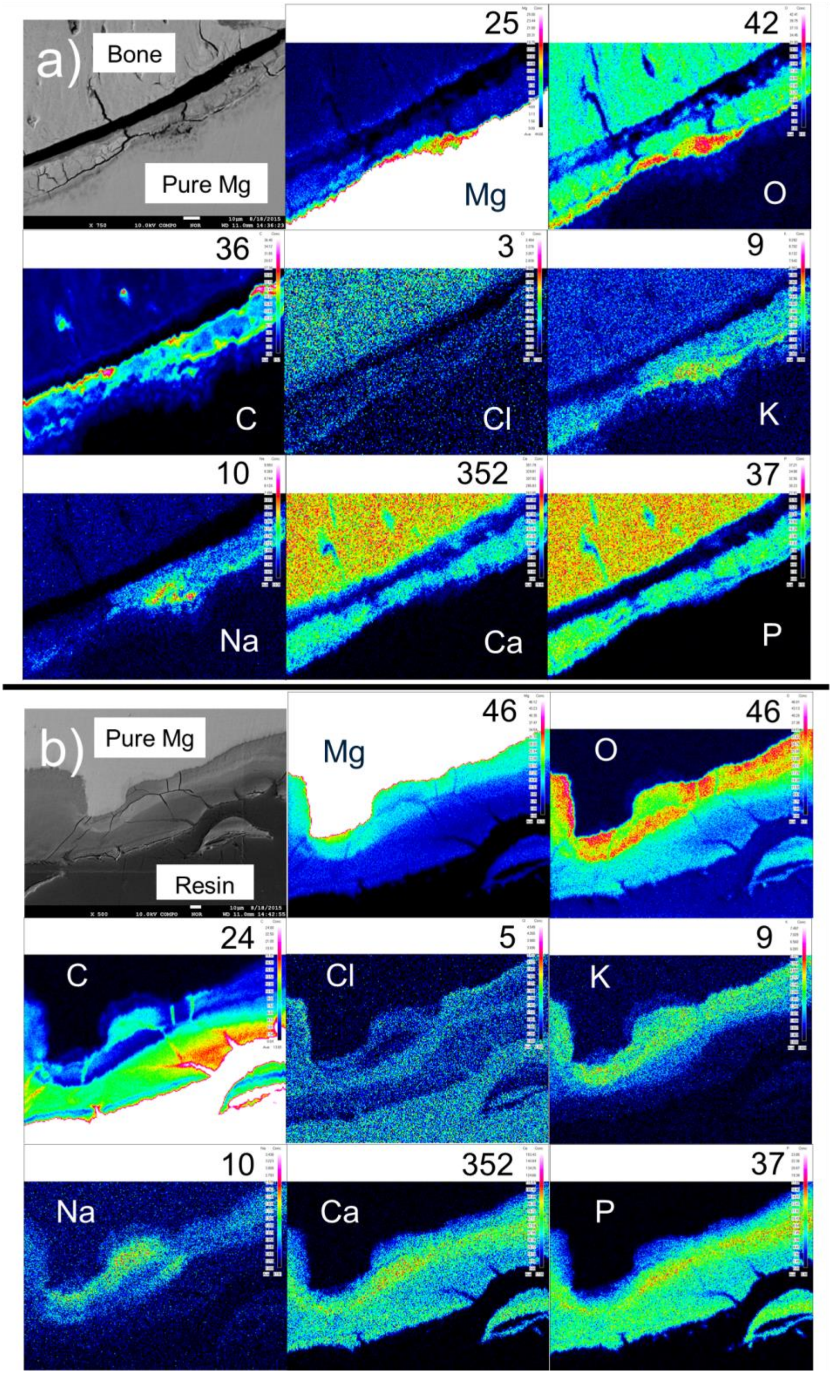

*Figure 41 continues in the next page.

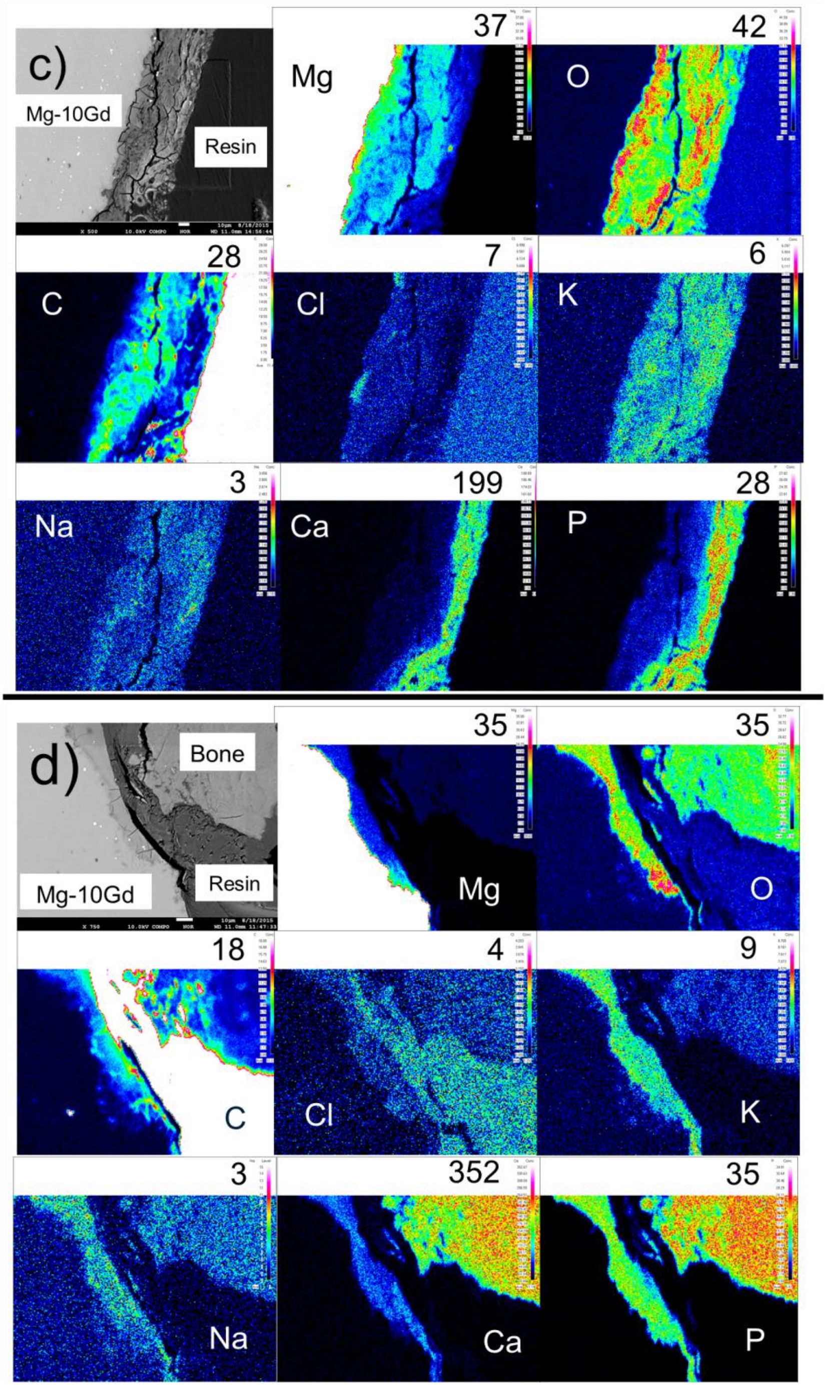

*Figure 41 continues in the next page.

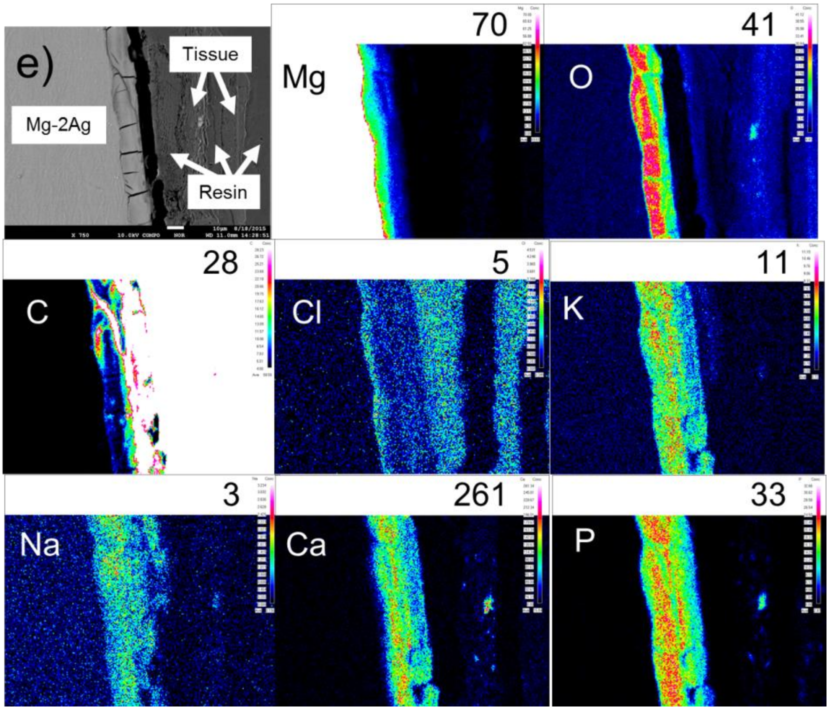

Figure 41: Elemental mapping of the degradation layer formed on implanted pins after 7 days. Different sites on each Mg based material are analysed: (a) Pure Mg in close contact with cortical bone; (b) Pure Mg at the intramedullary cavity; (c) Mg-10Gd at the intramedullary cavity; (d) Mg-10Gd in the vicinity of the cortical bone; and (e) Mg-2Ag at the intramedullary cavity. The elements mapped with different colour contrasts are Mg, O, C, Cl, K, Na, Ca and P. All maps were acquired with a resolution of 0.5 x 0.5 µm in approximately 1 h and 15 min. The scale on the upper-right site of each elemental map is an approximation of the concentration of that element corresponding to the maximum of the scale bar. White scale bars at each SEM image correspond to 10 µm.

Fig. 41b shows a much thicker layer without bone contact. As a result, this region is more exposed to the environment and to the body fluid flow, which causes locally a faster degradation process in this area. This faster degradation process is translated into a thicker surface film where clear differences in elemental content are distinguished. Conversely, Fig. 42c shows an exception to this observation since there is a relatively thick layer on the Mg pin in contact with cortical bone which presumably is related to a higher body fluid flow through this site. On the inner side next to the Mg based material, a higher Mg and O level is found compared to the outer side of this layer. In this area also a higher K, Na and Cl and slightly higher Ca and P content can be detected. At the outer side, a higher C content is detected which can indicate the presence of carbonate products. It is noteworthy that the resin applied for the sample preparation contains Cl and it can be confused with the Cl level at the degradation layer, especially in such a low concentration.

Fig. 41c and d depict the elemental mapping of the degradation layer formed on Mg-10Gd in vivo. Fig. 41c shows a region of the implant without bone contact. This area contains Mg, O, C, K, Ca and P homogeneously distributed and traces of Na and Cl. Ca and P are more intensely detected at the outer side of the rim which can be commonly found along the surface layer. This Ca and P containing sites are also observed (Fig. 41b). Fig. 41d shows a region of the implant in the vicinity of the original femoral bone. Mainly Mg, O, C, Ca and P are found together with K and traces of Na and Cl. This layer on Mg-10Gd has no significant differences with the one observed on pure Mg in Fig. 43a and b. Moreover, similarly as seen in Fig. 41a and b a difference in Ca and P between bone and degradation layer is highlighted with, perhaps, a small change in the Cl content.

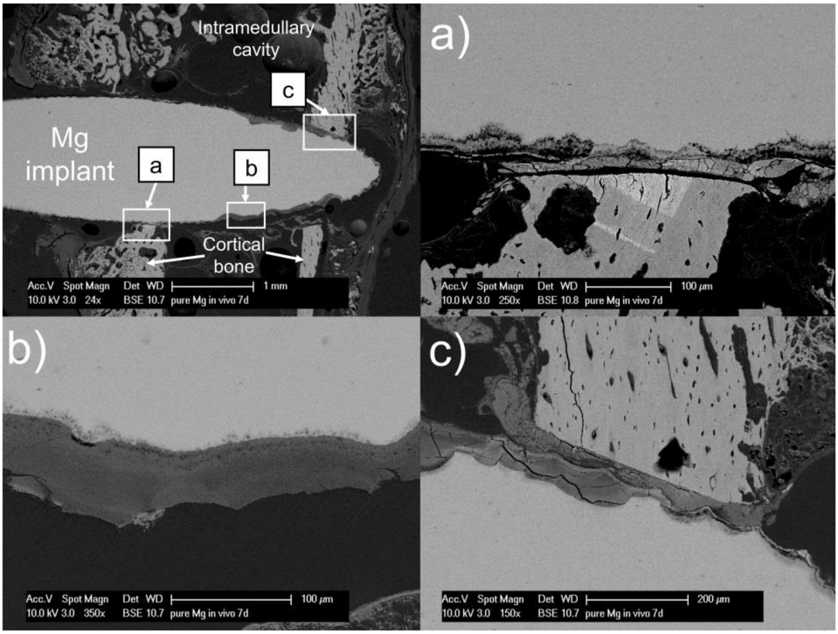

Figure 42: SEM images of pure Mg implanted for 7 days show differences in degradation layer depending on the bone contact and the local environment around the implant. (a) Depicts a slow degrading site characterized by a thin degradation layer deposition at an implant-bone contact site. (b) Displays a thick degradation layer in the intramedullary cavity indicating a faster

corrosion process. (c) Shows the degradation layer at an implant-bone contact site, where a thicker layer related to a faster degradation process is observed. This is an exception to the observations from Fig. 42a.

Finally, the elemental analysis of the degradation layer formed on Mg-2Ag at the medullary cavity is shown in Fig. 41e. On the one hand, the Mg and O content is homogeneously distributed being higher in the inner part of the layer compared to the outer side. On the other hand, the C content varies substantially in different areas. The Cl content can indicate the presence of the resin. The observed concentration variations can be explained by the presence of tissue, since no bone is visible. The Cl content might be also slightly higher at the inner side of the degradation layer next to the Mg-2Ag implant, although the Cl concentration detected is rather low.

As shown in Fig. 42, the degradation layer thickness can vary depending on the local environment where the sample is degrading. After 7 days of implantation, the thickness of the surface layer developed at the intramedullary cavity is approximately 0.67 ± 0.20 μm (Fig. 42b) and at the outer part of the cortical femoral bone is approximately 0.16 ± 0.03 μm (Fig. 42a). There are also differences at different implant-bone contact sites. Fig. 42a and c show two different sites where bone is in contact with the degradation layer. The degradation layer at the inner side of the cortical bone shown in Fig. 42c has a thickness of approximately 0.41 μm.

4.3.5. Initial surface

As shown in Fig. 43, the surface of the studied discs and pins have been analyzed in order to determine the status of the surface before the immersion and in vivo tests, respectively. As mentioned above, discs have been ground and polished before in vitro immersion tests. The contact with air and moisture can generate a thin oxide film which has been quantified by EDX in Fig. 43a. The O/Mg ratio can indicate the thickness of the oxide film. On the one hand, this O/Mg ratio for as-polished samples is lower than 0.1, and on the other hand, pins which have been delivered, sterilized and stored for 1 to 2 years, show a O/Mg ratio between 0.4 and 0.55. These oxides are also shown in Fig. 43b and can be identified as the grey areas on the pin surface. The image from Fig. 43b closely represents the surface finish of the Mg pins implanted. In literature it has been recently proven that storage can have an influence on the degradation behaviour of Mg based materials; thus, while storing the material, a natural ageing process has been observed as well as an increase in oxygen-enriched regions on the implant surface [39]. Thus, the pins are more oxidized compared to freshly ground discs applied in this study.

However, the thickness of this oxide layer is noticeably smaller than the degradation layer, due to the energy applied at the SEM (20 kV) and since Mg can still be detected through the greyish layer (see brighter areas within the grey areas in Fig. 43b). Thus the thickness of the oxide layer is considered to be at least lower than 1 μm, while the degradation layer will be in any case thicker than 10 μm. Thus the influence of this oxide layer is considered as moderate.

Furthermore, as depicted in Fig.43c and d particles of impurities are also observable on the pin surface. The EDX spectrum from Fig. 43c shows clear Fe, Cr and Ni peaks, indicating that these particles come presumably from a stainlesss steel tool used for the extrusion or the machining. Fig. 43d shows another particle containing Cu and Zn which might come from the starting material or from contamination during casting, i.e. previous castings on the same permanent mould. Thus, the surface preparation (or the lack of it) might have an influence on the in vivo behaviour.

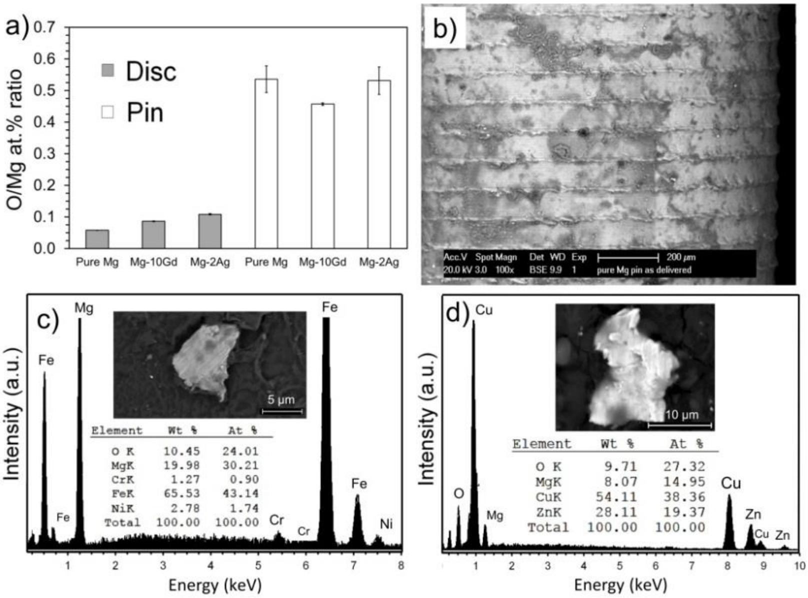

Element	Wt %	At %
O K	10.45	24.01
MgK	19.98	30.21
CrK	1.27	0.90
FeK	65.53	43.14
NiK	2.78	1.74
Total	100.00	100.00

Element	Wt %	At %
O K	9.71	27.32
MgK	8.07	14.95
CuK	54.11	38.36
ZnK	28.11	19.37
Total	100.00	100.00

Figure 43: Surface characterization of the studied pins and discs as tested. (a) Discs show a lower oxidation level by EDX analysis compared to pins which do not get any surface preparation. (b) shows the surface morphology in low magnification as an overview of the pin surface. The horizontal lines are machining marks due to turning. (c) and (d) show two particles of impurities and their respective EDX point analysis. These particles come from the processing and the starting material.

4.4. Discussion

4.4.1. Degradation layer

In PBS the degradation layer is mainly formed by $Mg(OH)_2$ and Mg-PO_4 mixed in a non-distinguishable manner due to a co-formation process (Fig. 39a). When the concentration of certain elements reaches the solubility limit, different compounds form the degradation layer. Moreover, in PBS, potassium phosphate can also nucleate on the surface and grow in a crystalline structure, as observed by Trinidad et al. [6]. This phenomenon is explained by the high amount of phosphate ions present in PBS. It is possible that the C detected is an artefact from the sample preparation presumably due to a smearing effect of the resin. The degradation layer in PBS is generally non-uniform, with a changing thickness. In HBSS, the degradation layer is similar, with $Mg(OH)_2$ and Mg-PO_4 but also a small amount of Mg-CO_3 (Fig. 39b). In contrast to products formed in PBS, no potassium phosphate crystals are found due to the low amount of PO_4^{3-} in solution. Finally, as demonstrated in Fig. 39c, the degradation layer in DMEM is composed of two layers. As reported the previous work [40], the first one next to the alloy surface contains $Mg(OH)_2$ and (Mg,Ca)-CO_3. The second layer, on top of the first one, is a thin (Mg,Ca)-PO_4 layer which is observed in Fig. 40c.

The degradation layer formed in vivo is comparable to the one observed in DMEM testing. The detection of Mg and O indicate the presence of $Mg(OH)_2$; C indicates (Mg,Ca)-CO_3; and Ca and P indicate Ca-PO_4 corrosion products. Supporting this, Yang et al. and Zong et al., reported $Ca_3Mg_3(PO_4)_4$ at the surface layer formed in Hanks solution by XRD [31, 41]. Hence, Ca-P layers might also include Mg in its structure, so that Ca-P can be defined as (Mg,Ca)-PO_4. The structure of this compound could be amorphous, and further studies could give light on this matter. It is also possible to detect Na and K with a low intensity which indicates that these two elements can also form phosphates or carbonates. The distribution of Na and K is homogeneous meaning that these elements are distributed along the degradation layer by a co-formation process. Similarly, as observed in DMEM (Fig. 39c), in animal experiments also Ca and P rich layers can be formed separately from $Mg(OH)_2$ and (Mg,Ca)-CO_3 (Fig. 41). Hence, this finding indicates the importance of the presence of Ca^{2+} and PO_4^{3-} ions in the electrolyte in order to allow calcium phosphate formation which leads to a degradation layer in DMEM comparable to the one formed in vivo (Fig. 39c and 41). Some authors already reported the presence of these layers on Mg based materials tested in HBSS [31, 41, 42], in DMEM [38], in blood [16], in SBF [43] and in animal experiments [44, 45]. Agha et al., recently showed the influence of different inorganic salts like Ca^{2+}, SO_4^{2-}, and HCO_3^{-}, present in cell culture media on the Mg degradation process and the degradation layer formation (Ca-P and Mg-CO_3 products) [37]. This demonstrates that DMEM is a testing medium closer to a more realistic situation, when sterilization is assured, in comparison to PBS and HBSS without Ca^{2+} also used in this study.

Along the surface layer formed in vivo, differences in thickness and composition can be found. Thus, it is difficult to identify one representative area of the whole degradation layer. These differences are caused by the environment in which the implant surface finds itself. Many influencing factors can be enumerated such as: bone contact and bone growth; fluid flow and its composition; and biological content (e.g. osteoclasts and osteoblasts).

It is also noteworthy that bone has higher Ca and P levels than the degradation layer, which can help to distinguish them (Fig. 41a and d). Thus, these Ca-P containing corrosion products have a different composition in comparison to hydroxyapatite which is only composed of Ca, P and O (and traces of Cl) while the degradation layer also contains hydroxides and carbonates.

4.4.2. Degradation rate analysis

a) In vitro

In vitro and in vivo degradation behaviour of pure Mg, Mg-10Gd and Mg-2Ag, all in disc and pin shape, are compared during the first 7 days. Mg-2Ag discs show the highest DR in the three in vitro testing conditions compared to pure Mg and Mg-10Gd. This could be explained by the presence of 1.88 wt.% of Ag, a larger grain size (43.7 µm) and high amount of Cl^- in PBS and HBSS. Ag is considered as an impurity which accelerates the Mg degradation process [18] by dissolving Mg around Ag-rich particles and releasing these particles. A higher Cl^- content in the electrolyte (e.g. in PBS and HBSS) will promote $Mg(OH)_2$ dissolution [46], exposing Mg and Ag and accelerating the degradation process even further. Therefore, the behaviour of Mg-2Ag in DMEM proves that closer to physiological testing in vitro leads to a less aggressive degradation process. Results from Mg-2Ag also indicate that a larger grain size also decreases the corrosion resistance of the Mg alloy [47].

In contrast, pure Mg and Mg-10Gd in disc shape show a stable and slow degradation compared to Mg-2Ag (Fig. 38 and Table 8). These two alloys have a smaller grain size (<22.3 µm) and a higher amount of Mn. According to literature, Mn forms intermetallics with Fe which are less favorable to promote galvanic dissolution, thus, Mn increases the Fe tolerance limit [48, 49]. Hence, Mn can reduce the negative influence of Fe on the corrosion behaviour explaining the slower degradation behaviour of pure Mg and Mg-10Gd discs in vitro. The surface preparation of discs facilitates the data interpretation since the impurities and oxidation at the sample surface influencing parameter can be suppressed from the analysis. However, in a real application this preparation might not be possible.

There is a systematic difference between DRs calculated in vitro by gravimetry and by H_2 generation (Table 8). The H_2 evolution gives lower DR compared to the ML method. This difference can be explained by the particle undermining model [50], and perhaps the dissolution of hydrogen in the Mg sample [25, 51, 52].

In order to stabilize the pH within the physiological range (between 7 and 8), using DMEM buffered with CO_2 and HCO_3^- and applying UV-C radiation for sterilization seems appropriate. Moreover, it mimics the natural human blood buffering system. This allows the presence of HCO_3^- which is another important ion in the electrolyte which promotes (Mg,Ca)-CO_3 formation at the surface layer. The stirring produces a dynamic flow making the sample and funnel an ‘open’ system avoiding a local pH increase inside the funnel which falsifies the in vitro data, as other authors reported [17, 32].

In summary, the PBS and HBSS with Ca^{2+} do not represent the degradation behaviour of Mg alloys in vivo because of the lack of relevant ions. This is indicated by the fast degradation of Mg-2Ag in PBS and HBSS while its behaviour under near physiological conditions with DMEM and in animal experiments is rather stable.

b) In vivo

In degradation tests in vivo, the Mg-10Gd alloy processed as a pin has the highest DR in comparison to pure Mg and Mg-2Ag (Table 8). However, the amount of gas pockets detected with Mg-10Gd is much lower than with pure Mg and Mg-2Ag (Fig. 39). Many mechanisms can explain the lack of gas bubbles at the first stage of the degradation process of Mg implants. (i) Gas might not be trapped around the implant at this early healing stage. (ii) As Kuhlmann et al. reported H_2 can be exchanged very quickly after implantation through tissue and skin [53]. (iii) It is known that Mg metal can store significant amounts of hydrogen [54]. Many authors use the dissolution of hydrogen in the Mg sample to explain the difference between the DRs calculated by hydrogen evolution and by ML [25, 51, 52]. (iv) Mg-RE alloys, e.g. Mg-10Gd, can form hydrides in cuboid shape absorbing hydrogen from the environment [40, 55, 56]. (v) In addition, hydrogen also might be incorporated in the degradation layer forming phosphate containing degradation products such as (Mg,Ca)-HPO_4 and (Mg,Ca)-$(H_2PO_4)_2$. Only the mechanism (iv) can explain the lack of gas cavities around implanted Mg-10Gd pins. Perhaps mechanism (i) could also explain it although the same procedure was applied during all the implantations.

If we compare the DRs of in vitro with those in vivo, we can observe that Mg-10Gd pins in vivo show the highest DR while Mg-10Gd discs in vitro have the lowest DR, together with pure Mg (Table 8). This could be due to the high amount of Ni and Fe detected in Mg-10Gd pins of 20 and 158 ppm, respectively. In this case, the higher amount of Ni and Fe contained in this alloy in pin shape indicates that the tolerance limits for these elements are exceeded, as Ni and Fe have the lowest tolerance limits [57]. These impurities could originate from the initial material, or be added to the Mg alloy by contact with steel tools which can contain Fe, Ni and Cr as shown by the particle found on the surface in Fig. 43c. Thus, the processing route can have a large impact on the degradation performance of the Mg alloy. Moreover, these results indicate that the higher amount of Gd in pin shape compared to discs does not seem to play an important role in reducing the negative influence of impurities.

Interestingly, Mg-2Ag discs also show in vitro the opposite behaviour of Mg-2Ag pins in vivo (Table 8). The larger grain size of discs (43.7 µm) versus pins (25.7 µm) does also seem to increase the degradation process. However, in contrast with what is known, the higher amount of Fe content in Mg-2Ag pins (357 ppm) compared to discs (50 ppm) does not seem to increase the DR. There is a slower fluid flow restricted by bone, and therefore, lower amount of Cl ions in contact with the Mg-2Ag pins in vivo which would accelerate the degradation process by the influence of Ag and Cl. In contrast, a large V/S ratio applied in vitro can explain the faster degradation of Mg-2Ag discs. In literature it is recommended to use a clinically relevant V/S ratio [30, 31]. These degradation results from DMEM immersion in vitro tests and in vivo experiments (Table 8) are, especially in the case of Mg-2Ag, in accordance with a previous study where Mg-2Ag showed the highest DR in in vitro conditions in DMEM with 10 vol.% of fetal bovine serum (FBS) [58].

In general, these materials behave in a different way under in vivo conditions as compared to in vitro. Firstly, this could be explained by the higher amount of impurities of Fe, Ni and Cu detected in the studied Mg pins as compared to discs. Mg-2Ag pins, for instance, have the highest Fe content, which is due to a different processing with several extrusion steps more than pure Mg and Mg-10Gd pins. Moreover, the in vivo and in vitro tests apply different conditions, and many factors such as ion concentration, pH level or blood flow as well as protein and different kind of cells can affect the DR of the materials [1, 4, 11, 25, 59-63]. Gas pockets are observed in previous studies showing that bone can completely heal even if the resorption is rapid and bubbles are large in vivo [35]. In addition, the lack of surface preparation of the pins before implantation might have an influence since the oxide film can slow down the degradation process while the impurities might accelerate it. Although, the influence of the oxide layer is considered as moderate, when using pins that were not polished or ground it increase the complexity of data interpretation.

4.5. Conclusions

In vitro and in vivo degradation behaviour of several alloys is compared after 7 days. The degradation layer has been characterized in order to compare results from lab and animal studies. The results attest to the following:

1. The physiological testing setup applied here, with DMEM as electrolyte, can not only maintain a physiological pH level, but also create a similar degradation layer to that in vivo on several Mg alloys providing comparable DRs. These rates, especially for Mg-2Ag are lower in DMEM and in vivo than in PBS and HBSS. This indicates that in vivo as well as in vitro under near physiological conditions are less aggressive testing conditions. The lower Cl^- ion concentration and the presence of Ca^{2+}, PO_4^{3} and HCO_3^- ions highly influence the degradation process of the studied Mg alloys and its consequent degradation layer formation. Hence, PBS and HBSS do not closely represent the degradation behaviour in vivo, because the degradation layer differs from what it is found in vivo.
2. The same Mg alloy from another manufacturing process leads to a different impurity content and microstructure, which seem to drive the degradation performance downplaying the role of alloying additions such as Gd and Ag. The importance of impurity and grain size control during the processing is thereby highlighted. The control of elements such as Fe and Ni which have a low tolerance limit must be reduced but others, e.g. Mn, can be desirable when the purity is low.
3. The initial surface can contain impurity particles as a result of the production process and a surface preparation is found recommendable in any Mg degradation study in order to facilitate data interpretation.
4. The elemental mapping revealed that hydroxyapatite in bone has higher Ca and P levels than the Ca-P rich degradation layer formed in vivo. Thus, these structures are different calcium orthophosphate structures and help to distinguish bone from the degradation layer formed on the implant surface by elemental mapping.

References

[1] F. Witte, J. Fischer, J. Nellesen, H.A. Crostack, V. Kaese, A. Pisch, F. Beckmann, H. Windhagen, Biomaterials 27 (2006) 1013-1018.
[2] Y. Li, C. Wen, D. Mushahary, R. Sravanthi, N. Harishankar, G. Pande, P. Hodgson, Acta Biomater. 8 (2012) 3177-3188.
[3] H. Li, Y. Zheng, L. Qin, Progress in Natural Science: Materials International 24 (2014) 414-422.
[4] A.H. Martinez-Sanchez, B.J.C. Luthringer, F. Feyerabend, R. Willumeit, Acta Biomater. 13 (2015) 16-31.
[5] L.-N. Zhang, Z.-T. Hou, X. Ye, Z.-B. Xu, X.-L. Bai, P. Shang, Frontiers of Materials Science 7 (2013) 227-236.
[6] J. Trinidad, G. Arruebarrena, I. Marco, I. Hurtado, E. Saenz de Argandona, Proc Inst Mech Eng H 227 (2013) 1301-1311.
[7] C. Schille, M. Braun, H.P. Wendel, L. Scheideler, N. Hort, H.P. Reichel, E. Schweizer, J. Geis-Gerstorfer, Mater. Sci. Eng.: B 176 (2011) 1797-1801.
[8] M. Alvarez-Lopez, M.D. Pereda, J.A. del Valle, M. Fernandez-Lorenzo, M.C. Garcia-Alonso, O.A. Ruano, M.L. Escudero, Acta Biomater. 6 (2010) 1763-1771.
[9] H. Wang, Y. Estrin, Z. Zúberová, Mater. Lett. 62 (2008) 2476-2479.
[10] N.I. Zainal Abidin, D. Martin, A. Atrens, Corros. Sci. 53 (2011) 862-872.
[11] L. Yang, N. Hort, R. Willumeit, F. Feyerabend, Corros. Eng. Sci. Techn. 47 (2012) 335-339.
[12] D. Tie, F. Feyerabend, W.-D. Mueller, R. Schade, K. Liefeith, K.U. Kainer, R. Willumeit, European Cells and Materials 25 (2013) 284-298.
[13] D. Tie, F. Feyerabend, N. Hort, R. Willumeit, D. Hoeche, Adv. Eng. Mater. 12 (2010) 699-704.
[14] F. Feyerabend, H. Druecker, D. Laipple, C. Vogt, M. Stekker, N. Hort, R. Willumeit, J. Mater. Sci. - Mater. Med. 23 (2012) 9-24.
[15] S.N. Dezfuli, Z. Huan, J.M.C. Mol, M.A. Leeflang, J. Chang, J. Zhou, Progress in Natural Science: Materials International 24 (2014) 531-538.
[16] F. Feyerabend, H.-P. Wendel, B. Mihailova, S. Heidrich, N.A. Agha, U. Bismayer, R. Willumeit-Römer, Acta Biomater. 25 (2015) 384-394.
[17] J. Hofstetter, E. Martinelli, A.M. Weinberg, M. Becker, B. Mingler, P.J. Uggowitzer, J.F. Löffler, Corros. Sci. 91 (2015) 29-36.
[18] H.E. Friedrich, B.L. Mordike, Magnesium technology, Springer-Verlag Berlin Heidelberg, 2006.
[19] D.A. Robinson, R.W. Griffith, D. Shechtman, R.B. Evans, M.G. Conzemius, Acta Biomater. 6 (2010) 1869-1877.
[20] L. Zhu, P. Wan, J. Duan, L. Tan, K. Yang, Progress in Natural Science: Materials International 24 (2014) 441-445.
[21] W.E. Mercer, J.E. Hillis, Society of Automotive Engineers, Detroit, MI (1992).
[22] N. Hort, Y. Huang, D. Fechner, M. Stoermer, C. Blawert, F. Witte, C. Vogt, H. Druecker, R. Willumeit, K.U. Kainer, F. Feyerabend, Acta Biomater. 6 (2010) 1714-1725.
[23] J. Kubasek, D. Vojtech, Trans. Nonferrous Met. Soc. China 23 (2013) 1215-1225.

[24] S. Galli, J.U. Hammel, J. Herzen, G. Szakács, F. Lukáč, M. Vlček, I. Marco, A. Wennerberg, R. Willumeit-Römer, R. Jimbo, Eur. Cell Mater. 30 (2015) 93.
[25] N.I. Zainal Abidin, B. Rolfe, H. Owen, J. Malisano, D. Martin, J. Hofstetter, P.J. Uggowitzer, A. Atrens, Corros. Sci. 75 (2013) 354-366.
[26] M. Schinhammer, J. Hofstetter, C. Wegmann, F. Moszner, J.F. Loeffler, P.J. Uggowitzer, Adv. Eng. Mater. 15 (2013) 434-441.
[27] J.A. Ryan, General guide for identifying and correcting common cell culture growth and attachment problems, Corning, Inc. Technical Bulletin, 2008.
[28] K. Deva, e. al., International Journal of Animal Biotechnology 1 (2011) 8-12.
[29] M.T. Madigan, Brock biology of microorganisms, Benjamin Cummings, San Francisco, 2012.
[30] Z. Zhen, T.-f. Xi, Y.-f. Zheng, Trans. Nonferrous Met. Soc. China 23 (2013) 2283-2293.
[31] L. Yang, E. Zhang, Materials Science and Engineering C-Biomimetic and Supramolecular Systems 29 (2009) 1691-1696.
[32] N.T. Kirkland, N. Birbilis, M.P. Staiger, Acta Biomater. 8 (2012) 925-936.
[33] ASTM-G31-72, Standard Practice for Laboratory Immersion Corrosion Testing of Metals, Philadelphia, Pennsylvania, USA, 2004.
[34] Grischuk, 11 (1957) 136.
[35] T. Kraus, S.F. Fischerauer, A.C. Hänzi, P.J. Uggowitzer, J.F. Löffler, A.M. Weinberg, Acta Biomater. 8 (2012) 1230-1238.
[36] S.F. Fischerauer, T. Kraus, X. Wu, S. Tangl, E. Sorantin, A.C. Hänzi, J.F. Löffler, P.J. Uggowitzer, A.M. Weinberg, Acta Biomater. 9 (2013) 5411-5420.
[37] N.A. Agha, F. Feyerabend, B. Mihailova, S. Heidrich, U. Bismayer, R. Willumeit-Römer, Mater. Sci. Eng.: C 58 (2016) 817-825.
[38] R. Willumeit, J. Fischer, F. Feyerabend, N. Hort, U. Bismayer, S. Heidrich, B. Mihailova, Acta Biomater. 7 (2011) 2704-2715.
[39] K. Bracht, N. Angrisani, J.M. Seitz, R. Eifler, A. Weizbauer, J. Reifenrath, Biomed Eng Online 14 (2015) 92.
[40] I. Marco, F. Feyerabend, R. Willumeit-Römer, O. Van der Biest, Mater. Sci. Eng.: C 62 (2016) 68-78.
[41] Y. Zong, G. Yuan, X. Zhang, L. Mao, J. Niu, W. Ding, Mater. Sci. Eng.: B 177 (2012) 395-401.
[42] H. Kuwahara, Y. Al-Abdullat, N. Mazaki, S. Tsutsumi, T. Aizawa, Mater. Trans.(Japan) 42 (2001) 1317-1321.
[43] S. Zhang, J. Li, Y. Song, C. Zhao, X. Zhang, C. Xie, Y. Zhang, H. Tao, Y. He, Y. Jiang, Y. Bian, Mater. Sci. Eng.: C 29 (2009) 1907-1912.
[44] L. Xu, G. Yu, E. Zhang, F. Pan, K. Yang, J. Biomed. Mater. Res. Part A 83A (2007) 703-711.
[45] Z. Li, X. Gu, S. Lou, Y. Zheng, Biomaterials 29 (2008) 1329-1344.
[46] W.-D. Mueller, M. Fernandez Lorenzo de Mele, M.L. Nascimento, M. Zeddies, J. Biomed. Mater. Res. Part A 90A (2009) 487-495.
[47] Y. Liu, D. Liu, C. You, M. Chen, Front. Mater. Sci. 9 (2015) 247-253.

[48] K.N. Reichek, K.J. Clark, J.E. Hillis, SAE transactions 94 (1985) 318-329.

[49] J.-Y. Lee, G. Han, Y.-C. Kim, J.-Y. Byun, J.-i. Jang, H.-K. Seok, S.-J. Yang, Metals and Materials Int. 15 (2009) 955-961.

[50] G.L. Song, A. Atrens, Adv. Eng. Mater. 1 (1999) 11-33.

[51] S. Remennik, I. Bartsch, E. Willbold, F. Witte, D. Shechtman, Mater. Sci. Eng.: B 176 (2011) 1653-1659.

[52] A. Atrens, G.-L. Song, M. Liu, Z. Shi, F. Cao, M.S. Dargusch, Adv. Eng. Mater. 17 (2015) 400-453.

[53] J. Kuhlmann, I. Bartsch, E. Willbold, S. Schuchardt, O. Holz, N. Hort, D. Höche, W.R. Heineman, F. Witte, Acta Biomater. 9 (2013) 8714-8721.

[54] K. Nogita, S. Ockert, J. Pierce, M.C. Greaves, C.M. Gourlay, A.K. Dahle, International Journal of Hydrogen Energy 34 (2009) 7686-7691.

[55] Q. Peng, Y. Huang, J. Meng, Y. Li, K.U. Kainer, Intermetallics 19 (2011) 382-389.

[56] W. Gan, Y. Huang, L. Yang, K.U. Kainer, M. Jiang, H.-G. Brokmeier, N. Hort, Journal of Applied Crystallography 45 (2012) 17-21.

[57] J. Hanawalt, C. Nelson, J. Peloubet, American Institute of Mining and Metallurgical Engineers (AIME) 147 (1942) 273.

[58] A. Myrissa, N.A. Agha, Y. Lu, E. Martinelli, J. Eichler, G. Szakács, C. Kleinhans, R. Willumeit-Römer, U. Schäfer, A.-M. Weinberg, Mater. Sci. Eng.: C 61 (2016) 865-874.

[59] W.D. Müller, M.L. Nascimento, M. Zeddies, M. Córsico, L.M. Gassa, M.A.F.L.d. Mele, Materials Research 10 (2007) 5-10.

[60] J. Walker, S. Shadanbaz, N.T. Kirkland, E. Stace, T. Woodfield, M.P. Staiger, G.J. Dias, J. Biomed. Mater. Res. Part B 100 (2012) 1134-1141.

[61] D. Xue, Y. Yun, Z. Tan, Z. Dong, M.J. Schulz, JOM Science & Technology 28 (2012) 261-267.

[62] G.E.J. Poinern, S. Brundavanam, D. Fawcett, Amer. J. Biomed. Eng. 2 (2012) 218-240.

[63] S. Shadanbaz, J. Walker, T.B. Woodfield, M.P. Staiger, G.J. Dias, J. Mater. Sci. Mater. Med. 25 (2014) 173-183.

Chapter 5:

Degradation testing of Mg alloys in Dulbecco’s modified eagle medium: influence of medium sterilization

Adapted from:

I. Marco, F. Feyerabend, R. Willumeit-Römer, O. van der Biest, Degradation testing of Mg alloys in Dulbecco's modified eagle medium: influence of medium sterilization. Mater. Sci. Eng.: C. 62 (2016) 68-78.

5.1. Introduction

In order to reproduce more closely an in vivo situation cell culture media, such as DMEM, could be an appropriate medium since it mimics body plasma and whole blood to some extent. Thus, in this chapter, DMEM is applied as the electrolyte for immersion experiments where 5 vol.% of CO_2 is added to air as a buffering system in a closed glove box. This atmosphere is commonly applied in incubators where cell-material interaction research is carried out. According to ISO 10993, sterility during evaluation of medical devices should be maintained during testing under cell culture conditions. However, DMEM contains sources of energy, such as glucose, vitamins and amino acids, thus, the electrolyte can support the growth of any contaminating microorganism [1, 2]. Because of this risk, experiments can only be performed for a limited time and in case of medium contamination it will be shown that the degradation behaviour of the Mg samples can be altered.

Hence, in this chapter, the influence of microorganisms proliferating in DMEM on Mg degradation is analysed by comparing different Mg alloys and pure Mg. Similarly as in chapter 4, silver (Ag) and gadolinium (Gd) have been selected as alloying elements in order to analyse fast and slow degrading Mg alloys.

5.2. Materials and methods

5.2.1. Material production

The starting materials utilized in this study for the Mg alloy production are: magnesium (99.99 %, Xinxiang Jiuli Magnesium co. Ltd, China), yttrium (99.95%, Grirem Adv. Mater. Co. Ltd., China), gadolinium (99.95%, Grirem Adv. Mater. Co. Ltd., China), a rare earth mixture (Grirem Adv. Mater. Co. Ltd., China) and silver (99.99%, ESG Edelmetall-Handel GmbH & Co. KG, Germany). Firstly, ingots were cast in a permanent mould at 680-720˚C in neutral atmosphere (Ar + SF_6) and heat treated for 6h at 420-430°C for Mg-Ag alloys and at 500-550°C for Mg-RE containing alloys. Pure Mg did not get a heat treatment because the purpose of this treatment was to homogenise the alloying elements in the ingot, and obviously, pure Mg lacks in alloying additions. Then samples were extruded at 370-440˚C from 30 mm diameter to 12 mm with a speed of 2.5-4.5 mm/s, except pure Mg and Mg-4Ag which was reduced in diameter from 110 mm to 12 mm at 300°C at 0.7 mm/s and 2.5 mm/s respectively. Finally specimens were machined into discs with 10 mm diameter and 1.5 mm thickness, each disc having approximately 180 mg mass. This processing was selected in order to obtain a fine and homogeneous grain size and microstructure. The summary of the production parameters can be found later in Table 12 (Section 6.2.1, page 156).

Table 9 summarizes the chemical compositions of the studied alloys as well as their grain size and density. The chemical composition of the alloys is determined by inductively coupled plasma optical emission spectroscopy (ICP-OES, Varian 720 ES) and the density by the Archimedes method immersing the samples in ethanol. The grain size is determined by optical microscopy and the linear intercept method.

Table 9. Chemical composition, grain size and density of pure Mg, Mg-4Y-3RE, Mg-Gd and Mg-Ag alloys. Mg is considered as balance.

	Y	Nd	Ce	Gd	Ag	Fe	Mn	Si	Ni	Co	Cu	Al	Grain size	Density
	w%	w%	w%	w%	w%	ppm	ppm	ppm	ppm	ppm	ppm	ppm	µm	g/cm^3
pure Mg	-	-	-	-	-	46	334	130	4	<1	14	45	22.6	1.740
Mg-4Y-3RE	3.95	2.16	0.96	-	-	87	166	55	19	<1	26	252	6.3	1.811
Mg-5Gd	-	-	-	3.99	-	50	57	63	6	<1	<10	41	5.9	1.786
Mg-10Gd	-	-	-	8.63	-	47	101	55	9	<1	<10	97	17.8	1.854
Mg-2Ag	-	-	-	-	1.88	50	82	90	4	<1	<10	38	43.7	1.762
Mg-4Ag	-	-	-	-	3.88	58	51	79	5	<1	<10	54	31.6	1.785
Mg-6Ag	-	-	-	-	5.97	47	1	50	4	<1	<10	6	34.6	1.815

5.2.2. In vitro immersion experiments

Immersion experiments are carried out in Dulbecco's modified eagle medium Glutamax-I (DMEM 61965, Life Technologies, Paisley, UK) within an atmosphere of 5 vol.% CO_2 under sterile or unsterile conditions inside a glove box. Fig.44 represents the setups used for these experiments. The setup shown in Fig. 44a was also applied as explained in Section 4.2.2. The 5% in volume of CO_2 is controlled with a CO_2 controller (ProCO2, BioSpherix, Lacona, USA) which includes a sensor inside the box and a feeding tube.

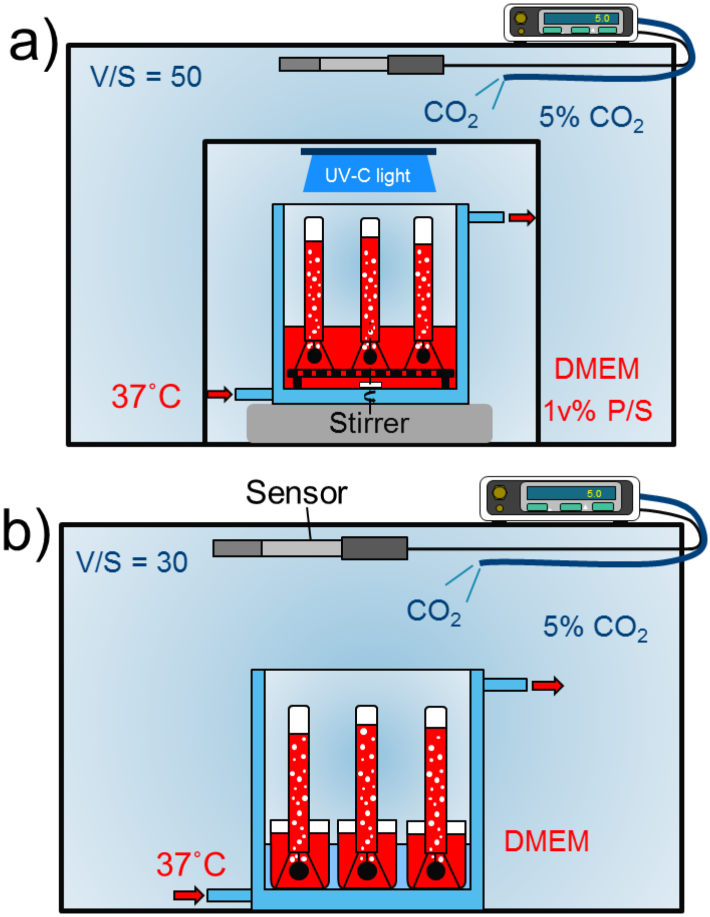

Figure 44: Immersion test setups: (a) a single stirred DMEM bath with 5% CO_2, UV-C radiation and penicillin streptomycin (P/S); (b) under unsterile conditions with each sample in a separate beaker, in order to isolate each sample from contamination.

Table 2 in page 36 shows the composition of DMEM [4, 5] in comparison to body plasma [6-8] and whole blood [9-11]. The main component of DMEM is NaCl, but it contains $NaHCO_3$ and HPO_4^{2-} as buffering agents, phenol red as a pH indicator, vitamins, glucose and amino acids up to 10.6 mM, with L-Alanyl-L-glutamine being the most present one. SO_4^{2-}, K^+, Ca^{2+} and Mg^{2+} ions are also present in smaller amounts.

The degradation rate (DR) is calculated from the mass loss and from the hydrogen generated as explained in Section 4.2.2. The chromic acid treatment, the surface preparation, the pH measurement and the temperature control were also applied as explained in the same section. XRD analysis of the degradation layer is done as explained in Section 3.2.3.

For the sterile conditions (Fig.44a) UV-C radiation is continuously applied and antibiotics, 1 vol.% of penicillin streptomycin (Penicillin-Streptomycin 10,000 U/mL, 15140-122, Gibco, Grand Island, NY), are added to the electrolyte in order to avoid or, at least, delay bacterial growth. The UV-C radiation is achieved with UV lamps (JKL BF8100 UVC, Thief River Falls, USA) with a wavelength of 254 nm. The solution volume to sample surface ratio (V/S) applied in this study is 30 mL/cm^2 and 50 mL/cm^2 for unsterile and sterile conditions, respectively, each disc having approximately 2 cm^2 surface area. Hence, a 600 mL DMEM bath is used to immerse 6 discs in sterile conditions and 70 mL per sample in separate beakers in unsterile conditions in order to isolate each solution and sample from contaminating each other. This ratio is mainly restricted by the geometry of the beakers and funnels to be able to install the eudiometer filled with electrolyte. Samples hang with an inert fishing line (Gamakatsu Co. Ltd) and a hole of 1 mm diameter next to the edge of the disc inside the funnel used to collect the gas generated. In sterile conditions, 6 samples of the same alloy are immersed in a 600 mL DMEM bath, hanging each sample inside a funnel with a eudiometer of 20 mL storage capacity on top. The dynamic fluid condition inside the funnel under sterile conditions is generated by a magnetic stirrer at approximately 200 rpm located under a polycarbonate plate with holes to allow fluid movement where the funnels are supported. In this way, the system is an open system avoiding a higher local pH inside the funnel and a decrease of the V/S ratio [12, 13].

For the unsterile conditions (Fig. 44b), in order to get relevant statistics, 6 samples of each alloy are also used. Statistical analysis was conducted by mean calculation with indication of standard deviation. Each sample is immersed in a separate beaker of 35 mm diameter and 50 mm height, with a funnel and an eudiometer. The volume of the eudiometers are 20 mL and 35 mL for sterile and for unsterile conditions, respectively, proportional to the expected amount of H_2. A control position is used without alloy sample in order to see the gas accumulation due to artifacts created by the stirring, the gases in solution, or the contamination.

The testing duration for unsterile conditions is 7-8 days and for sterile conditions it is not longer than 100 h because of the contamination risk after 4-5 days. Moreover, the recommendation is that too long immersion time should be avoided, because the pH and the species concentrations are far away from the true situation in vivo [14].

5.3. Results

5.3.1. Hydrogen evolution

Results from immersion experiments show a clear difference between sterile and unsterile conditions in DMEM (Fig. 45). In sterile conditions there is an increase of gas during the first 10 h for the tested alloys (Fig. 45a). After a maximum collected gas is registered (0.4-0.8 mL/cm^2) the bubbles decrease during the rest of the immersion time with an approximate rate of 0.1 $mL/cm^2/day$. In some cases the gas volume increases and standard deviations broaden because of the initiation of the contamination influence. The gas collected is considered to be CO_2 from the buffering system and H_2 from Mg corrosion. This is proven with a control sample position without Mg which also registers a similar gas evolution but lower in volume compared to funnels and eudiometers with Mg samples. The hydrogen evolution in DMEM under sterile conditions was previously shown in Section 4.3.1.a with pure Mg, Mg-10Gd and Mg-2Ag samples.

Without sterilization measures, H_2 evolution shows a different behaviour for these Mg-alloys (Fig. 45b). During the first day there is a gas accumulation lower than 1 mL/cm^2, which is comparable to the sterile conditions. However, after this first gas evolution there is a pronounced increase of H_2 (between 10-20 mL/cm^2). The following behaviour follows an asymptote for the rest of the immersion time, while the medium is contaminated by microorganisms until 7 days. There are no significant differences between Mg-Gd, Mg-Ag, pure Mg and Mg4Y3RE and if any it is mainly due to the contamination behaviour and not the alloy performance. The control position in this case reveals the same behaviour as for Mg containing tests but with a lower gas increase after 45 h. This difference is due to the Mg degradation process.

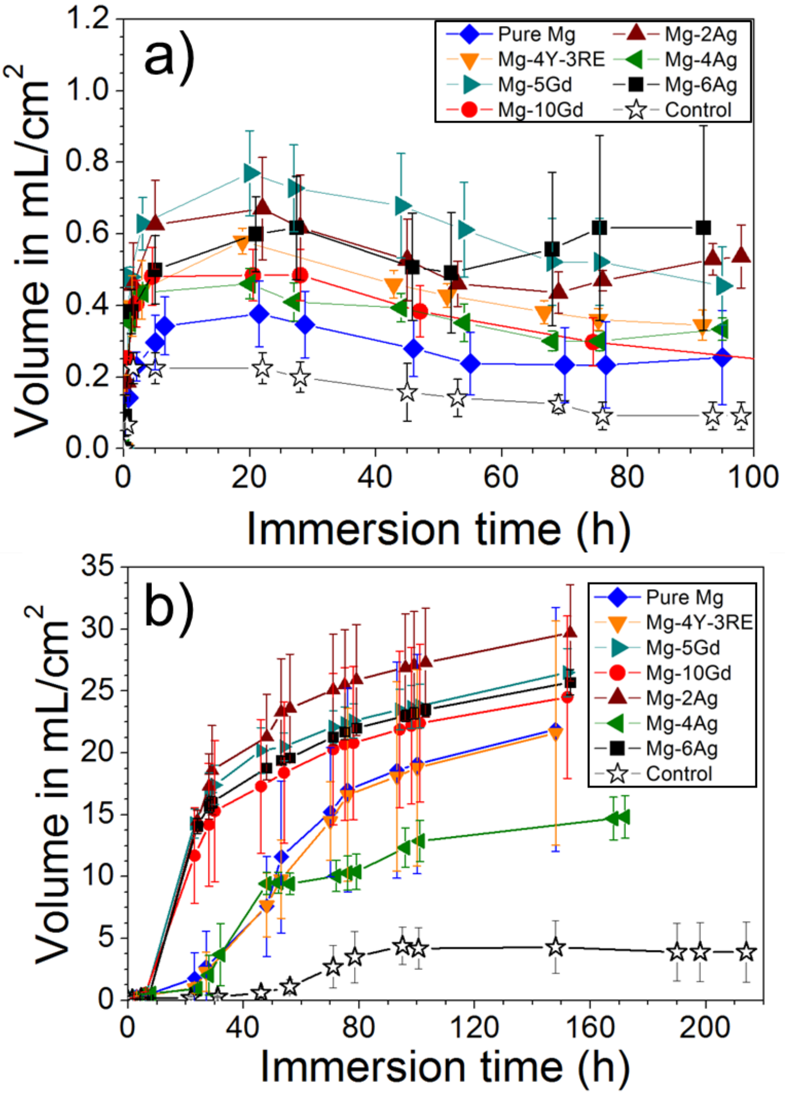

Figure 45: Gas evolution with immersed Mg-alloys under (a) sterile DMEM and (b) unsterile conditions. This gas evolution on Mg-alloys is lower than 1 mL/cm^2 in sterilized DMEM while in unsterilized DMEM 10-30 mL/cm^2 is registered.

5.3.2. pH measurement

The pH in sterilized DMEM is stable between 7.7 and 7.9 during the entire immersion time (Fig. 46a). The pH is stabilized in the physiological range due to a 5 vol.% of CO_2 but also because of two factors: a larger bath of 600 mL for the 6 samples tested in the same experiment and the stirring making a dynamic flow. In DMEM without sterilization the pH becomes acidic during the rapid H_2 generation period, with values between 6.3 and 6.8 (Fig. 46b). Then it increases back up to the physiological range. The solution becomes turbid and non-transparent which is an indication of contamination. In contrast, the increase of the pH at the control position after acidification is substantially lower than at the alloy testing positions which shows the influence of the degradation process on pH evolution. Every experiment followed a different pH evolution showing the random apparition of contamination and a lack of reproducibility.

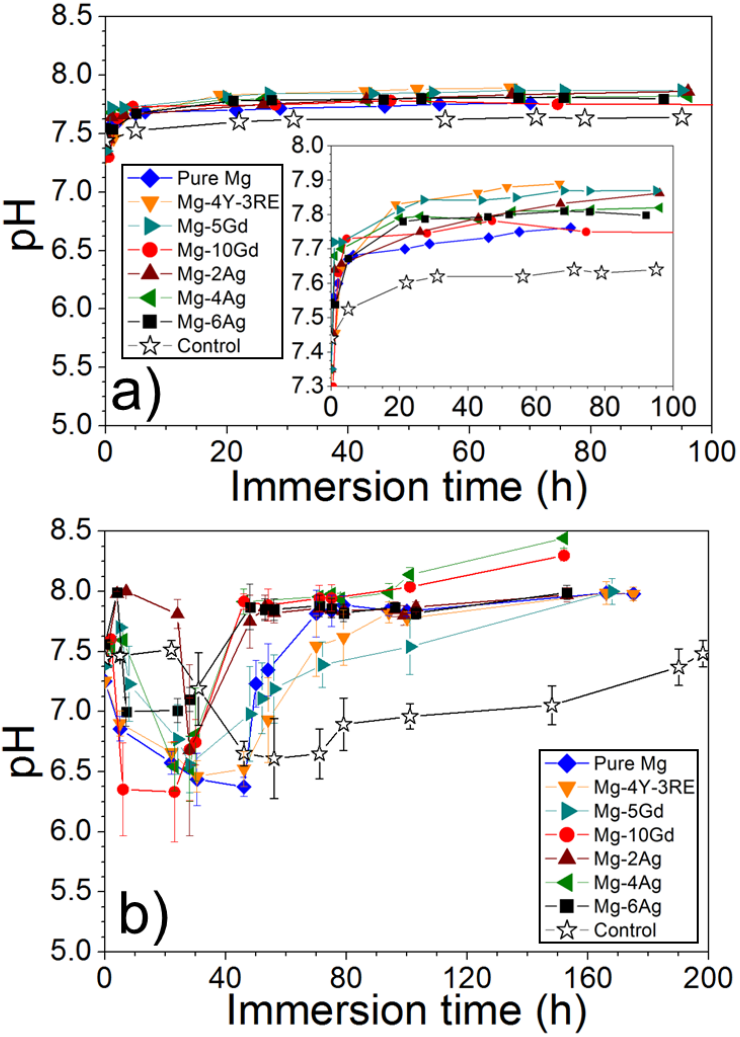

Figure 46: Change of pH of DMEM with immersed Mg-alloys under (a) sterile and (b) unsterile conditions. (a) shows a stable pH while (b) depicts the acidification of DMEM during Mg degradation.

5.3.3. Degradation rate

Fig. 47 depicts degradation rates of the different alloys compared to the mass reduction after immersion tests. This data and the degradation layer mass are shown in Table 10. The DR by hydrogen evolution is calculated at the last time-point registered, after 4-7 days and 6-8 days for sterile and unsterile conditions respectively. As discussed in Section 4.2, in both cases, two corrections have to be made from the gas evolution data: deduction of the gas collected at the control position, considered as air and CO_2, and addition of the H_2 in solution in DMEM defined by the solubility limit. Table 11 shows the H_2 and CO_2 solubility in water at 37°C which allows the approximate calculation of the amount of each gas in solution depending on the volume of electrolyte applied. Hence, the H_2 gas volume corrected is 1.88 mL/sample and 1.33 mL/sample for sterile and unsterile conditions, respectively, according to the electrolyte volume applied, in this case, 600 mL for sterile and 70 mL for unsterile conditions. This indicates the great influence that gas solubility can have on the gas evolution when a large volume of electrolyte is used.

The mass loss DR in sterile DMEM is generally lower than 2.6 mm/year (Fig. 47a and Table 10). H_2 DR shows systematically lower values, which can be due to the small amount of gas generated and the errors made during gas collection. For example, this could be because part of the H_2 is not collected in the funnels caused by the large volume applied and the stirring; or because solubility of H_2 is different in DMEM compared to H_2O. The sample mass during the test under sterile conditions is in fact not considerably reduced (lower than 2%). Basically all the Mg dissolved precipitate on the surface building a degradation layer with OH^-, HCO_3^- and PO_4^{3-}, which protects the disc during the test.

Table 10. Experimental data from immersion tests: degradation rates by H_2 and mass loss, the ratio between these rates, degradation layer mass and mass reduction after the immersion tests.

	Sterile DMEM					Unsterile DMEM				
	Hydrogen DR	Mass loss DR	H_2/ML ratio	Degradation layer mass	Mass reduction	Hydrogen DR	Mass loss DR	H_2/ML ratio	Degradation layer mass	Mass reduction
	mm/year	mm/year		mg	%	mm/year	mm/year		mg	%
pure Mg	0.57	1.1	0.54	3.1	0.5	4.5	5.8	0.77	21.2	12.5
Mg-4Y-3RE	0.60	1.3	0.46	4.3	0.4	3.5	5.0	0.71	25.1	7.6
Mg-5Gd	0.65	1.0	0.68	5.4	0.6	7.5	8.6	0.88	23.5	13.6
Mg-10Gd	0.20	0.4	0.49	3.3	0.2	6.3	7.8	0.80	23.9	12.8
Mg-2Ag	0.68	2.2	0.31	5.8	1.6	8.2	9.3	0.88	26.2	16.4
Mg-4Ag	0.59	1.2	0.49	5.1	1.9	2.8	4.7	0.59	20.2	9.2
Mg-6Ag	0.61	2.6	0.24	6.2	2.0	6.7	8.2	0.82	30.8	9.9

Table 11. H_2 and CO_2 solubility in water at 37°C and the gas in solution depending on the volume of electrolyte applied (600 mL and 70 mL). Data for H_2 from Ref. [15] and for CO_2 Ref. [16, 17].

Gas	Solubility at 37°C (mL/L)	Gas density at 37°C (mg/mL)	Volume of electrolyte (L)	Gas in solution (mL)
H_2	18.8	0.078	0.6	11.28
			0.07	1.32
CO_2	655.67	1.707	0.6	393.4
			0.07	45.9

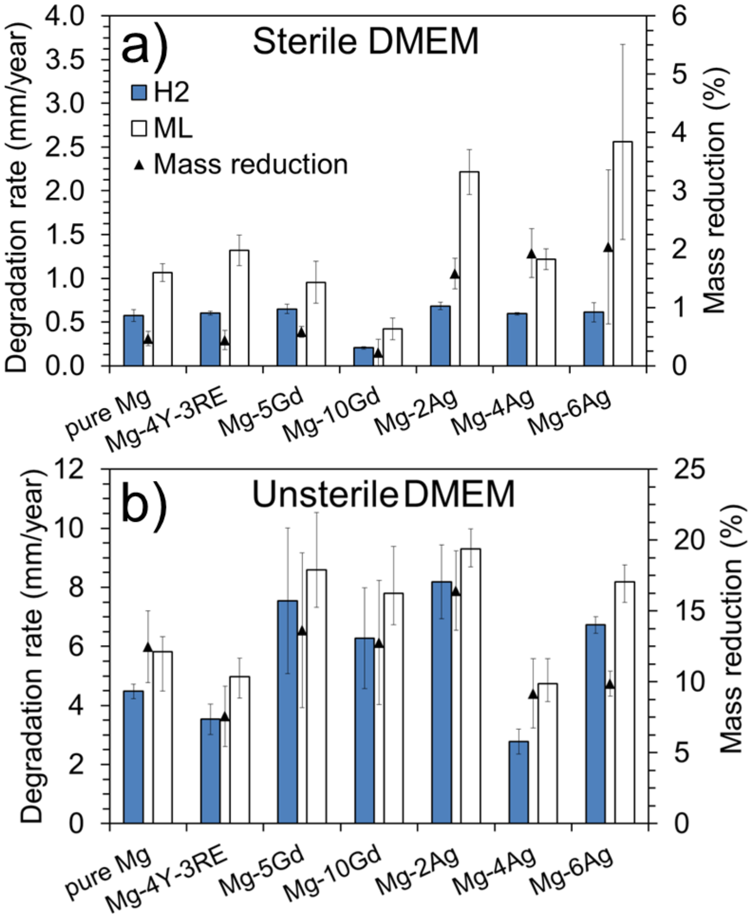

Figure 47: Degradation rates given by H_2 (H2) and mass loss (ML) are lower under sterile conditions (a) than in contaminated medium (b). The mass reduction in % is proportional to the DR in both conditions.

Under non sterilized conditions the mass loss rates are higher with values between 5.0 mm/year and 9.3 mm/year (Fig. 47b). As shown in Table 10, under these conditions the H_2 and mass loss show good correlation with a H_2/ML ratio between 0.59 and 0.88. The mass reduction shows that the sample loses considerable mass, after 160-190 h of immersion between 7.6% and 16.4%.

Fig. 48 shows the corrosion rate evolution calculated from H_2 data after correction for the control position gas and for the H_2 in solution. This DR evolution shows an asymptotic behaviour in sterile DMEM with higher rates at the beginning of the corrosion process. Under unsterile conditions, firstly the same behaviour as in sterile conditions is registered and, then, due to contamination and the acidic pH, a high DR is achieved followed by the same asymptotic behaviour as in sterile tests but trending to higher values.

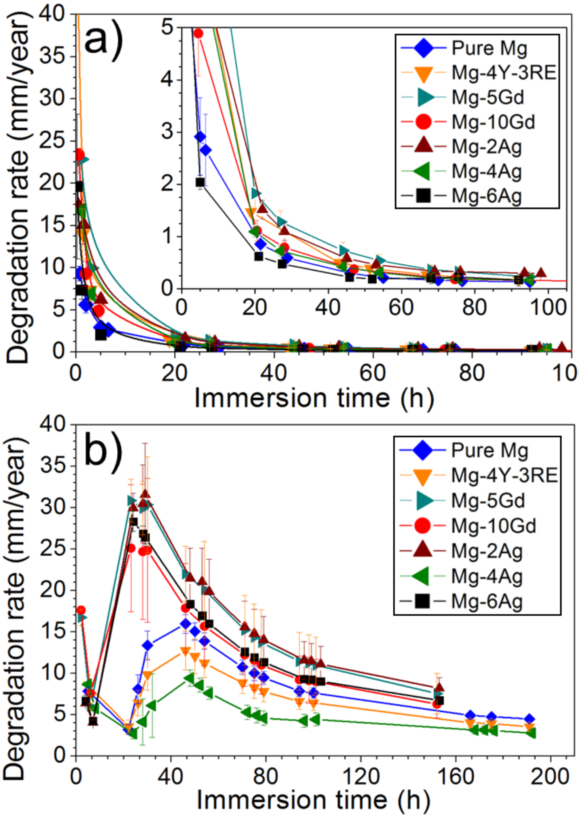

Figure 48: Degradation rate evolution over the immersion converted from the H_2 gas data shows the passivation of Mg-alloys in sterile DMEM (a) and the faster corrosion rates during the medium contamination under unsterile conditions (b).

5.3.4. Degradation layer formed in DMEM

In DMEM the degradation layer is composed of two different layers (Fig. 49). The first layer is a composite of $Mg(OH)_2$ and $(Mg,Ca)CO_3$, which is the first one precipitating at the magnesium-electrolyte interface. On top of this layer a Ca and P rich area can be found which is considered to be Ca phosphate layer. Fig.49a represents the corrosion double layer on top of pure Mg at a damaged site. Fig. 49b shows a 100-200 nm thick Ca phosphate rich layer (in white) and 7-8 µm thick underneath layer (in grey). Fig. 49c shows a thicker Ca phosphate layer region with a thickness between 1µm to 2 µm on top of a grey layer with 1 to 2 µm thickness. The EDX spectrum 1 reveals Mg, C and O peaks, demonstrating that $Mg(OH)_2$, which is one of the products formed on Mg in aqueous media, and $(Mg,Ca)CO_3$ compose this grey layer. The EDX spectrum 2 in Fig. 49 from the white area shows clear Mg, Ca, P, C and O intensity peaks. The C peaks can be explained by a larger interaction volume compared to the white layer, so that the conductive resin used is also measured. Hence, this layer is demonstrated to be a $Ca_x(PO_4)_y$ with Mg or $(Mg_x,Ca_y)(PO_4)_z$.

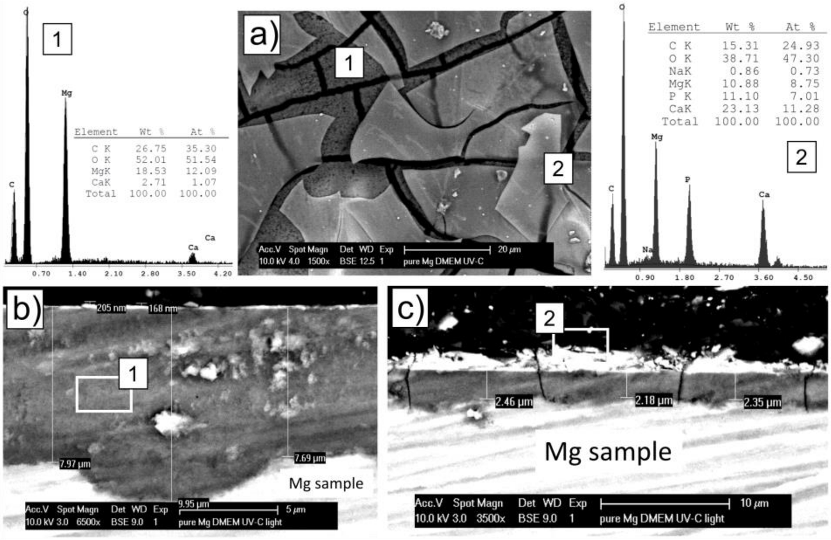

Element	Wt %	At %
C K	26.75	35.30
O K	52.01	51.54
MgK	18.53	12.09
CaK	2.71	1.07
Total	100.00	100.00

Element	Wt %	At %
C K	15.31	24.93
O K	38.71	47.30
NaK	0.86	0.73
MgK	10.88	8.75
P K	11.10	7.01
CaK	23.13	11.28
Total	100.00	100.00

Figure 49: Top view and cross sectioned SEM images of pure Mg immersed in sterile DMEM where (a) is top view of a damaged area of the degradation layer; (b) shows a cross section at a thick $Mg(OH)_2$ and $(Mg,Ca)CO_3$ layer site in grey and c) is the cross section at a thick Ca phosphate site in white on top of the hydroxide and carbonate layer. The EDX spectrum 1 corresponds to the grey layer in b) and EDX spectrum 2 to the Ca phosphate white layer in (c). Spectrum 2 shows that $Ca_x(PO_4)_y$ might contain Mg.

The difference between Mg samples degraded under sterilized and unsterilized DMEM is depicted in Fig. 50. The top view of this double layer formed in DMEM is shown in Fig. 50a. Cross sections of pure Mg and Mg-2Ag are shown in Fig. 50b and c respectively. The effect of the contamination is shown in Figs. 50d-f with a top view and cross sections of two sites. Microorganisms decrease the pH and presumably due to the acidic pH the $(Mg_x,Ca_y)(PO_4)_z$ top layer is removed, leaving the layer underneath unprotected. Mg is able to dissolve through this layer forming a thicker $Mg(OH)_2$ and $(Mg,Ca)CO_3$ layer up to 20-30 μm.

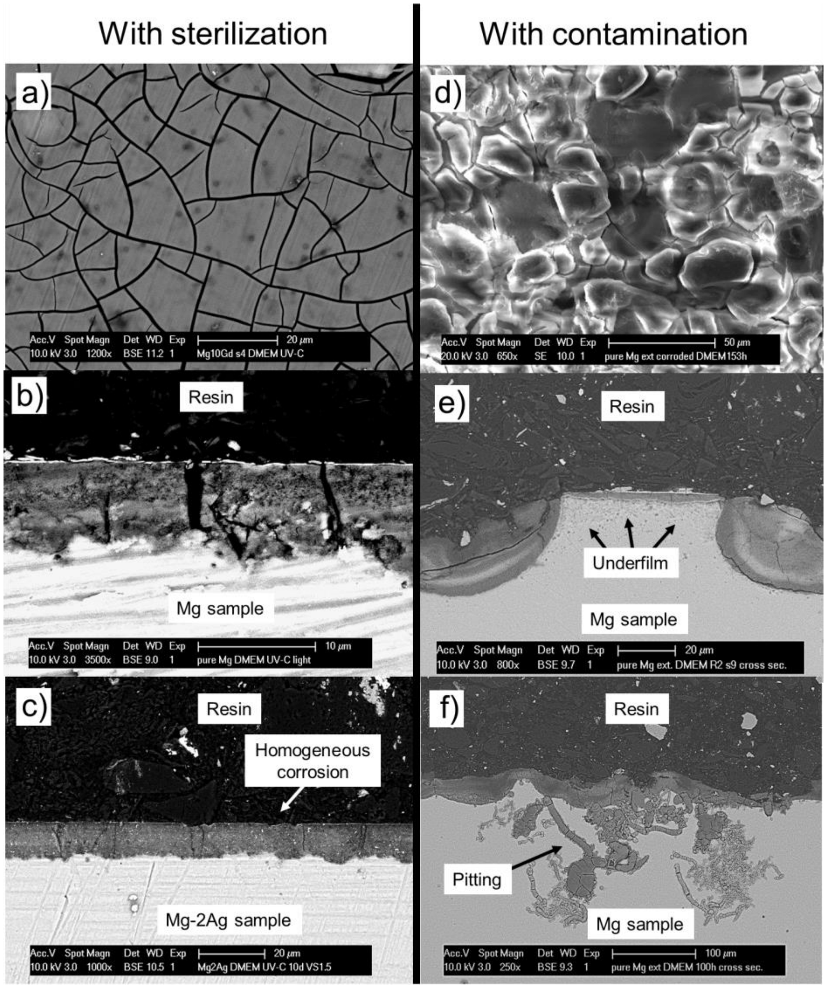

Figure 50: Degradation layer morphology of Mg samples degraded under sterile (a-c) and unsterile conditions (d-f) in DMEM, where (a) and (c) are top views and (b), (c), (e) and (f) are cross sections. (d) indicates that the acidic pH and perhaps microorganisms can dissolve the $(Mg_x,Ca_y)(PO_4)_z$ top

layer. (b) and (c) show homogeneous corrosion mode in sterile DMEM. (e) and (f) show less homogeneous, underfilm and at some sites pitting corrosion modes.

The degradation mode identified is mainly homogeneous corrosion in both conditions, with a similar behaviour for all the tested Mg alloys. However, underfilm and pitting corrosion mechanisms are also identified in contaminated medium, as shown in Fig. 50e and f respectively. This is related to the stochastic influence of contamination which can attack the surface of the sample locally dissolving the top Ca-P layer, as shown in Figs. 50d-f. Pitting corrosion is usually linked to the influence of Cl^- ions dissolving $Mg(OH)_2$ unprotecting some areas and creating pits in the sample. However, pitting is hardly observable and thereby it is not the main degradation mechanism.

5.3.5. XRD analysis

Often, due to the thin layers generated during Mg degradation, it is hard to detect the characteristic peaks of a degradation layer with the XRD technique. However, because of the relatively large thickness of this grey layer under unsterile conditions, $(Mg,Ca)CO_3$ crystalline structure can be successfully detected (Fig. 51), whereas only traces have been detected under sterile conditions. In this case, a grazing incident angle of 0.5° is applied to decrease the interaction depth and get more information from the surface.

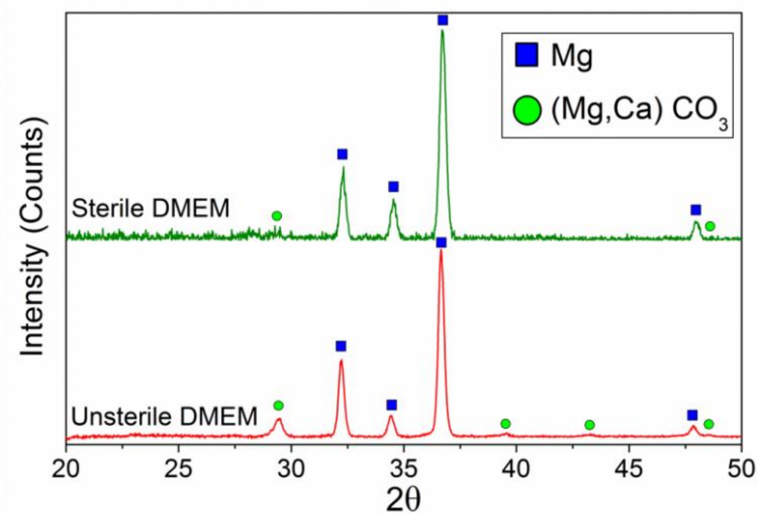

Figure 51: XRD pattern of the degradation layer formed on the Mg disc surface degraded in sterile and unsterile DMEM show the presence of $(Mg,Ca)CO_3$.

Hexagonal close-packed (HCP) magnesium is the main crystalline structure detected but also four characteristic peaks (29.46˚, 39.60˚, 43.30˚ and 47.84˚) from calcium carbonate $CaCO_3$ with a small shift (less than 0.22˚) which can be an indication of the presence of Mg. However, calcium phosphate crystalline structure, such as hydroxyapatite, has the most intense characteristic peak at 31.79˚ and Mg has an intense peak at 32.21˚ thus making the detection difficult. Furthermore, the Ca phosphate layer is relatively thin, thus diffraction peaks due to $(Mg_x,Ca_y)(PO_4)_z$ structures could not be unequivocally detected.

5.3.6. Macrographs

Macrographs of the samples show the morphology of the degradation layer and final surface appearance (Fig. 52). The degradation layer is dark under sterile conditions and whiter under unsterile ones under natural light, except for Mg-Ag alloys. The surface morphology after the chromic acid treatment shows a higher roughness on samples degraded under contaminated DMEM. After chromic acid treatment, denoted as cleaned, the degradation layer is removed revealing the Mg substrate surface morphology with valleys and peaks. Hence, the roughness of this layer is expected to be high. It is noteworthy that Mg-Ag alloys get a darker degradation layer compared to the other studied alloys. The similarity of the behaviour of different alloys can also be observed in Fig. 52.

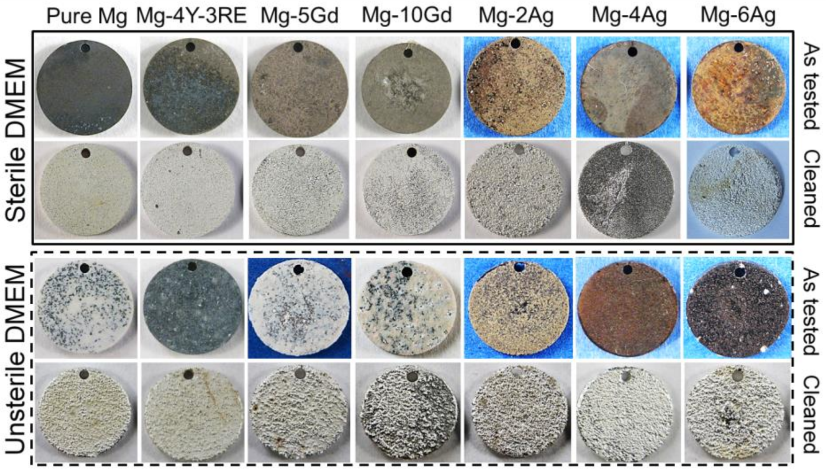

Figure 52: Macro pictures of the samples tested in sterilized DMEM (upper box) show a more uniform and less pronounced degradation process than under unsterilized conditions (lower dashed box).

5.4. Discussion

In the present study, the degradation behaviour of pure Mg, Mg-4Y-3RE, Mg-Gd and Mg-Ag in DMEM is analysed and a material specific corrosion testing setup is applied based on literature [13, 18, 19]. The main purpose is to define also the influence of medium sterilization on the degradation behaviour under near physiological conditions of fast and slowly degrading alloys, as previous studies showed [20], which are also candidates for biodegradable implant materials.

5.4.1. Degradation analysis

The degradation behaviour in DMEM is highly influenced by a degradation layer formation. In the first stage of degradation a layer composed of $Mg(OH)_2$ and $(Mg,Ca)CO_3$ is formed and on top a Ca and P rich layer can be found, denoted as $(Mg_x,Ca_y)(PO_4)_{z,}$ which is also reported in in vivo [24, 25] and in vitro studies [26-30]. Willumeit et al. also concluded that these type of corrosion products can appear during Mg corrosion in DMEM in the form of $MgCO_3$, tricalcium phosphate ($Ca_3(PO_4)_2$) or hydroxyapatite ($Ca_5(PO_4)_3$-X, X= Cl, OH…) [23]. The first layer is formed while Mg is starting to dissolve, reaching locally high concentrations of Mg^{2+}, Ca^{2+}, HCO_3^- and OH^-, from which $Mg(OH)_2$ and $(Mg,Ca)CO_3$ precipitate. The reason why this is the first layer formed can be explained with the higher amount of HCO_3^- compared to $H_2PO_4^-$ and HPO_4^{2-} in DMEM. Once the concentration of HCO_3^- decreases Mg^{2+}, Ca^{2+} and PO_4^{3-} can bind forming this top layer. Fig. 50 shows two different regions from sample cross sections tested in sterilized DMEM. It is observed that the thicker the $(Mg_x,Ca_y)(PO_4)_z$ layer is, the thinner the $Mg(OH)_2$ and $(Mg,Ca)CO_3$ layer underneath is. Hence it would appear that the corrosion of Mg is slowed down by the precipitation of the top phosphate layer, protecting the α-Mg from the electrolyte, demonstrating the importance of Ca^{2+} for Mg corrosion.

Thus, when choosing the testing electrolyte, it is important to consider the content of Ca^{2+} due to the possibility of forming Ca containing degradation layers on the Mg surface, such as $(Mg_x,Ca_y)(PO_4)_z$ and $(Mg,Ca)CO_3$ [23, 31]. Furthermore, the presence of HCO_3^-, HPO_4^{2-} and SO_4^{2-} ions can form also products which can protect the surface and this inhibit the detrimental effect of Cl^- [32].

The solution volume to sample surface ratio (V/S) may play an important role on Mg degradation results. When low V/S values are applied the Mg initial degradation reactions and degradation layer precipitation take place faster, giving reduced long term degradation rates. The difference between sterile and unsterile conditions in this study makes the influence of this parameter negligible because, as Kirkland et al. stated, for V/S values over 30 mL/cm^2 this parameter does not promote statistical differences in degradation rates [12].

Another parameter to discuss in connection with Mg corrosion is the Pilling-Bedworth (P-B) ratio. This ratio defines the relation between the metal volume and the (hydr)oxide volume, in this case, Mg and $Mg(OH)_2$. When P-B ratio is less than 1, this layer does not cover completely the metal [33]. In the case of Mg and magnesium hydroxide this ratio is 0.81 [34]. Hence, the low degradation rates in sterile DMEM indicate that $(Mg,Ca)CO_3$ combined with Mg hydroxide and the $(Mg_x,Ca_y)(PO_4)_z$ layer cover the studied Mg discs completely leading to adequate protection for all alloys with only slight differences between Mg-Gd and Mg-Ag binary systems. In parallel, amino acids and vitamins might play a role adsorbing to the surface as proteins do, making the degradation layer more protective [35-37].

Although, the H_2 evolution method in these tests can have many sources of errors, as discussed below in Section 4.2., most can be corrected when a control position without Mg is applied. Nevertheless, there is another mechanism which can avoid generating H_2 which can be detected by mass loss method. This mechanism is the well-known particle undermining model [38]. This model consists of the dissolution of the Mg around cathodic particles releasing them into the solution. Secondary phases, precipitates and grain boundaries represent a cathodic site with respect to the Mg grain, thus these sites and even Mg can be released as particles into the electrolyte. This leads to a decrease of the samples' mass without H_2 production, as Fig. 48 and Table 10 indicate. In the case of the studied Mg alloys, there are secondary phases in Mg-4Y-3RE, as in the commercial WE43 [39, 40]; and precipitation of Gd and Ag rich particles in Mg-Gd and Mg-Ag alloys, respectively. As shown in Fig. 53a, Mg_5Gd can precipitate at the grain boundaries [41] but also cubic particles can be found. As discussed in Section 4.4.1, these cuboids are considered to be Gd hydrides, as Peng et al. reported [42]. As shown in Fig. 53b, in Mg-Ag alloys, secondary phases with Ag can precipitate at the grain boundaries. As reported by Tie et al. [43], this phase is Mg_4Ag or perhaps partially it could be $Mg_{54}Ag_{17}$ or, as the newest stoichiometry indicates, Mg_3Ag. Hence, these secondary phases and hydrides can promote the particle undermining mechanism. Fig. 53c shows a Gd hydride particle which after the removal of the degradation layer is keeping its original shape. However, this influence is not considered the main reason for the difference between ML and H_2 methods in sterile DMEM testing since slow and homogenous degradation is detected for all the tested alloys and the gas data have many other sources of errors.

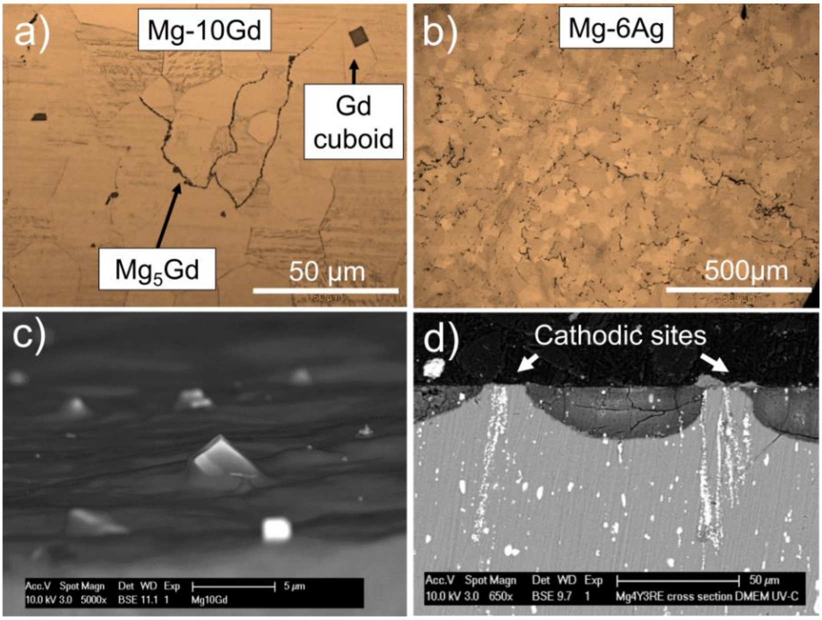

Figure 53: The presence of secondary phases in the studied alloys has mild influence in the degradation process in DMEM. (a) shows Mg_5Gd precipitates and Gd hydrides in cubic shape. (b) depicts Ag containing secondary phases at the grain boundaries in Mg-Ag alloys. (c) shows a Gd hydride cuboid being released as a full particle during the degradation process of Mg-10Gd. Finally (d) shows secondary phases from Mg-4Y-3RE acting as cathodes, where the H_2 evolution takes place, and the Mg around them acting as anodes, where Mg degrades forming a surface layer.

As shown in Fig. 48a and Table 9, the grain size of Mg-Ag alloys seems to be related to the DR determined under sterilization. Mg-2Ag has the highest grain size (43.7 µm), then Mg-6Ag (34.6 µm) and finally Mg-4Ag (31.6 µm). The DR follows a similar trend as Mg-2Ag, Mg-6Ag and Mg-4Ag have a DR of 2.2, 2.6 and 1.2 mm/year. The higher DR of Mg-6Ag as compared to Mg-2Ag can be explained by the higher Ag content. Thus, the grain size seems correlate the DR data when the impurity contents are similar. For pure Mg and RE containing Mg alloys, the smaller grain size seems to provide a lower DR. However, also the different alloying additions and impurity content should be taken into consideration. Thereby, this analysis should be done systematically increasing impurity content, grain size or alloying additions with the same Mg based material.

5.4.2. Influence of sterilization

In uncontaminated DMEM, tests are performed with 5 vol.% CO_2 applied to atmospheric air and stirring the same bath for all the samples. A rapid accumulation of gas is observed during the first minutes of immersion (Fig. 45a). This gas volume is comparable to the gas collected in a control position with an eudiometer without Mg sample. Thus, it is assumed to be air from pouring the electrolyte and CO_2 dissolved in the electrolyte. This gas is collected through the funnel because of the stirring and the large electrolyte volume applied (600 mL). Hence sufficient time for pH and CO_2 stabilization is recommended. Tie et al. also concluded that DMEM needs time to stabilize the pH within the physiological range (7.7-7.9) [5]. As other authors have also mentioned, the stirring produces a dynamic flow making this an 'open' system. In this manner, the local pH increase inside the funnel is avoided which would modify the in vitro data [12, 13]. After stabilization (Fig. 45a), the volume of the first collected gas bubble reduces and two mechanisms can be identified for this. On the one hand, CO_2 goes back in solution buffering the electrolyte, and on the other hand, while Mg corrosion is ongoing a small amount of hydrogen is being generated, as the mass loss data reveals. Thus, the gas evolution does not only reflect the Mg degradation process. Furthermore, in unsterile DMEM, there is a larger gas collection at the control position which is explained by CO_2 generation from glucose consumption by microorganisms (Fig. 45b) [44]. Thus, two corrections have to be made when the gas data is converted into a degradation rate. Firstly, the gas collected at a control position is deducted and, secondly, the H_2 soluble in DMEM is added, here approximated as the solubility in H_2O (Table 11). Note that if this H_2 in solution would not be corrected and when the DR of the tested material is low, the error made can be large. Moreover, if the atmospheric pressure fluctuates and temperature changes occur the error made is higher, especially when large volumes of electrolyte are applied [12, 13]. In conclusion, this data should be interpreted with special care because it has many sources of errors and this also elucidates the importance of including a control position.

The immersion results in contaminated DMEM show the ability of microorganisms and the acidic pH to remove the top $(Mg_x,Ca_y)(PO_4)_z$ layer, exposing the $Mg(OH)_2$ and $(Mg,Ca)CO_3$ layer to the medium and accelerating corrosion. This contamination starts during the first immersion hours turning the pH acidic (6.3-7) and increasing the hydrogen volume massively. This acidic pH is common in contaminated cell culture which can be caused by bacteria, yeast, fungi, viruses, parasites, mycoplasma and other living microorganisms, which can proliferate exponentially at this pH and temperature range [1, 2, 45]. Bacteria, for instance, produce lactic acid from glucose during metabolism, which leads to a decreased pH [46, 47]. Hence, the degradation layer dissolves at this low pH values, and for this reason, the degradation rate is then accelerated.

It is remarkable that the degradation behaviour of all Mg-Gd and Mg-Ag alloys are similar, with slightly faster degradation of Mg-Ag alloys as depicted in Fig. 48a. This shows the high influence of the testing environment despite the alloying elements, which can play a major role in other testing conditions, as concluded by previous studies [48]. Also no delayed acidic change or gas volume increase is observed for Ag containing alloys. Thus Ag antibacterial properties do not delay the medium contamination, which is understandable considering the low amount of silver compared to the electrolyte volume.

5.5. Conclusions

The influence of cell culture sterilization on the degradation behaviour of Mg and its alloys has been determined by hydrogen evolution, mass loss method and degradation layer characterization. The following conclusions can be drawn from this work:

1. Cell culture media have a composition very close to that of body plasma and whole blood, and one can expect that they can mimic closely the reactions taking place during Mg biodegradation in vivo. Nevertheless, microorganisms, such as bacteria, yeast, fungi, viruses, parasites and mycoplasma can contaminate cell culture media helped by the presence of energy sources (e.g. glucose), especially when cells are added to the medium. Thus, sterilization becomes necessary in order to avoid this contamination which deteriorates the mimicking of an in vivo situation. This sterilization can be achieved, or the contamination at least delayed, by applying UV-C radiation (254 nm) and the addition of antibiotics (e.g. penicillin/streptomycin) to the medium.
2. In general, the studied Mg samples tested in DMEM show passivation, and the samples corrode only during the first hours, then the degradation layer becomes stable and the samples show a strongly reduced degradation behaviour. In contrast, when the media is contaminated it acidifies, accelerating Mg degradation by dissolving degradation layers, such as $(Mg_x,Ca_y)(PO_4)_z$, which has shown its protective effect on Mg alloys.
3. Small differences in the degradation rates of the studied alloys are determined by mass loss in sterilized DMEM. These rates are not only defined by the environment, but also by material factors such as: alloying additions, grain size, impurity content, secondary phases and precipitates.

Mg-Ag alloys show the highest DR presumably due to the larger grain size and the influence of Ag additions, since the impurity contents in these alloys are comparable.

4. Two positive aspects of the experimental setup to mimic physiological conditions have been identified. First, the pH can be maintained in a physiological range, between 7.7 and 7.9, which indicates that HCO_3^-/CO_2 is an appropriate buffering system. And secondly, the stirring produces a dynamic flow making this an ‘open’ system avoiding a local pH increase inside the funnel which would falsify the in vitro data. Conversely, due to the small amount of H_2 created and the CO_2 buffering system, the gas evolution data are not sufficient to precisely follow the Mg degradation process. The use of a control sample position has been essential to detect this and its use is highly recommended.

References

[1] K. Deva, e. al., Int. Journal of Animal Biotechnology 1 (2011) 8-12.

[2] M.T. Madigan, Brock biology of microorganisms, Benjamin Cummings, San Francisco, 2012.

[3] F. Feyerabend, H. Druecker, D. Laipple, C. Vogt, M. Stekker, N. Hort, R. Willumeit, J. Mater. Sci. - Mater. Med. 23 (2012) 9-24.

[4] D. Tie, F. Feyerabend, N. Hort, R. Willumeit, D. Hoeche, Adv. Eng. Mater. 12 (2010) 699-704.

[5] A. Yamamoto, S. Hiromoto, Mater. Sci. Eng.: C 29 (2009) 1559-1568.

[6] J. Walker, S. Shadanbaz, N.T. Kirkland, E. Stace, T. Woodfield, M.P. Staiger, G.J. Dias, J. Biomed. Mater. Res. Part B 100 (2012) 1134-1141.

[7] J.L. Gamble, Chemical anatomy, physiology and pathology of extracellular fluid : a lecture syllabus, Dept. of Pediatrics, Harvard Medical School, Cambridge, 1941.

[8] F. Feyerabend, H.-P. Wendel, B. Mihailova, S. Heidrich, N.A. Agha, U. Bismayer, R. Willumeit-Römer, Acta Biomater. 25 (2015) 384-394.

[9] C. Prohaska, K. Pomazal, I. Steffan, Fresenius J. Anal. Chem. 367 (2000) 479-484.

[10] J.E. Gamble, Chemical anatomy, physiology and pathology of extracellular fluid, Cambridge, MA: Harvard University Press, 1967.

[11] N.T. Kirkland, N. Birbilis, M.P. Staiger, Acta Biomater. 8 (2012) 925-936.

[12] J. Hofstetter, E. Martinelli, A.M. Weinberg, M. Becker, B. Mingler, P.J. Uggowitzer, J.F. Löffler, Corros. Sci. 91 (2015) 29-36.

[13] Z. Zhen, T.-f. Xi, Y.-f. Zheng, Trans. Nonferrous Met. Soc. China 23 (2013) 2283-2293.

[14] Grischuk, 11 (1957) 136.

[15] J.J. Carroll, J.D. Slupsky, A.E. Mather, J. Phys. Chem. Ref. Data 20 (1991) 1201.

[16] R.L. David, CRC Handbook of Chemistry and Physics, Boca Raton, Boston, 1990-1991.

[17] M. Schinhammer, J. Hofstetter, C. Wegmann, F. Moszner, J.F. Loeffler, P.J. Uggowitzer, Adv. Eng. Mater. 15 (2013) 434-441.

[18] N.I. Zainal Abidin, B. Rolfe, H. Owen, J. Malisano, D. Martin, J. Hofstetter, P.J. Uggowitzer, A. Atrens, Corros. Sci. 75 (2013) 354-366.

[19] I. Marco, O. van der Biest, F. Feyerabend, R. Willumeit-Römer, Eur. Cell Mater. 28 Suppl. 3, (2014) 42.

[20] Z. Li, X. Gu, S. Lou, Y. Zheng, Biomaterials 29 (2008) 1329-1344.

[21] L. Xu, G. Yu, E. Zhang, F. Pan, K. Yang, J. Biomed. Mater. Res. Part A 83 (2007) 703-711.

[22] S. Zhang, J. Li, Y. Song, C. Zhao, X. Zhang, C. Xie, Y. Zhang, H. Tao, Y. He, Y. Jiang, Y. Bian, Mater. Sci. Eng.: C 29 (2009) 1907-1912.

[23] L. Yang, E. Zhang, Mater. Sci. Eng.: C 29 (2009) 1691-1696.

[24] Y. Zong, G. Yuan, X. Zhang, L. Mao, J. Niu, W. Ding, Mater. Sci. Eng.: B 177 (2012) 395-401.

[25] H. Kuwahara, Y. Al-Abdullat, N. Mazaki, S. Tsutsumi, T. Aizawa, Mater. Trans.(Japan) 42 (2001) 1317-1321.

[26] L. Li, J. Gao, Y. Wang, Surf. Coat. Technol. 185 (2004) 92-98.

[27] R. Willumeit, J. Fischer, F. Feyerabend, N. Hort, U. Bismayer, S. Heidrich, B. Mihailova, Acta Biomater. 7 (2011) 2704-2715.

[28] Y. Xin, T. Hu, P.K. Chu, Acta Biomater. 7 (2011) 1452-1459.

[29] G. Song, A. Atrens, D. St John, X. Wu, J. Nairn, Corros. Sci. 39 (1997) 1981-2004.

[30] N.B. Pilling, R.E. Bedworth, J. Inst. Metals 29 (1923) 529-591.

[31] H.E. Friedrich, B.L. Mordike, Magnesium technology, Springer-Verlag Berlin Heidelberg, 2006.

[32] C.L. Liu, Y.J. Wang, R.C. Zeng, X.M. Zhang, W.J. Huang, P.K. Chu, Corros. Sci. 52 (2010) 3341-3347.

[33] L. Yang, N. Hort, R. Willumeit, F. Feyerabend, Corros. Eng. Sci. Techn. 47 (2012) 335-339.

[34] C. Liu, Y. Xin, X. Tian, P.K. Chu, JOM Research 22 (2007) 1806-1814.

[35] G.L. Song, A. Atrens, Adv. Eng. Mater. 1 (1999) 11-33.

[36] Y.H. Kang, D. Wu, R.S. Chen, E.H. Han, J. Magnes. Alloys 2 (2014) 109-115.

[37] T. Rzychoń, A. Kiełbus, J. of Achievem. Mater. Manufact. Eng. 21 (2007) 31-34.

[38] N. Hort, Y. Huang, D. Fechner, M. Stoermer, C. Blawert, F. Witte, C. Vogt, H. Druecker, R. Willumeit, K.U. Kainer, F. Feyerabend, Acta Biomater. 6 (2010) 1714-1725.

[39] Q. Peng, Y. Huang, J. Meng, Y. Li, K.U. Kainer, Intermetallics 19 (2011) 382-389.

[40] D. Tie, F. Feyerabend, W.-D. Mueller, R. Schade, K. Liefeith, K.U. Kainer, R. Willumeit, Eur. Cells Mater. 25 (2013) 284-298.

[41] M. Gottfredsson, H. Erlendsdottir, S. Gudmundsson, Antimicrob Agents Chemother 35 (1991) 2658-2661.

[42] J.A. Ryan, General guide for identifying and correcting common cell culture growth and attachment problems, Corning, Inc. Technical Bulletin, 2008.

[43] S. Baron, Medical Microbiology, University of Texas Medical Branch at Galveston, Galveston, Texas, 1996.

[44] S. Yamazaki, T. Kaneko, N. Taketomo, K. Kano, T. Ikeda, Biosci. Biotechnol. Biochem. 66 (2002) 2100-2106.

[45] I. Marco, F. Feyerabend, R. Willumeit-Römer, O. van der Biest, TMS2015 Supplemental Proceedings, John Wiley and Sons, Inc., (2015) 497-506.

Chapter 6:

Degradation behaviour of binary Mg-Gd and Mg-Ag alloys for biodegradable implant applications

6.1. Introduction

The current chapter is a continuation of the in vitro study shown in Chapter 4, where in addition to pure Mg, Mg-10Gd and Mg-2Ag also Mg-4Y-3RE (Nd and Ce), Mg-5Gd, Mg-4Ag and Mg-6Ag alloys are studied. Here, the same three in vitro degradation testing conditions from Chapter 4 are applied. The analysis of these alloys permits to distinguish the influence of different parameters with a role in the immersion testing results, such as: alloying additions of RE and Ag, impurity content, grain size and the applied electrolyte. Moreover, the microhardness of these alloys is compared indicating the increase of the mechanical properties due to the alloying additions. Polarization measurements with the RDE are also applied in order to compare the results with the initial DR calculated by the hydrogen evolution during the first day. PDP measurements with RDE are also compared to static measurements, where no rotation is applied, in order to determine the improved reproducibility. Finally, observations on the degradation mechanism of the studied alloys and corrosion product formation are described.

6.2. Experimental methods

6.2.1. Materials and methods

These Mg-based materials produced in disc shape are the same as in Chapter 5 and the material production is also explained in Section 5.2.1. The parameters applied for the material production are summarized in Table 12.

Table 12. Parameters applied for the processing of the studied Mg alloys.

	Casting	Heat treatment		Extrusion			
	T (˚C)	T (˚C)	Duration (h)	T (˚C)	Ø$_{initial}$ (mm)	Ø$_{final}$ (mm)	Speed (mm/s)
pure Mg	680	-	-	300	110	12	0.7
Mg-4Y-3RE	720	550	6	370	30	12	3-4
Mg-5Gd	720	550	6	440	30	12	3-4
Mg-10Gd	720	550	6	440	30	12	3-4
Mg-2Ag	720	420	6	370	30	12	2.5
Mg-4Ag	680	420	6	300	110	12	2.5
Mg-6Ag	720	430	6	370	30	12	2.5

For the microstructure analysis the surface of the samples was prepared by grinding with SiC sandpaper of 1000 grit to 4000 grit (Matador 991A, Remscheid, Germany), and finally by polishing with a diamond suspension of 3 µm (Kemet, Maidstone, England). Then, pure Mg and RE containing alloys were etched in picric acid solution (6g of picric acid, 5mL of acetic acid, 10 mL of H_2O and 100 mL of ethanol) for 2 s, while the etching of Mg-Ag alloys was done as quickly as manually possible (less than 1 s). The grain size was determined by optical microscopy and the linear intercept method applying the software ImageJ (version 1.47v, Wayne Rasband).

The density has been measured with Archimedes's method comparing the mass of the samples in air and in ethanol. The Vicker's microhardness was measured with a FV-700 device (Future-Tech Corp., Tokyo, Japan) at a load of 0.3 kg. The chemical composition and impurity content were determined by inductively coupled plasma optical emission spectroscopy (ICP-OES, Varian 720 ES apparatus). For this analysis, samples are dissolved in nitric acid (70%, Sigma-Aldrich). The impurity content in these alloys are shown in Table 9 in page 133 (Section 5.2.1) and grain size, density and microhardness data are shown in Table 13. The specific microhardness, which is the ratio between microhardness and density is also included in Table 13, since this ratio indicates the improvement in mechanical properties taking into account the increase in density as well.

Table 13. Grain size, density, microhardness and specific microhardness of pure Mg, Mg-4Y-3RE, Mg-Gd and Mg-Ag alloys.

	Grain size µm	Density g/cm^3	HV 0.3 kg/mm^2	Specific microhardness (kg/mm^2)/(g/cm^3)
pure Mg	22.6	1.730	43.8±3.2	25.3
Mg-4Y-3RE	6.3	1.811	104.6±19.3	57.8
Mg-5Gd	5.9	1.786	60.0±6.0	33.6
Mg-10Gd	17.8	1.854	87.8±12.3	47.4
Mg-2Ag	43.7	1.762	49.0±4.0	27.8
Mg-4Ag	31.6	1.785	54.8±5.1	30.7
Mg-6Ag	34.6	1.815	58.9±4.0	32.5

6.2.2. In vitro testing

Similarly as in Section 5.2.2, the two different testing setup configurations were applied using PBS and HBSS as in Fig.37a and DMEM as in Fig. 37b. As explained in Section 5.2.2. (pages 134-136), UV-C radiation and antibiotics (penicillin-streptomycin) were applied to avoid the influence of contamination when DMEM was used under physiological conditions. The degradation rate (DR) is calculated from the mass loss and from the hydrogen generated as explained in Section 4.2.2. The chromic acid treatment, the surface preparation, the CO_2 control, the pH measurement, the sample surface finishing and the temperature control were also applied as explained in the same section. XRD analysis of the degradation layer was done as explained in Section 3.2.3. Experiments were performed with six samples of each alloy. Under physiological conditions an empty control position was used without a sample in order to see the gas accumulation and pressure fluctuations due to artifacts. The solution volume to sample surface ratio (V/S) applied in this study was 30 ml/cm^2 for PBS and HBSS testing and 50 ml/cm^2 for immersion in DMEM. The testing duration under physiological conditions, in DMEM, was 4-5 days while in PBS and HBSS it was 4-7 days.

The composition of the different used media in comparison with body plasma was shown in Chapter 1 (Table 2, page 36). Generally, in these media, ions like Ca^{2+} , HCO^{3-}, HPO_4^{2-} and SO_4^{2-} are present and they inhibit the detrimental effect of Cl^- [1]; but the main component of all the media was NaCl, in some cases with rather high concentration compared to body plasma. Thus special attention must be paid to different level of Cl^- due to its great influence on Mg degradation. PBS includes 11.98 mM of potassium phosphate monobasic (KH_2PO_4) and 2.06 mM of sodium phosphate dibasic (Na_2HPO_4) anhydrous. HBSS contains less than 0.5 mM amount of these two phosphate ions and also 4.17 mM of carbonate ions (HCO_3^-) as buffering compounds.

6.2.3. Polarization measurements

The potentiodynamic polarization experiments with the rotating disc electrode (RDE) and those under non-dynamic conditions were performed as explained in Section 3.2.2 with the same electrochemical cell setup. PBS, HBSS and DMEM were used as electrolytes at 37±0.5°C for these measurements. The surface preparation was done by grinding with 1000 and then 4000 grit SiC paper, and polishing with a 3 µm diamond suspension. Finally, the corrosion current density calculation was done with the Tafel extrapolation as explained in Section 3.2.2. The conductivities of PBS, HBSS and DMEM at 37°C are 20.5, 13.7 and 21.3 mS/cm, respectively.

6.3. Results

6.3.1. Microhardness

The density and microhardness of the alloys used for this study are indicated in Table 13. The microhardness increase in Mg-Gd alloys is noteworthy. For extruded pure Mg the determined microhardness is 43.8 kg/mm^2; while Mg-5Gd shows 60 kg/mm^2 (37% higher), and Mg-10Gd 87.8 kg/mm^2 (2 times higher). This increase is due to precipitation hardening and the positive influence of the Gd atoms in solid solution. Mg-Ag alloys, for instance, show hardness values between 49 and 59 kg/mm^2. The density, however, also increases with the introduction of alloying additions. The ratio microhardness/density can indicate the mechanical strength of the Mg alloy taking into account the material weight. According to this ratio the ranking of the studied alloys remains the same as the microhardness ranking but with reduced differences. Mg-4Y-3RE and Mg-10Gd show the highest improvement, then Mg-5Gd and Mg-Ag alloys. Mg-Ag alloys show a small increase as compared to pure Mg which, as expected, is the last one in the ranking. The highest increase includes a RE alloying addition of 7 to 10 wt.%. The improvement in specific microhardness is 128% and 87%, for Mg-4Y-3RE and Mg-10Gd respectively. Mg-5Gd shows an increased microhardness of approximately 33%. Mg-Ag alloys show that 2-6 wt.% of Ag increases specific microhardness of the alloy between 10% and 28% with increasing values with the higher Ag content.

6.3.2. Microstructure

Microstructure images of the studied alloys are shown in Fig. 54. On the one hand, pure Mg and Mg-10Gd show a relatively large grain size, 22.6 and 17.8µm respectively, while Mg-4Y-3RE and Mg-5Gd have a grain size of 6.3 and 5.9µm, respectively. Mg-Ag alloys, on the other hand, were produced with a relatively large grain size: Mg-2Ag 43.7µm, Mg-4Ag 31.6µm and Mg-6Ag 34.6µm. As shown in Fig. 55b, a large amount of secondary phases and precipitated intermetallics have been observed in Mg-4Y-3RE due to the presence of Y, Nd and Ce [2, 3].

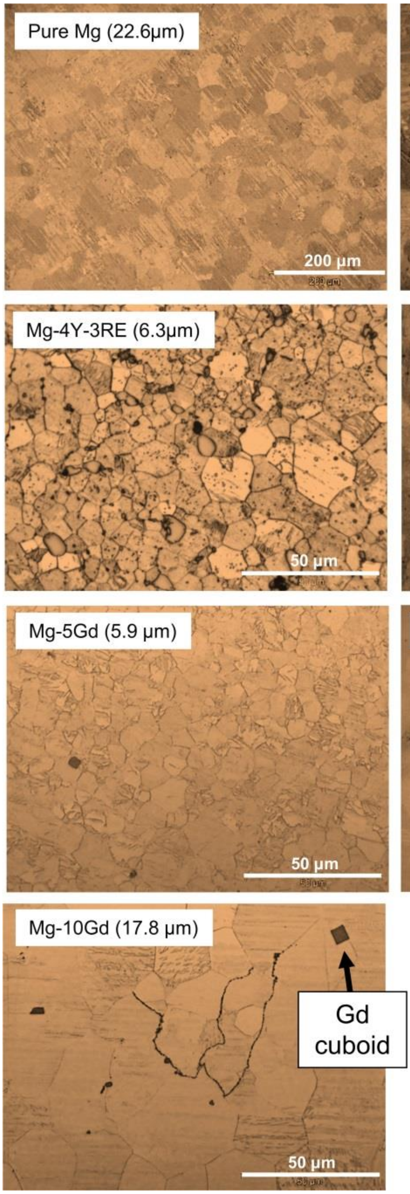

Figure 54. Optical microscopy images show the bigger grain size of Mg-Ag alloys. Pure Mg and Mg-10Gd have a medium grain size and Mg-4Y-3RE and Mg-5Gd a small grain size (±6 µm). Precipitation and Gd rich cuboids are identified in Mg-RE alloys.

Similarly, Mg-Gd alloys show the precipitation of Gd with impurities and Gd rich cuboids can also be found (Fig. 55a), as mentioned in Sections 4.4.1 and 5.4.1. Qiuming et al. observed GdH_2 cubic particles in Mg-Gd alloys [4]. Thus, these cubes could be GdH_2 particles forming during the casting due to the moisture in the air leading to hydrogen generation during the casting. The presence of DyH_2 has also been proven in Mg-20Dy alloys which similarly could also precipitate with other RE elements [5]. Fig. 54a depicts variations in Gd content in the BSE image which are aligned with the extrusion direction. Similar variations in alloy composition have also been found in Mg-2Ag and Mg-6Ag alloys. However, Mg-4Ag samples do not show these Ag concentration gradients. Perhaps, this could be related to the different extrusion and casting temperature applied to Mg-4Ag.

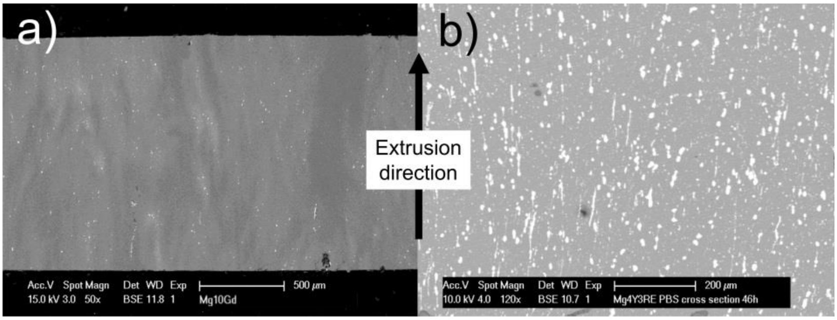

Figure 55. SEM images showing (a) the inhomogeneous distribution of Gd in Mg-10Gd and (b) secondary phases in Mg-4Y-3RE both oriented in the extrusion direction. Bright areas in both images indicate the presence of a heavier element than Mg, in this case, Gd, Ce, Y and Nd.

6.3.3. Immersion testing

a) Hydrogen and pH evolution

The hydrogen and pH evolution has been studied in three different media, finding a different behaviour for almost every Mg based material in each media. Figs. 56 and 57 show, respectively, the gas and pH evolution as a function of time. In PBS and HBSS an approximately linear H_2 evolution is registered. However, the slopes are different depending on the tested material. On the one hand, pure Mg, Mg-4Y-3RE, Mg-5Gd and Mg-10Gd show a similar H_2 evolution in PBS and HBSS. Hank's solution is slightly more aggressive than PBS to these alloys. The pH also shows higher values in HBSS (9-9.5) than in PBS (<8.5) during the entire immersion time, demonstrating that HBSS has a weak buffering power. On the other hand, Mg-Ag alloys have a higher H_2 slope in PBS than in HBSS with similar pH values (9.5-10.5) comparing between these alloys.

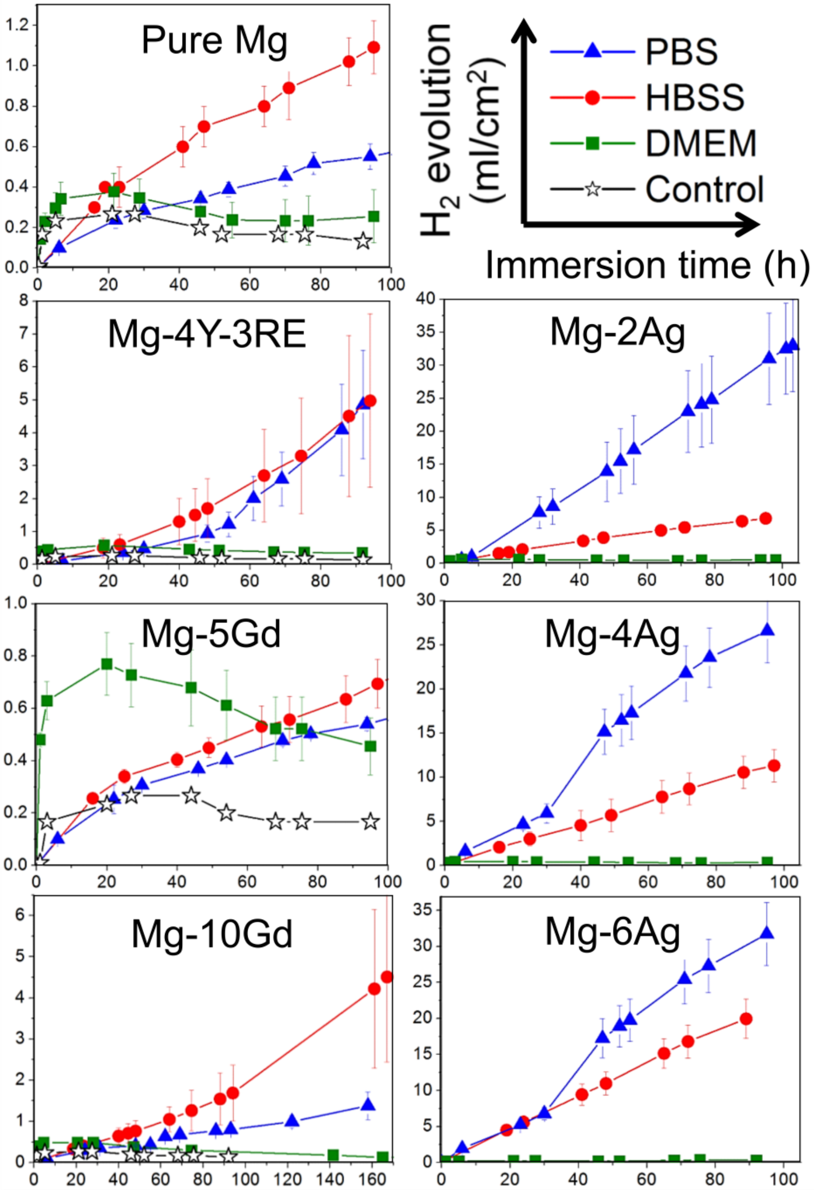

Figure 56. Mean hydrogen evolution during immersion testing for 4-7 days in PBS, HBSS and DMEM of pure Mg, Mg-4Y-3RE, Mg-Gd and Mg-Ag alloys. The position control is only applied in tests with DMEM as electrolyte.

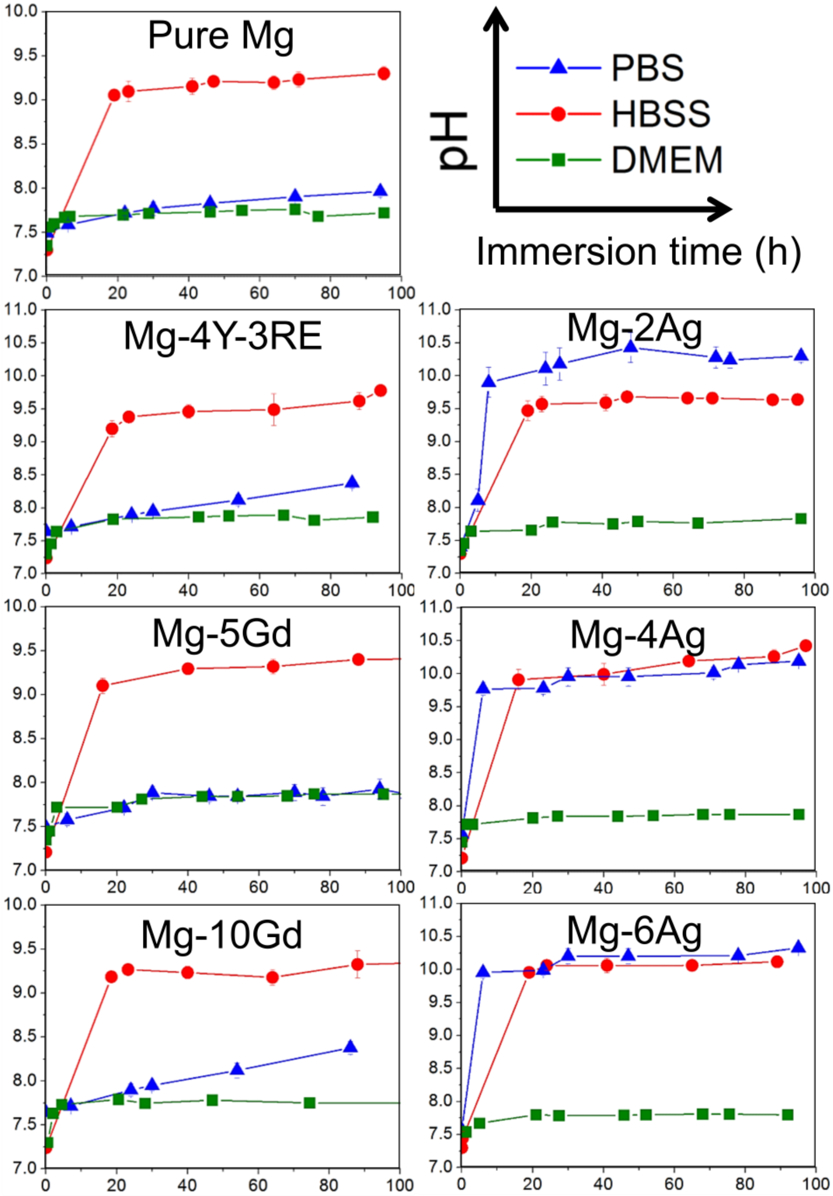

Figure 57. Mean pH evolution during immersion testing of pure Mg, Mg-4Y-3RE, Mg-Gd and Mg-Ag alloys in PBS, HBSS and DMEM for 4 days.

As reported in Section 4.3.1a, in DMEM the corrosion process of these Mg based alloys is slower. There is a first gas increase during the first 10h reaching a maximum collected gas of 0.4-0.8 ml/cm^2. Then, the bubbles decrease during the rest of the immersion time with an approximate rate of 0.1 ml/cm^2/day. With a position control sample (without sample) a similar gas evolution is registered, but lower in volume, proving that some gas is CO_2 from the buffering system. Due to the nature of the corrosion process of Mg the rest must be H_2. The gas volume detected at the control position can be deducted from that collected above the samples in order to calculate the DR. This fact is also discussed in Section 5.3.1, where the corrosion tests in DMEM are assessed. Thus similarly as in Section 5.3.1, the hydrogen dissolved in the liquid has been added to the gas data since H_2 will only be collected when the electrolyte is saturated.

b) Optical macrographs

Fig. 58 contains macro images of the samples after the testing in the three media and after the chromic acid corrosion product removal.

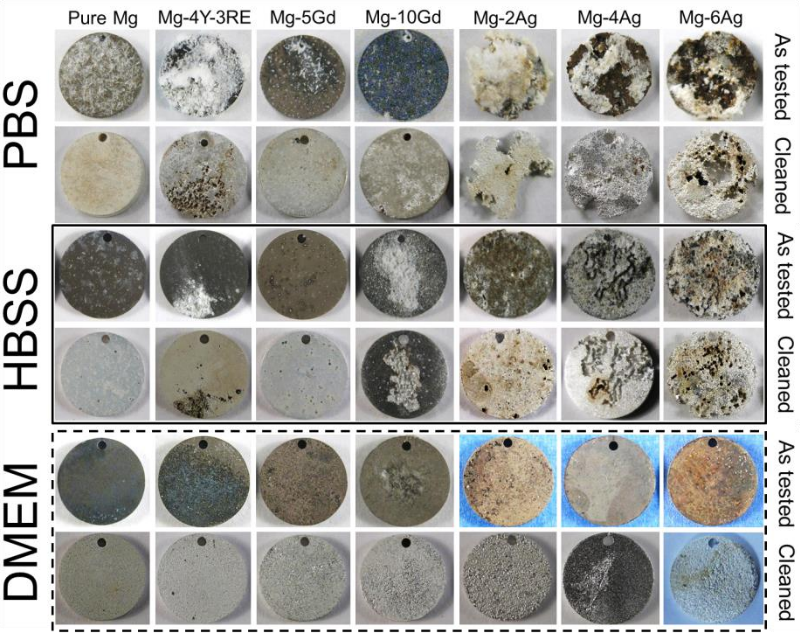

Figure 58. Optical macrographs of samples as tested in PBS, HBSS and DMEM and after chromic acid cleaning.

In PBS and HBSS, severe localized and pitting corrosion can be seen on Mg-Ag alloys, while pure Mg and Mg-Gd alloys show generally an homogeneous corrosion mode, although pits can also be found by SEM imaging. The corrosion of Mg-4Y-3RE is localized at some sites but by and large it is homogeneous. This corrosion mode could be attributed to the presence of secondary phases. The corrosion products formed under these conditions can be very voluminous and in case of PBS they remain mostly attached to the sample, while generally, in HBSS they get suspended in the solution, as shown in Section 6.3.6.

As shown previously in Section 5.3.6, a less aggressive degradation process is observed in DMEM. In this case, homogeneous corrosion is identified for every Mg-based material, with small differences. Under these conditions a homogeneous degradation layer is deposited which protects the sample from the electrolyte, and no voluminous corrosion products are observed.

c) Degradation rate (DR)

As mentioned in Section 6.2.1, DRs are calculated from mass loss and from hydrogen generation. The DR, the mass difference between before and after the testing, denoted as mass reduction (MR), and the mass difference between before and after the chromic acid treatment, denoted as degradation layer mass (DLM), are summarized in Table 14. The DR given by mass loss and by the H_2 gas at the end of the immersion is shown Fig. 59c. Mass loss and H_2 methods correlate closely. The DRs given by these two methods show systematically slightly higher values by mass loss than H_2. This can be explained with the particle undermining model [6], and perhaps the dissolution of hydrogen in the Mg sample [7-9].

The mass reduction and the degradation layer mass are found to be proportional to the DRs. It is noteworthy that in PBS slow degrading samples do not reduce their total mass including the degradation layer; hence these materials increase by between 0.6 and 1.8% of their mass during the test. Similarly, Mg-2Ag shows this behaviour in HBSS, gaining 3.7% of mass, despite the fact that its degradation layer mass is the highest of all these alloys. This shows how voluminous and thick the corrosion products can get, by forming compounds between Mg and species present in the electrolyte (OH^-, PO_4^{2-} or CO_3^{2-}).

The H_2 evolution also allows the calculation of the DR as a function of the immersion time. Fig. 59 shows the DR evolution in the three media. In parallel to the results shown in Fig. 56 and Fig. 58, Mg-Ag alloys show the highest DR in PBS and HBSS. In PBS Mg-Ag rates increase and then stabilize, while Mg-Gd and pure Mg have a stable low DR. Mg-4Y-3RE show an exponential trend in PBS, as well as in HBSS. The DRs in HBSS are stabilized during the entire immersion duration. In DMEM the DR evolution shows a first high rate and when the degradation layer develops this rate is reduced, reducing the differences between all the Mg alloys.

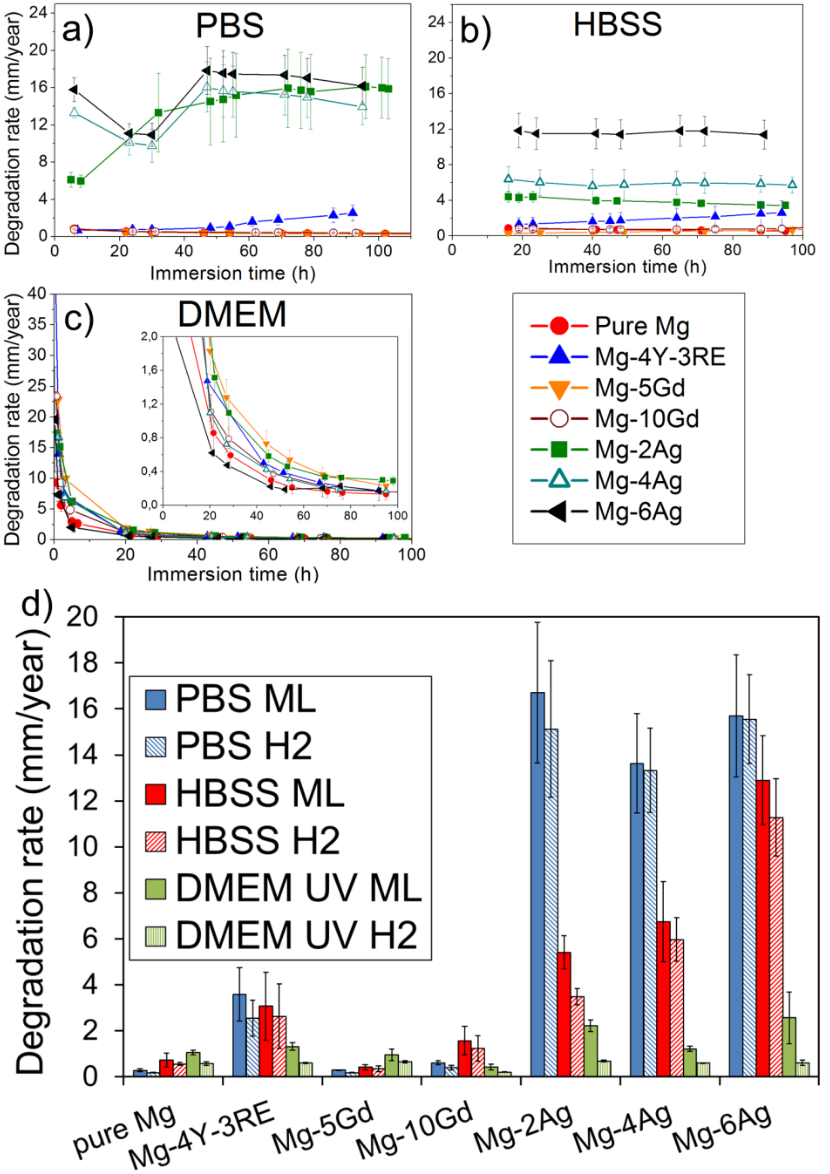

Figure 59. The degradation rate (DR) evolution in PBS (a), HBSS (b) and DMEM (c). Rates are stable in the first two media while in DMEM there is a higher first rate but when the degradation layer develops this rate is reduced, also decreasing the rate differences between alloys. d) shows the DR calculated for the last time point by mass loss and H_2 gas.

Table 14. Degradation rates in mm/year calculated by mass loss (DR ML) and H_2 evolution (DR H_2), mass reduction in % (MR) and degradation layer mass in mg (DLM) data.

Materials	PBS				HBSS				DMEM			
	DR ML (mm/year)	DR H_2 (mm/year)	MR (%)	CLM (mg)	DR ML (mm/year)	DR H_2 (mm/year)	MR (%)	CLM (mg)	DR ML (mm/year)	DR H_2 (mm/year)	MR (%)	CLM (mg)
pure Mg	0.3	0.2	-0.7	3.1	0.7	0.6	0.3	2.1	1.1	0.6	0.5	3.1
Mg-4Y-3RE	3.6	2.6	-1.8	17.1	3.1	2.6	0.6	9.2	1.3	0.6	0.4	4.3
Mg-5Gd	0.3	0.2	-0.6	3.0	0.4	0.3	0.3	3.3	1.0	0.6	0.6	5.4
Mg-10Gd	0.6	0.4	-0.7	5.5	1.6	1.2	0.7	9.8	0.4	0.2	0.2	3.3
Mg-2Ag	16.7	15.1	12.6	52.1	5.4	3.5	-3.7	25.0	2.2	0.7	1.6	5.8
Mg-4Ag	13.6	13.3	9.9	34.4	6.8	6.0	5.2	16.9	1.2	0.6	1.9	5.1
Mg-6Ag	15.7	15.6	12.0	39.5	12.9	11.3	12.2	23.3	2.6	0.6	2.0	6.2

6.3.4. Polarization measurements with RDE

Fig. 60 compares the polarization curves obtained under static and under dynamic conditions, with the use of the RDE, of the studied Mg alloys in PBS. A schematic representation of how i_{corr} and E_{corr} are calculated is also shown Fig. 60.

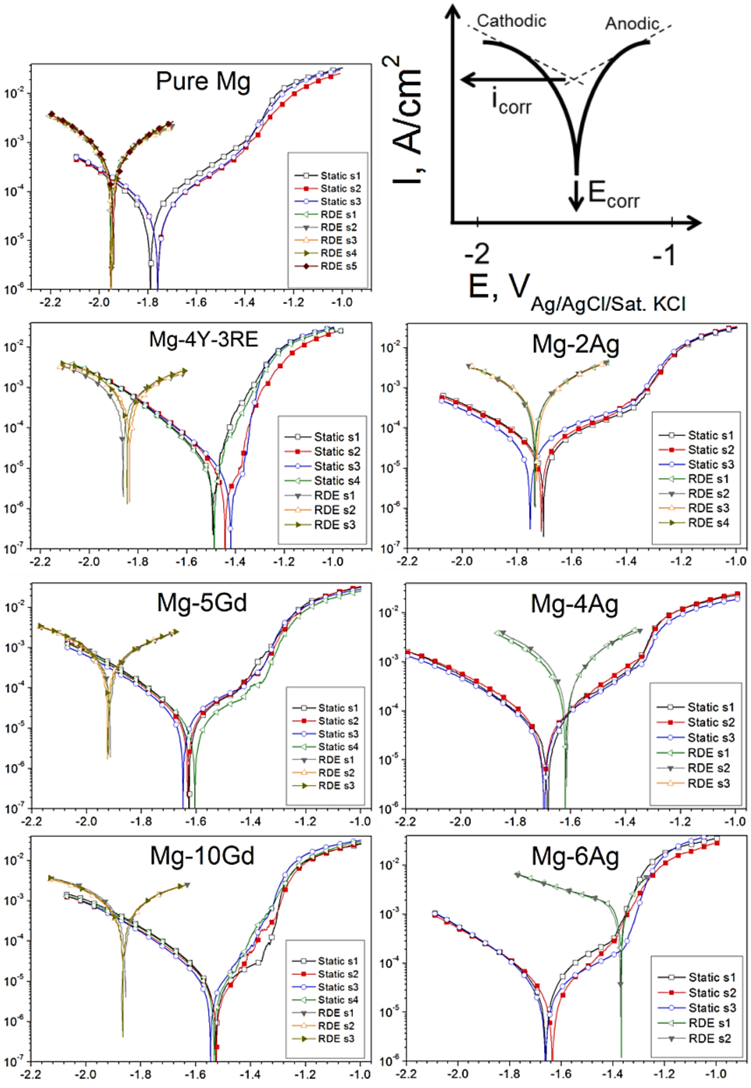

Figure 60. Polarization curves of pure Mg, Mg-4Y-3RE, Mg-Gd and Mg-Ag alloys in PBS at 37±0.5°C (5 mV/s) comparing static and dynamic conditions (2000 rpm) with a rotating disc electrode (RDE). Under static conditions 3-4 samples were applied while under stirring at 2000 rpm 2-5 samples were used. Results with the RDE show systematically higher i_{corr} values and a shift of E_{corr}.

The corrosion potential (E_{corr}) is shifted towards anodic values under static conditions with pure Mg, Mg-4Y-3RE and Mg-Gd alloys while the corrosion potential of Mg-Ag shows a shift towards more negative values as compared to measurement with the RDE. The measured current densities (i_{corr}) by Tafel extrapolation also show higher values when no rotation is applied. As mentioned in Section 3.3.6, no pronounced anodic curves are determined with the RDE which is related to the lack of degradation layer deposition and the enhanced catalytic surface theory. The i_{corr} and E_{corr} shifts are also related to the influence of the degradation layer deposition. As mentioned in section 3.3.2, the presence of a layer between the Mg sample and the electrolyte can represent a potential step. The electron exchange rate between anodic and cathodic reactions will be slowed down by this degradation layer. Finally, when rotation is applied, the same polarization curve is obtained repeatedly for each Mg alloy while under static conditions these curves show a slightly larger deviation.

Tables 15 and 16 show, i_{corr} and E_{corr} data, respectively, from the above mentioned comparison. In addition, measurements with DMEM in both conditions, and HBSS with the RDE are also included. i_{corr} values are higher when the RDE is applied in PBS and HBSS (>5 A/m^2) compared to static conditions in PBS (<0.6 A/m^2). However, in DMEM i_{corr} is lower under dynamic conditions (<0.62 A/m^2) than under static ones (>0.8 A/m^2), except for Mg-4Ag and Mg-6Ag.

Table 15. Current density (i_{corr}) in A/m^2 determined by the Tafel extrapolation under static conditions in PBS and DMEM, and under dynamic conditions (2000 rpm) in PBS, HBSS and DMEM. The i_{corr} data shown is the mean with indication of the standard deviation.

	Static		RDE		
	PBS	DMEM	PBS	HBSS	DMEM
Pure Mg	0.57±0.18	2.19±0.21	5.47±0.25	7.93±0.26	0.405±0.021
Mg-4Y-3RE	0.07±0.05	2.41±1.41	7.03±0.64	7.37±0.07	0.212±0.064
Mg-5Gd	0.17±0.04	1.09±0.49	6.23±0.68	7.20±0.48	0.204±0.092
Mg-10Gd	0.07±0.02	1.20±0.48	7.88±0.65	6.96±0.01	0.420±0.161
Mg-2Ag	0.39±0.01	1.03±0.29	6.07±0.20	9.27±0.85	0.620±0.176
Mg-4Ag	0.41±0.05	0.86±0.44	7.83±0.86	12.33±2.64	1.183±0.053
Mg-6Ag	0.40±0.16	1.16±0.48	14.58±0.92	22.9±2.40	1.873±0.382

Interestingly, Mg-Ag alloys show, under rotation, an increased i_{corr} in the three electrolytes corresponding to an increasing amount of the Ag content. In contrast, under static conditions there is not such a trend.

As shown in Table 16, E_{corr} also shows a considerable shift when rotation is applied. Pure Mg shows more cathodic values with the RDE in PBS and HBSS, closer to the standard reduction potential of Mg at 25°C, -2.37 V vs standard hydrogen electrode, except in DMEM. In the case of dynamic measurement, E_{corr} of Mg-Ag alloys trend to increase towards more noble values. This trend could be explained by a faster degradation process which promotes the degradation product formation on the surface shifting the measured potentials, even when rotation is applied. Under static conditions, Mg-Ag alloys do not show the highest E_{corr} values indicating the stochastic influence of applying static conditions. The standard deviation of E_{corr} in PBS is generally lower with the RDE. However, there are some exceptions which could be due to differences in sample impurity level and composition. In any case, the use of the RDE seems to increase the reproducibility.

Table 16. Corrosion potential (E_{corr}) in V vs Ag/AgCl electrode sat. KCl measured by linear sweep polarization under static conditions in PBS and DMEM, and under dynamic conditions (2000 rpm) in PBS, HBSS and DMEM. The E_{corr} data shown is the mean with indication of the standard deviation.

	Static		RDE		
	PBS	DMEM	PBS	HBSS	DMEM
Pure Mg	-1.767±0.016	-1.920±0.032	-1.947±0.004	-1.969±0.007	-1.841±0.010
Mg-4Y-3RE	-1.458±0.037	-1.708±0.051	-1.843±0.007	-1.877±0.031	-1.605±0.003
Mg-5Gd	-1.636±0.024	-1.769±0.030	-1.916±0.004	-1.967±0.002	-1.709±0.036
Mg-10Gd	-1.532±0.010	-1.689±0.042	-1.857±0.005	-1.930±0.002	-1.730±0.032
Mg-2Ag	-1.730±0.038	-1.749±0.039	-1.744±0.009	-1.626±0.006	-1.758±0.025
Mg-4Ag	-1.692±0.007	-1.633±0.045	-1.617±0.004	-1.487±0.007	-1.724±0.009
Mg-6Ag	-1.652±0.016	-1.641±0.023	-1.369±0.003	-1.474±0.049	-1.675±0.021

6.3.5. Initial degradation rates

Fig. 61 compares the initial DR calculated from the gas collected at the first timepoint to the DR determined when the RDE is applied. The i_{corr} determined for each Mg alloy can be transformed into DR by the Stern-Geary equation [10]. The DR from i_{corr} with the RDE data is depicted in Fig. 61a. For comparison, Fig. 61b shows the initial degradation calculated from the hydrogen evolution. This data is determined by the initial hydrogen evolution at the first time point as indicated in Fig. 59a-c.

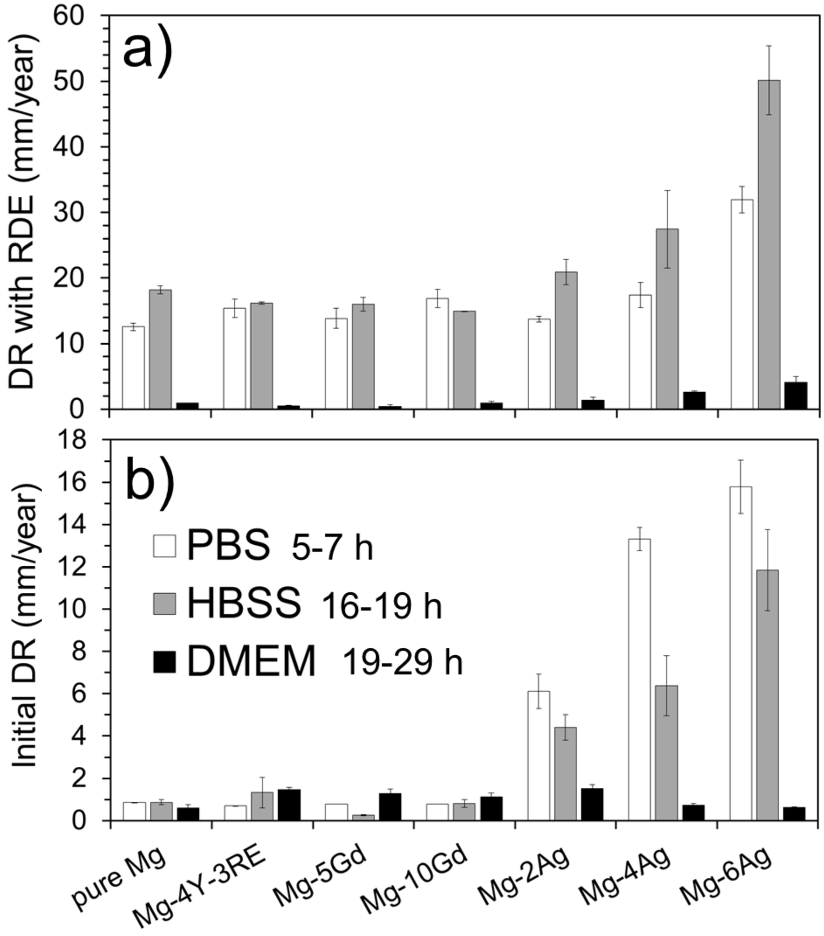

Figure 61. Comparison of (a) DRs obtained by polarization experiments and (b) initial DR calculated from the hydrogen evolution of the studied alloys in PBS, HBSS and DMEM. The timepoint when the DR is calculated by the H_2 generation for each media is indicated next to the legend.

It can be observed in Fig. 61a that pure Mg, Mg-4Y-3RE, and Mg-Gd alloys show similar initial DRs which are lower than 2 mm/year. As mentioned above, Mg-Ag alloys have an increasing current density with increasing amount of Ag, which is also indicated by the higher initial DR also with increasing amount of Ag.

In Fig. 61b, it is noteworthy that a lower initial DR is measured for Mg-2Ag in PBS as compared to the long term DR, shown in Fig. 59a. This change is not observed for the other Mg-Ag alloys. Conversely, the initial DRs of Mg-Ag alloys in DMEM are not significantly higher than the rest of the studied alloys. This is because the initial gas evolution in DMEM is not accurately representing the corrosion process.

Thus, it is possible to observe a similar trend for these Mg alloys, so that the DR determined by polarization experiments with the RDE might approximate the initial degradation behaviour of the Mg based material. However, DRs determined by linear polarization provide higher values than the ones calculated from the initial hydrogen evolution.

6.3.6. Corrosion products in HBSS

During degradation testing in HBSS, especially with Mg-Ag alloys, a large amount of corrosion products suspended in the electrolyte can be observed, as shown in Fig. 62a. These products can be collected after the test by evaporating the electrolyte and collecting the powder. These corrosion products, from Mg-4Ag test, have been analysed with XRD technique (Fig. 62b). Mainly Mg hydroxide is detected, although traces of AgCl, AgO_2 and Ag are also identified. This powder collection has been done after every immersion test in HBSS allowing its quantification (Fig. 62c). Pure Mg and Mg-5Gd produce the smallest amount of suspended corrosion product, 1.7 mg/sample; then Mg-10Gd, Mg-2Ag and Mg-4Y-3RE, 10.8, 6.5 and 8.0 mg/sample, respectively; and finally Mg-4Ag generates 81.9 mg/sample and and Mg-6Ag 82.7 mg/sample. This indicates the pronounced influence of Ag on Mg-Ag alloys corrosion.Taking into accound that one sample weighs approximately 180 mg, these corrosion products are not negligible. Perhaps these results also indicate that the tolerance limit of Ag in these alloys might be between 2 and 4 wt.% when tested in HBSS.

The reason why this powder has not been analysed in PBS or DMEM is because during immersion tests in PBS these products remain attached to the sample and in DMEM corrosion product release is not observed.

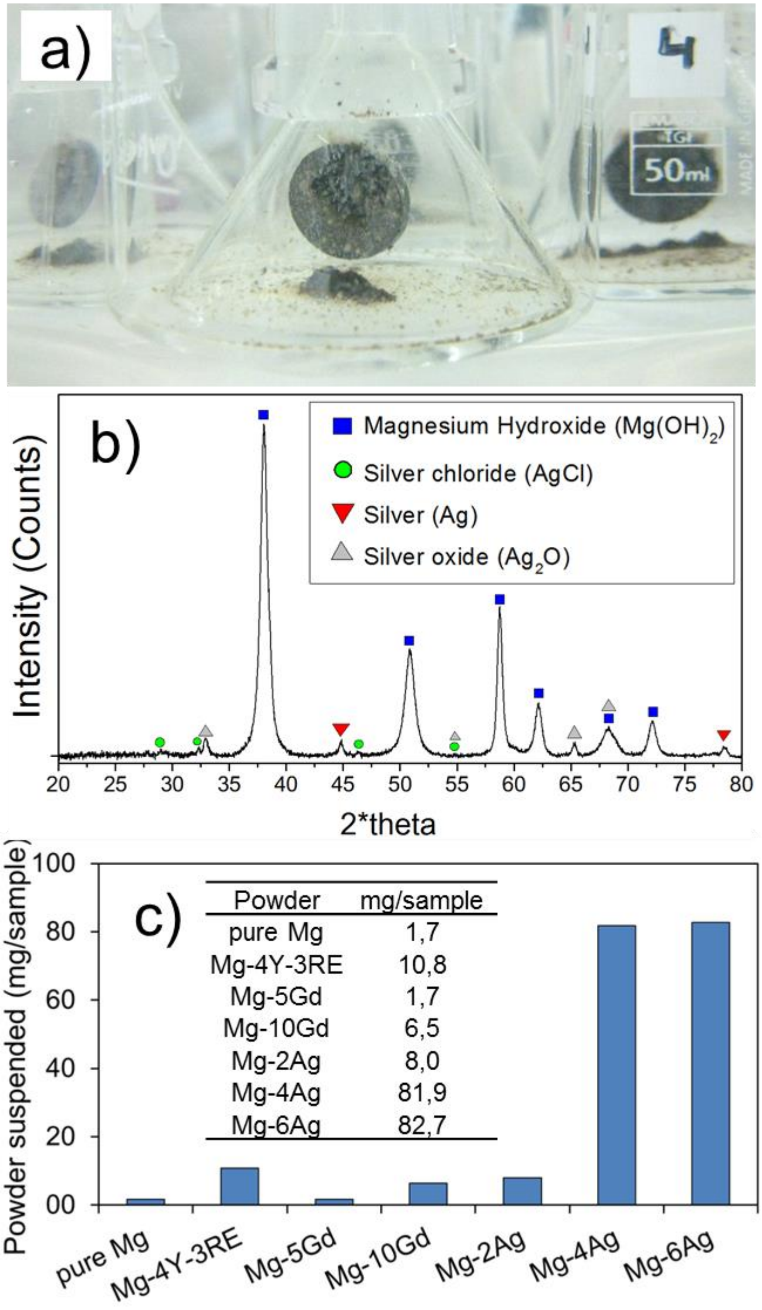

Powder	mg/sample
pure Mg	1,7
Mg-4Y-3RE	10,8
Mg-5Gd	1,7
Mg-10Gd	6,5
Mg-2Ag	8,0
Mg-4Ag	81,9
Mg-6Ag	82,7

Figure 62. Corrosion products deposited in HBSS during Mg-4Ag testing. (a) is a picture taken during the immersion test. (b) shows the powder characterization with XRD. (c) shows the gravimetric quantification of the powder formed during testing of the Mg based materials.

6.3.7. Degradation layer

The degradation layer has been previously analysed in Section 4.3.4.a by elemental mapping analysis. Additionally, the degradation layer formed in DMEM is also studied by SEM-EDX in Section 5.3.4. In the current section, the degradation layer has been characterized by SEM imaging in back-scattered electron (BSE) mode to get elemental contrast and with EDX to analyse qualitatively the elements composing this layer. This SEM-EDX analysis also allows identifying the corrosion mechanisms of pure Mg in the three media applied: PBS, HBSS and DMEM.

Pitting and underfilm corrosion have been observed in PBS (Figs. 63a and b). Underfilm corrosion can be observed by the porosity found underneath the degradation layer and pitting corrosion by the $Mg(OH)_2$ channels formed in the material. In these channels also Cl can be found, as shown in Fig. 63a (EDX 2). The degradation layer is made of $Mg(OH)_2$ and $Mg-PO_4$, with traces of Na and K (Fig. 63a EDX 1) and also K and P rich crystals (Fig. 63c).

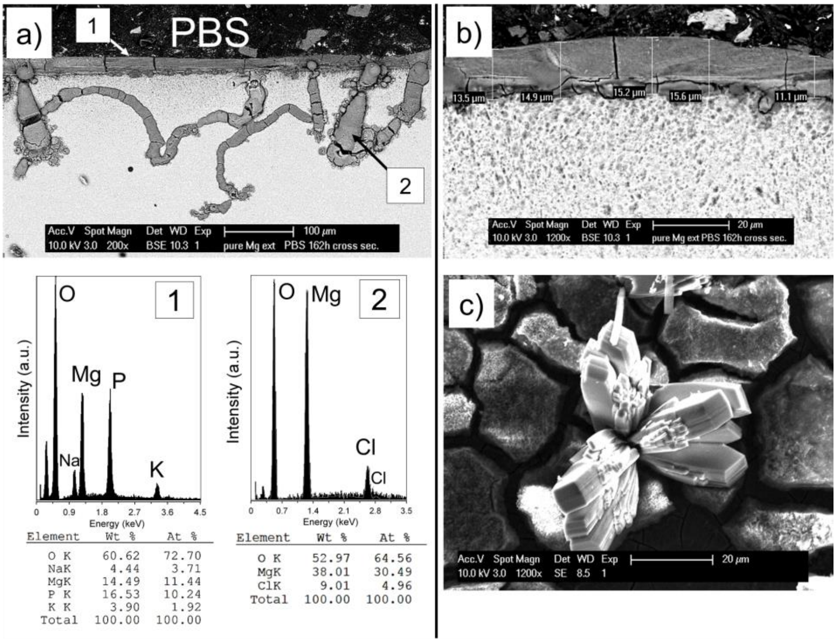

Element	Wt %	At %
O K	60.62	72.70
NaK	4.44	3.71
MgK	14.49	11.44
P K	16.53	10.24
K K	3.90	1.92
Total	100.00	100.00

Element	Wt %	At %
O K	52.97	64.56
MgK	38.01	30.49
ClK	9.01	4.96
Total	100.00	100.00

Figure 63. SEM-EDX analysis of the degradation layer formed on pure Mg tested in PBS for 162 h with a V/S ratio of 40. (a) shows the homogeneous and pitting corrosion modes. EDX point analysis of the degradation layer (point 1) and the products formed inside the channels (point 2) are also shown. (b) shows the porosity under the corrosion layer formed which

indicates underfilm corrosion mode. (c) depicts a K-PO_4 crystal formed on top of the corrosion layer, which could be quite voluminous in case of fast degrading alloys (see Fig. 58, Mg-Ag alloys).

Fig. 64 shows the SEM-EDX analysis of the degradation layer formed in HBSS. As in PBS, pitting (Fig. 64a) and underfilm (Fig. 64b) corrosion modes are also observed in HBSS with a slightly different degradation layer composition. In this case the PO_4^{3-} content is lower and HCO_3^- is included, thus the degradation layer is mainly formed by $Mg(OH)_2$, Mg-PO_4 with traces of Na (Fig. 64a EDX 1). Additionally, C is also detected indicating that a small amount of Mg carbonate could precipitate. This carbonate could also include traces of Ca at some sites. As shown in Fig. 64a EDX 2, Cl has also been detected at the channels formed by pitting.

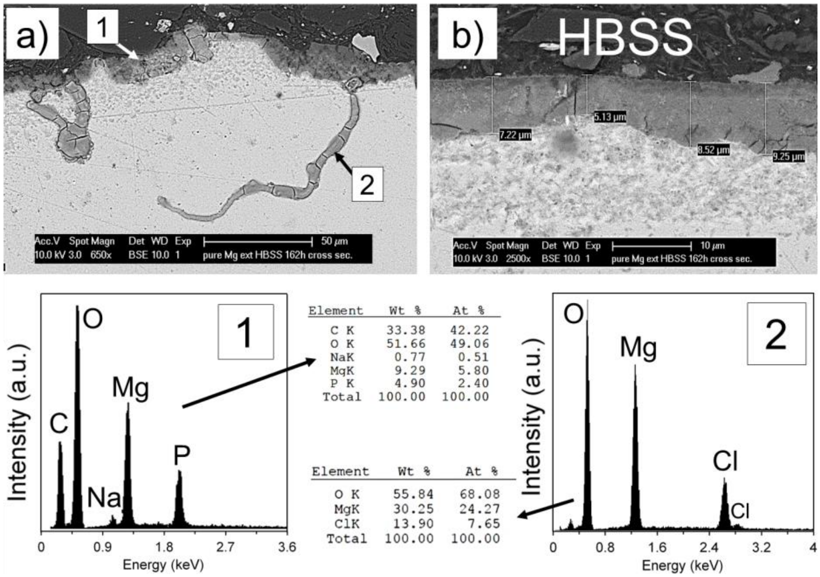

Element	Wt %	At %
C K	33.38	42.22
O K	51.66	49.06
NaK	0.77	0.51
MgK	9.29	5.80
P K	4.90	2.40
Total	100.00	100.00

Element	Wt %	At %
O K	55.84	68.08
MgK	30.25	24.27
ClK	13.90	7.65
Total	100.00	100.00

Figure 64. SEM imaging and EDX elemental analysis of the degradation layer formed on pure Mg tested in HBSS for 311 h with a V/S ratio of 40. (a) shows an overview of the degradation modes: uniform and pitting corrosion. EDX point analysis of both degradation layer (point 1) and products formed inside the pitting channels (point 2) are also shown. (b) shows also porosity under the 10 µm thick degradation layer indicating the underfilm corrosion mechanism.

In contrast, the degradation layer formed in DMEM differs from the previous results. In DMEM, the degradation layer is composed of $Mg(OH)_2$ and $(Mg,Ca)CO_3$ as a first layer, with a thin (Mg,Ca)-PO_4 layer on top (Fig. 65b, c and d). EDX analysis of point 1 from Fig. 65b shows the presence of O and

Mg with traces of C and Ca at the first layer formed. EDX from point 2 (Fig. 65b), for instance, shows a higher Ca and P content. This different layer composition, as compared to the layers formed in PBS and HBSS, is due to the high content of HCO_3^- and the presence of Ca^{2+} in the electrolyte.

As shown in Fig, 65a, the degradation mode is homogeneous, although some sites can differ from others regarding the corrosion layer thickness and the presence or absence of the (Mg,Ca)-PO_4 containing layer. Areas with a thin degradation layer (<1 µm) can also be found. The sites covered by a thin layer are considered to act as cathodic sites. These sites promote the hydrogen reaction and they are composed of secondary phases or precipitates containing REE as shown later in Fig. 67b. Porosity at some sites of the $Mg(OH)_2$ and (Mg,Ca)CO_3 containing layer has also been found (Fig. 65e). This porosity could be one way for the electrolyte to reach the Mg surface.

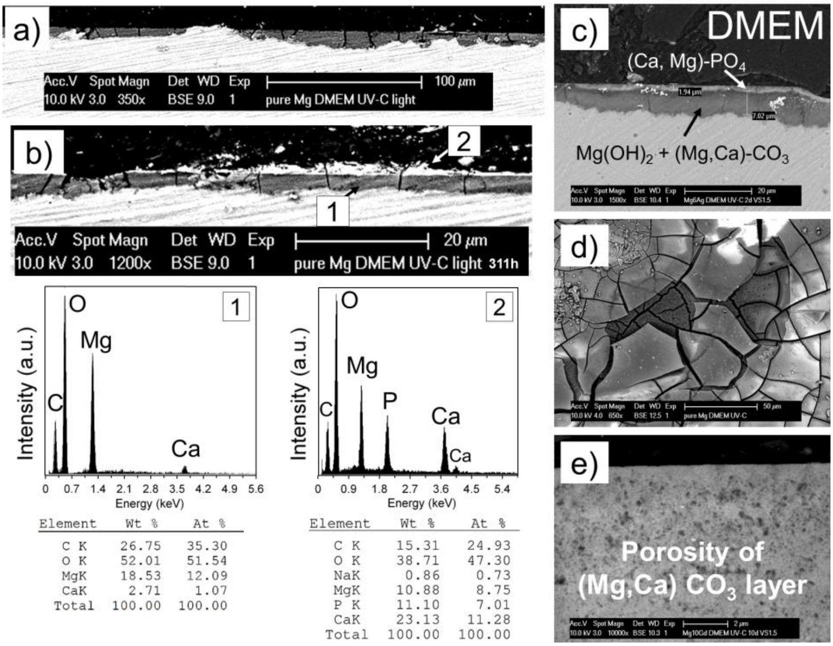

Element	Wt %	At %
C K	26.75	35.30
O K	52.01	51.54
MgK	18.53	12.09
CaK	2.71	1.07
Total	100.00	100.00

Element	Wt %	At %
C K	15.31	24.93
O K	38.71	47.30
NaK	0.86	0.73
MgK	10.88	8.75
P K	11.10	7.01
CaK	23.13	11.28
Total	100.00	100.00

Figure 65. SEM-EDX analysis of the degradation layer formed in pure Mg tested in DMEM for 311 h with a V/S ratio of 40. (a) shows a site of the degradation layer where only one layer is found, while (b) shows a site with two layers. As indicated in (c) these two layers are: $Mg(OH)_2$ and (Mg,Ca)-CO_3 as a first layer forming, and (Mg,Ca)-PO_4 layer is the second layer formed on top of the first one. (d) shows the top view of the these layers at a damaged region. (e) indicates that the (Mg,Ca)-CO_3 containing layer is porous at some sites.

6.4. Discussion

In general, results of this study reveal different degradation behaviour of pure Mg, Mg-4Y-3RE, Mg-Gd and Mg-Ag alloys. These results depend on both the testing conditions applied and composition and microstructure of the material.

6.4.1. Corrosion modes

The main corrosion modes observed in PBS and HBSS are homogeneous and underfilm corrosion with most of the tested materials. At some sites, the influence of pitting corrosion is also identified. In contrast to other alloys, Mg-Ag alloys show severe localized corrosion in PBS and HBSS (Fig. 58). In DMEM homogeneous and at some sites underfilm corrosion is identified. The different corrosion modes observed for the same Mg based material indicates the importance of the composition of the applied electrolyte. In this case, a lower Cl^- level and the presence of Ca^{2+} and HCO_3^- ions in the electrolyte seem to promote a more protective degradation layer. Also the CO_2 buffering applied can have an influence since it adds HCO_3^- ions to the solution, and it keeps the system within the physiological pH range at 7.8±0.1 (Fig. 57). These conditions seem to promote the homogeneous degradation mode.

6.4.2. Degradation layer models

Fig. 66 depicts schematically the degradation layers formed on pure Mg in PBS, HBSS and DMEM. As presented in Section 6.3.7, the degradation layer formed in PBS is mainly formed by $Mg(OH)_2$ and $Mg\text{-}PO_4$ (Fig. 66a). In general, these two structures are mixed in a non-distingishable manner due to a co-precipitation process. When the concentration of certain elements reaches the solubility limit, different compounds precipitate forming the degradation layer. Moreover, also $K\text{-}PO_4$ crystals are observed on top of the degradation layer (Fig. 63c). This formation is common in PBS since its main buffering agents are HPO_4^{2-} and $H_2PO_4^-$. This type of crystals was also reported by Trinidad et al. [11].

In HBSS, the degradation layer is similar to the one formed in PBS. In this solution among Mg hydroxide and phosphate a small amount of $MgCO_3$ can be formed (Fig. 64a EDX 1). However, due to the lower amount of PO_4^{3-} in HBSS solution as compared to PBS, no $K\text{-}PO_4^{3-}$ crystals are found. The degradation layer in this medium is generally less homogeneous, with a changing thickness. As shown in Section 6.3.6, in tests with Mg-Ag alloys, corrosion products such as Mg hydroxide can be released into the electrolyte

(Fig. 62). As shown in Fig. 67a, the shape of the Mg hydroxide is sponge-like and can get quite voluminous comparing to the degradation layer. Bright dots containing Ag can also be observed in the $Mg(OH)_2$ containing layer. These Ag particles are also detected by XRD as shown in Fig. 62.

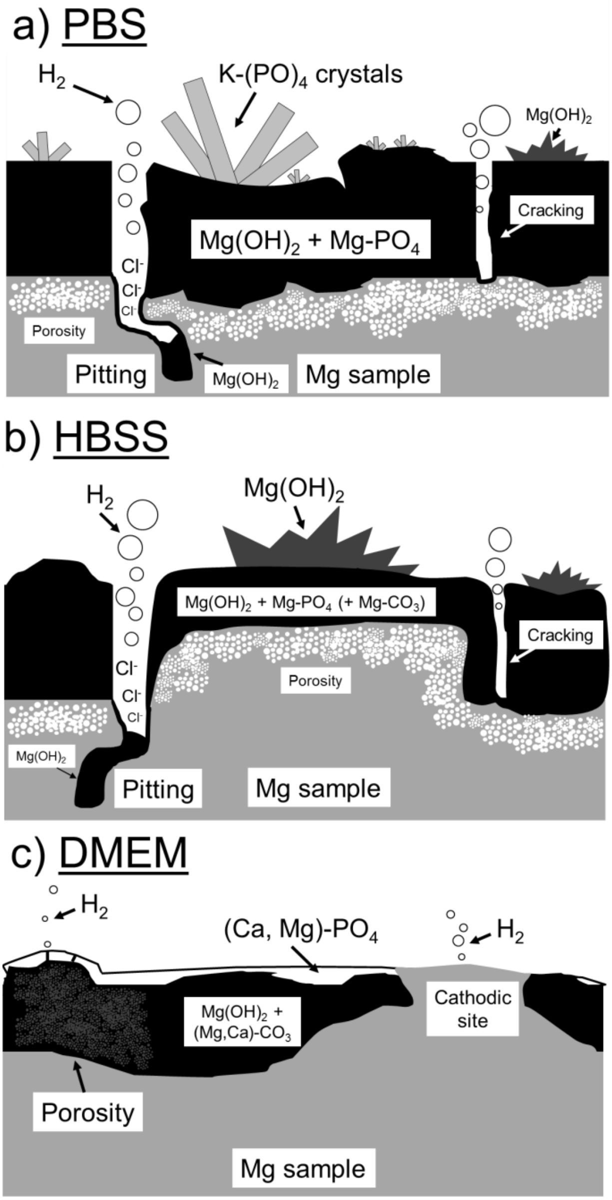

Figure 66. Schematic representation of the degradation layer and corrosion modes determined for pure Mg in (a) PBS, (b) HBSS and (c) DMEM. Degradation products and layer composition are indicated, as well as, the pitting, porosity and cracking.

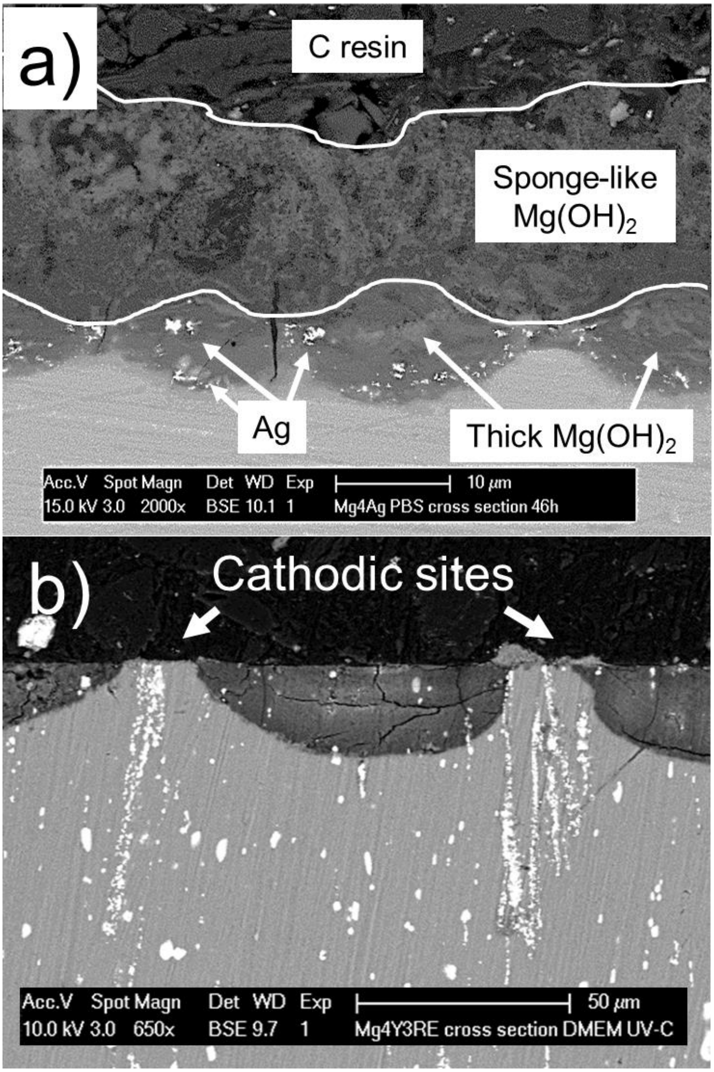

Figure 67. Interaction of alloying elements and degradation layer. (a) The degradation layer formed in PBS on Mg-6Ag contains Ag (bright spots) and two layers can be distinguished: a sponge-like and a thick one. (b) RE precipitates found in the cross section of Mg-4Y-3RE after testing in DMEM acting as cathodic sites.

Finally, as shown above in Fig. 65, the degradation layer in DMEM is composed of two layers. (i) The first one depositing contains $Mg(OH)_2$ and $(Mg,Ca)\text{-}CO_3$. This first layer is at some sites porous (Fig. 65e). This porosity can allow the electrolyte to penetrate this layer down to the Mg surface. (ii) The second layer, on top of the first one, is a thin $(Mg,Ca)\text{-}PO_4$ layer. This $(Mg,Ca)\text{-}PO_4$ layer has also been observed in vivo [12], in HBSS [13] and

SBF [14]. The degradation rate data show the protective character of the (Mg,Ca)-PO_4 layer reducing the degradation rate of the Mg based material. This protective influence is specially highlighted by the low DR of three Mg-Ag alloys in DMEM as compared to PBS and HBSS.

As shown previously in Chapter 5.4.1, cathodic sites can also be found where precipitates or secondary phases are present (Fig. 67b). These sites connect galvanically with the surrounding Mg promoting its dissolution. However, this mechanism is less aggressive in DMEM than in PBS and HBSS presumably due to the lower Cl^- (115.68 mM in DMEM, 140 mM in PBS and 143.26 mM in HBSS) and higher HCO_3^- ionic content (44.05 mM in DMEM, none in PBS and 4.17 mM in HBSS).

Agha et al., recently showed the influence of different inorganic salts present in cell culture media, such as Ca^{2+}, SO_4^{2-} and HCO^{3-}, on the Mg degradation process and the degradation layer formation [15]. This study concluded that: (i) $MgSO_4$ has no significant influence on the degradation process although it increases the degradation layer heterogeneity; (ii) $CaCl_2$ reduces the DR enhancing Ca-PO_4 precipitation; (iii) $NaHCO_3$ does not influence the DR although in combination with $CaCl_2$ both enhance the formation of $MgCO_3$ and Ca-PO_4 products; and finally (iv) $NaHCO_3$ plays the most important role and high concentrations (>27 mM) were not recommented. These results are in agreement with the current study.

It is known that pitting is induced by Cl^- ions. As introduced in Section 1.3, Cl^- ions can dissolve the protective $Mg(OH)_2$ layer increasing the pH and forming soluble $MgCl_2$ which has a rather high solubility limit (5.6 M in water at room temperature) [16-18]. In comparison, $Mg(OH)_2$ has a solubility limit in water of $1.1 \cdot 10^{-4}$ M. Hence, this mechanism exposes the unprotected area to the electrolyte promoting the degradation process. Thus, a stronger pitting influence is also expected in PBS and HBSS due to the higher Cl^- level. Commonly the pits are filled with $Mg(OH)_2$ and $MgCl_2$, as proven by the EDX 2 in Figs. 63a and 64a.

6.4.3. Influence of impurities

As introduced in Section 1.5.1, impurities are known for having an important role on Mg degradation. Hofstetter et al. showed that ultrahigh-purity Mg degrades very slowly in vivo with a rate of 10 μm/year [19], breaking the paradigm in biomaterial science that Mg corrodes quickly. Hence, impurity control during all the processing steps of the Mg biomaterials seems necessary.

As mentioned in Section 1.5.1, elements such as Fe, Ni, Mn and Si must be included in the corrosion analysis, since Cu and Co are normally not an issue. Hanawalt defined their tolerance limit as 170 ppm for Fe and 5 ppm for Ni [20]. Recent studies recommend taking also into account the Mn and Si content because they can have a role on Mg corrosion [19-23]. (i) The presence of traces of Si promotes precipitation of larger Fe-rich impurity particles in Mg alloys [24]. (ii) Mn forms intermetallics with Fe that are less favorable to promote galvanic dissolution, and thus, Mn increases the Fe tolerance limit [6, 25-28]. The chemical composition of the studied Mg alloys is shown in Table 9 in Section 5.2.1 (page 133) together with the grain size.

Table 17 compares the degradation rates of the Mg alloys studied in this work with the results published in literature. In general, these data do not correlate closely, although there are exceptions, and to understand the differences in DR between studies, impurity and microstructure data should also be provided. Kubasek et al. provided impurity and DR data in their study of Mg-RE alloys which included Mg-Gd alloys [29]. Interestingly, Mg-1Gd alloy had a Ni impurity content of 180 ppm while Mg-3Gd and Mg-5Gd only had 8 ppm and 3 ppm respectively. The DR for Mg-1Gd was approximately 24 mm/year in what they described as simulated physiological solution (9 g/L NaCl), while the other Mg-Gd alloys showed a DR<0.5 mm/year. Furthermore, the study from Kubasek et al. shows a lot higher DR in immersion tests for Mg-5Gd T4 treated samples as compared to as-cast samples. This could be due to unexpected impurity additions during the heat treatment. E.g. one can imagine that Fe atoms can diffuse into the Mg sample by contact of the sample with steel moulds and tools. Thus, DR results cannot be attributed to nominal alloy tested without considering the impurity content.

Table 17. Comparison of the degradation rates in mm/year of this work with the literature. This table continues in the next page.

Alloy	DR	Electrolyte	Method	Reference
Pure Mg	0.3	PBS	Immersion test	This work
	0.7	HBSS	Immersion test	This work
	1.1	DMEM + 5% CO_2	Immersion test	This work
	0.55	α-MEM+15% FBS + 5% CO_2	Immersion test	Cecchinato et al. [30]
	0.52	DMEM	PDP	Tie et al. [31]
	0.77	DMEM + 10% FBS + 5% CO_2	Immersion test	Myrissa et al. [32]
	0.38	-	In vivo (1 week)	Myrissa et al. [32]
	0.13	-	In vivo (4 week)	Myrissa et al. [32]

*Table 17 continues on the next page.

Alloy	DR	Electrolyte	Method	Reference
Mg-4Y-3RE	3.6	PBS	Immersion test	This work
	3.1	HBSS	Immersion test	This work
	1.3	DMEM + 5% CO_2	Immersion test	This work
	0.47	D-PBS	Immersion test	Trinidad et al. [33]
	0.32	phosphate buffered SBF	PDP	Xu et al. [34]
	4.47	phosphate buffered SBF	Immersion test	Xu et al. [34]
	1.20	SBF	PDP	Erinc et al. [35]
	0.04	SBF	Immersion test	Hanzi et al. [36]
	1.01	α-MEM+15% FBS	Immersion test	Cecchinato et al. [30]
	1.06	DMEM + 10% FBS	Immersion test	Charyeva et al. [37]
	1.56	-	In vivo	Gu and Zheng [38]
	0.70	-	In vivo (3 months)	Krause et al. [39]
	1.44	-	In vivo (6 months)	Krause et al. [39]
Mg-5Gd	0.3	PBS	Immersion test	This work
	0.4	HBSS	Immersion test	This work
	1.0	DMEM + 5% CO_2	Immersion test	This work
	3.8	1% NaCl (21.5°C)	Immersion test	Hort et al. [40]
	0.29	SBF (9 g/L NaCl)	PDP -cast	Kubasek et al. [29]
	0.32	SBF (9 g/L NaCl)	Immersion test - cast	Kubasek et al. [29]
	0.73	SBF (9 g/L NaCl)	PDP -T4	Kubasek et al. [29]
	>22	SBF (9 g/L NaCl)	Immersion test - T4	Kubasek et al. [29]
Mg-10Gd	0.6	PBS	Immersion test	This work
	1.6	HBSS	Immersion test	This work
	0.4	DMEM + 5% CO_2	Immersion test	This work
	1.3	1% NaCl (21.5°C)	Immersion test	Hort et al. [40]
	1.81	DMEM + 10% FBS + 5% CO_2	Immersion test	Myrissa et al. [32]
	0.58	-	In vivo (1 week)	Myrissa et al. [32]
	0.53	-	In vivo (4 week)	Myrissa et al. [32]
	0.67	α-MEM+15% FBS + 5% CO_2	Immersion test	Cecchinato et al. [30]

*Table 17 continues on the next page.

Alloy	DR	Electrolyte	Method	Reference
Mg-2Ag	16.7	PBS	Immersion test	This work
	5.4	HBSS	Immersion test	This work
	2.2	DMEM + 5% CO_2	Immersion test	This work
	0.54	DMEM	PDP (static)	Tie et al. [31]
	0.25	DMEM + 10% FBS + 5% CO_2	Immersion test	Myrissa et al. [32]
	0.72	-	In vivo (1 week)	Myrissa et al. [32]
	0.3	-	In vivo (4 week)	Myrissa et al. [32]
	0.5	α-MEM+15% FBS + 5% CO_2	Immersion test	Cecchinato et al. [30]
Mg-4Ag	13.6	PBS	Immersion test	This work
	6.8	HBSS	Immersion test	This work
	1.2	DMEM + 5% CO_2	Immersion test	This work
	0.6	DMEM	PDP (static)	Tie et al. [31]
Mg-6Ag	15.7	PBS	Immersion test	This work
	12.9	HBSS	Immersion test	This work
	2.6	DMEM + 5% CO_2	Immersion test	This work
	0.71	DMEM	PDP (static)	Tie et al. [31]

Regarding the Fe content in the studied alloys, Fe is determined between 46 and 58 ppm, except for Mg-4Y-3RE with 87 ppm of Fe. The Ni level is also higher in Mg-4Y-3RE (19 ppm) compared to the rest of the Mg alloys (<10 ppm). Thus, the higher Ni and Fe contents can explain the higher DR of Mg-4Y-3RE as compared to the other Ag free alloys studied in PBS and HBSS. Therefore, these results indicate that in order to control the DR of the Mg samples the Fe and Ni contents should be lower than 58 ppm and 10 ppm respectively. It is noteworthy that the Al content detected in Mg-4Y-3RE is also the highest. This is probably due to contamination during processing. Al can form secondary phases, but the content is not considered high enough (<252 ppm) to precipitate $Mg_{17}Al_{12}$. In any case, controlling impurity inclusions coming from previous Mg-alloy processing with the same equipment by proper maintenance and cleaning is recommended.

The Mn content in pure Mg is 334ppm. This is rather high compared to the other alloys: Mg-4Y-3RE (166 ppm), Mg-5Gd (57 ppm), Mg-10Gd (101 ppm), Mg-2Ag (82 ppm), Mg-4Ag (51 ppm) and Mg-6Ag (1 ppm). Since the corrosion rate of pure Mg in PBS, HBSS and DMEM did not exceed 1.1 mm/year in any case, the higher Mn content indicates its positive influence in these low purity Mg samples [25]. In PBS and HBSS the DR of pure Mg is 0.3 and 0.7 mm/year respectively, therefore, the positive influence of Mn could be enhanced when the Cl content of the electrolyte is higher.

Regarding the Si content no noteworthy trend is found related to the DR data. All the tested alloys contain between 50 and 90 ppm of Si, except pure Mg which has 130 ppm of Si. This Si level seems to be too low to accelerate the degradation process. Perhaps the higher amount of Mn in pure Mg could counteract the negative effect of Fe and Si. Thus, the Si level is not considered relevant in this analysis although some studies indicated its importance [24].

6.4.4. Influence of the microstructure

a) Mg-4Y-3RE alloy

Mg-4Y-3RE alloy contains Y, Nd and Ce and, as shown in Fig. 54, this alloy contains many secondary phases and precipitates in its microstructure. It is known that rare-earths can pick up impurities to form precipitates which are less harmful than the impurities themselves [41]. This is similar to the previously mentioned influence that Mn has. Perhaps, impurity precipitation and small grain size (6.3 µm) of Mg-4Y-3RE are the reasons why the DR of Mg-4Y-3RE is not too high (< 3.6 mm/year), even though, it has the highest Fe and Ni content.

b) Mg-Gd alloys

Both studied Mg-Gd alloys show a moderate DR in all the immersion tests. Mg-5Gd (<1.0 mm/year) shows a slower DR as compared to Mg-10Gd (<1.6 mm/year). This is in contradiction to what Hort et al. reported (Table 17). Hort concluded that Mg-5Gd degrades faster than Mg-10Gd. Hence, our results could be explained by the smaller grain size of Mg-5Gd (5.9 µm) as compared to Mg-10Gd (17.8 µm). The low amount of Fe and Ni (Table 9 in Section 5.2.1, page 133) in these alloys seems to influence positively the corrosion resistance. Note that in our study, the measured Gd content is between 1 and 1.4 wt.% lower than the nominal composition aimed at. Thus, perhaps these alloys should be considered as Mg-4Gd and Mg-9Gd.

Regarding the microstructure of Mg-Gd alloys, Gd precipitation and Gd rich cuboids have been observed in both studied Mg-Gd alloys (Fig. 54). These cuboids are already reported in Sections 4.4.3 and 5.4.1 and here the analysis is done by EDX. As shown in Fig. 68a, these cuboids are stable particles which after chromic acid cleaning can be observed attached to the surface. Particles with this shape are generally found in RE containing alloys [2, 3]. Although, Kubasek et al. defined these cuboids as the eutectic Mg_5Gd [29], some authors demonstrated the apparition of Gd and Dy hydride cubic particles in Mg-Gd and Mg-Dy alloys, respectively [4, 5]. As shown in Fig. 68b, the Mg/Gd at.% ratio measured by EDX on such a particle is lower than the ratio of 5:1. Unfortunately, the quantification of the cuboid composition by EDX is only an approximation. Firstly, the interaction volume of the electron beam is expected to be larger than the GdH_2 particle. Secondly there is an overlapping of Mg-K (1.253 keV) and Gd-M (1.185 keV) peaks (Fig. 68b). In any case, here it is also considered that these cuboids are insoluble GdH_2 particles. These particles could form during casting or while the material is stored in contact with air containing moisture. In a real application, e.g. for orthopaedic fracture stabilisation, these particles might remain encapsulated at the bone or absorbed by the body and redistributed to spleen and liver, as Gd containing contrast agents do in magnetic resonance scans [42].

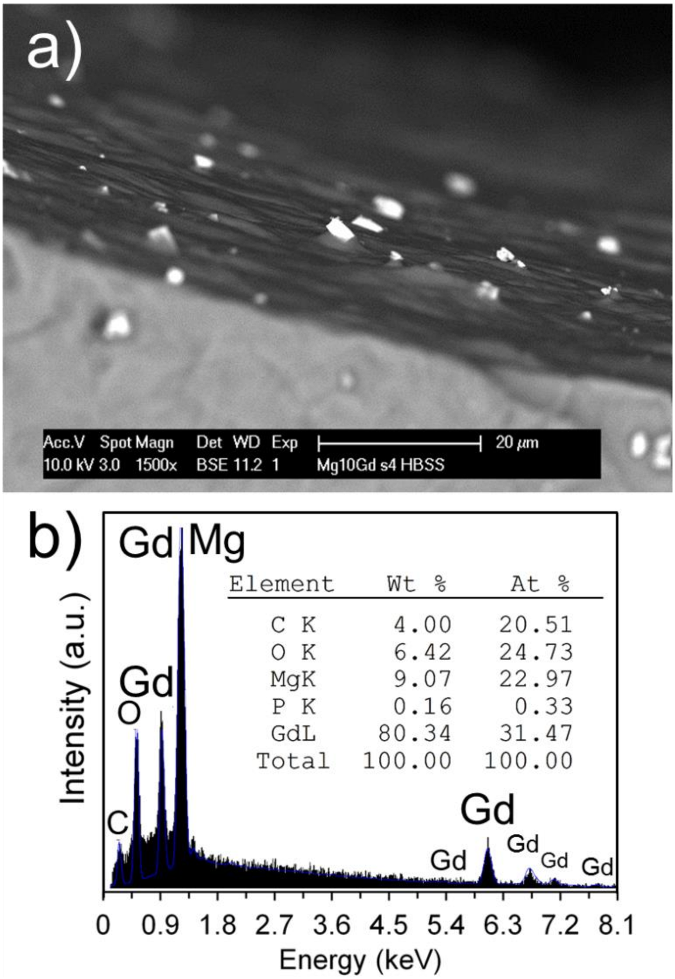

Element	Wt %	At %
C K	4.00	20.51
O K	6.42	24.73
MgK	9.07	22.97
P K	0.16	0.33
GdL	80.34	31.47
Total	100.00	100.00

Figure 68. (a) Gd cuboids remaining on the Mg-10Gd surface after degradation testing in HBSS and chromic acid treatment. (b) EDX spectrum of a Gd cuboid indicating a high Gd content.

c) Mg-Ag alloys

As shown in Fig. 59 and Table 14, Mg-Ag alloys show an increased DR in PBS and HBSS as compared to the other tested alloys. In DMEM Mg-Ag DR is also higher but the difference with the other alloys is drastically reduced. Since the impurity content is comparable to other alloys (Table 9 Section 5.2.1, page 133), the higher DR is presumably due to a larger grain size and the presence of Ag, as also stated in Section 5.4.1.

Table 18 shows the relation between DRs determined by ML of Mg-Ag alloys and their grain size. The grain size of Mg-Ag alloys seems to be related to the DR calculated at the end of the immersion test in PBS. Mg-2Ag has the highest grain size (43.7 µm), compared to Mg-6Ag (34.6 µm), and Mg-4Ag (31.6 µm) and the DRs in PBS rank these alloys in the same order as the grain size. However, DRs in HBSS rank Mg-Ag alloys according to their Ag content. The DMEM data interpretation is not direct. A combination of the influence of the grain size and Ag content could explain the DRs determined by ML in DMEM. Nevertheless, the differences between the DRs of the Mg-Ag alloys are small.

Table 18. DRs determined by ML of Mg-Ag alloys in PBS, HBSS and DMEM and the grain size and Fe and Ni impurity content of the same alloys.

Alloy	DR PBS (mm/year)	DR HBSS (mm/year)	DR DMEM (mm/year)	Grain size (µm)	Fe content (ppm)	Ni content (ppm)
Mg-2Ag	16.7	5.4	2.2	43.7	50	4
Mg-4Ag	13.6	6.8	1.2	31.6	58	5
Mg-6Ag	15.7	12.9	2.6	34.6	47	4

It is noteworthy that the initial DR measured for Mg-2Ag in PBS (6.1 mm/year) (Fig. 61b) is lower as compared to the long term DR. Possibly the larger grain size of Mg-2Ag influences the long term behaviour rather than initial one.

As reviewed in Section 1.5.2.b, Ag is considered as an impurity which accelerates the Mg degradation process [23], presumably by microgalvanic corrosion dissolving Mg around Ag-rich particles and releasing these particles. As shown in Fig. 69a, there is locally concentrated precipitation at some sites of Mg-6Ag alloy. These particles are expected to promote severe localized corrosion at these sites where they are concentrated. Therefore, Mg around these Ag-rich particles dissolves into the electrolyte releasing these particles and causing a faster mass loss of the material. Note that this mass loss mechanism would not produce hydrogen, therefore, a lower DR by hydrogen evolution method as compared to mass loss method can be expected.

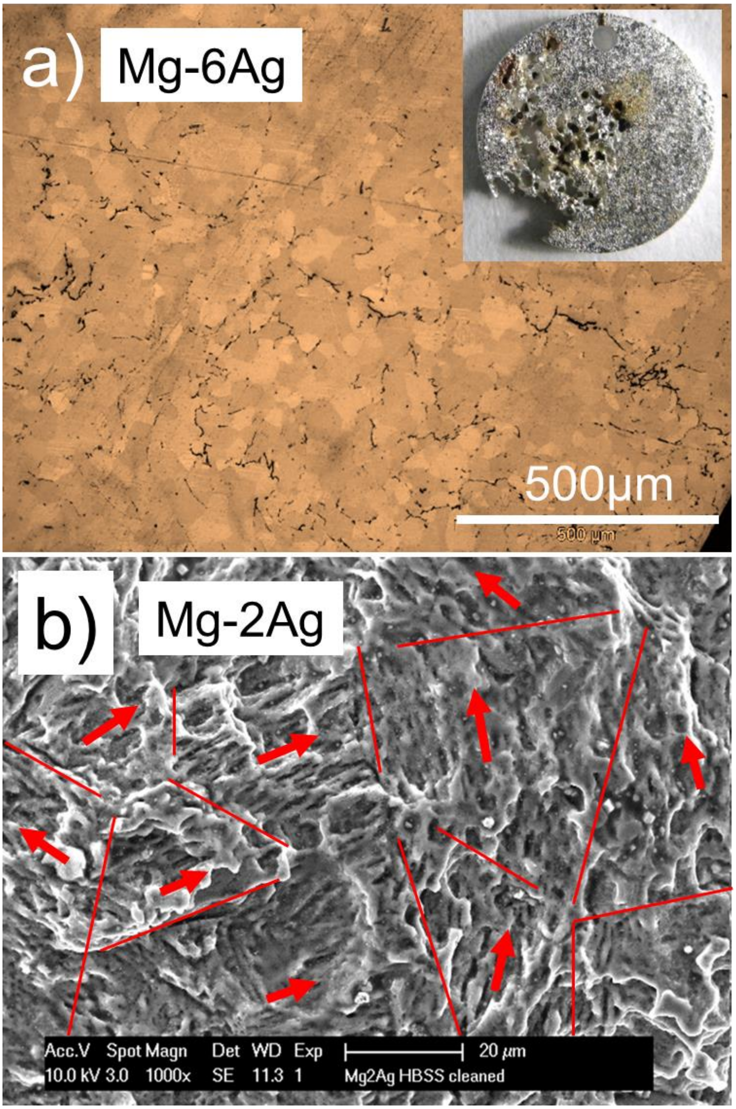

Figure 69. (a) Precipitation in Mg-6Ag samples has been observed which will presumably help to localize the corrosion process. (b) Preferential corrosion direction in grains on Mg-2Ag in HBSS has been observed. This porosity takes a direction which, presumably, depends on the sample texture.

Moreover, another mechanism which can explain the Mg-Ag corrosion was discussed in Section 4.4.2. A higher Cl^- content in the electrolyte (e.g. in PBS and HBSS) will promote the dissolution of $Mg(OH)_2$ from the degradation layer [46], exposing Mg and Ag and accelerating the degradation process even further. As shown in Fig. 67a, silver can also be found at the degradation layer. When the Cl^- content is high $Mg(OH)_2$ is less stable and these Ag particles are exposed and partly dissolve, binding Cl^- ions and forming AgCl. AgCl has a very low solubility limit in water ($1.3 \cdot 10^{-5}$ M at room temperature) which means that only 1.9 mg of AgCl will dissolve in one litre of water. Thus most of the AgCl formed precipitates as a solid particle. As shown in Fig. 62, AgCl is suspended with $Mg(OH)_2$ in HBSS tests. Supporting these findings, Tie et al. also found AgCl as corrosion products from Mg-Ag degradation [31]. Hence, as a conclusion, a higher Cl^- level will induce a less stable degradation layer exposing the Mg and Ag to corrode microgalvanically and releasing AgCl and $Mg(OH)_2$ products in solution. And finally, this can explain why Mg-Ag alloys degrade faster in PBS and in HBSS than in DMEM (Fig. 59 and Table 18).

In this study, preferential corrosion direction in grains has also been observed (Fig. 69b) as Lee et al. also stated [25]. This is related to the underfilm corrosion mode under the degradation layer, as the porosity of the Mg grain is oriented depending on the sample texture. This is considered to play a mild role in the mechanical integrity as long as there is no strong texturized material.

6.4.5. Polarization with RDE

In this thesis, PDP measurements from a rotating disc are proven to be a better testing method rather than when no electrolyte flow is induced on the Mg electrode surface. The rotation avoids the degradation layer formation and the influence of the negative difference effect during measurements. Firstly, the polarization curves can be obtained repeatedly reducing the data deviation, and thus, improving the reproducibility of the experiments as shown by Fig. 60. Secondly, no pronounced anodic curves are measured in any polarization when the RDE is applied. Hence, the role of the negative difference effect is weakened, or in other words, the degradation layer deposition which enhances the catalytic cathodic activity during anodic polarization is reduced [43]. Furthermore, i_{corr} measured in PBS and HBSS is generally lower (Fig. 60 and Table 15) and E_{corr} is shifted when no rotation is applied (Fig. 60 and Table 16). These shifts are related to the influence of the degradation layer deposited under static polarization which can represent a potential step and protect the Mg surface from dissolving. However, in DMEM i_{corr} is higher under static conditions. This is presumably due to the high content of HCO_3^-/CO_3^{2-} ions in the electrolyte which can stimulate Mg carbonate precipitation under static conditions.

The DR calculated from the i_{corr} obtained by PDP with rotation seems more comparable to the initial DR determined by hydrogen evolution than when no rotation is applied. This similarity is highlighted by the increase of both i_{corr} and initial DR of Mg-Ag alloys with increasing amount of Ag. Despite this similar trend, the DR values from i_{corr} are remarkably higher than the DR data calculated from the hydrogen data (Fig. 61). The differences between DRs are observed because when Mg with a pristine surface is initially immersed the degradation process takes place faster. Then, after a few minutes, the degradation layer forms slowing down the process. In contrast, under dynamic polarization this layer is not formed. Hence, in view of the above, the initial DR is lower when it is calculated by the hydrogen collection after a few hours or at the first day.

Thus, polarization with the RDE can provide representative data of a specific material-electrolyte system repeatedly. This data is indicative of the initial degradation response and more comparable to the initial DR determined by immersion tests.

6.5. Conclusions

The corrosion behaviour of pure Mg, Mg-4Y-3RE, Mg-Gd and Mg-Ag alloys have been determined in three different electrolytes: PBS, HBSS and DMEM. Polarization measurements have also been applied with and without the RDE. The following conclusions can be drawn from this study:

1. The relevance of a high Fe and Ni impurity content has been identified on the degradation behaviour of the studied alloys. The Mn also plays a beneficial influence on the corrosion resistance of Mg when the impurity levels of the material are not higher than 45 ppm and 10 ppm for Fe and Ni, respectively. Results also indicate that a fine grain size, around 6 μm, has also a positive influence.
2. According to the corrosion performance of these alloys, pure Mg and Mg-Gd alloys with the grain size and impurity level here determined (50-60 ppm of Fe, and <10 ppm of Ni) are candidate implant materials due to their controlled and homogeneous degradation in all the three media (<1.5 mm/year). Mg-Ag alloys have also shown a similar behaviour in DMEM to pure Mg and Mg-Gd alloys, while in PBS and HBSS the degradation was accelerated due to the higher Cl^- ion content but also the larger grain size. Thus, binary Mg-Ag alloys can also be implant candidates which can

corrode faster under physiological conditions but also in a controlled manner (between 2.6 and 1.2 mm/year), with the antibacterial added value of Ag.

3. Alloying additions of REs in Mg-Gd and Mg-4Y-3RE alloys show the greatest increased microhardness, so that the mechanical properties of these alloys are also expected to be improved as compared to pure Mg. These alloys might perform suitably during clinical applications as the implant might be needed e.g. for load-bearing applications.
4. The testing conditions are found extremely important as they define the degradation process of a Mg based material. Mg samples show pitting, underfilm and homogeneous corrosion in PBS and HBSS, and when Ag is present in the alloy the corrosion process is severely localized. The degradation layer in PBS and HBSS is composed of $Mg(OH)_2$ and Mg-phosphate with traces of Na and K. In DMEM with CO_2 added to the atmosphere, the overall mechanisms are homogeneous and underfilm corrosion for all the studied Mg alloys. The surface film is composed of two layers: (i) $Mg(OH)_2$ and Mg-carbonate on the inner part; (ii) calcium phosphate in the outer part. Due to the similar composition of DMEM compared to body plasma (the lower Cl^- ion content, the presence of Ca^{2+} and HCO_3^- ions) and CO_2 buffering system, the degradation characterization here performed in DMEM is expected as the most representative of an in vivo situation.
5. Polarization measurements from a rotating disc electrode seem to indicate the initial degradation behaviour during immersion testing. This method can provide reproducibly the intrinsic response of a Mg based material in a certain electrolyte, avoiding both: (i) the influence of the degradation layer formation on polarization curves and (ii) the enhanced catalytic reaction during anodic polarization.

References

[1] G. Song, A. Atrens, D. St John, X. Wu, J. Nairn, Corros. Sci. 39 (1997) 1981-2004.
[2] Y.H. Kang, D. Wu, R.S. Chen, E.H. Han, J. Magnes. Alloys 2 (2014) 109-115.
[3] T. Rzychoń, A. Kiełbus, J. Achievem. Mater. Manufacturing Eng. 21 (2007) 31-34.
[4] Q. Peng, Y. Huang, J. Meng, Y. Li, K.U. Kainer, Intermetallics 19 (2011) 382-389.
[5] W. Gan, Y. Huang, L. Yang, K.U. Kainer, M. Jiang, H.G. Brokmeier, N. Hort, Journal of Applied Crystallography 45 (2012) 17-21.
[6] G.L. Song, A. Atrens, Adv. Eng. Mater. 1 (1999) 11-33.
[7] S. Remennik, I. Bartsch, E. Willbold, F. Witte, D. Shechtman, Mater. Sci. Eng. B-Advanced Functional Solid-State Materials 176 (2011) 1653-1659.
[8] N.I. Zainal Abidin, B. Rolfe, H. Owen, J. Malisano, D. Martin, J. Hofstetter, P.J. Uggowitzer, A. Atrens, Corros. Sci. 75 (2013) 354-366.
[9] A. Atrens, G.-L. Song, M. Liu, Z. Shi, F. Cao, M.S. Dargusch, Adv. Eng. Mater. 17 (2015) 400-453.
[10] M. Stern, A.L. Geary, J. Electrochem. Soc. 104 (1957) 56-63.
[11] J. Trinidad, G. Arruebarrena, I. Marco, I. Hurtado, E.S. de Argandoña, Proc. Inst. Mech. Eng. H 227 (2013) 1301-1311.
[12] Z. Li, X. Gu, S. Lou, Y. Zheng, Biomaterials 29 (2008) 1329-1344.
[13] H. Kuwahara, Y. Al-Abdullat, N. Mazaki, S. Tsutsumi, T. Aizawa, Mater. Trans.(Japan) 42 (2001) 1317-1321.
[14] L. Li, J. Gao, Y. Wang, Surf. Coat. Technol. 185 (2004) 92-98.
[15] N.A. Agha, F. Feyerabend, B. Mihailova, S. Heidrich, U. Bismayer, R. Willumeit-Römer, Mater. Sci. Eng.: C 58 (2016) 817-825.
[16] M. Jamesh, S. Kumar, T.S.N.S. Narayanan, Corros. Sci. 53 (2011) 645-654.
[17] W.-D. Mueller, M. Fernandez Lorenzo de Mele, M.L. Nascimento, M. Zeddies, J. Biomed. Mater. Res. Part A 90A (2009) 487-495.
[18] H.R. Bakhsheshi-Rad, M.H. Idris, M.R. Abdul-Kadir, A. Ourdjini, M. Medraj, M. Daroonparvar, E. Hamzah, Mater. Design 53 (2014) 283-292.
[19] J. Hofstetter, E. Martinelli, A.M. Weinberg, M. Becker, B. Mingler, P.J. Uggowitzer, J.F. Löffler, Corros. Sci. 91 (2015) 29-36.
[20] J. Hanawalt, C. Nelson, J. Peloubet, American Institute of Mining and Metallurgical Engineers (AIME) 147 (1942) 273.
[21] J. Hofstetter, M. Becker, E. Martinelli, A.M. Weinberg, B. Mingler, H. Kilian, S. Pogatscher, P.J. Uggowitzer, J.F. Löffler, JOM 66 (2014) 566-572.
[22] J. Hofstetter, E. Martinelli, S. Pogatscher, P. Schmutz, E. Povoden-Karadeniz, A.M. Weinberg, P.J. Uggowitzer, J.F. Löffler, Acta Biomater. (2015) 347-353.

[23] H.E. Friedrich, B.L. Mordike, Magnesium technology, Springer-Verlag Berlin Heidelberg, 2006.
[24] L. Yang, X. Zhou, S.-M. Liang, R. Schmid-Fetzer, Z. Fan, G. Scamans, J. Robson, G. Thompson, J. Alloys Compd. 619 (2015) 396-400.
[25] J.-Y. Lee, G. Han, Y.-C. Kim, J.-Y. Byun, J.-i. Jang, H.-K. Seok, S.-J. Yang, Metals and Materials International 15 (2009) 955-961.
[26] M. Liu, P.J. Uggowitzer, A.V. Nagasekhar, P. Schmutz, M. Easton, G.-L. Song, A. Atrens, Corros. Sci. 51 (2009) 602-619.
[27] M. Liu, P. Uggowitzer, P. Schmutz, A. Atrens, JOM 60 (2008) 39-44.
[28] K.N. Reichek, K.J. Clark, J.E. Hillis, SAE trans. 94 (1985) 318-329.
[29] J. Kubasek, D. Vojtech, Trans. Nonferrous Met. Soc. China 23 (2013) 1215-1225.
[30] F. Cecchinato, N.A. Agha, A.H. Martinez-Sanchez, B.J.C. Luthringer, F. Feyerabend, R. Jimbo, R. Willumeit-Römer, A. Wennerberg, PLoS ONE 10 (2015) e0142117.
[31] D. Tie, F. Feyerabend, W.-D. Mueller, R. Schade, K. Liefeith, K.U. Kainer, R. Willumeit, European Cells & Materials 25 (2013) 284-298.
[32] A. Myrissa, N.A. Agha, Y. Lu, E. Martinelli, J. Eichler, G. Szakács, C. Kleinhans, R. Willumeit-Römer, U. Schäfer, A.-M. Weinberg, Mater. Sci. Eng.: C 61 (2016) 865-874.
[33] J. Trinidad, G. Arruebarrena, I. Marco, I. Hurtado, E. Saenz de Argandona, Proc Inst Mech Eng H 227 (2013) 1301-1311.
[34] L. Xu, E. Zhang, D. Yin, S. Zeng, K. Yang, J. Mater. Sci. - Mater. Med. 19 (2008) 1017-1025.
[35] M. Erinc, W.H. Sillekens, R. Mannens, R.J. Werkhoven, TNO Industrie en Techniek (2009).
[36] A.C. Hänzi, I. Gerber, M. Schinhammer, J.F. Löffler, P.J. Uggowitzer, Acta Biomater. 6 (2010) 1824-1833.
[37] O. Charyeva, F. Feyerabend, R. Willumeit-Römer, D. Zukowski, C. Gasqueres, G. Szakacs, N.A. Agha, N. Hort, F. Gensch, F. Cecchinato, R. Jimbo, A. Wennerberg, K.S. Lips, MOJ toxicology 1 (2015) 1-6.
[38] X.-N. Gu, Y.-F. Zheng, Front. Mater. Sci. China 4 (2010) 111-115.
[39] A. Krause, N. Höh, D. Bormann, C. Krause, F.-W. Bach, H. Windhagen, A. Meyer-Lindenberg, JOM Science 45 (2009) 624-632.
[40] N. Hort, Y. Huang, D. Fechner, M. Stoermer, C. Blawert, F. Witte, C. Vogt, H. Druecker, R. Willumeit, K.U. Kainer, F. Feyerabend, Acta Biomater. 6 (2010) 1714-1725.
[41] W.-j. Liu, F.-h. Cao, Z. Zhang, J.-q. Zhang, Corros. Sci. and Protec. Techn. 21 (2009) 82-84.
[42] P. Wedeking, K. Kumar , Nucl. Med. Biol. 20 (1993) 679-691.
[43] D. Tie, F. Feyerabend, W.-D. Mueller, R. Schade, K. Liefeith, K.U. Kainer, R. Willumeit, European Cells and Materials 25 (2013) 284-298.
[44] I. Marco, O. Van der Biest, Corros. Sci. (2015).

Chapter 7:
Mg-MOF biodegradable coatings as drug carrier on Mg temporal implants

Adapted from:

I. Marco, N. Campagnol, S. Mostofi, O. Van der Biest. Mg-MOF biodegradable coatings for drug delivery on Mg temporal implants. Surface and coating technology. In preparation.

7.1. Introduction

As introduced in Section 1.10.1, metal organic frameworks (MOFs) are interesting materials for biomedical applications due to their drug carrying capacity [1], which is due to their large BET surface (7.000 m^2/g) [2]. Horcajada et al. showed that MOFs can act as drug nanocarriers [3-5]. MOFs, however, have never been applied on any implant material. Ameloot et al. investigated the electrochemical synthesis of MOFs as a coating by deposition during anodic polarization [6]. This technique uses the dissolved ions from the anode to build the MOF with a linker present in the electrolyte. Mg can be used as the metal in the MOF structure, which is called Mg-MOF. These type of MOFs have been successfully synthesised hydrothermally with DHTA (2,5-dihydroxyterephthalic acid) as organic linker and $MgNO_3$ as a metal source [7]. Two different structures can be formed: CPO-26-Mg and CPO-27-Mg. Regarding toxicity, DHTA has shown a low toxicity in animal experiments, which makes it a biomaterial ligand candidate [8-10]. Some authors consider MOFs as “bio-friendly” materials [11].

This Chapter demonstrates that Mg-MOF formed with DHTA can be added to a Mg substrate by electrochemical synthesis. This study also assesses the degradation properties of Mg with these coatings by immersion and polarization methods. Finally, the biocompatibility is evaluated by cell viability tests with bone related cells. This could be the first steps towards a new biodegradable drug delivery system to control the post-implantation inflammation of bioabsorbable Mg implant tuning the Mg degradation process.

7.2. Materials and methods

7.2.1. Material

The pure Mg samples applied in this study are the same pure Mg discs applied in the previous chapters. Their production description is given in Section 3.2.1

7.2.2. Mg-MOF synthesis

Mg discs were embedded in epoxy resin and connected electrically with silver epoxy glue (E-Solder 3021, Schwabach, Germany) to be used as working electrodes. The surface of the electrode was approximately 0.8 cm^2. The surface preparation was done firstly by grinding with 1000 and then 4000 grit SiC paper (Matador 991A, Remscheid, Germany), and finally by polishing with diamond suspension of 3 μm (Kemet, Maidstone, England).

Fig. 70a shows the electrochemical cell used for this synthesis. Pt foil and Ag/AgCl saturated with KCl (with a potential of +197 mV against standard hydrogen electrode) were used in the electrochemical cell as counter and reference electrodes respectively. The ligand used in this research was 2,5-dihydroxyterephthalic acid (DHTA, 382132, Sigma Aldrich St. Louis, USA). The electrolyte composition used for the synthesis was: 60 mM DHTA, 10 vol.% H_2O and 90 vol.% absolute ethanol (99.8+%, Acros Organics NV). Another solution with 120 mM DHTA was also applied to observe the difference. Also two different cell configurations were applied for 20 ml and 10 ml volume. The temperature was set at 60˚C. The measured electrolyte conductivity is 76 μS/cm and the pH 2.7.

During potentiostatic dissolution 4 V vs open circuit potential (OCP) were applied for 1 h, and the electrolyte was not changed for consecutive samples in a series of experiments, keeping a similar distance between electrodes. In order to avoid electrolyte volume reduction due to ethanol evaporation the cell was closed (see Fig. 70b). Fig. 70c represents the DHTA molecule and two different Mg-MOF coordinated structures CPO-26-Mg and CPO-27-Mg. The software Mercury 3.5.1 was used to represent the two MOF structures with the data from Dietzel et al. [7]. CPO stands for Coordination Polymer from Oslo. In some studies CPO-27-Mg is also called Mg-MOF-74 [12]. Two types of Mg-MOF coatings were distinguished. These are designated as Mg-MOF thin and Mg-MOF thick depending on the amount of Mg-MOF synthesised on top of the Mg electrode. These two types of samples will be analysed for corrosion and cell viability as separate groups.

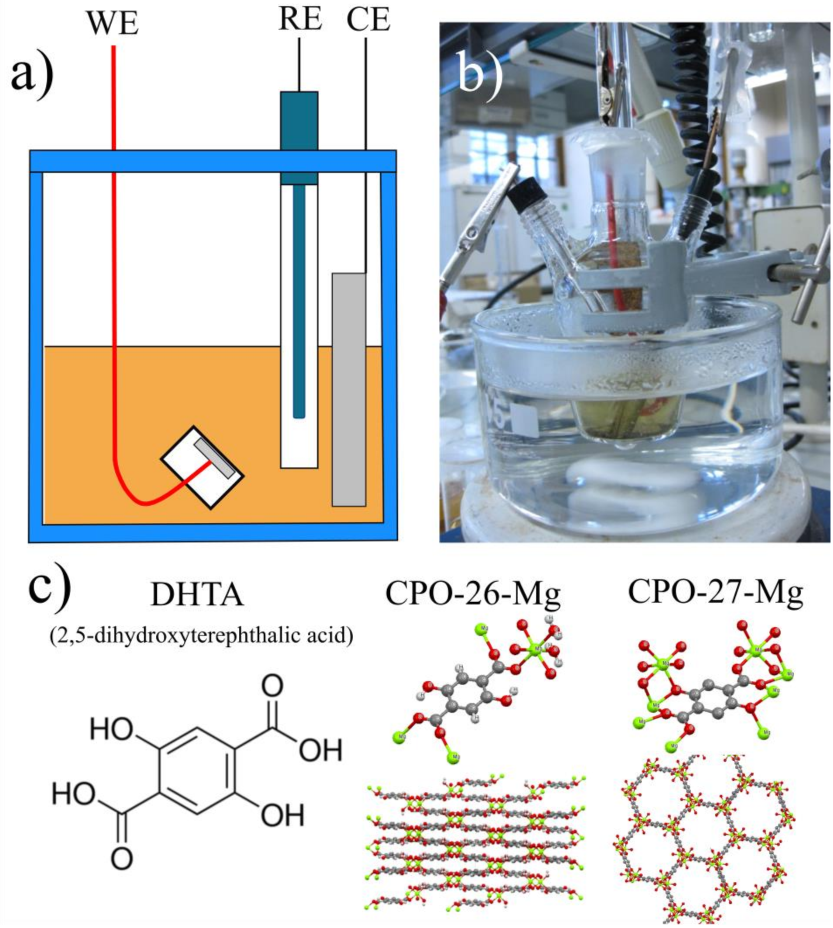

Figure 70: Electrochemical cell used for the Mg-MOF synthesis. (a) shows the scheme of the cell; (b) shows the cell setup and (c) depicts DHTA, CPO-26-Mg and CPO-27-Mg structures from left to right (source of data Ref. [7]). The colour of the spheres represent different elements: C is grey, O is red, H is white and Mg is green.

7.2.3. Degradation testing

Immersion tests and electrochemical methods, such as open circuit potential (OCP), potentiodynamic polarization (PDP), or linear sweep polarization, were applied for corrosion characterization of Mg electrodes with a Mg-MOF layer deposited on top. Mg samples with a pristine surface were used as a control. After Mg-MOF synthesis on the Mg electrodes, samples for immersion and EIS tests were prepared by cutting the cable and covering the site where the cable was with epoxy resin in order to isolate the sample electrically.

7.2.4. Immersion tests

Immersion tests were performed in HBSS without Ca^{2+} and Mg^{2+} (HBSS, life technologies 14175, Grand Island, USA) at 37 ± 0.5 °C for 4 days with an electrolyte volume to surface ratio (V/S) of 75 ml/cm^2. Basically these immersion tests are done as described in Section 4.2.2. Experiments were performed in duplicates with each type of sample. Hydrogen and pH were monitored during the immersion test. Samples were laying inside a funnel (35mm diameter x 50mm height) with an eudiometer inverted on top. The eudiometer was used to collect the hydrogen gas generated and their capacity was 35 mL. The mass loss was determined as in the Section 4.2.2 after cleaning the samples in chromic acid for 1 h to remove the corrosion products. This treatment could also remove partially the Mg-MOF deposited on the disc surface. Therefore, mass loss method will presumably provide higher degradation rates.

7.2.5. Polarization measurements

OCP and polarization experiments with the rotating disc electrode (RDE) as working electrode are performed with the same cell and parameters explained in Section 3.2.2. The data analysis is also done as in the same section. The surface of the working electrode exposed in the RDE clamp was approximately 0.5 cm^2. The electrolyte used was also HBSS at 37 ± 0.5°C. The conductivity of HBSS at 37°C is 13.7 mS/cm. The Tafel extrapolation and data analysis is also done as in the section mentioned above.

7.2.6. Cell viability

A preliminary investigation about the cytotoxicity of Mg discs with Mg-MOF thin and thick layers was performed. The cytotoxicity was analysed by a cell viability test with murine MC 3T3-E1 pre-osteoblast cells obtained from European collection of cell cultures (ECACC, Salisbury, UK). These cells can mirror the cellular behaviour of human bone cells in contact with the implant during a clinical situation aiming bone healing purposes. Cells were cultured in Eagle’s minimum essential medium (Sigma-Aldrich, St. Louis, MO, USA) supplemented with 10% fetal bovine serum (Sigma-Aldrich), 100 U/mL penicillin, 100 µg/mL streptomycin and 2 mM glutamine (these 3 reagents are from Invitrogen, Carlsbad, CA, USA) at 37 °C, 5 vol.% CO_2 and 95 % relative humidity. MC 3T3-E1 cells were seeded onto the samples at a density of $5 \cdot 10^4$ cells. Cells were incubated for 30 minutes (under cell culture conditions) to allow initial adhesion. Subsequently 4 mL of medium were added to each well. Cells were cultured for 24 h and 48 h on the samples. After 24 h and 48 h samples were removed from the culture medium and live-dead staining (Invitrogen, Carlsbad, CA, USA) was applied to the specimens. Samples were visualized by inverted fluorescent microscopy (Nikon GmbH, Düsseldorf, Germany) with a magnification of 10x. The applied filters were Fluorescence isothiocyanate conjugated (FITC) (Ex: 460-500 nm; Em: 510-560 nm; Mirror at 505 nm) and Texas red (Ex: 540-580nm; Em: 600-660; Mirror at 595 nm). Each experiment was performed in duplicates with: pure Mg as control and Mg-MOF thin and thick layers. Thin Mg-MOF coated samples were stained without cells to see the influence of the staining on the coating.

7.2.7. X-ray diffraction

The Mg-MOF structure was analysed by XRD as explained in Section 3.2.3. This analysis compares the obtained structures with the ones reported by Dietzel et al. [7] shown in Fig. 70c.

7.3. Results and discussion

7.3.1. Electrochemical synthesis

At the beginning of the process the electrolyte does not contain any Mg^{2+}. In order to electro-synthesize Mg-MOF both the Mg^{2+} and 2,5-dihydroxyterephthalate molecule concentration have to reach the saturation limit. Thus, the applied procedure consists of polarizing potentiostatically consecutive samples dissolving the Mg electrode and increasing the Mg^{2+} ion concentration in the setup shown in Fig. 70a and b. Consequently, the Mg^{2+} concentration increases after each potentiostatic polarization for 1 h. As explained in Section 7.2.2, two electrochemical cell volume sizes of 10 mL and 20 mL and two electrolytes with 60 mM and 120 mM DHTA concentration were applied.

The evolution of pH and charge transfer with a 10 mL cell and 60 mM DHTA electrolyte during 8 consecutive polarizations is shown in Fig. 71. The pH increases linearly with each polarization of 1 h. The charge transfer is directly related to the amount of Mg^{2+} dissolved. This data is derived from the current density measured, integrated over the time of each experiment and divided by the surface area of the sample-electrode interface. Thus the charge transfer shows a maximum at 21 C after polarizing 2 samples. These samples show a thick but non-uniform layer of Mg-MOF particles deposited on the surface next to the edge of the disc. As shown below in Fig. 75 the particle size contained in these so-called thick layers can be as large as 400 μm. However, the particle size is very variable and, in general, the thick Mg-MOF layers are larger than 100 μm. Then the charge decreases down to 10-13 C and it is at this stage when more homogeneous and thin Mg-MOF layers are deposited. Also as shown later in Fig. 76c, the particle size of the thin layers is very variable although it is certainly smaller than 100 µm. Finally, when the DHTA concentration starts to decrease the charge starts to increase again. This behaviour occurs when several samples have been covered with Mg-MOF the concentration of DHTA starts to decrease, so that no more yellowish Mg-MOF is deposited as shown on samples 7 and 8 in Fig. 71.

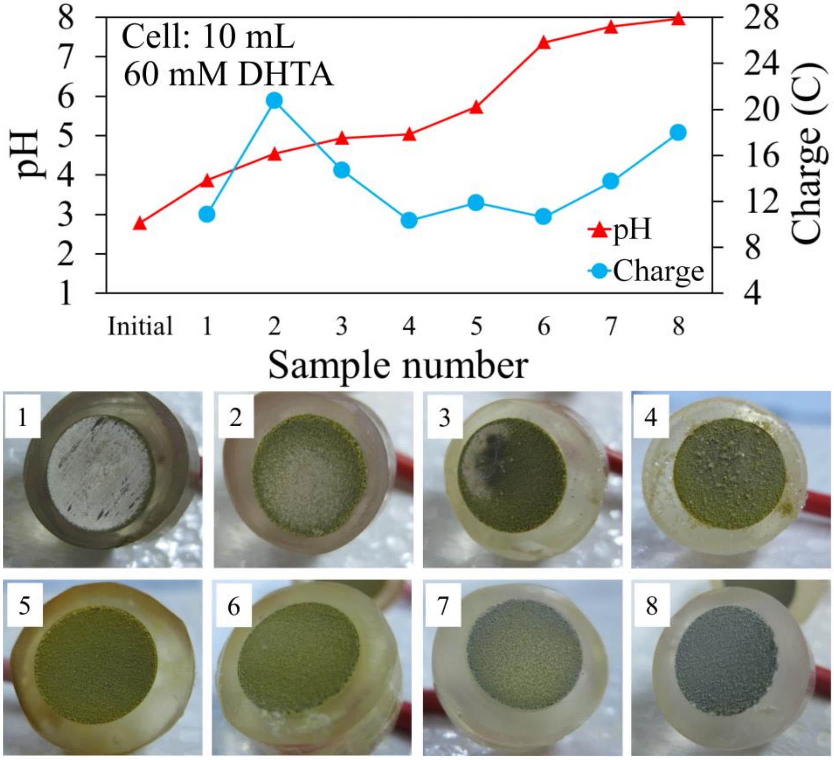

Figure 71: pH evolution and charge consumed over consecutive potentiostatic polarizations of different Mg electrodes for Mg-MOF electro-synthesis on the electrode surface. The electrolyte volume applied is 10 mL and the DHTA concentration is 60 mM.

Similarly, as depicted in Fig. 72, when a cell of 20 mL is applied the first charge maximum is only reached at the 7th polarization. Homogeneous and thin Mg-MOF layers are deposited after this 7th polarization. The DHTA concentration decrease is registered at the 12th sample. In this case, the pH increases almost linearly up to a pH of 8. Hence, when the volume of the cell is larger, reaching a high Mg^{2+} ion concentration is delayed, and more samples have to be dissolved to start depositing homogeneous layers.

This electro-synthesis process can be accelerated when the initial DHTA concentration in the electrolyte is increased up to 120 mM. Fig. 73 shows that only with the first two polarized samples in a 10 mL cell a thick Mg-MOF with larger crystals can be deposited (as shown later in Fig. 75). The third sample starts to show uncovered areas, which is attributed to the decrease of DHTA concentration in the electrolyte. The pH in these experiments does not reach higher values than 4.

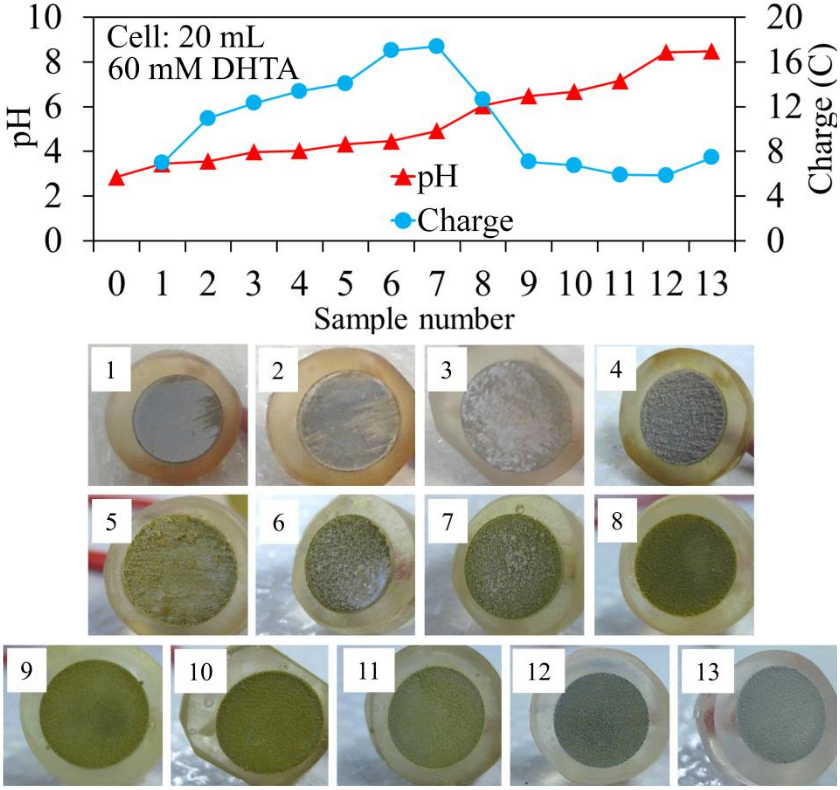

Figure 72. pH and charge evolution for Mg-MOF electro-synthesis with an electrolyte volume of 20 mL and a DHTA concentration of 60 mM. In this case, a higher volume decreases the chemical kinetics delaying the Mg-MOF deposition; therefore, more samples are needed to get thin Mg-MOF layers.

These results show the importance of the electrolyte volume since small volumes induce faster concentration changes. Therefore, a small volume accelerates reaching a charge maximum and Mg^{2+} ion saturation, and delays the linker concentration minimum. The electro-synthesis procedure can be continued with more consecutive samples by adding a 50% of the initial solution to the already used solution. In this way, DHTA concentration is increased and volume changes due to evaporation are corrected. Note that the water content will slightly increase after several cycles. It is also possible to add DHTA.

Hence, this process is explained as follows. Firstly, Mg dissolves increasing the concentration of Mg^{2+} ions. A few samples are potentiostatically dissolved for 1 h in order to reach a high Mg^{2+} concentration. Once a high concentration in the electrolyte is reached Mg combines with DHTA to form Mg-MOF. The deposition occurs at the Mg surface since it is in the vicinity of the electrode where the concentration is the highest. When this electrosynthesis is performed consecutively with several electrodes the DHTA content starts to become deficient for the Mg-MOF synthesis. Thus, the process is controlled by both the DHTA mass transport as DHTA is consumed at the Mg surface and by charge transfer because Mg is electrochemically dissolved.

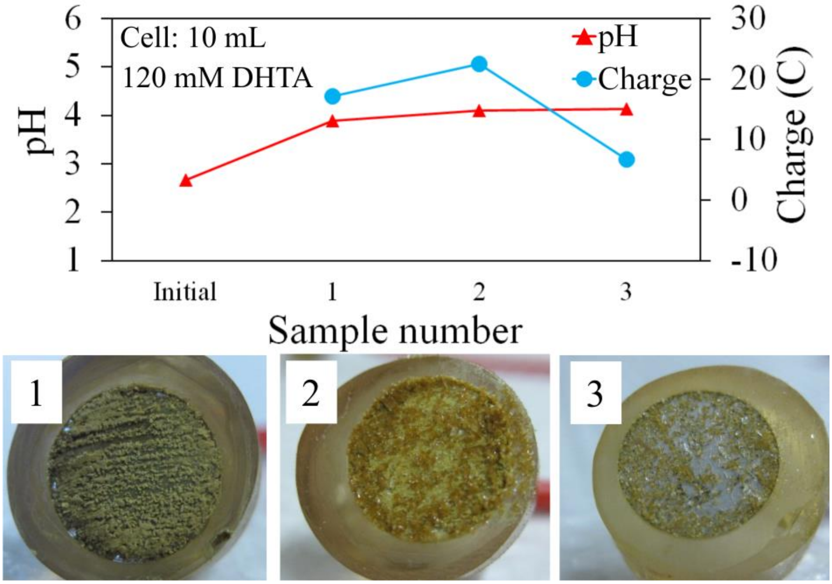

Figure 73. Mg-MOF electrosynthesis results for three consecutive potentiostatic polarizations of different Mg electrodes. In this case, the electrolyte volume applied is 10 mL and the DHTA concentration 120 mM.

The measured current densities during the experiments shown in Figs. 71, 72 and 73 were between 150 and 400 μA/cm^2. Thus, the current flow is slow due to the low conductivity of the electrolyte.

Due to the anodic potential applied to force the Mg dissolution reaction and the presence of water in the electrolyte the hydrogen evolution reaction is promoted. This H_2 evolution at anodic potentials is related to the negative difference effect from the Mg corrosion as explained previously in Section 1.7.4. Since the bubbles are observed from the beginning of the electro-synthesis process these gas bubbles are considered as H_2 gas, and a large amount of H_2 can be observed because of the anodic potential applied of +4 V vs OCP.

As shown in Fig. 74a and b, Mg-MOF is also formed in the electrolyte and at the counter electrode. This phenomenon is explained by the electrochemically induced cathodic deposition [29]. Thus, Mg^{2+} ions can diffuse and reach the entire cell where together with DHTA both reach the precipitation concentration. Possibly the Mg-MOF synthesis on the counter electrode could be caused by an electrophoretic process which is possible considering the structure of DHTA.

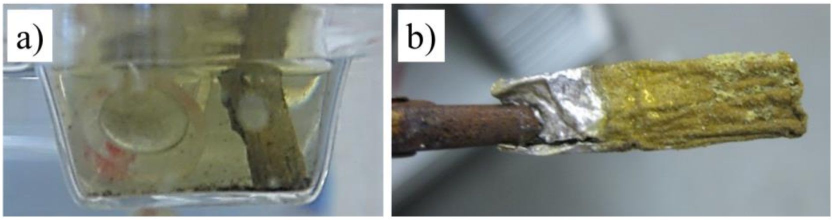

Figure 74. Macro images showing that (a) Mg-MOF is also synthesized in the electrolyte (b) and on the counter electrode, respectively.

7.3.2. SEM analysis

Fig. 75 depicts a thick Mg-MOF layer morphology deposited in 120 mM DHTA solution. This layer is composed of two different Mg-MOF structures CPO-26-Mg and CPO-27-Mg, denoted with numbers 1 and 2 in Fig. 75, respectively. The EDX spectrum from area 1 in Fig. 75 shows a lower Mg intensity peak compared to spectrum 2 and taking C and O peaks as references. As shown above in Fig. 70c, the CPO-26-Mg and CPO-27-Mg structures contain different amount of Mg and O. The CPO-27-Mg includes more Mg ions in its structure than CPO-26-Mg. Thus, the crystals like the ones in area 1 are likely to be CPO-26-Mg, whereas area 2 is considered as CPO-27-Mg. In these spectra, the oxygen intensity decreases as the Mg one increases. As shown in Fig. 73b, CPO-27-Mg is formed of thin needle-like crystals arranged in a ball shape. The quantification shown in Fig. 75 is only an approximation of the real composition especially because C is hardly quantifiable by EDX.

Similarly, Fig. 76 shows a thin Mg-MOF layer deposited on the 5th electrode in 60 mM DHTA solution. As shown in Fig. 76b, the same two structures can be identified but, in this case, the size of both structures is smaller. The needle-like balls are identified as CPO-27-Mg and cube-shaped particles as CPO-26-Mg. The particle size of these thin layers is very variable although it is certainly smaller than 100 µm (Fig. 76c). As observed in Fig. 76b this coating is not completely uniform and some areas are not covered.

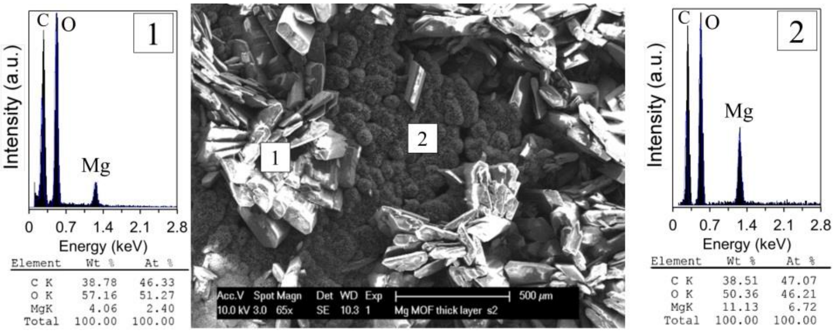

Figure 75: Thick Mg-MOF layer morphology deposited during the 2nd polarization in 10 ml of solution with 120 mM of DHTA showing CPO-26-Mg and CPO-27-Mg structures. The SEM image at the top shows both Mg-MOF morphologies. The EDX spectra identified as 1 and 2 indicate different O and Mg contents differentiating both Mg-MOF structures formed with DHTA: CPO-26-Mg and CPO-27-Mg, respectively.

Mg-MOF coating attachment is attributed to mechanical adhesion. During anodic dissolution, a rough surface is created at the Mg anode and crystals are mechanically confined inside the voids and anchored to the substrate. Moreover, the Mg-MOF layers appear to be constituted by continuous films of intergrown crystals with good adhesion to each other as shown in Fig. 75 and 75b. In literature, the adhesion of MOF crystals to the surface is reported for some cases as very poor, since MOF film detachment has been observed for flat substrates and they can be washed off just by rinsing with warm ethanol [13, 14]. Although here the MOF adhesion is not investigated, it is not considered poor.

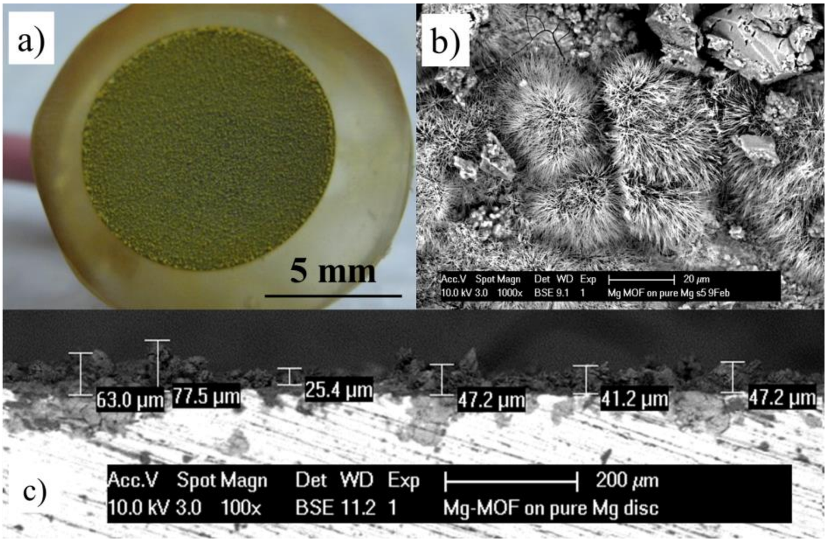

Figure 76: Thin Mg-MOF layer morphology deposited during the 5th polarization in 10 mL of solution with 60 mM of DHTA, also showing CPO-26-Mg and CPO-27-Mg structures. (a) is a macro picture; and (b) and (c) are a both SEM images showing the two Mg-MOF structures and the Mg-MOF layer thickness, respectively.

7.3.3. XRD analysis

Dietzel et al. studied the Mg-MOF synthesised hydrothermically in an autoclave and reported its crystallographic XRD data [7]. As shown in Fig. 74 ions can migrate far from the electrode surface and bind the ligand thereby synthesizing Mg-MOF in solution. This Mg-MOF powder can be collected by completely dehydrating this solution. Fig. 77 shows the XRD pattern of this powder compared to the two structures in which Mg can bind to the linker. As shown in Fig. 77, the XRD spectrum of the powder contains the characteristic CPO-27-Mg and CPO-26-Mg intensity peaks, confirming the presence of both CPO-26-Mg and CPO-27-Mg structures in this powder. Similarly, the same pattern as the powder is measured from the Mg-MOF deposited on the Mg electrodes but with a lower intensity (data not shown).

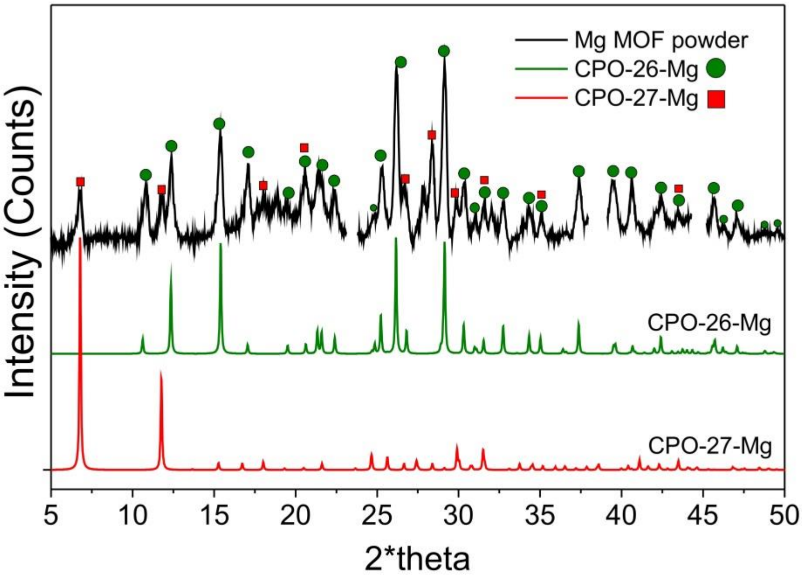

Figure 77: XRD patterns comparing the synthesized Mg-MOF powder with its two theoretical structures, proving that these two structures are present in the synthesized Mg-MOF powder.

7.3.4. Corrosion properties

a) Immersion tests

Fig. 78 depicts the degradation process in HBSS of Mg samples with a thin and thick Mg-MOF layer on top and pure Mg as reference. The hydrogen evolution shows a faster degradation rate when a thick Mg-MOF layer is deposited on a Mg electrode (Fig. 78a) by a hydrogen generation rate of 3.3 ml/cm^2/day. Thin Mg-MOF degrades faster than pure Mg but 3 times slower than samples with a thick Mg-MOF, by a hydrogen rate of 1.1 ml/cm^2/day. Pure Mg has the lowest rate (0.28 ml/cm^2/day). One of the two samples tested as thick Mg-MOF had to be removed from the test as the maximum hydrogen volume that can be collected was exceeded. The pH during testing of these three types of samples ranged between 9 and 9.5 being higher for samples denoted as thick Mg-MOF layers (Fig. 78b). The degradation rate calculated from the hydrogen collected at each time point is shown in Fig. 78c. Thick Mg-MOF samples degrade with a variable rate between 5 and 15 mm/year. Thin Mg-MOF and the pure Mg control degrade approximately at 2.3 and 0.6 mm/year respectively. Note that the initial behaviour of Mg control and thin Mg-MOF samples are comparable during the first 24h.

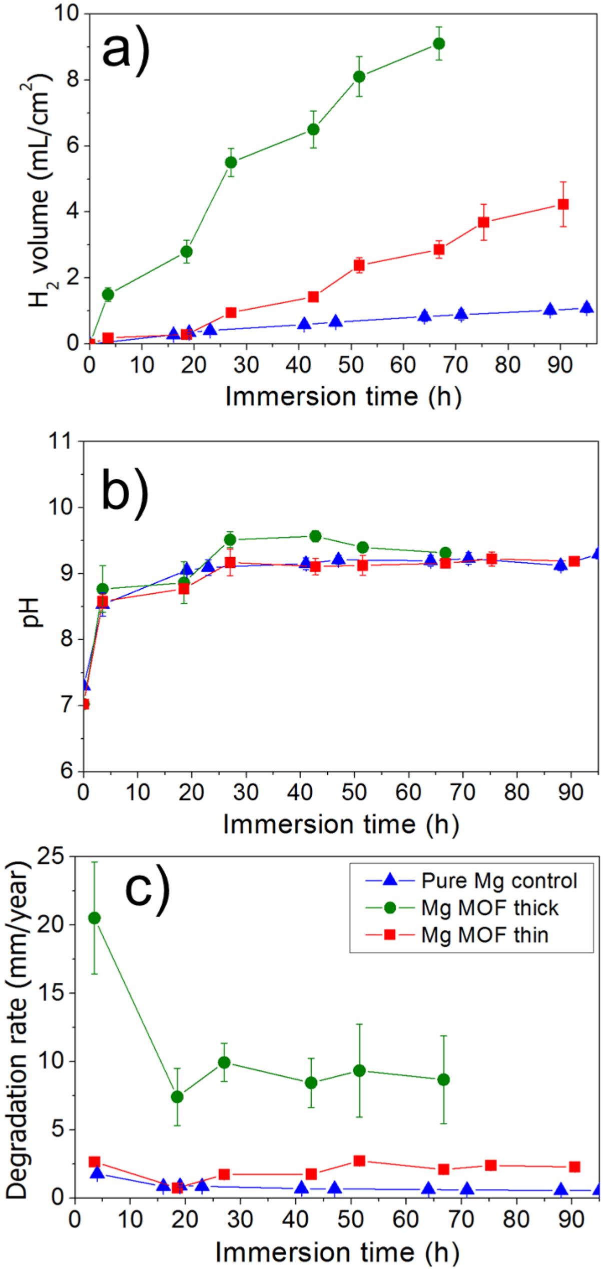

Figure 78: (a) Hydrogen, (b) pH and (c) degradation rate evolution determined by H_2 collection over immersion time of pure Mg electrodes with thin and thick Mg-MOF layer on top and pure Mg as a control in HBSS at 37˚C. These results indicate that Mg-MOF accelerates the degradation process showing that thin Mg-MOF layer can have a more acceptable corrosion profile.

Fig. 79 shows degradation rates calculated at the end of the immersion tests and macro images of samples before the immersion tests and after the removal of the corrosion products. The degradation rates are calculated by gravimetry measuring the mass loss (ML) after chromic acid treatment and by H_2 gas collection applying ideal gases law and considering that 1 mol of Mg is related to 1 mol of H_2 generated. On the one hand, the degradation rate by ML of pure Mg, electrodes with thin and thick Mg-MOF layers are: 0.7, 6.9 and 24.6 mm/year respectively. On the other hand, rates calculated by total H_2 generation are 0.6, 2.3 and 11.38 mm/year. The chromic acid treatment is done for corrosion product removal but the remaining Mg-MOF is also completely removed by this treatment, which can explain the higher degradation rates determined by ML than by H_2.

As also shown in Fig. 79, localized corrosion is identified on samples with Mg-MOF layers on top due to the high Cl^- content in HBSS and because samples are neither completely nor homogeneously covered by Mg-MOF [15]. Deep pits found on the samples might reach the silver glue used for connecting the cable to the Mg disc for electrode preparation. Thus, the corrosion process is accelerated as Mg and Ag have opposite standard reduction potentials (-2.37 V and +0.80 V vs standard hydrogen electrode (SHE), respectively) [15], forming a galvanic cell and promoting Mg degradation. This is the reason why one of the thick Mg-MOF samples was removed earlier from the test. When the Mg is covered with a thin Mg-MOF this influence is less pronounced. Thus, a thick Mg-MOF layer will promote severe localized corrosion while with thin layers this influence is not so severe.

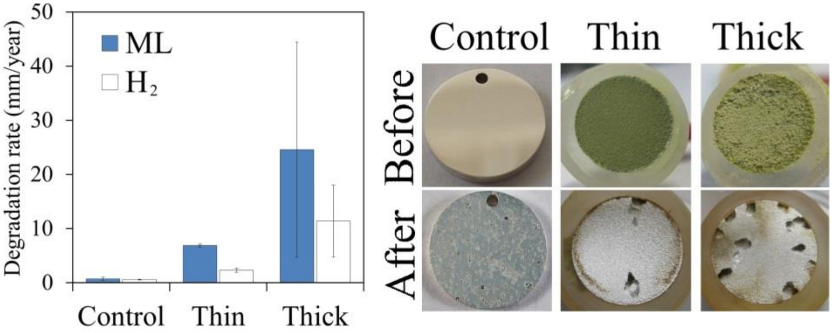

Figure 79: Degradation rate of pure Mg, as control, and Mg electrodes with thin and thick Mg-MOF layers calculated at the end of the immersion test of by mass loss (ML) and hydrogen evolution (H_2). Macro images from the sample before the immersion testing and after the product removal procedure with chromic acid solution are also shown. The diameter of each disc is 10 mm.

b) OCP and PDP analysis

Polarization and OCP measurements from a rotating disk electrode (RDE) can help to identify the initial degradation behaviour of samples with Mg-MOF coating (Fig. 80 and Table 19). Fig. 80a shows increased OCP values of thick and thin Mg-MOF coated samples (-1.540 V and -1.746 V, respectively) as compared to the Mg control (-1.955 V). This difference in OCP is related to the potential step that the Mg-MOF coating represents. The thicker the layer formed, the larger the measured potential step. PDP measurements shown in Fig. 80a also indicate a similar corrosion potential (E_{corr}) change comparing to the OCP. The similar OPC and E_{corr} values determined for each sample indicate minimum changes on the sample surface during the measurements due to the positive influence of applying dynamic conditions with the RDE [16]. However, as shown in Table 19, there is a difference of 50-60 mV between the OCP and E_{corr} of thick Mg-MOF samples. This indicates a faster degradation activity and changes on the surface due to the concomitant Mg corrosion process.

The current density (i_{corr}) calculated by Tafel extrapolation can indicate quantitatively the initial degradation rate of the samples at immersion tests. i_{corr} values for Mg control and thin and thick Mg-MOF samples are: 6.2, 1.4±0.6 and 5.4±0.4 A/cm^2 respectively. Thus, pure Mg shows the highest initial degradation rate followed closely by thick Mg-MOF samples. However, thin Mg-MOF samples show slower initial degradation behaviour. Thus, thin Mg-MOF layers improve the degradation behaviour of the Mg samples, although the long term behaviour shows localized corrosion due to the inhomogeneous nature of these layers.

Table 19 also shows the anodic (β_a) and the cathodic slopes (β_b) calculated by Tafel extrapolation and the polarization resistance (R_p). R_p is calculated from the i_{corr}, β_a and β_b by the Stern-Geary equation as shown in Eq. 13 in Section 1.7.1 [17]:

$$R_p = \frac{\beta_a \, \beta_c}{2.3 \, (\beta_a + \beta_c) \, i_{corr}} \qquad R_p \text{ from } i_{corr} \quad (13)$$

According to the Stern-Geary equation the i_{corr} and R_p are inversely proportional, thereby a higher i_{corr} is translated into a lower R_p. Pure Mg has the highest R_p (470 mΩ m^2) followed by thick Mg-MOF samples (314±40 mΩ m^2) and thin Mg-MOF coated samples (79±35 mΩ m^2).

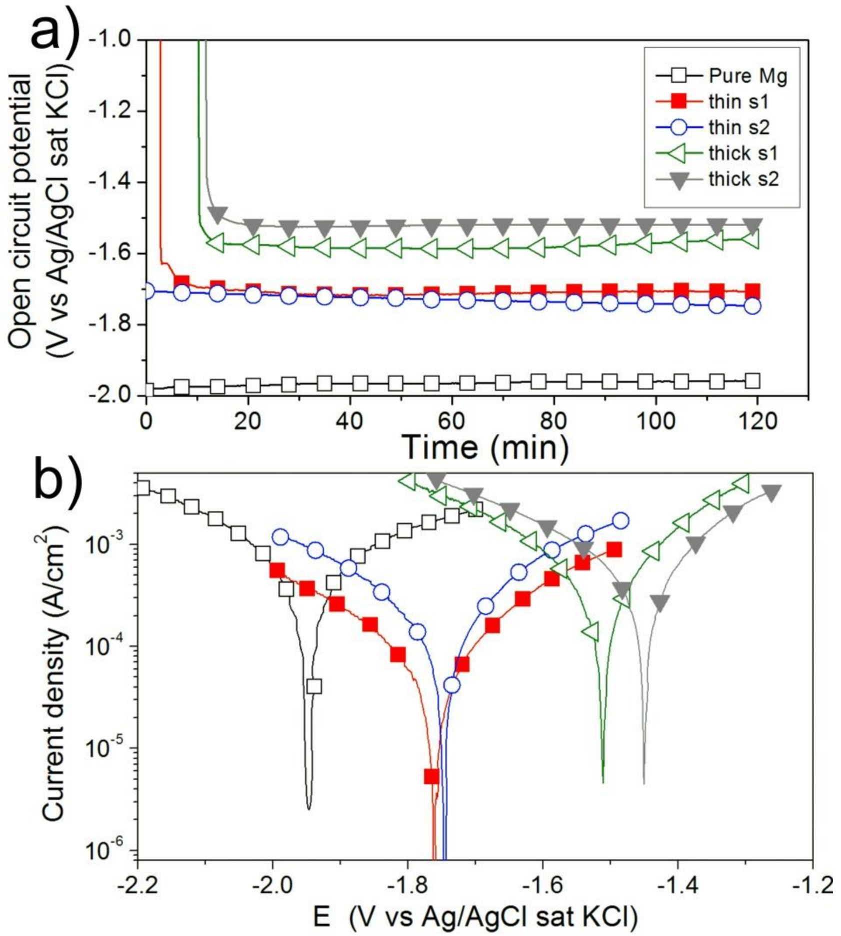

Figure 80: a) Open circuit potential (OCP) during 2 min from Mg control, and two thin and two thick Mg-MOF coated samples using RDE. b) Polarization curves of the same samples after the OCP measurement.

Table 19. Polarization data obtained by Tafel extrapolation. The reference electrode is the Ag/AgCl saturated with KCl.

HBSS	OCP (V vs ref.)	E_{corr} (V vs ref.)	i_{corr} (A/cm^2)	β_a (mV/decade)	β_c (mV/decade)	R_p (mΩ m^2)
Mg control	-1,955	-1,951	6,2	424	298	470
Thin Mg-MOF s1	-1,751	-1,762	0,8	225	279	44
Thin Mg-MOF s2	-1,742	-1,747	2,0	246	294	114
Thick Mg-MOF s1	-1,560	-1,511	5,8	251	320	354
Thick Mg-MOF s2	-1,519	-1,451	5,0	211	308	274

Data from non-coated pure Mg are not in agreement with the data from immersion tests as pure Mg degrades slower than Mg-MOF coated Mg in HBSS. The higher i_{corr} from PDP measurements with pure Mg is because of the lack of initial coating covering the pristine Mg surface, which can induce a faster initial degradation. In less than 1 day the degradation is slowed down due to the natural corrosion layer formation. The i_{corr} data from Mg electrodes with thin and thick Mg-MOF layers are in agreement with immersion test results, since Mg samples with a thin Mg-MOF layer on top degrade slower than the ones with a thick layer.

7.3.5. Cell viability

Fig. 81 depicts the cytotoxicity of Mg discs with thin and thick Mg-MOF layers as compared to pure Mg control. As shown in Fig. 81a, cells are completely healthy and attached to the pure Mg control with a normal morphology after 24h. However, no cells are viable on the surface of neither thin nor thick Mg-MOF layers (Fig. 81d and c).

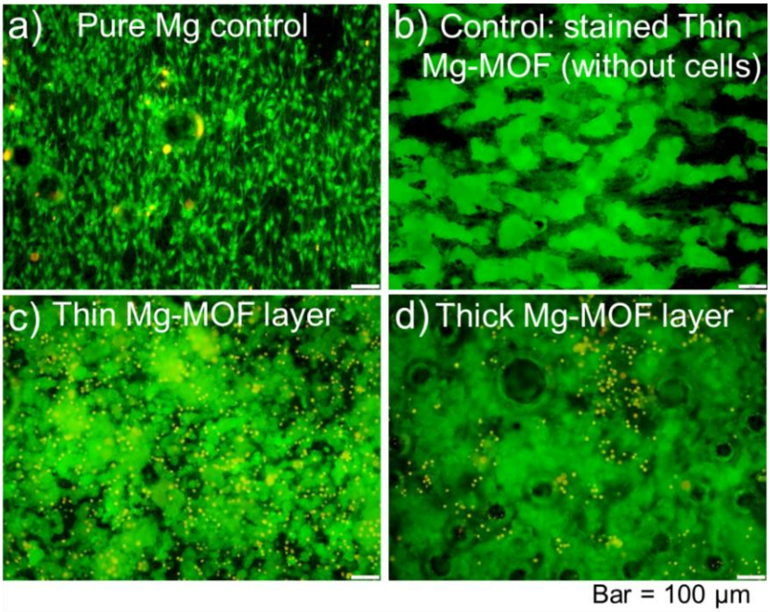

Figure 81: Fluorescence microscopy analysis after 24h in indirect contact with pre-osteoblast cells (MC3T3-E1) incubated in MEM + 10% FBS. These results show dead cells in contact with the Mg-MOF while cells in contact with pure Mg as control remain healthy.

The yellow spots visible on the surface in Figs. 81c and d are most likely unhealthy cells. If cells are yellow after the staining applied and using fluorescent microscopy, this means they are stained both red and green (shown as yellow when the two colours overlap). Because they will only stain green if they are alive, this likely means that the cells were alive for some time but after 24 h they are unhealthy or dying. Usually, if they were dead, they would completely detach from the material during the washing steps of the followed staining protocol, not being visible at all.

Importantly, these unhealthy/dying cells do not necessarily mean that the material is toxic to cells. The cells used are adherent cells, which would die when they are not attached to a surface. Therefore it is possible that the cells are dying simply because they are not attaching to the material. The fact that they are not attaching to the material is clear from their rounded and not spread shape.

To further assessing the cytocompatibility of the material in vitro tests recommended by ISO 10993 could also be applied, such as direct contact, agar diffusion, or an elution test [18]. These tests would separate the potential toxic effect of the materials from the inability of cells to adhere to the MOF layer.

Fig. 81b depicts thin Mg-MOF coated samples stained without having contact with cells showing the influence of the live dead staining on the coating. Thus, the fluorescent dye can stain this nanoporous material on the Mg surface and therefore a green background is visible.

7.4. Conclusions

Mg-MOF layers are successfully deposited on pure magnesium as a first step towards a new drug delivery system for biodegradable Mg implants. The key parameters of the anodic electrosynthesis process applied here are: (i) the electrolyte composition (ii) and volume; (iii) and the applied potential and (iv) time for Mg dissolution. In this work, an ethanol based electrolyte with a concentration of 2,5-dihydroxyterephthalic acid (DHTA), as linker, of 60 mM is recommended in a 10 mL volume cell. The electrosynthesis is achieved by applying 4 V against the open circuit potential of the Mg electrode during 1 h for depositing thin and homogeneous Mg-MOF layers. These layers are composed of the two structures in which DHTA and Mg combine, CPO-26-Mg and CPO-27-Mg. It is possible to add 50% more volume of the initial solution to the electrolyte already used in order to continue electro synthesizing Mg-MOF on more consecutive samples after the 7th sample.

Samples coated with thin Mg-MOF layers, with particles smaller than 100 µm, degrade faster in HBSS than uncoated samples. Thus the biodegradation process of the implant can be accelerated. This could be desirable in case of slowly degrading implants in vivo. Corrosion results indicate that thick Mg-MOF layers, with particle sizes between 100 and 400 µm, are not recommendable.

However, preliminary cell viability investigations indicate that Mg-MOF layers might be cytotoxic although additional assays to confirm the potential cytotoxic effect should also be performed. The use of other ligands with reduced in vitro cytotoxicity also needs to be explored in future work and the drug delivery function needs to be verified.

References

[1] S. Keskin, S. Kızılel, Industrial and Engineering Chemistry Research 50 (2011) 1799-1812.

[2] O.K. Farha, I. Eryazici, N.C. Jeong, B.G. Hauser, C.E. Wilmer, A.A. Sarjeant, R.Q. Snurr, S.T. Nguyen, A.Ö. Yazaydın, J.T. Hupp, JACS 134 (2012) 15016-15021.

[3] P. Horcajada, T. Chalati, C. Serre, B. Gillet, C. Sebrie, T. Baati, J.F. Eubank, D. Heurtaux, P. Clayette, C. Kreuz, J.-S. Chang, Y.K. Hwang, V. Marsaud, P.-N. Bories, L. Cynober, S. Gil, G. Ferey, P. Couvreur, R. Gref, Nat Mater 9 (2010) 172-178.

[4] P. Horcajada, C. Serre, G. Maurin, N.A. Ramsahye, F. Balas, M. Vallet-Regi, M. Sebban, F. Taulelle, G. Ferey, JACS 130 (2008) 6774-6780.

[5] P. Horcajada, C. Serre, M. Vallet-Regí, M. Sebban, F. Taulelle, G. Férey, Angewandte Chemie International Edition 45 (2006) 5974-5978.

[6] R. Ameloot, L. Stappers, J. Fransaer, L. Alaerts, B.F. Sels, D.E. De Vos, Chemistry of Materials 21 (2009) 2580-2582.

[7] P.D.C. Dietzel, V. Besikiotis, R. Blom, JOM Chemistry 19 (2009) 7362-7370.

[8] A. corporation, Acute Oral Toxicity Study of Terephthalic Acid in RatsAcute Oral Toxicity Study of Terephthalic Acid in Rats, vol IITRI Study #1557IITRI Study #1557, Conducted by IIT Research InstituteConducted by IIT Research Institute, 1990.

[9] A.C. Co, Acute Dermal Toxicity Study of Terephthalic Acid in Rabbits., vol Test Study Reference: IITRI SN 1558, TA# 445F, 1990.

[10] A.C. Co, Acute Inhalation Toxicity study of Purified Terephthalic Acid in Rats, vol ITRI Study #1158, Conducted by IIT Research Institute, 1987.

[11] P. Horcajada, R. Gref, T. Baati, P.K. Allan, G. Maurin, P. Couvreur, G. Férey, R.E. Morris, C. Serre, Chemical Reviews 112 (2012) 1232-1268.

[12] N.L. Rosi, J. Kim, M. Eddaoudi, B. Chen, M. O'Keeffe, O.M. Yaghi, JACS 127 (2005) 1504-1518.

[13] N. Campagnol, T. Van Assche, T. Boudewijns, J. Denayer, K. Binnemans, D. De Vos, J. Fransaer, JOM Chemistry A 1 (2013) 5827-5830.

[14] N. Campagnol, T. Van Assche, L. Stappers, J.F.M. Denayer, K. Binnemans, D.E. De Vos, J. Fransaer, ECS Transactions 61 (2014) 25-40.

[15] B.A. Shaw, Corrosion resistance of magnesium alloys, ASM int., UK, 2003.

[16] I. Marco, O. Van der Biest, Corros. Sci. 102 (2016) 384-393.

[17] M. Stern, A.L. Geary, J. Electrochem. Soc. 104 (1957) 56-63.

[18] I. 10993, Biological evaluation of medical devices, 2009.

Chapter 8:
Conclusions and future perspective

Magnesium is a promising material for temporal implant applications and it will certainly be used in biomedicine increasingly in the future. Magnesium has shown in many studies that it is a highly biocompatible material in animal and in clinical studies. Furthermore, as demonstrated by many authors such as Kraus et al. [1] Mg is able to completely degrade during the bone healing process. The applications where biodegradable Mg implants can be used are many. For this reason, the approach of tailoring the degradation rate of the Mg based material to allow fast and slow resorption remains valid. The scientific community is, nowadays, developing a large Mg alloy data base analysing mechanical and degradation properties.

During this PhD thesis the degradation profiles of different Mg alloys have been analysed finding a great variability depending not only on the material and its processing, but also on every parameter of the testing method. Alloying additions, microstructure and, especially, impurity content have been found strongly related to the degradation performance.

8.1. Main achievements and outlook

The main achievements obtained in this study can be summarized as follows:

- **Polarization data with the rotating disc electrode (RDE) are more reproducible and are considered to represent more closely the initial degradation behaviour of the material.**

Polarization experiments are commonly used to characterize the degradation behaviour of different Mg alloys. However, when tests are performed under static conditions a higher irreproducibility is detected. This is mainly attributed to the degradation product formation on the Mg surface, such as $Mg(OH)_2$. This formation is considered to have a rather stochastic influence on the results. When dynamic conditions are applied, at a rotation speed higher than 1500 rpm, degradation product deposition is minimized.

As shown in Section 3.3.6, the use of RDE also reduces the influence of the negative difference effect (NDE) since a pronounced anodic current increase is not measured when the RDE is applied. This is explained by the extremely low amount of corrosion products observed on the surface as compared to static measurements. These products can act as cathodes which exchange electrons with the Mg around them, acting as the anode. Therefore, the external circuit does not measure these electrons, and the corrosion and H_2 reactions are accelerated without being fully registered. All these observations are consistent with the enhanced catalytic surface theory as an explanation for the negative difference effect (NDE). Hence, the monovalent Mg ion theory should no longer describe the NDE.

With the use of the RDE more symmetric anodic and cathodic curves are determined, which allows simple Tafel extrapolation providing repeatedly similar results even in different media. Furthermore, polarization measurements from a RDE are considered to indicate the initial degradation behaviour during immersion testing. Unfortunately, the long term behaviour also depends on the corrosion layer precipitation, and therefore, this method only provides the intrinsic response of the pristine surface of a Mg based material in a certain electrolyte.

- **Testing in DMEM represents in vivo conditions more closely than PBS and HBSS (without Ca^{2+} and Mg^{2+}).**

The physiological testing setup applied in Chapters 4, 5 and 6 with DMEM as electrolyte and under sterilization measures, can maintain the physiological pH level, and induce a degradation layer on the Mg samples and a degradation rate (DR) more comparable to in vivo conditions.

Two positive aspects of the experimental setup to mimic physiological conditions have been identified. Firstly, the pH can be maintained in a physiological range, between 7.7 and 7.9, which indicates HCO_3^-/CO_2 as an appropriate buffering system. And secondly, the stirring produces a dynamic flow renewing the electrolyte in the vicinity of the Mg surface avoiding a local pH increase which would influence the in vitro data.

The surface film formed on Mg immersed in DMEM is composed of two layers: $Mg(OH)_2$ and Mg-carbonate on the inner part; and calcium phosphate in the outer part. During in vivo tests, although Mg forms a less homogeneous degradation layer, the same elements are present in it with Ca and P richer areas and Mg carbonate and hydroxide.

The similarity in DRs between DMEM testing and in vivo is highlighted by the low rate determined for Mg-2Ag under these two conditions, while high rates are determined in PBS and HBSS (Sections 4.3.2 and 4.3.3). Hence, in vivo as well as in vitro physiological conditions are less aggressive testing conditions. The lower Cl^- ion concentration and the presence of Ca^{2+}, PO_4^{3+} and HCO_3^- ions highly influence the degradation process of the studied Mg alloys and the consequent degradation layer formation. Additionally, DMEM with the CO_2 buffering system has a similar composition as body plasma. Therefore, the degradation testing performed in DMEM is expected to be the most representative of in vivo conditions while PBS and HBSS (without Ca^{2+} and Mg^{2+}) do not simulate physiological conditions as well.

However, after assessing the gas evolution in DMEM tests in Sections 4.3.1.a, 5.3.1 and 6.3.3.a, it is found that the data do not accurately represent the degradation process, especially in short term. This is due to the small initial amount of H_2 created and the initial gas collection because of the CO_2 buffering system. In order to increase the data accuracy, the use of a control sample (without Mg sample) is highly recommended.

As shown in Chapter 5, the sterilization of DMEM can be maintained, or the contamination at least delayed, by applying UV-C radiation (with a wavelength of 254 nm) and the addition of antibiotics (e.g. penicillin/streptomycin) to the medium. This is necessary in order to avoid Mg corrosion acceleration by contamination and so continue mimicking the in vivo conditions more closely. However, sterile conditions cannot be maintained indefinitely in a standard lab environment and the tests should be stopped before medium contamination occurs.

- **Impurity content and grain size play a major role in the Mg degradation behaviour.**

The in vivo and in vitro comparison (Chapter 4) has shown that the same Mg alloy produced by a similar processing with small variations leads to a different impurity content and microstructure. Consequently, impurities and grain size drive the degradation performance downplaying the role of alloying additions, in this case Gd and Ag.

Thus, the relevance of a high Fe and Ni impurity content on the degradation behaviour of Mg alloys has been identified in these studies. Moreover, Mn seems to play a beneficial influence on the degradation process of Mg when the purity of the material is high (Fe<45 ppm and Ni<10 ppm) but not ultra-high.

In Chapter 6, it is also indicated that a small grain size between 5 and 20 µm has a positive influence. Mg-Ag alloys show the highest DRs presumably due to the larger grain size but also due to the Ag additions, since the impurity contents in the alloys in disc shape are comparable.

- **Gd can increase and Ag decrease the corrosion resistance of Mg binary alloys, whereas mechanical properties are improved.**

In Chapter 6, Mg-Gd alloys with the grain size and impurity levels determined (50-60 ppm of Fe, and <10 ppm of Ni) are found as suitable implant candidate materials due to their controlled and homogeneous degradation in PBS, HBSS and DMEM (<1.5 mm/year).

Mg-Ag alloys have shown a similar behaviour in DMEM to pure Mg and Mg-Gd alloys, while in PBS and HBSS the degradation was accelerated due to the higher Cl^- ion content but also the larger grain size. Thus, binary Mg-Ag alloys can also be implant candidates which can corrode faster under physiological conditions but also in a controlled manner (between 2.6 and 1.2 mm/year), with the antibacterial added value of Ag.

Pure Mg for instance, also showed homogeneous and controlled degradation behaviour in PBS, HBSS and DMEM. This is due to the positive influence of a higher Mn content in these disc-shaped alloys.

Alloying additions of REs in Mg-Gd and Mg-4Y-3RE alloys show the highest increase in microhardness, indicating that the mechanical properties of these alloys are also improved as compared to pure Mg. These alloys might be suitable during clinical applications where Mg implants are to be used for load-bearing applications.

As shown in Chapter 4, Gd has been detected together with impurity elements in particles present in the degradation layer. These particles and GdH_2 cuboids (shown in Sections 5.4.1 and 6.4.4.b) might get encapsulated at the bone site or be resorbed by the body. Ag rich precipitates can also be found at the degradation layer during the degradation process, as indicated in Section 6.4.4.c. The initial surface can contain some of these particles or impurity rich particles as a result of the implant production and preparation process (Section 4.3.5) and a surface preparation is found recommendable in any Mg degradation study in order to facilitate data interpretation.

- **Mg-MOF electro-synthesis is successfully achieved as a first step towards a new drug delivery system on biodegradable Mg implants.**

As shown in Chapter 7, the electrochemically aided Mg-MOF synthesis depends on the electrolyte used in the cell (electrolyte composition, its low conductivity and volume) and the potentiostatic parameters (applied potential and time for Mg dissolution).

However, Mg-MOF coatings have been found to be able to accelerate the degradation rate of the Mg substrate and even promote localized corrosion mode during immersion tests. The corrosion acceleration could be due to the working electrode preparation with silver epoxy glue. In that case, a different behaviour could be expected with a coated Mg implant.

Finally, preliminary cell viability investigations indicate that Mg-MOF layers might not be biocompatible. Perhaps, other linkers might show a better biocompatibility in contact with bone cells. Further research opportunities are identified after this study.

8.2. Suggestions for future work

Based on the results and conclusions of this thesis, the following suggestions are made for further research:

- **Investigate the influence of impurities**

As shown in Chapters 4 and 6, the influence of impurities has been highlighted. Therefore, the systematic study of the influence of impurities with the same material seems an interesting option as future work. As mentioned in Section 1.5.1, Hanawalt and co-workers elucidated the effects of different impurities in Mg such as Fe, Co, Cu and Ni on the resultant corrosion but only in NaCl based solutions. This future study here proposed should quantify the actual tolerance limit of Fe, Ni or Si under more physiological conditions or even in vivo, and analyse the beneficial effect of Mn.

Results from Chapters 4, 5 and 6 indicate that the degradation behaviour can be modified by the impurities and therefore the control and/or addition of impurities during the processing seems an interesting opportunity to tailor the degradation rate of Mg implants.

- **Studies with identical Mg biomaterials in vitro and vivo**

The results shown in this thesis in Chapter 4 indicate that the Mg degradation data can be hard to interpret due to the many influencing factors. In order to be able to compare results from in vitro and in vivo studies more accurately a study with the same nominal material is recommended. The surface preparation should also be the same for the Mg samples in both type of studies. In this way the actual degradation rate and corrosion mode can be compared and, as a result, an improved degradation testing protocol could be defined.

- **Clinical studies with Mg-Gd and Mg-Ag alloys**

The results from Chapters 4 and 6, indicate that the studied Mg-Gd and Mg-Ag alloys have a uniform and controlled degradation rate under physiological conditions. Mg-Gd alloys show increased mechanical properties and homogeneous and slow degradation (< 1.6 mm/year) under all the testing conditions. Mg-Ag alloys for instance do show an increased degradation rate, although not higher than 3 mm/year under physiological conditions, and Ag might have an increased antibacterial influence on the Mg alloy. These antibacterial properties are also of interest and it is currently under investigation within partners from the MagnIM project. Long term in vivo experiments with Mg-10Gd and Mg-2Ag pins showed an appropriate degradation behaviour [2]. In vitro cytotoxicity and cell material tests also showed suitable biocompatibility and small differences between these two alloys [3, 4]. Therefore, these Mg-Gd and Mg-Ag binary alloys could be appropriate materials for implantation in humans. During a real application, these alloys could provide a constant DR with a desirable homogeneous degradation and without influencing the healing process or losing mechanical integrity too soon. These alloys could reach the completely absorption after 1-2 years, depending on the application and the implant size. Hence, clinical studies with these materials with controlled impurity content and surface preparation seem the logical next step after all the studies performed within the MagnIM project.

- **Investigation of different linkers to build Mg-MOF layers and further studies**

Metal organic frameworks (MOFs) are novel materials and their applicability for biomedical purposes is still not completely known. The initial study of Mg-MOF as a potential drug nano-carrier on Mg implants, shown in Chapter 7, is considered as novel research and many studies could derive from the present one. For instance, different linkers can be used to deposit Mg-MOF structures in order to improve the biocompatibility of these coatings. Linkers such as fumaric acid, trimesic acid or amino terephthalic acid have also been investigated by Horcajada et al. aiming at drug delivery applications [5].

In the study presented in Chapter 7, Mg-MOF is deposited on a Mg substrate but the procedure to deposit Mg-MOF on the entire implant surface with irregular shapes, such as screw shape is a possibility as future work. Moreover, the corrosion behaviour of fully coated metallic implants would be highly interesting.

Although, the drug delivery of thermally synthesized MOF has been investigated by Horcajada et al. [5], the drug delivery mechanisms of Mg-MOF and the procedure to determine drug loading capacity, entrapment efficiency and release still needs to be defined.

References

[1] T. Kraus, S.F. Fischerauer, A.C. Hänzi, P.J. Uggowitzer, J.F. Löffler, A.M. Weinberg, Acta Biomater. 8 (2012) 1230-1238.

[2] A. Myrissa, N.A. Agha, Y. Lu, E. Martinelli, J. Eichler, G. Szakacs, C. Kleinhans, R. Willumeit-Römer, U. Schäfer, A.-M. Weinberg, Mater. Sci. Eng.: C 61 (2016) 865–874.

[3] F. Cecchinato, N.A. Agha, A.H. Martinez-Sanchez, B.J.C. Luthringer, F. Feyerabend, R. Jimbo, R. Willumeit-Römer, A. Wennerberg, PLoS ONE 10 (2015) DOI:10.1371/journal.pone.0142117.

[4] O. Charyeva, F. Feyerabend, R. Willumeit-Römer, D. Zukowski, C. Gasqueres, G. Szakacs, N.A. Agha, N. Hort, F. Gensch, F. Cecchinato, R. Jimbo, A. Wennerberg, K.S. Lips, MOJ toxicology 1 (2015) 1-6.

[5] P. Horcajada, T. Chalati, C. Serre, B. Gillet, C. Sebrie, T. Baati, J.F. Eubank, D. Heurtaux, P. Clayette, C. Kreuz, J.-S. Chang, Y.K. Hwang, V. Marsaud, P.-N. Bories, L. Cynober, S. Gil, G. Ferey, P. Couvreur, R. Gref, Nat. Mater. 9 (2010) 172-178.

Curriculum Vitae

Iñigo Marco

Date of birth: 05 September 1988
Place of Birth: Vitoria-Gasteiz, Spain
Nationality: Spanish
Email: inigo.marco88@gmail.com

Education background:

2012-2016, KU Leuven, Belgium

- PhD study in Materials Engineering
- Thesis: Degradation testing of magnesium and its alloys aiming at biodegradable implant applications.

2009-2012, Mondragon University, Spain

- Master degree in Industrial Engineering (option: Materials Engineering)
- Thesis: Development of biodegradable magnesium scaffolds by replication casting.

2006-2009, Mondragon University, Spain

- Bachelor degree in Industrial Design
- Thesis: Ergonomics related to product design and its use.

List of publications

Peer reviewed journal papers

I. Marco, O. Van der Biest. Polarization measurements with rotating disc electrode for magnesium degradation characterization. Corros. Sci. 102 (2016) 384-393.

I. Marco, F. Feyerabend, R. Willumeit-Römer, O. Van der Biest, Degradation testing of Mg alloys in Dulbecco's modified eagle medium: Influence of medium sterilization. Mater. Sci. Eng.: C. 62 (2016) 68-78.

I. Marco, A. Myrissa, F. Feyerabend, R. Willumeit-Römer, A. Weinberg, O. Van der Biest. In vivo and in vitro biodegradation comparison of pure Mg, Mg-10Gd and Mg-2Ag: a short term study. Eur. Cell Mater. Revision under review.

I. Marco, N. Campagnol, S. Mostofi, O. Van der Biest. Mg-MOF biodegradable coatings for drug delivery on Mg temporal implants. In preparation.

J. Trinidad, **I. Marco**, G. Arruebarrena, J. Wendt, D. Letzig, E. Saenz De Argandona: Processing of magnesium porous structures by infiltration casting for biomedical applications. Adv. Eng. Mater. Vol. 16, (2014) pp. 241-247.

J. Trinidad, G. Arruebarrena, **I. Marco**, I. Hurtado, E. Saenz de Argandoña: Effectivity of fluoride treatment on hydrogen and corrosion product generation in temporal implants for different magnesium alloys. Proc. Inst. Mech. Eng. Part H, Vol. 227 (2013) pp. 1301-1311.

A. Gil-Santos, **I. Marco**, N. Moelans, N. Hort, O. Van der Biest. Microstructure study and degradation performance of biodegradable Mg-Si-Sr implant alloys. Mater. Sci. Eng.: C. 71 (2016) 25-34.

S. Galli, G. Szakács, F. Lukáč, M. Vlček, A. Gil-Santos, **I. Marco,** N.-A. Agha, S. Mostofi, F. Checcinato, A. Myrissa, O. Charyeva, R. Willumeit-

Römer. The implementation of biodegradable magnesium implants for clinical use: a stony path. In preparation.

S. Galli, J.-U. Hammel, N.-A. Agha, G. Szakács, **I. Marco**, F. Lukac, M. Vlcek, J. Herzen, F. Cecchinato, Y. Naito, T. Zander, F. Wieland, A.Wennerberg, R. Willumeit-Römer, R.Jimbo. Degradation behaviour and bone response of 3 biodegradable magnesium alloys in comparison with titanium: an in vivo investigation. In preparation.

Full papers in international conference proceedings

I. Marco, F. Feyerabend, R. Willumeit-Römer, O. Van der Biest: Influence of testing environment on the degradation behavior of magnesium alloys for bioabsorbable implants. TMS2015 Supplemental Proceedings. John Wiley & Sons Inc., (2015) pp. 497-506.

Participations in international conferences

I. Marco, O. Van der Biest. The use of rotating disk electrode to improve Mg degradation characterization by polarization experiments. 7th Biometal, Carovigno, Italy. 23-28 August 2015; oral talk.

I. Marco, N. Campagnol, J. Fransaer, O. Van der Biest. Mg-MOF biodegradable coatings for drug delivery on Mg temporal implant. 7th Biometal, Carovigno, Italy. 23-28 August 2015; poster.

S. Galli, J.U. Hammel, J. Herzen, G. Szakács, F. Lukáč, M. Vlček, **I. Marco**, A. Wennerberg, R. Willumeit-Römer, R. Jimbo. Corrosion behaviour of 3 Mg-alloys in bone: a high-resolution investigation. 7th Biometal, Carovigno, Italy. 23-28 August 2015.

A. Gil-Santos, G. Szakacs, **I. Marco**, N. Moelans, N. Hort, O. Van der Biest. Effect of composition on the microstructure and properties of candidate Mg-Si-Sr alloys for resorbable material applications. 7th Biometal, Carovigno, Italy. 23-28 August 2015.

I. Marco, F. Feyerabend, R. Willumeit-Römer, O. Van der Biest. Polarization measurements with rotating disk electrode for characterization of the degradation of Mg-Gd and Mg-Ag binary alloys. 3rd Euro BioMAT, Weimar, Germany. 21-22 April 2015; poster and shor oral talk.

I. Marco, F. Feyerabend, R. Willumeit-Römer, O. Van der Biest. Influence of testing environment on the degradation behavior of magnesium alloys for bioabsorbable implants. TMS 144th Annual Meeting and Exhibition.

Symposium of Advanced Materials in Dental and Orthopedic Applications. Orlando, FL, USA, 15-19 March 2015; oral talk.

I. Marco, O. Van der Biest, F. Feyerabend, R. Willumeit-Römer. Comparison of the degradation behaviour of binary Mg-Ag and Mg-Gd alloys in PBS and DMEM. Mater. Sci. Eng. (MSE 2014) biomaterials symposium, 23-25 September 2014; poster and short oral talk.

I. Marco, O. Van der Biest, F. Feyerabend, R. Willumeit-Römer. Comparison of the degradation behaviour of binary Mg-Ag and Mg-Gd alloys in PBS and in physiological conditions. 6th Biometals 2014: Eur. Cell Mater., vol 28. Suppl. 3 (2014) p. 42; poster and short oral talk.

Seminars

Magnesium as biodegradable implant material (seminar). MRC meeting (KU Leuven). 26th February 2015.

Magnesium resorption for biomedical applications (seminar). KU Leuven, Department of materials engineering (MTM). 26th June 2014.

In vitro degradation of Mg-alloys under physiological conditions (seminar). Institute of Materials Research, Helmholtz-Zentrum Geesthacht (HZG), Germany. 10th December 2012.